# Modification of Space Charge Transport in Nanocrystalline Cerium Oxide by Heterogeneous Doping

by

Scott J. Litzelman

B.S. Materials Science and Engineering
North Carolina State University, 2002



SUBMITTED TO THE DEPARTMENT OF MATERIALS SCIENCE AND ENGINEERING
IN PARTIAL FULFILLMENT OF THE REQUIREMENTS FOR THE DEGREE OF

DOCTOR OF PHILOSOPHY
IN MATERIALS SCIENCE AND ENGINEERING

AT THE
MASSACHUSETTS INSTITUTE OF TECHNOLOGY

FEBRUARY 2009



Authored by _____
Scott J. Litzelman
Department of Materials Science and Engineering
November 7, 2008

Certified by _____
Harry L. Tuller
Professor of Ceramics and Electronic Materials
Thesis Supervisor

Accepted by _____
Christine Ortiz
Associate Professor of Materials Science and Engineering
Chair, Departmental Committee on Graduate Students

Modification of Space Charge Transport in Nanocrystalline
Cerium Oxide by Heterogeneous Doping
by
Scott J. Litzelman

Submitted to the Department of Materials Science and Engineering
on November 7, 2008
in Partial Fulfillment of the Requirements for the Degree of
Doctor of Philosophy in Materials Science and Engineering

ABSTRACT

In the search for new materials for energy conversion and storage technologies such as solid oxide fuel cells, nano-ionic materials have become increasingly relevant because unique physical and transport properties that occur on the nanoscale may potentially lead to improved device performance. Nanocrystalline cerium oxide, in particular, has been the subject of intense scruntiny, as researchers have attempted to link trends in electrical conductivity with the properties of space charge layers within the material. In this thesis, efforts designed to intentionally modify the space charge potential, and thus the space charge profiles and the macroscopic conductivity, are described.

Nanocrystalline $CeO_2$ thin films with a columnar microstructure were grown by pulsed laser deposition. A novel heterogeneous doping technique was developed in which thin NiO and $Gd_2O_3$ diffusion sources were deposited on the ceria surface and annealed in the temperature range of 700-800°C in order to diffuse the cations into the ceria layer exclusively along grain boundaries. Time-of-flight secondary ion mass spectrometry (ToF-SIMS) was utilized to measure the diffusion profiles. A single diffusion mechanism, identified as grain boundary diffusion, was observed. Using the constant source solution to the diffusion equation, grain boundary diffusion coefficients on the order of $10^{-15}$ to $10^{-13}$ $cm^2/s$ were obtained for Ni, as well as Mg diffusion emanating from the underlying substrate.

Microfabricated Pt electrodes were deposited on the sample surface, and electrical measurements were made using impedance spectroscopy and two-point DC techniques. The as-deposited thin films displayed a total conductivity and activation energy consistent with reference values in the literature. After in-diffusion, the electrical conductivity decreased by one order of magnitude. Novel electron-blocking electrodes, consisting of dense yttria-stabilized zirconia and porous Pt layers were fabricated in order to deconvolute the ionic and electronic contributions to the total conductivity. In the as-deposited state, the ionic conductivity was determined to be $pO_2$-independent, and the electronic conductivity displayed a slope of -0.30. The ionic transference number in the as-deposited state was 0.34. After annealing either with or without a diffusion source at temperatures of 700-800°C, both the ionic and electronic partial conductivities decreased. The ionic transferene numbers with and without a diffusion source were 0.26 and 0.76, respectively.

Based on the existing framework of charge transport in polycrystalline materials, carrier profiles associated with the Mott-Schottky and Gouy-Chapman models were integrated in order to predict conductivity values based on parameters such as grain size and the space charge potential. Mott-Schottky profiles with a space charge potential of 0.44V were used to describe the behavior of the ceria thin films in the as-deposited state. It is proposed that annealing at temperatures of 700°C and above resulted in segregation of acceptor impurity ions to the grain boundary, resulting in Gouy-Chapman conditions. The best fit to the annealed data occurred for a space charge potential of 0.35 V: a decrease of approximately 90 mV from the as-deposited state. In addition, a high-conductivity interfacial layer between the $CeO_2$ and substrate was detected and was determined to influence samples with no surface diffusion source to a greater degree than those with NiO or $Gd_2O_3$.

Thesis Supervisor: Harry L. Tuller
Title: Professor of Ceramics and Electronic Materials

CONTENTS

FIGURES

Figure Page

Figure Page

Figure Page

Figure Page

Figure Page

Figure Page

Figure Page

TABLES

ACKNOWLEDGEMENTS

While in some ways a Ph.D. is a very individual effort, it is never successfully completed alone. I have been blessed in many ways with a wonderful support network, both personally and professionally. First, I would like to thank my doctoral advisor, Professor Harry Tuller. Under Professor Tuller's guidance over the past six years, I have grown by leaps and bounds (I hope!) as a young scientist. He has been a patient and supportive mentor, and I am truly grateful to have been a member of his research group. I would also like to thank my thesis committee for their time and advice on this project. It has been a priviledge to work with Professors Yet-Ming Chiang, Paula Hammond, and Carl Thompson.

An important phase of this study took place while I was a visiting student in the research group of Professor Manfred Martin at the Institute for Physical Chemistry at RWTH Aachen University in Aachen, Germany. I am grateful to have been the recipient of the Charlemagne Scholarship, which allowed me to travel to Aachen to perform secondary ion mass spectrometry (SIMS) studies. I would particularly like to thank Dr. Roger De Souza, who took me under his wing in Aachen and taught me the fundamentals of SIMS. A great deal of time was spent in the SIMS lab with Dr. De Souza, waiting for a SIMS run to finish while trying to explain the American and British senses of humor to each other. Thanks to the students of the Martin group, my stay in Germany was also very enjoyable. I had not anticipated becoming a witness to the battle between Kölsch and Alt bier. I would also like to thank my student counterparts at the University of Karlsruhe, Benjamin Butz and Christoph Peters, for the fruitful collaboration on nano-ionics and fun times in Germany and the U.S.

Many thanks go to the graduate students, post-docs, and visiting scientists of the Tuller group. As colleages and friends, they taught me many important technical skills, helped me navigate the ups and downs of research, and were always around for lively discussions and lots of coffee. Thanks to this group of people, my time at MIT was very enriching: Jürgen Fleig, Tsachi Avrahami, Yongki Min, Todd Stefanik, Huankiat Seh, Dilan Seneviratne, Josh Hertz, Avner Rothschild, Il-Doo Kim, Anja Bierberle-Hütter, Kathy Sahner, WooSik Kim, Jussi Hiltunen, Takeo Hyodo, Martin Soegaard, Cecilia Solis, WooChul Jung, George Whitfield, Yoonsil Jin, Kengo Haga, Jae-Min Hong, and Luanne Rolly. I would also like to thank Kurt Broderick of the Exploratory Materials Laboratory and Tim McClure, Libby Shaw, and Scott Speakman of the Center for Materials Science and Engineering for invaluable technical help and advice. Also, I would not have gotten very far without the help of two great administrative assistants, Sally Honda and Teri Chung.

I am also greatful for the wonderful friends that I made at MIT. The cast and crew of the Muddy Charles Pub provided me with a release valve and more than a few interesting stories during my time as a bartender. In particular, I want to thank John Mills and Joe Contrada for getting me started in my second career at MIT. It somehow seems appropriate that so much time spent in a pub was balanced by my experiences with the Tech Catholic Community, led by Fr. Paul Reynolds and Fr. Richard Clancy. TCC provided me with the opportunity for prayer, reflection, and the chance to be part of a great community (it also helped me find a spouse)! I would also like to thank my friends, especially my former roommates Carl Dohrman, Chris Fischer, Tim Mueller, and Asher Sinensky. I will never forget the fun times at 174 Morrison Ave.

I would like to thank my family for their support during a seemingly endless time spent at university. Without the encouragement and love of Mom, Dad, Marie, and Jenny, I certainly would have never made it this far. Thank you. Finally, I would like to thank my wonderful and loving wife Christine, my rock of support. Christine showed me infinite patience and love as she listened to my rants over failed experiments and excited stories of success during this thesis. I am blessed to have her as a best friend and lifelong companion.

# CHAPTER 1. INTRODUCTION

## *1.1 Motivation*

Of the many scientific and technological advances of the 20th century, the rise of solid state electronics would certainly rank among the most significant, as revolutions in computation, communication, and information technologies were enabled that today are virtually taken for granted. Beginning with the first point contact transistor, fabricated by John Bardeen, Walter Brattain, and William Shockley at Bell Laboratories in 1947 [1], a series of advancements in solid state electronics ultimately led to the replacement of vacuum tubes devices based on thermionic emission with transistors. The shift to logic devices constructed solely from the 'solid state' allowed for fabrication of integrated circuits, first demonstrated in 1959 by Jack Kilby of Texas Instruments and Robert Noyce of Fairchild Semiconductor [2], as well as scaling described by Moore's Law [3] that have made today's digital age possible. While there is much debate today as to whether Moore's Law, which describes a doubling of devices on a chip every 18 months, remains valid, it is clear that the evolution of solid state electronics remains a scientific and technological marvel.

Analogous to solid state electronics, though much less mature in terms of miniaturization and commercialization, is the field of solid state *ionics*. This field, as implied by its moniker, is concerned with the chemistry and physics of ionic materials in the solid state, particularly the motion of mass and charge. Like the field of solid state electronics, the motivation for research in solid state ionics is driven by crucial technological applications, such as fuel cells for energy conversion, batteries for storage, and sensors for environmental monitoring [4]. A material that exemplifies solid state ionics is the solid electrolyte, a material with high ionic conductivity but very low electronic conductivity. As shown in Figure 1, both battery and fuel cell technologies depend on high ionic conduction for efficient operation of electrolytes. It is also evident that mixed ionic and electronic conduction (MIEC) is required for other components within these technologies, particularly electrodes.

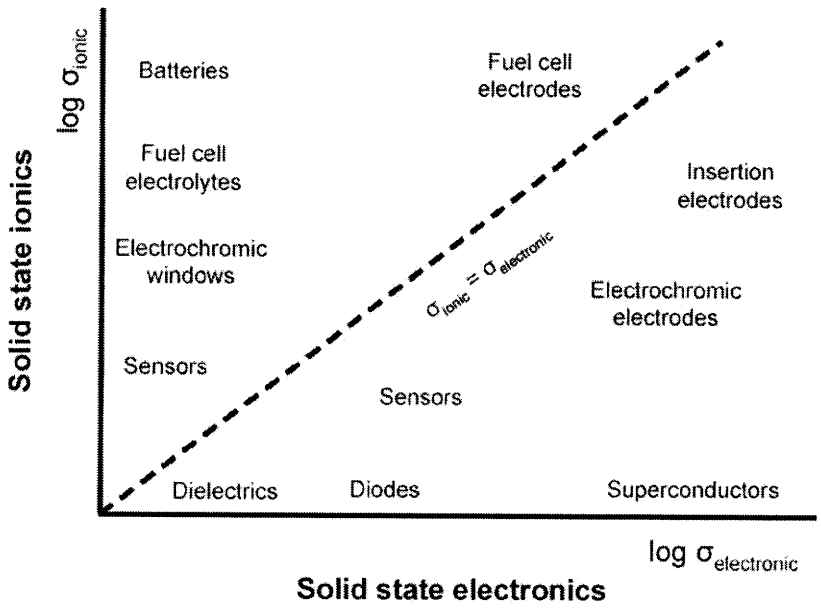


**Figure 1: Material applications, classified by fields of solid state electronics and ionics. Adapted from Tuller [5].**

It is not a coincidence that much of the research today in solid state ionics is focused on energy and the environment. For several decades, scientists have made it increasingly clear that the world's dependence on fossil fuels for power generation will have a grave impact on the environment and quality of life for future generations. Energy sources such as coal, petroleum and natural gas are a source of pollutants that exacerbate the greenhouse effect, global warming, and the depletion of the ozone layer. In 2005, fossil fuel consumption in the U.S. resulted in the release of 6.1 billion metric tons of $CO_2$ into the atmosphere [6]. Historically, there has been a strong correlation between the $CO_2$ concentration in the atmosphere and the average temperature of the Earth and, as shown in Figure 2, the increase in atmospheric $CO_2$ levels to 400 ppm and above is widely expected to have severe and potentially irreversible implications for the global environment. The majority of this increase emanates from the burning of fossil fuels.

Other rationales for reducing the current reliance upon fossil fuels are strategic and economic in nature. In 2005, one-third of the approximately 100 quadrillion BTUs consumed by the U.S. was imported; approximately 40% of all U.S. energy consumption was based on petroleum [7]. As both a scarce and non-renewable resource, reliance upon petroleum is not sustainable due to ever-increasing costs and the inevitable depletion of this resource. Additionally, the global distribution of petroleum resources creates a delicate political balance, for the United States must work with OPEC countries

that may be unstable and/or hostile to the U.S. For all of these reasons and more, the search for new methods of energy conversion and storage is now considered worldwide to be of vital importance. Solid state ionics is expected to play a key role in this effort, as materials limitations is currently one of the largest factors hindering the advancement of clean energy technologies.

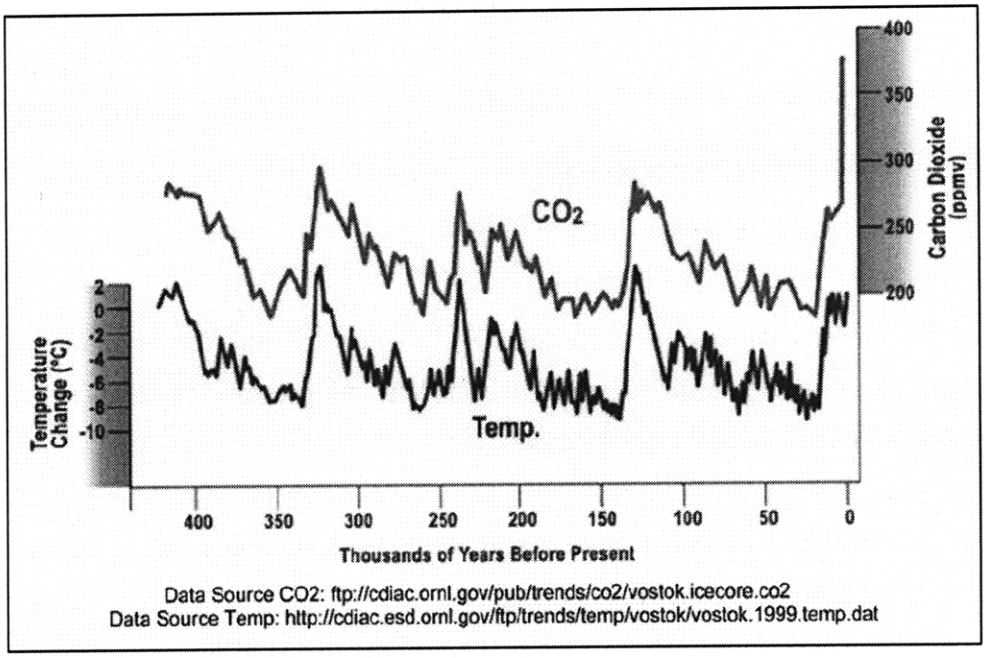


**Figure 2: Historical and current trends for $CO_2$ concentration and Earth temperature shifts [7].**

### *1.2 Ionic and Electronic Conduction in Electroceramic Materials*

The first experimental phenomenon suggesting electrical transport by carriers other than electrons dates back to Michael Faraday in 1833 [8]. Faraday observed an increase in the electrical conductivity of $Ag_2S$ with temperature, opposite the typical trend of metallic conductors. The concept of what is now the solid electrolyte fuel cell, namely the generation of electricity through separation of air and fuel by a membrane, was first conceived by Gaugain in 1853 [9]. According to Knauth and Tuller [4], "The first major invention using solid electrolytes was the discovery by Nernst [10] of an electric lighting device..." This device eventually incorporated a material, $Zr_{0.74}Y_{0.26}O_{2-x}$, known as the 'Nernst mass' [11] (also known as yttria-stabilized zirconia, or 'YSZ'), though the lighting device was eventually replaced by the tungsten filament. It is interesting to note that the Nernst mass is virtually identical to the YSZ composition used in most high temperature SOFCs today. It is not clear to the author whether this observation reflects more on the ingenuity and skill of the late 19$^{th}$/early 20$^{th}$ century scientists, or on the overall lack of new materials development in solid

state ionics!

The unifying feature of the technologies mentioned above is ionic conduction: the flow of electrical current through the motion of ions. In the most general form, the total electrical conductivity of a material is the sum of the electronic and ionic partial conductivities:

$$\sigma_{total} = \sigma_{ionic} + \sigma_{electronic} \tag{1}$$

where each partial conductivity is defined as:

$$\sigma_j = z_j q \mu_j c_j \tag{2}$$

where $z$ is the carrier charge, $q$ is the elementary charge, $\mu$ is the carrier mobility, and $c$ is concentration. As discussed with regard to the applications presented in Figure 1 , there are essentially three classes of electrical conductors:

1. Electronic conductors, such as metals and doped semiconductors (Si, GaAs, etc.)
2. Ionic conductors, such as $Ag_2S$ and YSZ
3. Mixed conductors (MIEC), such as $(La,Sr)(Co,Fe)O_3$ (LSCF)

It is convenient to define a parameter that is indicative of the primary conduction type and the degree of mixed conduction. This parameter is known as the transference number, where the ionic transference number (or alternatively, the electronic transference number) is defined as:

$$t_i = \frac{\sigma_{ion}}{\sigma_{ion} + \sigma_{el}} \tag{3}$$

To enable optimal performance of a solid oxide fuel cell (SOFC), for example, the ionic transference number of the electrolyte must be close to unity in order to avoid cell losses due to electronic leakage currents. For many materials, the mechanism of conduction via electrons or holes is well-described by the traditional band model in which delocalized carriers conduct freely within their electronic band. In this case, the mobility typically decreases with temperature by a power law, $T^{-\eta}$, where $\eta$ often assumes values of 2.3 and lower, and the carrier concentration increases exponentially [12]. As a diffusion process, the mechanism of ionic conduction differs notably from electronic band conduction. While the carrier concentration of ionic defects, like their electronic counterparts, is thermally-activated in the intrinsic regime, the mobility is also thermally-activated. This is illustrated

by examination of diffusion as an atomistic diffusion 'jumping' process, here in the general case of self-diffusion by a vacancy mechanism [13]:

$$D^* = fa^2 \nu \exp\left(\frac{S_V^m + S_V^f}{k}\right)\exp\left(-\frac{H_V^m + H_V^f}{kT}\right) \tag{4}$$

where $f$ is the correlation factor (less than unity for correlated motion), $a$ is the interatomic distance, $\upsilon$ is the jump frequency, and $S_V^m$, $S_V^f$, $H_V^m$, $H_V^f$ are the vibrational and formation entropies and enthalpies of migration and formation, respectively. By combining the temperature independent terms into a pre-exponential factor $D^{*o}$ and the enthalpy terms into $E$, a more common expression for $D^*$ is:

$$D^* = D^{*o} \exp\left(-\frac{E}{kT}\right) \tag{5}$$

For any crystal structure, an energy barrier described by $H_V^m$ exists between two equivalent sites that must be overcome in order for the jump to take place. This atomistic diffusivity yields insight into the ionic conductivity, as the diffusivity of an ionic defect is related to its drift mobility in an electric field by the Nernst-Einstein equation:

$$\frac{D}{\mu} = \frac{kT}{zq} \tag{6}$$

In practice, the concentration of ionic charge carriers is fixed extrinsically through homogeneous doping. The two most common examples are YSZ and cerium gadolinium oxide (CGO), where $Y^{3+}$ and $Gd^{3+}$ substitute on $Zr^{4+}$ and $Ce^{4+}$ sites, respectively, and are in turn electrostatically compensated by the formation of oxygen vacancies. Thus, the concentration of conducting ionic species is directly proportional to the doping content. Since these fluorite compounds have a very high solubility of similarly-sized aliovalent dopants, with several reports suggesting solid solutions of up to 40% in $CeO_2$ [14, 15], the doping levels can become quite high. Unfortunately, the ionic conductivity does not increase monotonically with doping concentration: a maximum exists above which additional doping results in *reduced* conduction, as shown in Figure 3.

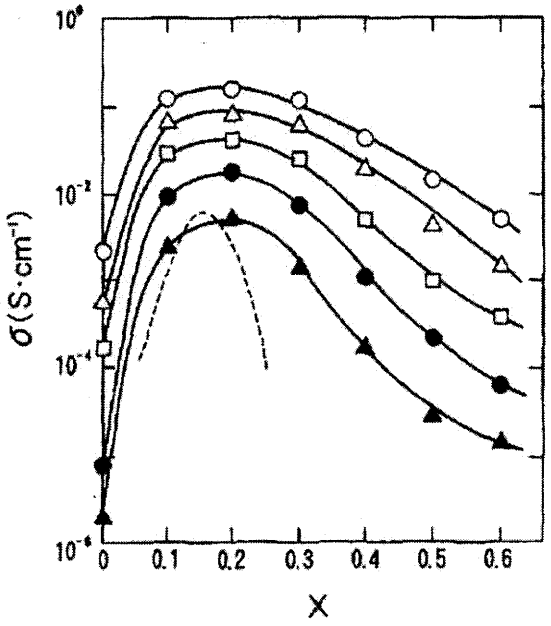


**Figure 3: Conductivity versus Sm concentration in $(CeO_2)_{1-x}$ $(SmO_{1.5})_x$: open circles 900°C, open triangles 800°C, open squares 700°C, closed circles 600°C, closed trianges 500°C, dashed line Ca-doped $ZrO_2$ 800°C [16].**

There are several theories to describe this phenomenon, all of which indicate reduced oxygen vacancy mobility. One common theory proposes the widespread formation of defect associates with low mobility, such as $\left\{A'_{Ce}V_O^{\bullet\bullet}\right\}^{\bullet}$ [17]. A recent theory suggests that the change in 'atomistic landscape,' due to the changing activation barrier with different types of neighboring cation pairs, is the primary factor limiting mobility [18]. Regardless of the specific mechanism, it is clear that the need for materials with improved ionic conductivity cannot be achieved by simply doping existing materials to a higher concentration.

### *1.3 Properties of Cerium Oxide*

Cerium oxide, also known as 'ceria,' is a fascinating and versatile material that has been researched extensively for over 40 years. Ceria is simple enough that it is often used as a model system for fundamental studies in mixed ionic-electronic conduction, yet it is also sufficiently subtle and complex to remain intriguing to researchers. While ceria is most prominently studied for its role as an SOFC electrolyte, it also has applications in catalysis, electrochromic materials, and as electrode materials [17]. The basic properties of $CeO_2$ are listed in Table 1.

| Property | Value | Ref. |
|---|---|---|
| Structure | Calcium fluoride | |
| Space group | Fm3m | 19 |
| Melting point | ~ 2475°C | 19 |
| Lattice parameter (room temperature) | 0.541134 nm | 20 |
| Refractive index (visible) | 2.1 | 21 |
| Relative dielectric constant | 25 | 22 |
| Linear thermal expansion (Room temp. to 500°C) | $11.5 \times 10^{-6}$ $K^{-1}$ | 23 |

**Table 1: Fundamental physical properties of $CeO_2$**

$CeO_2$ is an example of a MIEC: its conductivity depends on the oxygen activity in the surrounding atmosphere as well as the impurity content, whether that is the result of intentional doping or simply background impurities. Electronic conductivity in $CeO_2$ occurs via a small polaron hopping mechanism between the 3+ and 4+ states of Ce [24-26]. The ionic conductivity takes place via oxygen vacancy conduction that results from substitution of acceptor dopants in the solid. An important property of $CeO_2$ is its capacity for oxygen deficiency, as $CeO_2$ can be reduced to $CeO_{2-x}$ at elevated temperatures and low $pO_2$. This is illustrated in Figure 4 as a function of temperature and $pO_2$ [27]. It can be seen that nonstoichiometry as great as $CeO_{1.9}$ can be achieved at partial pressures of $10^{-8}$ atm and less at temperatures of approximately 1300°C.

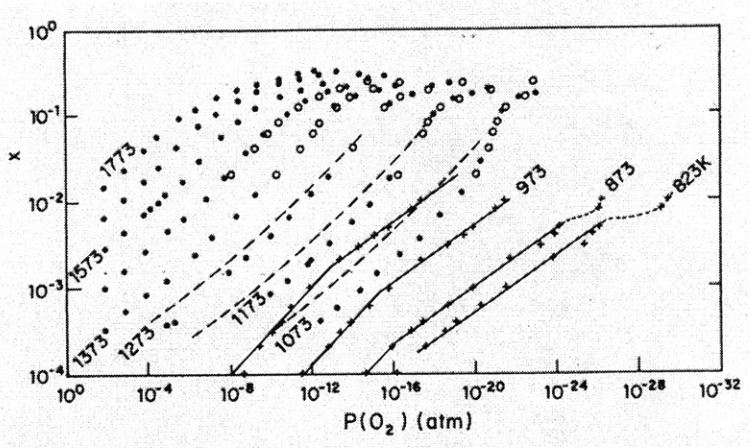


**Figure 4: Oxygen deficiency, $x$, of $CeO_{2-x}$ as a function of temperature and $pO_2$, as compiled by Riess, *et al.* Shown are data from Tuller and Nowick (dashed lines) [26], Panlener, *et al.* (•) [28], Bevan and Kordis (○) [29], as well as experimental (+) and theoretical (solid lines) results from Ref. 27.**

The reduction occurs via a transition from $Ce^{4+}$ to $Ce^{3+}$, which is also written as $Ce_{Ce}'$ in Kröger-Vink notation. Based on oxygen self-diffusion research, it is widely accepted that the charge compensating defects in reduced $CeO_2$ are oxygen vacancies and not interstitial Ce species [30]. In the typical case of microcrystalline $CeO_2$ at ambient pressure, the electrical conductivity is often extrinsically-controlled by the acceptor content. This behavior is essentially $pO_2$-independent, as the concentration of ionic species compensating the acceptor dopants is significantly higher than any atmosphere-induced nonstoichiometry in this intermediate range. Upon reduction at low $pO_2$, the creation of oxygen vacancies, usually double-charged and represented by $V_O^{\bullet\bullet}$, is charge-compensated by the release of electrons. The hole conductivity within the partial pressure range of interest, $10^{-26}$ to 1 atm, is negligible [24].

For the ceria system, the partial conductivities found in Eq. 2 can be expanded as:

$$\sigma_{ion} = 2q\left[V_O^{\bullet\bullet}\right]\mu_{V_O^{\bullet\bullet}} \tag{7}$$

$$\sigma_{el} = nq\mu_e = nq\left(\frac{\mu_o}{T}\right)\exp\left(-\frac{E_H}{kT}\right) \tag{8}$$

where $\mu_O$ is a temperature-independent constant, $E_H$ the hopping energy, and $k$ is Boltzmann's constant. The oxygen vacancy concentration in Eq. 7 can be controlled either by acceptor dopants or by the reduction reaction

$$O_O^x \longrightarrow V_O^{\bullet\bullet} + 2e' + \tfrac{1}{2}O_2(g) \tag{9}$$

and its corresponding equilibrium constant, $K_R$

$$K_R(T) = \left[V_O^{\bullet\bullet}\right]n^2 P_{O_2}^{1/2} \tag{10}$$

The temperature dependence of this constant is

$$K_R(T) = K_R^o \exp\left(-\frac{\Delta H_R}{kT}\right) \tag{11}$$

where $K_R^o$ is a temperature-independent constant and $\Delta H_R$ is the enthalpy of formation for oxygen vacancies. Given the relevant ionic and electronic defects, the electroneutrality expression is

$$2\left[V_O^{\bullet\bullet}\right] = n + \left[A_{Ce}'\right] \tag{12}$$

Combining the two expressions for the reduction constant (Eqs. 10 and 11) as well as Eq. 8, one can arrive at an expression that describes the electronic conductivity as a function of both temperature and $pO_2$

$$\sigma_{el}T = \sigma_O \exp\left(-\frac{E_A}{kT}\right)P_{O_2}^{-r} \tag{13}$$

where $\sigma_o$ is a temperature-independent constant, $E_A$ is the activation energy, and $r$ is the exponential term that depends on the type of charge compensation.

It is now appropriate to consider the Brouwer approximations [31] for the various $pO_2$ regimes of conduction. At low $pO_2$, the reduction reaction dominates and $CeO_2$ behaves intrinsically; the corresponding Brouwer approximation is

$$2\left[V_O^{\bullet\bullet}\right] = n \tag{14}$$

Substituting this approximation into Eq. 10 and rearranging leads to

$$n = \left(2K_R\right)^{1/3} P_{O_2}^{-1/6} \tag{15}$$

The exponent in Eq. 13, $r$, is -1/6 and $E_A$ becomes

$$E_A = \frac{\Delta H_R}{3} + E_H \tag{16}$$

At higher $pO_2$, oxygen vacancies are compensated, and in fact determined, by the acceptor concentration. This is known as 'extrinsic' behavior.

$$2\left[V_O^{\bullet\bullet}\right] = \left[A_{Ce}'\right] \tag{17}$$

The electron concentration is now given by

$$n = \left(\frac{2K_R}{\left[A_{Ce}'\right]}\right)^{1/2} P_{O_2}^{-1/4} \tag{18}$$

The $pO_2$ exponent is -1/4 and $E_A$ is

$$E_A = \frac{\Delta H_R}{2} + E_H \tag{19}$$

Finally, the total conductivity may be found by combining Eqs. 7 and 13:

$$\sigma = 2q\left[V_O^{\bullet\bullet}\right]\mu_{V_O^{\bullet\bullet}} + \frac{\sigma_O}{T}\exp\left(-\frac{E_A}{kT}\right)P_{O_2}^{\ -r} \tag{20}$$

In 1959, Ruloph [32] studied the electrical conductivity of pure $CeO_2$ and found a $pO_2$ dependence of -1/5.6. Vinokurov and co-workers [33] described $CeO_2$ as being a MIEC, though the transference number for $CeO_{1.9}$ is approximately 0.028 [17]. Such a negative slope indicates conduction via electrons; as mentioned above, this n-type conduction takes place via small-polaron hopping [24]. Small polarons are defects where the electron is trapped at a site due to displacement of the surrounding ions. The small polaron is denoted in this case by $Ce_{Ce}'$ and conduction takes place by a coupled motion of the electron and lattice displacement. This 'hopping' is thermally activated and has been described in Eq. 8. The hopping energy is shown as a function of nonstoichiometry in Figure 5:

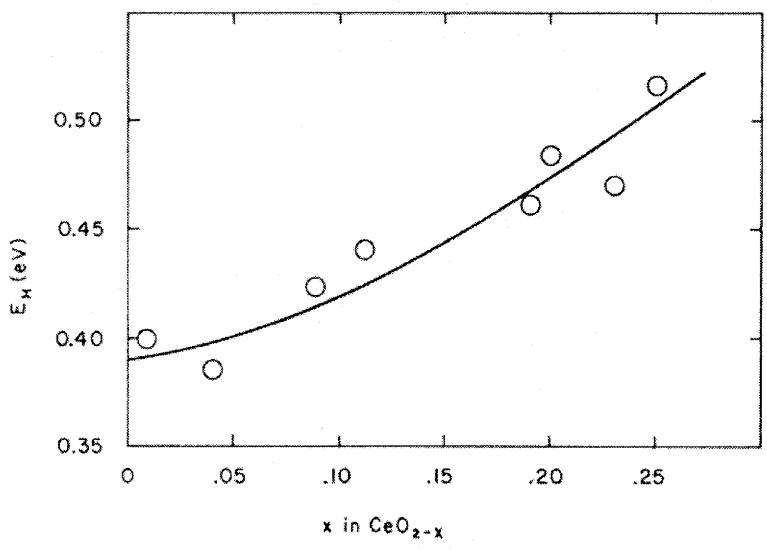


**Figure 5: Hopping energy, $E_H$ as a function of nonstoichiometry [24].**

This data shows $E_H$ to vary roughly between 0.4-0.5 eV over the nonstoichiometry range of interest. For values of $x$ = 0.07 and above, Naik and Tien [25] report values that are in good agreement with Figure 5. In the near-stoichiometry range, however, the values reported in Ref. 25 were about 0.2 eV lower.

The total electrical conductivity of pure $CeO_{2-x}$ is plotted as a function of $x$ in Figure 6:

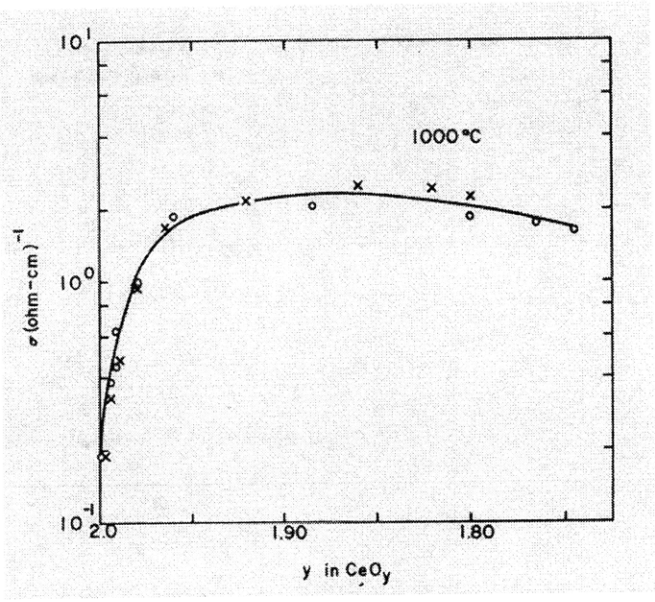


**Figure 6: Conductivity of $CeO_{2-x}$ (y = 2-x) at 1000°C as a function of nonstoichiometry [24].**

With increased oxygen deficiency, the conductivity saturates and a maximum is reached near a composition of $CeO_{1.90}$. Tuller and Nowick attributed the conductivity decrease beyond this composition to both decreased mobility, evident by the increasing $E_H$ with $x$ in Figure 5, and a decreased carrier concentration. The latter phenomenon was proposed to result form local ordering of the oxygen vacancies and a subsequent immobilization of some of the $Ce^{3+}$ ions. This concept was previously suggested by Subba Rao, *et al.*, who examined the properties of the related compounds $PrO_{2-x}$ and $TbO_{2-x}$ [34].

An Arrhenius plot of the electrical conductivity is found in Figure 7. Data for both single crystals and sintered polycrystalline samples are shown. The data from 600 to 900°C for both specimen types is clearly in good agreement, which suggests that no significant impediment of electrical conduction is associated with grain boundaries in this material. This observation is also supported by the work of Brugner and Blumenthal [35], who also compared the conductivity of single crystals and sintered polycrystalline samples and found them to be comparable.

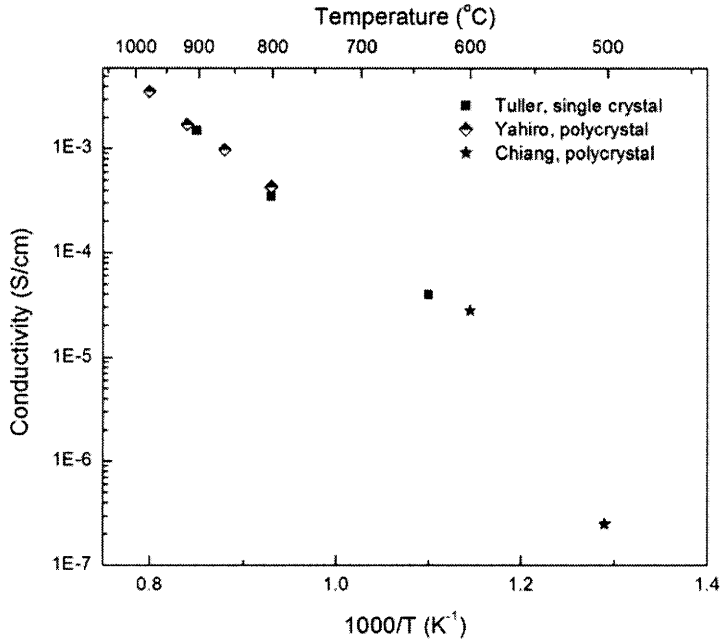


**Figure 7: Arrehnius plot of the conductivity for single crystals [26], and sintered polycrystalline samples at $pO_2$ = 0.21 atm [36, 37].**

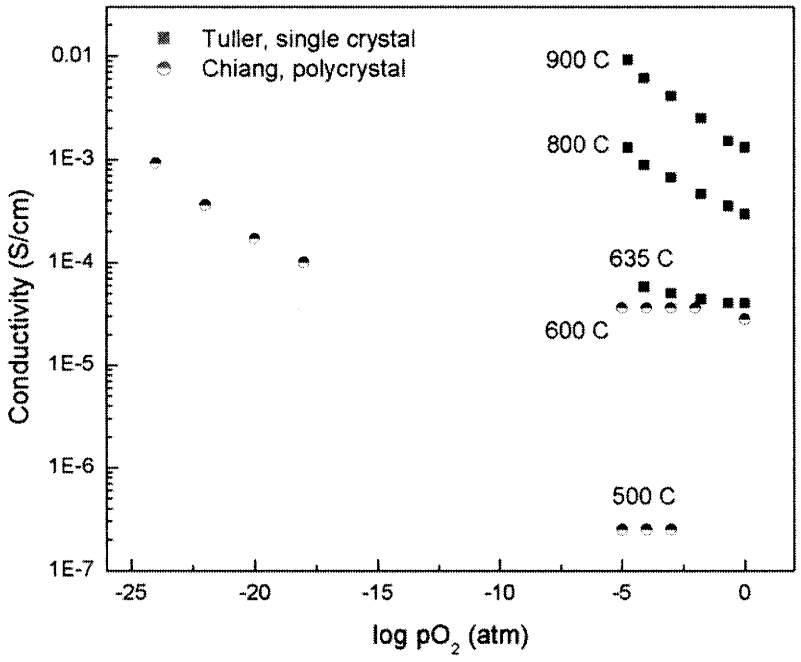


**Figure 8: Conductivity as a function of $pO_2$ for single crystal (squares, Ref. 26) and polycrystals (filled circles, Ref. 37).**

The electrical conductivity of $CeO_2$ is plotted in Figure 8 as a function of $pO_2$. It is clear that $CeO_2$ becomes increasingly conductive at lower $pO_2$ due to an increased electron concentration that is

formed to compensate the increasing number of oxygen vacancies. It is interesting to note, though not unexpected, that the reduction reaction dominates at a comparably higher $pO_2$ at higher temperatures. This is due to the thermally-activated nature of the reaction. At lower temperatures such as 500-600°C, the $pO_2$ dependence from $10^{-2}$ to $10^{-5}$ atm is flat and thus indicative of dominant ionic carriers. However, at temperatures such as 800 and 900°C, the slope approaches -1/4 and the same partial pressure range is clearly dominated by the reduction reaction and the corresponding electronic conductivity.

As seen in Eq. 13, a plot of $\ln(\sigma_{el}T)$ vs. inverse temperature will yield a slope that is proportional to $E_A$. Knowledge of the appropriate compensating mechanism and $E_H$ allows one to substitute this value into Eqs. 16 or 19 in order to find the formation enthalpy for doubly ionized oxygen vacancies, $\Delta H_R$. The value of this reduction enthalpy in bulk $CeO_2$ has been reported to range between 3.94 [38] and 4.67 eV [26]. However, most of the scientific and commercial interest pertains to doped $CeO_2$, with much of the technological interest relating to SOFC electrolytes. Kevane, *et al.* first reported that the addition of up to 10 wt% CaO in $CeO_2$ resulted in extrinsic ionic conduction [39]. This defect reaction is written as

$$CaO \xrightarrow{CeO_2} Ca''_{Ce} + V_O^{\bullet\bullet} + O_O^x \tag{21}$$

Many of the rare earth oxides and lanthanides are soluble in $CeO_2$. Figure 9 shows the relation between maximum ionic conductivity and size of the dopant cation in ceria systems. It is evident that substitution of $Ce^{4+}$ with $Sm^{3+}$ results in the maximum electrical conductivity, though the scarcity of samarium has led to a focus on gadolinium as the primary acceptor in ceria-based systems, as discussed below.

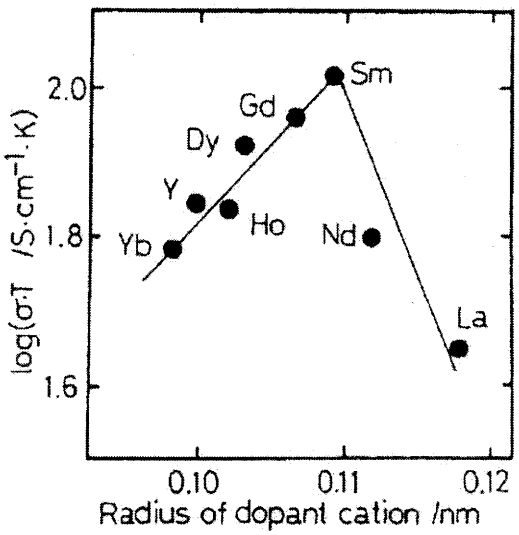


**Figure 9: Ionic conductivity at 800°C versus size of the dopant cation in $(CeO_2)_{0.8}(LnO_{1.5})_{0.2}$ [40].**

Kilner studied the effect of ionic radius on conductivity and found that a correlation exists between $\sigma_{ion}$ and $r_{dopant}/r_{host}$ (known as "R") [41, 42]. His findings suggest that R should be greater than or equal to 1 in order to minimize the defect association energy. Kim studied the change of the lattice parameter as a function of doping content [43]. His conclusion was that the ideal dopant would be the one that changed the lattice parameter the least, since a minimization of internal stresses would intuitively lead to higher ionic conductivity. The arguments of Kilner and Kim are supported by the fact that Gd and Sm lead to the highest conductivity in doped ceria systems. The incorporation of Gd is given as:

$$Gd_2O_3 \xrightarrow{2CeO_2} 2Gd'_{Ce} + V_O^{\bullet\bullet} + 3O_O^x \qquad (22)$$

CGO is commonly prepared in the concentration range of $CeO_2$:10% $Gd_2O_3$ (CGO-10) to $CeO_2$:20% $Gd_2O_3$ (CGO-20). At ambient oxygen partial pressure, these compositions result in high ionic conductivity and negligible electronic conductivity.

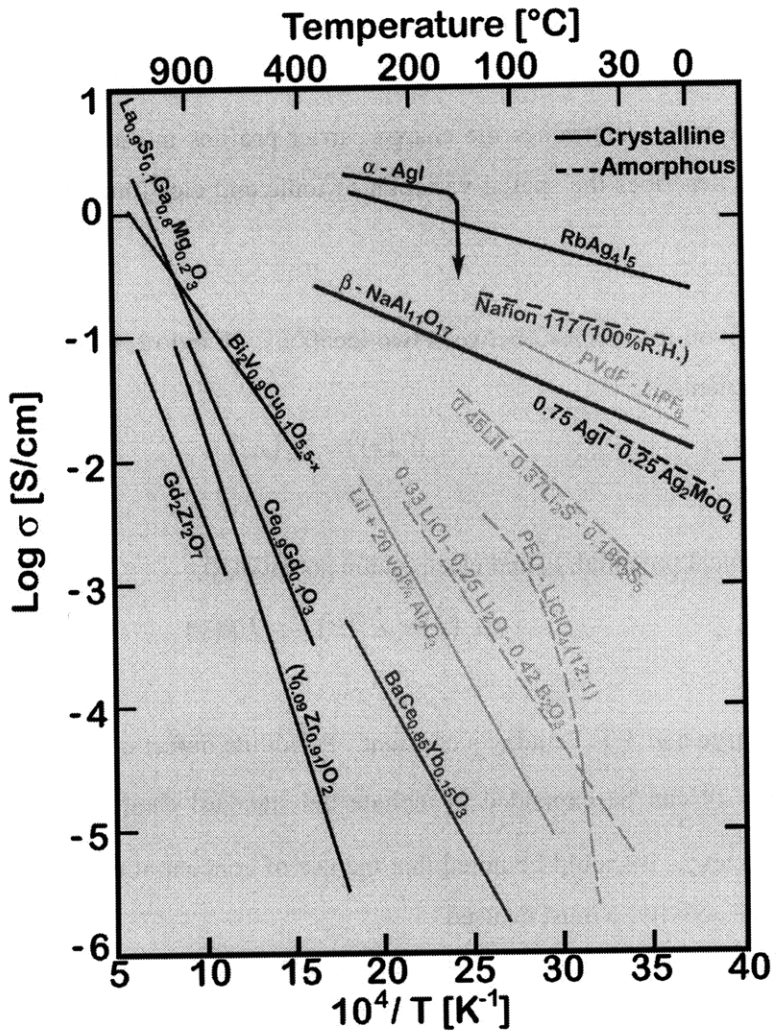


**Figure 10: The electrical conductivity of common electrolytes [44].**

The conductivity of CGO-10 and other solid electrolytes is shown in Figure 10. It is interesting to note that, while $(Y_{0.09}Zr_{0.91})O_2$ (YSZ-09) is one of the most common SOFC electrolytes, CGO-10 is at least half an order of magnitude more conductive. This can be attributed to the chemical stability of YSZ-09, which is greater than CGO-10 with respect to reducing atmospheres on the anode side of the fuel cell. Despite this, its high ionic conductivity makes CGO desirable for intermediate temperature SOFCs, especially in the range of 500-600°C, because reduction on the anode side is less prevalent [45].

### *1.4 Properties of Space Charge Regions*

Ionic solids, while neutrally-charged overall, do contain local areas of electrostatic charge known as space charge regions. Crystalline symmetry is broken at interfaces such as grain boundaries and

surfaces, and the subsequent redistribution of anions and cations leads to local charge. The space charge potential, $\Delta\phi = \phi(0) - \phi(\infty)$, where $\phi(0)$ is the potential at the interface and $\phi(\infty)$ is the reference value in the bulk, determines the charge carrier profiles in the space charge layer. This section quantitatively describes the spatial variation of ionic and electronic defects within the space charge layer.

The equilibrium condition for species $j$ between two locations, $x1$ and $x2$, is given by the constancy of the electrochemical potential:

$$\tilde{\mu}_j(x1) = \tilde{\mu}_j(x2) \tag{23}$$

consisting of the chemical potential, $\mu$, and electrostatic potential, $\phi$:

$$\tilde{\mu}_j(x) = \mu_j(x) + z_j F\phi(x) \tag{24}$$

where $z_j$ is the net charge and $F$ is Faraday's constant. For dilute defect concentrations, the chemical potential term in Eq. 24 can be expanded to include the standard chemical potential, $\mu_j^o$, and the concentrations of species $j$. It should be noted that the use of concentration is only valid for a dilute solution; otherwise the activity, $a$ must be used.

$$\mu_j = \mu_j^o + RT\ln c_j \tag{25}$$

Substituting into Eq. 23, the following electrochemical equilibrium is found:

$$\mu_j^o + RT\ln c_j(x1) + z_j F\phi(x1) = \mu_j^o + RT\ln c_j(x2) + z_j F\phi(x2) \tag{26}$$

or

$$\frac{c_j(x2)}{c_j(x1)} = \exp\left[-z_j F\left(\frac{\phi(x2)-\phi(x1)}{RT}\right)\right] \tag{27}$$

Equation 27 demonstrates that an electrical potential difference is compensated by non-uniform chemical profiles in order to preserve electrochemical equilibrium. At or near an interface, one can rewrite Eq. 27 and define the concentration enhancement, $\zeta$, between position $x$ (i.e. within the space charge region) and the bulk ($x = \infty$) [46]:

$$\zeta_A^{1/z_j} = \exp-\frac{F[\phi(x)-\phi(\infty)]}{RT} \tag{28}$$

Equation 28 can be rewritten more conveniently to express the change in charge concentration relative to the bulk concentration as a function of the local electrical potential:

$$\left(\frac{c_j(x)}{c_{j\infty}}\right)^{1/z_j} = \exp\left(-\frac{e}{k_B T}\Delta\phi(x)\right) \tag{29}$$

In order to find the concentration profiles, one must solve for the spatial variation of the electrical potential. Beginning with the first of Maxwell's equations (Gauss' law for electricity),

$$\nabla \cdot E = \frac{\rho}{\varepsilon} \tag{30}$$

and the definition of an electric field:

$$E = -\nabla\phi \tag{31}$$

a partial differential equation is found as a specific example of Poisson's equation:

$$\nabla^2\phi = -\frac{\rho}{\varepsilon_o\varepsilon_r} = -\frac{z_j e c_j}{\varepsilon_o\varepsilon_r} \tag{32}$$

Poisson's equation and Eq. 29 can be combined to form the Poisson-Boltzmann differential equation:

$$\nabla^2\phi(\vec{r}) = -\frac{e}{\varepsilon_o\varepsilon_r}\sum_j z_j c_{j\infty}\exp\left(-\frac{z_j e\phi(\vec{r})}{kT}\right) \tag{33}$$

which can be simplified for the common case of electrostatic potential variation in one dimension and one predominant defect:

$$\frac{d^2\phi}{dx^2} = -\frac{e z_j c_{j\infty}}{\varepsilon_o\varepsilon_r}\exp\left(\frac{-z_j e}{kT}\Delta\phi(x)\right) \tag{34}$$

Equation 34 represents an ordinary differential equation requiring two boundary conditions and a reference point for the potential, commonly set to 0 in the bulk. The following derivation, presented by Evans and Wennerström, yields the spatial variation of the electrostatic potential under Gouy-Chapman conditions, which specify redistribution of all charged defects [47]. One boundary

condition is a zero slope in the potential in the bulk ($d\varphi/dx = 0$ as $x \rightarrow \infty$). Equation 34 can be simplified via the identity:

$$\frac{d}{dz}\left(\frac{df}{dz}\right)^2 = 2\frac{d^2 f}{dz^2}\frac{df}{dz} \tag{35}$$

yielding

$$\frac{d}{dx}\left(\frac{d\phi}{dx}\right)^2 = -\frac{2e}{\varepsilon_o \varepsilon_r}\left(\frac{d\phi}{dx}\right) z_j c_{j\infty} \exp\left(\frac{-z_j e\phi}{kT}\right) \tag{36}$$

the right-hand side can be rewritten in a simpler form as:

$$= \frac{2kT}{\varepsilon_o \varepsilon r}\ c_{j\infty}\frac{d}{dx}\exp\left(-\frac{z_j e\phi}{kT}\right) \tag{37}$$

Setting the limits of integration to be $x$ and $\infty$ and taking the square root, one arrives at the following nonlinear first-order differential equation:

$$\frac{d\phi}{dx} = -\left(\frac{8kTc_{j\infty}}{\varepsilon_o \varepsilon_r}\right)^{1/2} \sinh\left(\frac{z_j e\phi}{2kT}\right) \tag{38}$$

which can be integrated to

$$\phi(x) = \frac{2kT}{z_j e}\ln\left(\frac{1+\Theta\exp\left(-x/\lambda\right)}{1-\Theta\exp\left(-x/\lambda\right)}\right) \tag{39}$$

where $\lambda$ is the Debye length:

$$\lambda = \sqrt{\frac{\varepsilon_o \varepsilon_r kT}{2z_j{}^2 e^2 c_{j\infty}}} \tag{40}$$

and $\Theta$ is the profile parameter:

$$\Theta = \tanh\left(\frac{z_j e\Delta\phi}{4kT}\right) \tag{41}$$

Equation 38 can be combined with one of the boundary condition at $x = 0$, $d\phi/dx = -\sigma/\varepsilon_o\varepsilon_r$ (where $\sigma$ is the surface charge density) to find a relation between the charge density and the space charge potential:

$$\sigma = \sqrt{8kTc_{j\infty}\varepsilon_o\varepsilon_r}\,\sinh\left(\frac{ze\phi(0)}{2kT}\right) \tag{42}$$

Finally, by combination of eqns. 29 and 39, the spatial profiles of defects in the space charge region are found:

$$\frac{c_j(x)}{c_{j\infty}} = \left(\frac{1+\Theta\exp\left(-x/\lambda\right)}{1-\Theta\exp\left(-x/\lambda\right)}\right)^{2z_j} \tag{43}$$

The Gouy-Chapman analysis above is valid only when all defect species can redistribute in the space charge region. At reduced temperatures, it is often the case that the defect controlling the Debye length is insufficiently mobile to redistribute in response to the excess grain boundary charge. In this case, the depleted defects are often neglected, and the charge density in Poisson's equation is determined only by the dopant content. This is known as the Mott-Schottky approximation [48, 49], and the immobile carrier in ceria is typically the ionized background acceptor. Poisson's equation is simplified and becomes

$$\frac{\partial^2\phi}{dx^2} = -\frac{z_j e c_{j\infty}}{\varepsilon_o\varepsilon_r} \tag{44}$$

and with boundary conditions $\phi'(\lambda^*) = 0$ and $\phi(\lambda^*) = \phi_\infty = 0$ can be integrated to yield (relative to the bulk reference potential, commonly set to zero):

$$\Delta\phi(x) = -\frac{z_j e c_{j\infty}}{\varepsilon_o\varepsilon_r}(x-\lambda^*)^2 \tag{45}$$

where $\lambda^*$ is the depletion (space charge) width [50]:

$$\lambda^* = \sqrt{\frac{2\varepsilon_o\varepsilon_r\Delta\phi(0)}{z_j e c_{j\infty}}} \tag{46}$$

and can also be expressed in terms of the Debye length:

$$\lambda^* = \lambda\sqrt{\frac{4z_j e}{kT}\Delta\phi(0)} \tag{47}$$

Two distinct differences can be seen in the relation for the space charge width in the Mott-Schottky boundary conditions compared to Gouy-Chapman. When the majority defect cannot redistribute, the space charge width is dependent on the space charge potential, and the depletion width is greater in spatial extent due to a reduced charge screening ability. The expression for the potential difference as a function of $x$ can be substituted into the original equation for carrier enhancement/depletion to give the concentration dependence:

$$\frac{c_i(x)}{c_{i\infty}} = \exp\left[-\frac{z_i}{z_j}\left(\frac{x-\lambda^*}{2\lambda}\right)^2\right] \tag{48}$$

where defect $i$ is enhanced or depleted, and defect $j$ is the majority defect that determines the space charge width. For the case of oxygen vacancies depleted in the space charge regions, $z_i = 2$ and $z_j = 1$:

$$\frac{c_V(x)}{c_{V\infty}} = \exp\left[-\frac{1}{2}\left(\frac{x-\lambda^*}{\lambda}\right)^2\right] \tag{49}$$

and the corresponding electron concentration can be expressed as:

$$\frac{c_n(x)}{c_{n\infty}} = \exp\left[\left(\frac{x-\lambda^*}{2\lambda}\right)^2\right] \tag{50}$$

or

$$\frac{c_n(x)}{c_{n\infty}} = \left(\frac{c_V(x)}{c_{V\infty}}\right)^{-1/2} \tag{51}$$

To facilitate visualization of the difference in defect profiles for these two models, schematic profiles are plotted in Figure 11 for the predominant defects in ceria for a space charge potential of 0.4 V and an acceptor concentration of 300 ppm at 500°C. Under these conditions, depletion of oxygen vacancies and enhancement of electrons are predicted in both models in response to a positive potential in the grain boundary core. It is evident, however, that the natures of the profiles differ considerably. In the Gouy-Chapman case, there is a very large change in carrier concentration within

only the first few nanometers from the grain boundary core. Thus, most of the enhancement/depletion effects occur approximately within one Debye length. Under Mott-Schottky conditions, the change in carrier concentration is less severe, yet still more than three orders of magnitude. On the other hand, the extent of non-uniformity is much larger than the Debye length, due to reduced charge screening resulting from the immobile acceptor. A quantitative discussion of the differences between the Gouy-Chapman and Mott-Schottky models is presented in Section 4.6.

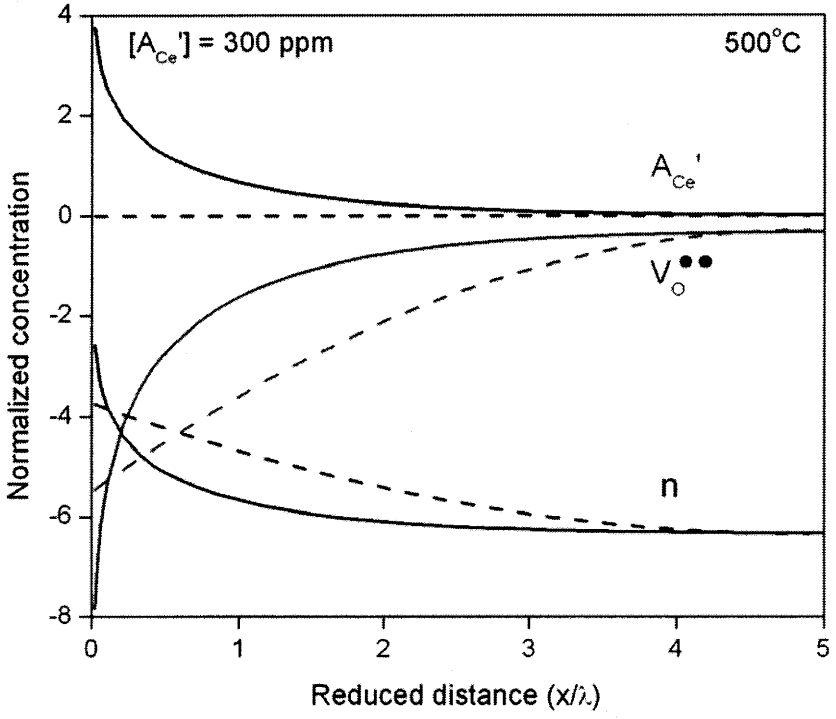


**Figure 11: Space charge profiles of acceptor dopants, oxygen vacancies, and electrons near a grain boundary interface with a space charge potential of + 0.4 V, according to both the Gouy-Chapman (solid lines) and Mott-Schottky (dotted lines) models.**

### *1.5 Nano-ionic Materials for Advanced Energy Technologies*

Over the past decade, researchers have begun to explore a new frontier in solid state ionics: 'nano-ionics.' Defined by crystallite sizes and/or layer thicknesses on the order of nanometers, the field of nano-ionics arose from the natural progression of powder size to ever-smaller dimensions. Gleiter published one of the first comprehensive reports on nanocrystalline materials, which focused primarily on the physical and thermodynamic properties of metals [51]. In the field of ionic materials, Tuller predicted that nanostructuring could lead to improvements in vital technologies such as SOFCs, solid state batteries, electrochromic windows, and chemical sensors [52]. Such predictions

were supported by a logical geometric argument: as the grain size of a material decreases, the fractional volume occupied by grain boundaries increases. Since the properties of grain boundaries are distinct from the bulk, one may then expect grain boundary properties to begin to dominate as the grain size decreases. For example, the diffusivity of an atom or ion is known to be many orders of magnitude faster along a grain boundary that in the bulk [53]; thus, oxide ionic conductivity, which is controlled by the diffusion of oxygen ions, could potentially be enhanced in a nanocrystalline electrolyte.

Maier presented much of the theoretical framework of nano-ionics in a series of papers that focused on the unique thermodynamics and defect chemistry in small particle systems [54-56]. Most of the exploratory research in nano-ionics has focused on ceria [37, 57-63]. Chiang and co-workers [37] first observed that the decrease from microcrystalline to nanocrystalline grain sizes was accompanied by two distinct changes in the electrical conductivity, shown in Figure 12. First, the conductivity of the nanocrystalline samples was found to be approximately two orders of magnitude higher. Second, the nanocrystalline samples showed a negative $pO_2$ dependence resembling an n-type semiconductor, whereas the microcrystalline samples with identical composition showed no $pO_2$ dependence, indicative of an oxygen vacancy dominant regime controlled by compensating acceptor impurities.

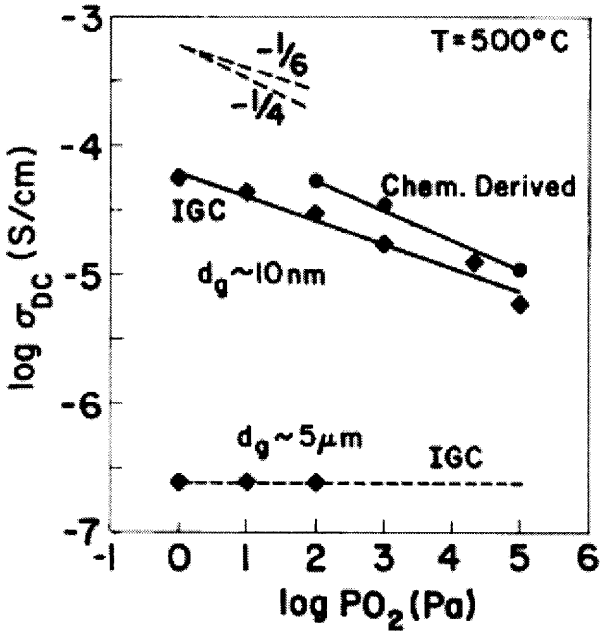


**Figure 12: The electrical conductivity of microcrystalline and nanocrystalline $CeO_2$ as a function of pO2 at 500°C. From Ref. 37.**

These observations were later quantitatively described by Tschöpe [61] and Kim [62] within the

context of the space charge model. Utilizing the model of conduction in polycrystalline materials developed by Maier [64], Tschöpe calculated the 'apparent' bulk ionic and electronic conductivities for various background acceptor concentrations and space charge potentials.

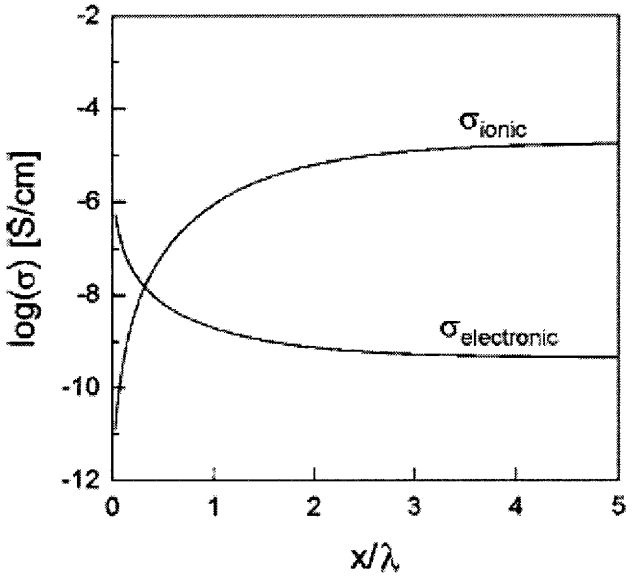


**Figure 13: Grain size dependence of the partial conductivities in ceria at 500°C, for a background acceptor concentration of 1000 ppm and a space charge potential of + 0.55 V [65].**

It can be seen in Figure 13 that, as the grain size decreases, the partial electronic and ionic conductivities increase and decrease, respectively, exponentially. Tschöpe reported that the experimental data of nanocrystalline ceria from various research groups was fitted best by a space charge potential of + 0.55 V [65]. The positive polarity of this value indicates, as shown in Figure 13, that electrons are enhanced in the space charge layer and oxygen vacancies depleted. This model is consistent with the experimental trends shown in Figure 12: a change in predominant conduction type from ionic to n-type electronic as the grain size decreases from the order of microns to nanometers. Another characteristic of ceria altered by nanostructuring is the activation energy of the electrical conductivity. Tuller and Nowick measured a bulk activation energy of 1.96 eV; as per Eq. 16, the electron mobility and enthalpy of reduction were reported to be 0.4 eV [24] and 3.94-4.67 eV [26, 38], respectively. In contrast, Chiang and co-workers measured activation energies of 0.99 and 1.16 eV for specimens prepared by inert gas condensation and chemical processing, respectively [37]. These values are approximately one-half that of the bulk value, implying either reduced enthalpies of electron mobility and/or reduction. The prevailing assumption, chosen by all authors cited above with regard to nanocrystalline studies, is that the activation energy of the mobility of electrons does

not vary significantly with grain size [66]. Thus, the lower activation energy has been associated with a smaller enthalpy of reduction in nanocrystalline ceria [37, 57].

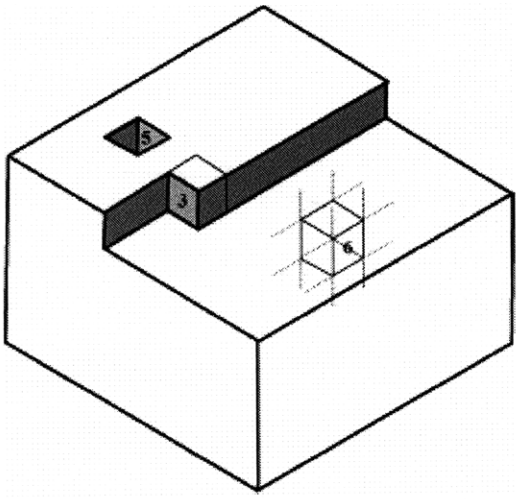


**Figure 14: Schematic of three separate sites in a crystalline material: surface particle, kink, and bulk, with the accompanying number indicating the number of bonds [67].**

Such a concept is supported by a simple physical model that describes the energy required to form a defect as proportional to the number of bonds associated with a given position. As shown in Figure 14, the number of bonds associated with surface particles and kinks is lower than in the bulk. It is therefore believed that the energy to create a defect is lower at a free surface (or correspondingly, grain boundary) compared to the bulk. This simple model is supported by the work of Sayle, *et al.*, who implemented computer simulations using the Born model of interatomic potentials [68]. The authors reported that the formation energy at certain types of surfaces was approximately one-third that of the bulk value. Thus, several researchers have ascribed the reduced activation energy in nanocrystalline ceria to a lower enthalpy of formation for oxygen vacancies, due to the large volume fraction of grain boundaries.

Tschöpe argued that the grain size dependence of the activation energy could be described by the space charge model. The space charge potential exists because of the difference in the standard chemical potential of oxygen vacancies between the bulk and grain boundary:

$$\Delta\mu^{O}_{V_O^{\bullet\bullet}} = \mu^{O}_{V_O^{\bullet\bullet},GB} - \mu^{O}_{V_O^{\bullet\bullet},bulk} \tag{52}$$

Through a numerical solution of the Poisson-Boltzmann differential equation, Tschöpe concluded that

a space charge potential of 0.55 V would arise from a $\Delta\mu^{O}_{V_O^{\bullet\bullet}}$ value of -1.8 eV. The parameter $\Delta H_{R,GB}$ was defined by subtracting this value from the bulk formation enthalpy from Ref. 26: 4.67 eV – 1.8 eV $\approx$ 2.9 eV. Analogous to the argument by Chiang and co-workers, this represents a lower enthalpy of formation for oxygen vacancies in the grain boundary core, and leads to a smaller activation energy.

An alternative model for charge conduction in nanocrystalline ceria was presented by Kim and Maier [62, 69]. In that work, the authors prepared nominally-undoped ceria and 0.15 mol% CGO bulk samples of approximately 30 nm grain size. Using impedance spectroscopy on traditional samples such as Pt / $CeO_2$ (or CGO) / Pt, as well as electron-blocking specimens such as Pt / CGO / YSZ / Pt, where YSZ serves to block the electronic carriers, the ionic and electronic contributions to the total conductivity were deconvoluted. As shown below in Figure 15 and Figure 16, the ceria and 0.15 mol% CGO specimens demonstrate quite distinct responses to the polarization measurement. In the case of the CGO sample, the measured current is constant as a function of time which is indicative of predominant ionic conduction. Conversely, the current-time characteristics for ceria show decay over approximately the first 100 seconds of the measurement. This decay is indicative of initial electronic transport that is then blocked by the YSZ layer. The authors demonstrated in both cases that the current-voltage characteristics were linear, indicative of operation within the Ohmic regime.

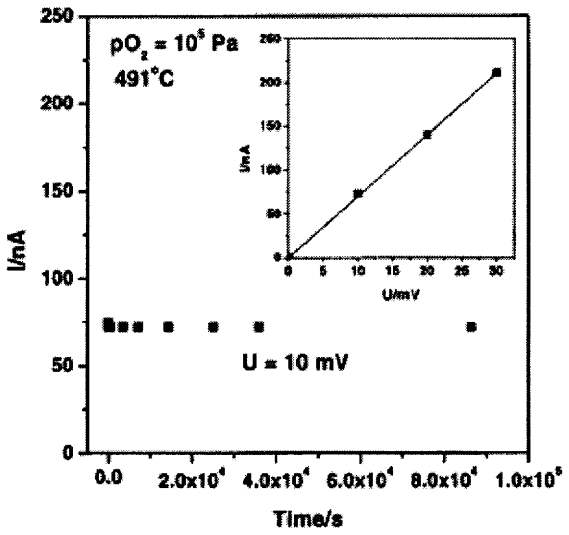


**Figure 15: Time-dependent current characteristics of 0.15 mol% CGO, demonstrating dominant ionic conduction. The inset indicates measurements within the Ohmic I-V regime [62].**

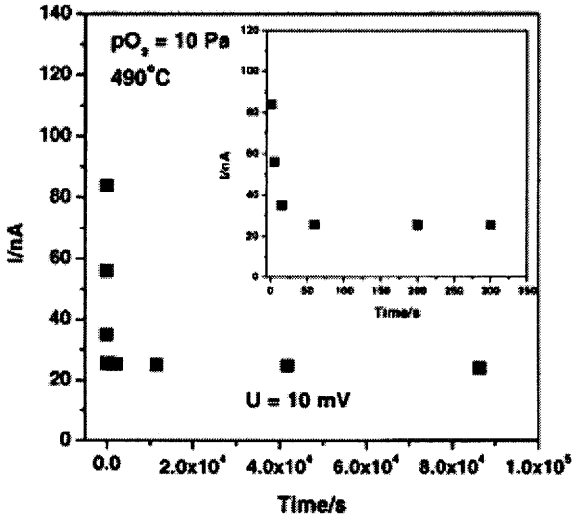


**Figure 16: Time-dependent current characteristics for ceria, demonstrating a blocking effect of electrons. Additional data (not shown here) also indicates an Ohmic I-V regime [62].**

In Figure 17 and Figure 18, the partial pressure and temperature dependence of the bulk and grain boundary conductivities are shown. There is no observed $pO_2$ dependence for the bulk and grain boundary conductivities in the range of $10^{-5}$ to $10^{-1}$; this feature, as discussed above, is associated with conduction by ionic species. In this case, the conductivity of 0.15 mol% CGO is dominated by oxygen vacancies. In Figure 18, the CGO bulk conductivity is found to be between three and four orders of magnitude higher than the total grain boundary conductivity. Such reduced grain boundary conductivity relative to the bulk has been reported in several polycrystalline oxides, particularly YSZ [70-72] and doped ceria [73, 74]. In microcrystalline form, this reduction often occurs as a result of thin second phases that form at grain boundaries, particularly $SiO_2$ [75, 76]. Aoki, *et al.* studied the specific grain boundary conductivity as a function of grain size from 140 nm to 11.4 μm in Ca-stabilized zirconia (CSZ) [77]. In that work and others [71, 72], the specific grain boundary conductivity was observed to increase monotonically with decreasing grain size, which was attributed to grain-size dependent segregation of impurities. However, glassy phases located at the grain boundaries are not the only source for the impediment of charge transport—Aoki and co-workers reported that for the most pure grain boundaries with no detectable second phase, the specific grain boundary conductivity was still two orders of magnitude lower than in the bulk [77].

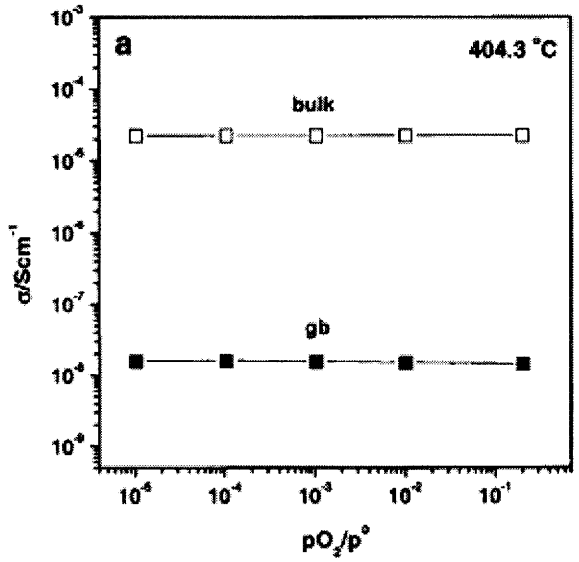


**Figure 17: Partial pressure dependence of the bulk and grain boundary conductivities for 0.15 mol% CGO at 404°C [62].**

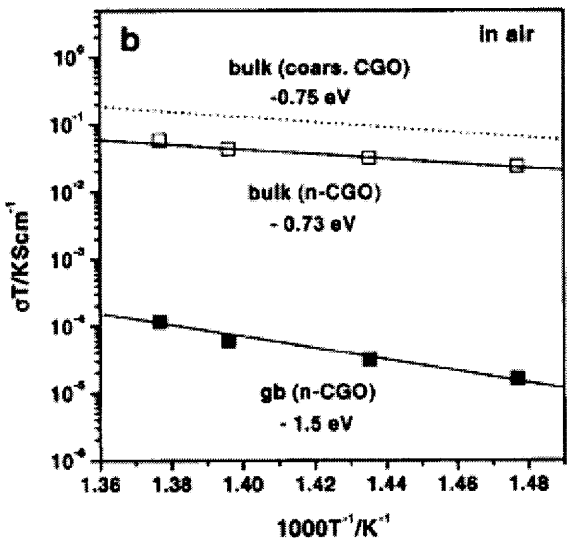


**Figure 18: Arrhenius plot of the electrical conductivity of the bulk and grain boundaries of 0.15 mol% CGO [62].**

The data in Figure 19 and Figure 20 highlight the distinct differences between nominally-undoped ceria and 0.15 mol% CGO. First, the partial pressure dependence of the total conductivity in Figure

19 (filled squares), demonstrates that electrons are the dominant charge carrier, in good agreement with previous reports [37, 57, 59]. Furthermore, the ionic conductivity (open squares), found via the use of blocking electrodes, was $pO_2$ independent over the range of $10^{-4}$ to $10^{-1}$. Subtracting this ionic conductivity from the total yields the electronic partial conductivity leads to a slope of approximately -1/4, in good agreement with the extrinsic Brouwer approximation (Eq. 17). The activation energy of the total conductivity, shown in Figure 20, is larger than the value reported by Chiang, *et al.* [37], but similar to the activation energy reported by Hwang and Mason [57].

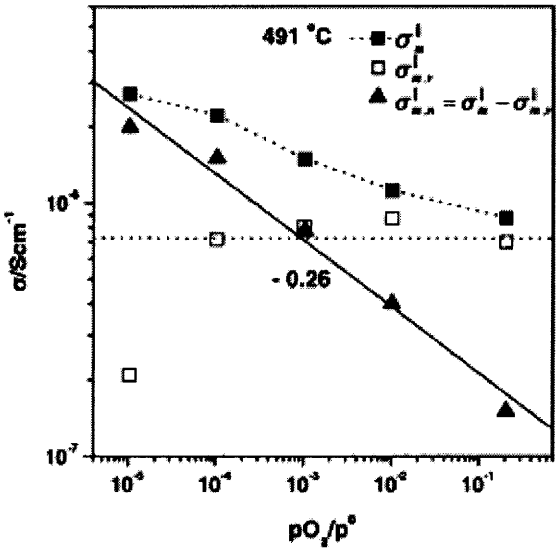


**Figure 19: Partial pressure dependence of the ionic, electronic, and total conductivity of nanocrystalline ceria at 491°C [62].**

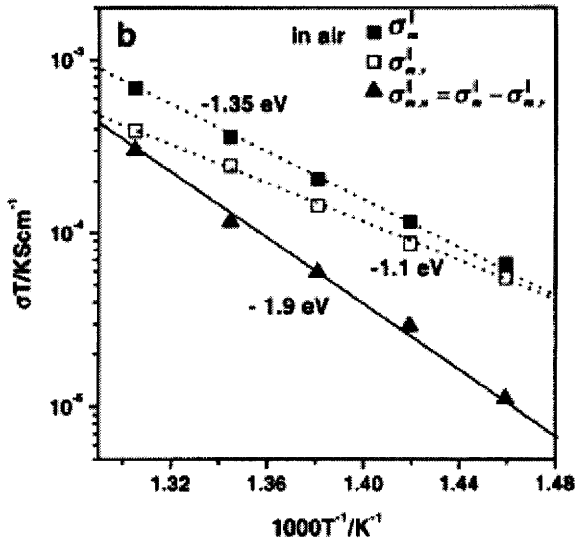


**Figure 20: Arrhenius plot of the ionic, electronic, and total conductivity of nanocrystalline ceria [62].**

Suzuki and co-workers examined the properties of nanocrystalline ceria thin films, as well as $Ce_{0.9}Gd_{0.1}O_{2-x}$ (CGO-10) and $Ce_{0.8}Gd_{0.2}O_{2-x}$ (CGO-20), all prepared by a polymer precursor spin-coating process [58, 59]. The electrical conductivity of the ceria, CGO-10 and CGO-20 was measured as a function of $pO_2$ from 600-900°C. The plot of ceria and CGO-10 of 20 and 30 nm grain size, respectively, is shown in Figure 21. Two observations can be made: first, the conductivity of CGO-10 is a factor of 7 greater than ceria at 600°C near ambient $pO_2$. Second, the negative $pO_2$ slope of ceria indicates electronic conduction, in good agreement with the nanocrystalline data in Figure 12. In contrast, there is no CGO-10 $pO_2$ dependence near ambient pressure, which is indicative of predominant conduction by ionic defects. Thus, the electronic-to-ionic transition upon nanoscaling of ceria is not observed for CGO-10 in this partial pressure range. This apparent lack of a nano-ionic effect near ambient $pO_2$ can be understood with consideration of the role of doping concentration on

the depletion length. The susceptibility of an electrolyte to grain boundary nano-ionic effects is dependent on the width of the depletion zone relative to the grain size. This depletion width is represented by the Debye length (Eq. 40) in the Gouy-Chapman model or by the depletion width described in Eq. 47 for the Mott-Schottky model. In both models, the depletion width is proportional to $c_{j\infty}^{-1/2}$, and thus the impact of the space charge layer is reduced as the dopant concentration increases, due to a smaller depletion length. For example, using a value of 0.25 V for the space charge potential of a nanocrystalline 8 mol% YSZ sample [78], the depletion width, $\lambda^*$, resulting from the Mott-Schottky model is expected to be approximately 4 Å at 500°C. While this value is four times larger than the corresponding Debye length, it is nevertheless so small relative to even nanocrystalline-sized grains that no significant nano-ionic effect is expected.

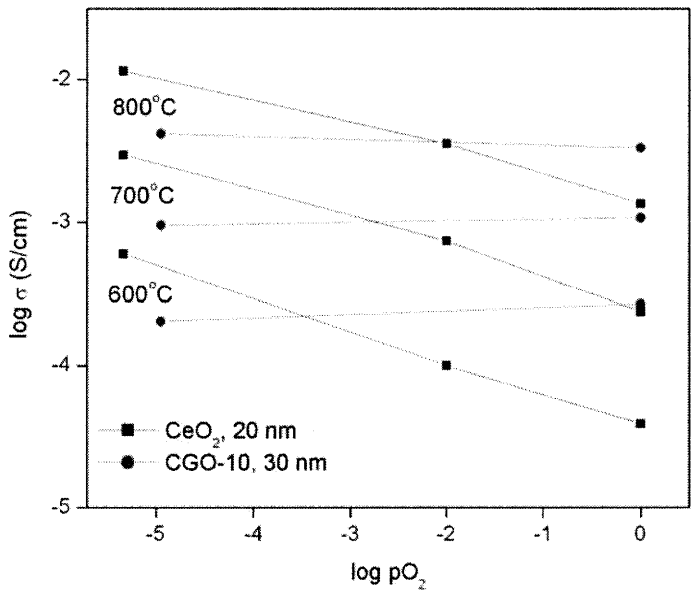


**Figure 21: $pO_2$ dependence of the conductivity of $CeO_2$ and CGO-10 in the $pO_2$ range of $10^{-5}$ to 1. Figure adapted from [58,59].**

The above combination of experimental data and analytical modeling of ceria serves as one of the best-understood examples of nanocrystalline effects on charge transport in a mixed ionic-electronic conducting (MIEC) electroceramic material to date. In other systems, particularly YSZ, the effect is not as clear. Indeed, the evidence of nano-ionic effects in ceria has been rather contradictory in nature. Kosacki and co-workers fabricated YSZ specimens with a grain size of 20 nm and found the conductivity, shown in Figure 22, to be enhanced by approximately two orders of magnitude compared to the microcrystalline state [79]. In contrast, the results of Peters, *et al.* as a function of

grain size and temperature indicate a monotonic decrease of conductivity as the grain size decreases, as demonstrated below in Figure 23 [80]. To date, there is no clear explanation or consensus regarding the contradictory nature of the reported conductivities of nanocrystalline YSZ.

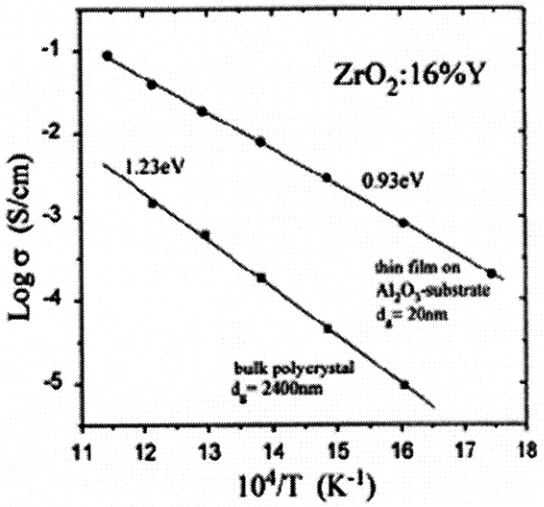


**Figure 22: Arrhenius plot of YSZ conductivity for grain sizes of 20 nm and 2400 nm, showing a conductivity increase with nanoscaling [79].**

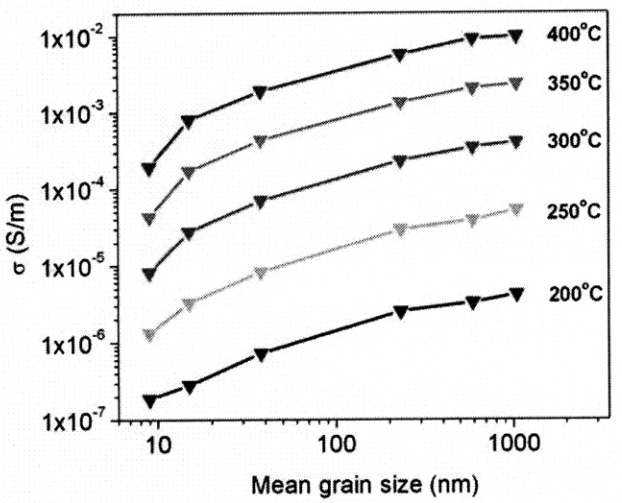


**Figure 23: Conductivity of 8 mol% YSZ as a function of grain sizes from 8 to 1000 nm, showing a conductivity decrease with nanoscaling [80].**

Nano-ionic effects in electroceramic materials may also occur by means other than reduction of grain size. One method is the fabrication of ionic heterostructures, where the nanoscaling occurs in the thickness of epitaxially-grown layers of alternating composition. A notable example of this technique was demonstrated by Sata and co-workers, who fabricated $CaF_2/BaF_2$ nanoscaled multilayers by molecular beam epitaxy (MBE) [81]. In that work, the period of the $CaF_2/BaF_2$ layers was varied from 16 to 430 nm, and two key observations were made: first, that the conductivity of all multilayers was larger than the bulk values for either compound, and second, that the conductivity increased as the period decreased. Since the layers were grown by MBE, no grain boundaries existed to further convolute the conductivity change. The authors proposed that the conductivity enhancement resulted from a transfer of $F^-$ ions from the $BaF_2$ to $CaF_2$ layers, resulting in an "artificial ion conductor." Further details of this nano-ionic effect are discussed in section 1.6.

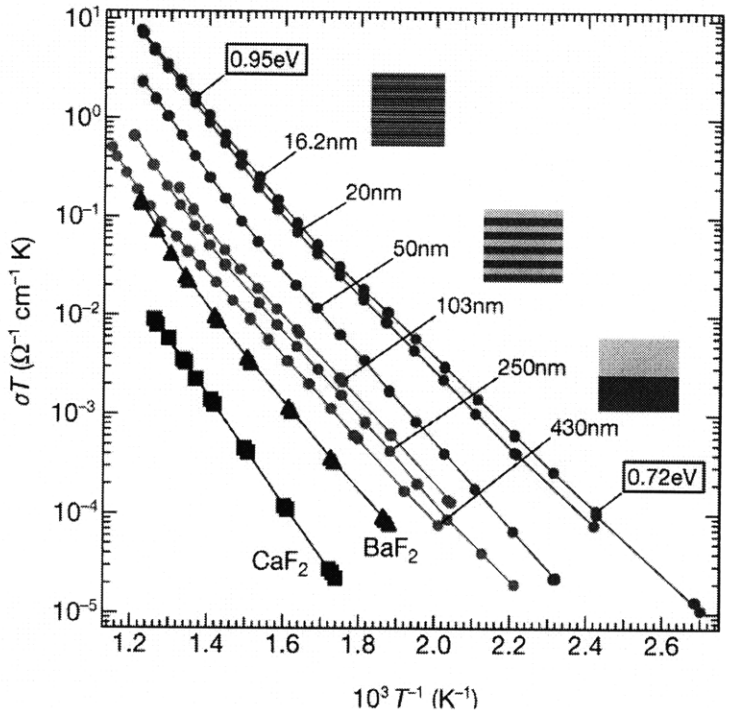


**Figure 24: Arrhenius plot of the ionic conductivity of $CaF_2/BaF_2$ multilayers for period spacings of 16 to 430 nm. Also plotted are the bulk conductivity values for $CaF_2$ and $BaF_2$ [81].**

Yet another avenue to enable nano-ionics is investigation of the interface between a thin film and its underlying substrate. As discussed below for two-phase solid electrolytes, such an interface can serve as a form of a heterogeneous dopant and can lead to increased ionic conductivity. Precisely such an effect was reported by Kosacki, *et al.*, who observed an enhancement in the ionic conductivity of 10 mol% YSZ thin films for film thicknesses of less than 60 nm [82, 83]. Epitaxial YSZ films were deposited on MgO substrates by pulsed laser deposition—the change in ionic conductivity with film thickness is shown in Figure 25. The absence of grain boundaries indicates that the size effect must occur elsewhere in the sample; the authors reported that enhancement of the electrical conductivity occurs only for film thicknesses less than 60 nm. The authors proposed that a highly-conductive interfacial layer of approximately 1.6 nm thickness exists at the YSZ and MgO interface, and that this layer is responsible for the observed conductivity enhancement. Changes in conduction due to the interfacial space charge layer in this thesis are discussed in depth in Section 4.7.

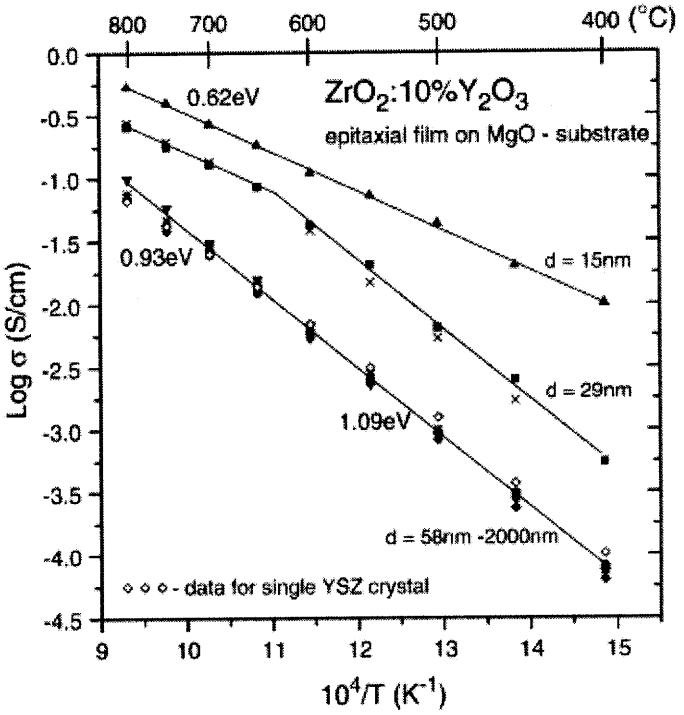


**Figure 25: Arrhenius plot of the ionic conductivity of 10 mol% YSZ for film thicknesses varying from 15 to 2000 nm [83].**

As can be seen, nano-ionic effects may impact the properties and performance of electroceramic materials in multiple ways, via nanocrystalline grain sizes, ionic heterostructures, and film/substrate interactions. The net result of these nano-ionic effects is often subtle, though a decade of research conducted by various institutions has resulted in an improved understanding and appreciation of nano-ionics as an emerging field. The foundation of this thesis is based on the concept of nanocrystallinity affecting transport properties in a non-trivial manner. Through the work of Chiang, *et al.* [37], Tschöpe [61], and Kim and Maier [62], it is now known that the transition from microcrystalline to nanocrystalline ceria results in a shift from predominant ionic to electronic conductivity and an increase in total electrical conductivity. The existence of a naturally-occurring positive space charge potential, on the order of 0.3 to 0.6 V, results in an accumulation of electrons and depletion of oxygen vacancies in the space charge layer.

### *1.6 Heterogeneous Doping of Solid Electrolytes*

The typical method utilized to control the electrical conductivity of an ionic solid is homogeneous doping, in which donor and/or acceptor species substitute on a lattice site. Such doping occurs uniformly throughout the material, and the ionized defect must be compensated by the formation of

an additional defect, either electronic or ionic, in order to preserve charge neutrality. There is, however, another method with which the electrical conductivity can be controlled: *heterogeneous* doping. This concept was first demonstrated in dramatic fashion by Liang in 1973 [84]. In that study, the *insulating* compound $Al_2O_3$ was added as a second phase to the ionic conductor LiI, and the ionic conductivity was subsequently *increased* by up to 50 times relative to pure LiI.

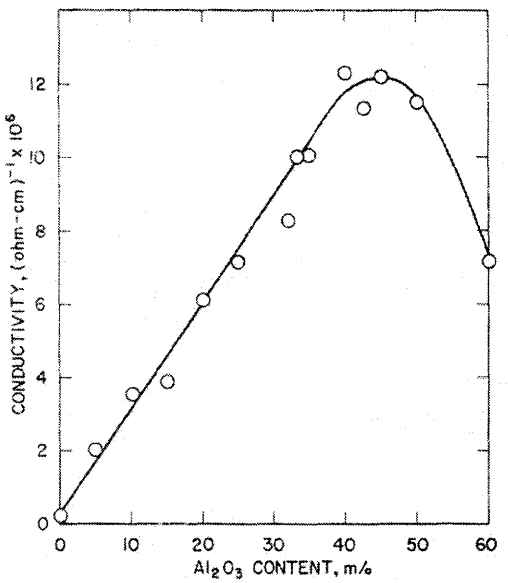


**Figure 26: Ionic conductivity of LiI as a function of $Al_2O_3$ content in mol% [84].**

While the improvement of ionic conductivity via an insulating phase may appear counter-intuitive, the concept was first discussed with respect to the space charge model by Wagner [85]. A thorough review and analysis of this effect was later presented by Maier [46]. Similar to the space charge models described above for grain boundary effects, the conductivity enhancement in systems such as LiI:$Al_2O_3$ have been attributed to fast conduction along interfacial space charge regions near the LiI—$Al_2O_3$ interface. Such a system may be visualized in a manner similar to the grain boundary effect discussed in Sections 1.4 and 1.5 and illustrated in Figure 11. In this case, the symmetry is broken not by a grain boundary, but rather an interface between two phases. Analogous to the discussion above, defects can be enhanced or depleted in this space charge layer, and the spatially-varying conductivity will depend on the relative mobility of the charge-carrying defects. Indeed, it is shown in Figure 27 that the conductivity may increase or decrease monotonically as the boundary is approached, or potentially reach a local minimum. In this LiI:$Al_2O_3$ system, the space charge layer induced by the LiI/ $Al_2O_3$ interface is enhanced in the high-mobility $I^-$ species, resulting in enhanced ionic conductivity relative to the single phase.

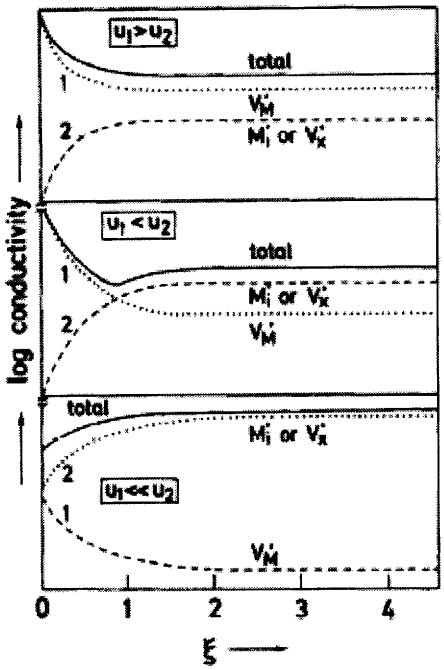


**Figure 27: Localized conductivity for Frenkel defects near an interface, with varying relative mobilities ($u_1$ and $u_2$) [46].**

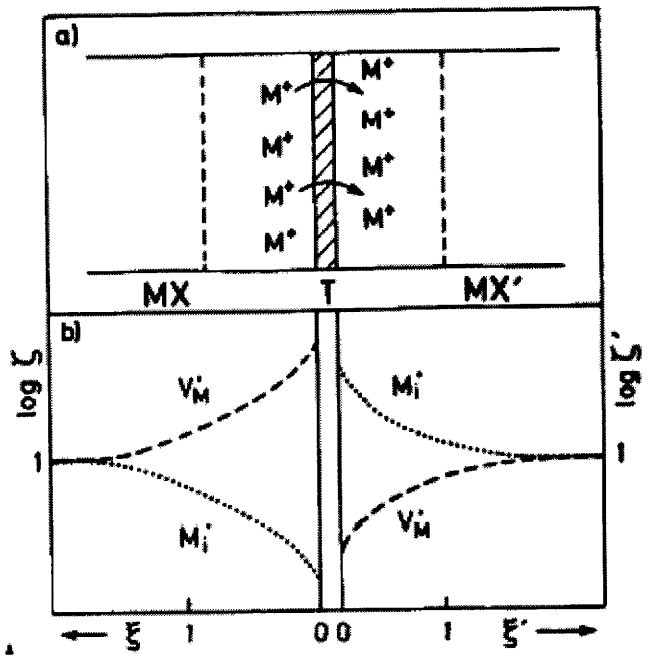


**Figure 28: Above: schematic of ionic transfer of a metal from one Frenkel solid to another. Below: concentration profiles established due to the ionic transfer [46].**

The heterogeneous doping effect is also observed at other interfaces, such as multilayered materials and film/substrate interfaces. As described above, this effect has been associated with the performance enhancement of $CaF_2/BaF_2$ ionic heterostructures. Figure 24 depicts the conductivity enhancement of the multilayer relative to the two end-members, and the increasing magnitude of the effect with decreasing period [81]. Though the defect profiles are similar to what is observed near a grain boundary or second phase, subtle differences result from the asymmetric carrier redistributions in the two chemically-distinct materials, shown in the lower portion of Figure 28. Guo and co-workers proposed a model in which $F_i'$ defects are depleted and $V_F^\bullet$ enhanced in the space charge region of the $BaF_2$ layers, based on the observed activation energies and the large difference in mobility between the enhanced and depleted ionic defects [84]. This can also be described as a transfer of $F^-$ ions from the $BaF_2$ to $CaF_2$ layer, shown schematically in the upper portion of Figure 28. As a result, the concentration of the high-mobility $V_F^\bullet$ charge carriers is increased in the $BaF_2$ layer, resulting in higher ionic conductivity. In the same report, the authors also concluded that the properties of the ionic heterostructure are best described by the Mott-Schottky model, with a modification to include an impurity gradient near the layer interface.

It can thus be seen that heterogeneous doping presents unique, though sometimes non-intuitive opportunities for modification of material properties outside the normal realm of homogeneous doping. In particular, heterogeneous effects have led to appreciable improvements in the ionic conductivity of systems such as LiI with $Al_2O_3$ second phases [84] and $BaF_2/CaF_2$ multilayers [81]. The logical question now emerges: are there other means by which heterogeneous doping may be employed to alter material properties in a desirable manner? The doping of grain boundaries via heterogeneous in-diffusion from surface diffusion sources is proposed below.

### *1.7 Grain Boundary Diffusion in Ionic Materials*

Diffusion is the process of mass transport in response to various driving forces. Generally, the flux of a species, such as charge, heat, mass, etc., can be represented as a summation of conjugate forces along with the direct and coupling coefficients [13]:

$$J_\alpha = \sum_\beta L_{\alpha\beta} F_\beta \tag{53}$$

where $F$ is the conjugate force and $L$ is the Onsager coefficient, defined as:

$$L_{\alpha\beta} = \frac{\partial J_\alpha}{\partial F_\beta} \tag{54}$$

Diffusion is most often studied under a chemical potential gradient, where species move from regions of high activity to low activity. Fick's First Law is a specific example of equation 54, where the only driving force is the chemical potential gradient, simplified in the dilute limit as concentration:

$$\vec{J} = -D\nabla c \tag{55}$$

Accumulation or depletion of a species is described by divergence of the flux, and Fick's Second Law emerges as:

$$\frac{\partial c}{\partial t} = -\nabla \cdot \vec{J} \tag{56}$$

and in one dimension this simplifies to the familiar form:

$$\frac{\partial c}{\partial t} = D\frac{\partial^2 c}{\partial x^2} \tag{57}$$

Given the appropriate boundary conditions, it is this differential equation that must be solved in order to calculate diffusion coefficients from an experimental measurement. In solid materials, there are several categories of diffusion and various mechanisms by which it may take place. The most common types of diffusion are bulk, grain boundary, surface, and diffusion along dislocations. Mechanisms include vacancy, interstitital, and interstitiality [13]. It is well-known that diffusion along grain boundaries is typically much faster than in the bulk, often by 3-6 orders of magnitude [53]. A grain boundary is an interface between two adjacent crystallites, known as 'grains.' Some degree of misorientation exists between the two grains, and so the grain boundary serves as a region of disorder, bridging the gap between single crystal grains.

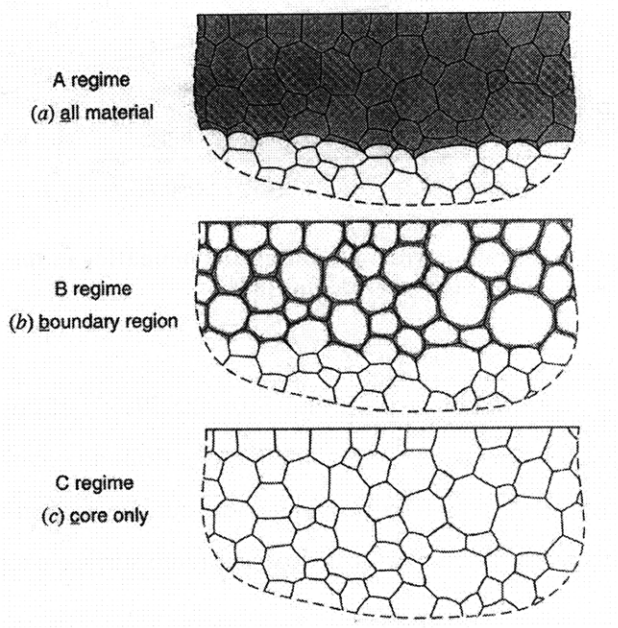


**Figure 29: Schematic of the three Harrison regimes: A.) homogeneous diffusion through all areas, B.) diffusion along grain boundaries with bulk penetration, and C.) exclusive grain boundary diffusion [13].**

Harrison described three distinct diffusion regimes, shown in Figure 29, that occur in a polycrystalline material [87]. The Harrison regime A is a regime where diffusion occurs uniformly throughout the material, and is described by an effective diffusion coefficient, $D^*$, that is a linear combination of the bulk and grain boundary processes:

$$D^* = (1-\eta)D_b + \eta D_{GB} \tag{58}$$

where $D_b$ and $D_{GB}$ are the bulk and grain boundary diffusivities, respectively, and $\eta$ is the fraction of sites within the grain boundary region. Type B diffusion, the regime observed most often experimentally, consists of bulk and grain boundary components as in regime A, but with unequal

penetration and thus a non-homogeneous diffusion front. In this regime, the diffusing species move quickly and further along grain boundaries, with slow but appreciable penetration into the bulk, particularly near the surface. An example of such a diffusion profile is shown in Figure 30:

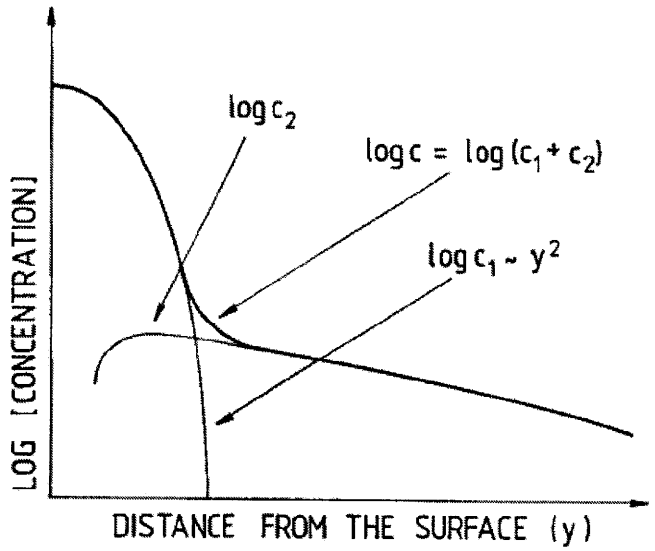


**Figure 30: Schematic of type B diffusion, with bulk diffusion dominating in the near-surface region and grain boundary diffusion dominating at greater depths [88].**

Based on work by Fisher [89], Whipple [90], and Suzuoka [91], LeClaire outlined a method for separating the bulk and grain boundary diffusion coefficients from a convoluted profile [92]. In that method, the bulk diffusivity is first found by fitting the near-surface section of the depth profile to the solution to the diffusion equation for an infinite source and rapid surface exchange [93]:

$$\frac{c(z,t)}{c_O} = erfc\left(\frac{z}{2\sqrt{D_b t}}\right) \tag{59}$$

Once $D_b$ is known, the product of the grain boundary diffusivity and grain boundary width, δ, is given as:

$$\delta D_{GB} = 1.322\sqrt{\frac{D_b}{t}}\left(-\frac{\partial \ln c}{\partial z^{6/5}}\right)^{-5/3} \tag{60}$$

The final Harrison regime is the C-regime. In this type of diffusion, mass transport in the bulk is negligible and the only motion of atoms and/or ions occurs in the grain boundary regions. This regime is rarely reported in the literature, as it only occurs at lower temperatures, and the small amount of diffusing species is difficult to detect analytically. In this case, a single diffusion

coefficient is sufficient to describe mass transport, as only one mechanism is observed. Mishin and Herzig proposed a modification to the Harrison classification scheme for nanocrystalline materials, where the diffusion length in the grain boundary may become larger than the grain size [94]. In this system, new regimes such as C′, $B_2'$, A′, and $A_O$ are introduced; progression of regimes with increasing temperature is divided into four categories from 'coarse-grained' to 'special ultrafine-grained,' depending on the magnitude of the grain size relative to the diffusion length.

Because the diffusion of oxygen in the ceria system is directly related to its ionic conductivity, oxygen transport has been studied extensively [44, 95, 96]. However, only recently has cation transport in fluorite materials begun to be examined. This is due, in part, to the knowledge that cation diffusion is significantly slower than oxygen in nonstoichiometric fluorites. For example, at 1250°C, the diffusion coefficients in $Ce_{0.9}Gd_{0.1}O_2$ (CGO-10) can be estimated from the work of Kilner and co-workers to be approximately $3x10^{-6}$ $cm^2/s$ for O [97] and $5x10^{-15}$ $cm^2/s$ for Fe [98]. Despite the slower transport of cations, this area is crucial for study since some solid state behaviors, such as degradation processes like creep [99] and kinetic demixing [100] are controlled by the slowest species [101]. Kilo has compiled a thorough review of bulk and grain boundary diffusion of transition metals in $ZrO_2$, typically at temperature of 1000°C and above [102].

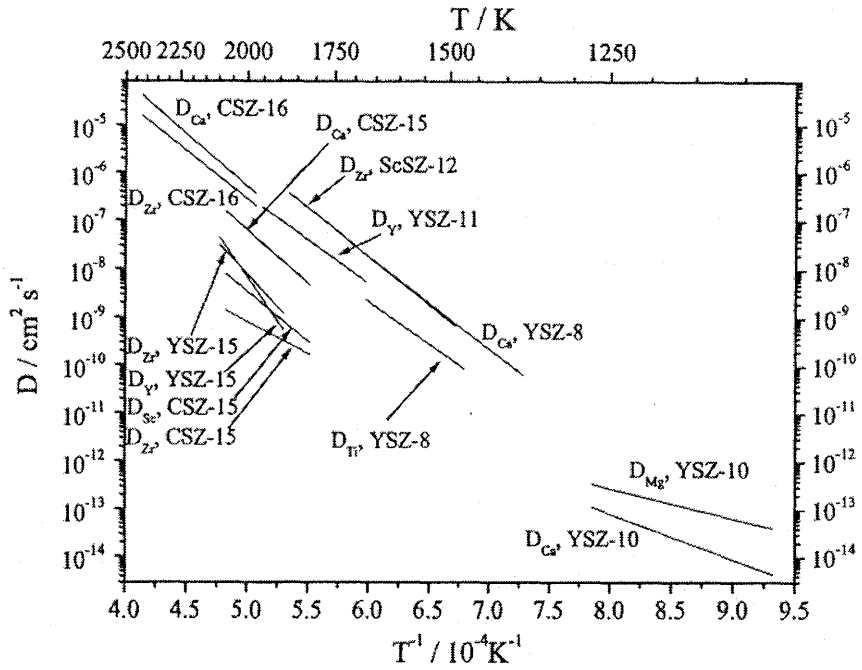


**Figure 31: Values of the grain boundary diffusion coefficient for various cations in the YSZ system. Compiled by Kilo [102].**

To the best of the author's knowledge, the only study of cation diffusion in the ceria system was reported by Sirman and Kilner, who examined the diffusion of Co and Fe in the bulk of CGO-10 [98]. As mentioned above, the value of the diffusion coefficient for both species was determined to be on the order of $5x10^{-15}$ to $1x10^{-14}$ $cm^2/s$. The activation energies were reported to be 5.7 ± 2.3 eV and 6.7 ± 1.5 eV for Co and Fe, respectively.

Several features can at this point be noted regarding the study of diffusion in electroceramic materials. First, there is overall very little data regarding the diffusion of cation species in fluorite materials, particularly ceria. In recent years this trend has begun to change, though much work remains to be done. Even less data exists for cation diffusion along grain boundaries. In addition, quantification of grain boundary diffusion becomes increasingly complex in nanocrystalline materials, as some of the assumptions and boundary conditions in the traditional LeClaire method are not valid in nanocrystalline materials [103]. Finally, there is no reported data for grain boundary cation diffusion in fluorites at temperatures below 1200°C, as most studies are undertaken with bulk microcrystalline samples, and higher temperatures are required for sufficiently signal-to-noise ratios from the analytical instrument of use.

### *1.8 Deconvolution of Transport Mechanisms by Hebb-Wagner Polarization*

There are several experimental techniques that can be employed to separate electronic and ionic contributions to the total electrical conductivity. One of the most common is known as Hebb-Wagner polarization [104, 105]. In this method, a blocking electrode is employed that is capable of one conduction type but not both. A schematic of the Hebb-Wagner structure for the case of ion blocking is in shown in Figure 32. The current-voltage relationship for this structure was derived by Wagner [105]:

$$I = I_{el} = -\frac{kTA}{qL}\left[\sigma_e(0)\left(1-\exp\left(-\frac{qV}{kT}\right)\right)+\sigma_h(0)\left(\exp\left(\frac{qV}{kT}\right)-1\right)\right] \tag{61}$$

where $A$ is cross-sectional area, $q$ is the elementary charge, $L$ is the length of the MIEC, $V$ is the applied voltage, and $\sigma_e$ and $\sigma_h$ are the partial electron and hole conductivities in the MIEC adjacent to the reversible electrode, respectively.

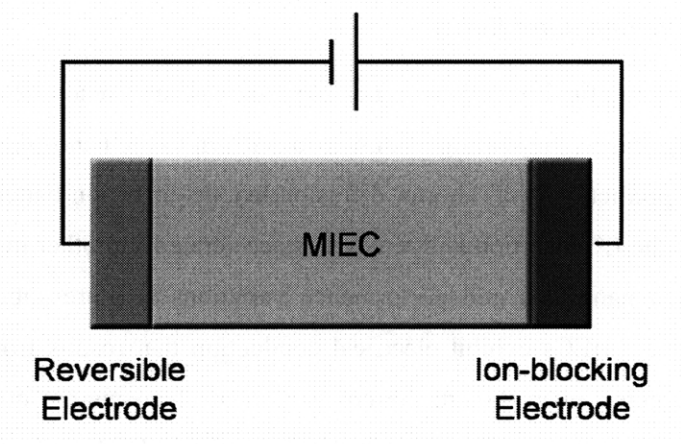


**Figure 32: Schematic diagram of the Hebb-Wagner structure. In this representation, the motion of ionic species is blocked at the electrode to the right, enabling measurement of the electronic conductivity of the MIEC.**

While this method may appear straightforward at first, there are several complications that may occur, leading to false conclusions. A review by Riess highlights many of these possible complications and provides suggestions for improved electrode designs, such as a four-point configuration [106, 107]. These potential complications must be considered during the interpretation of data obtained from Hebb-Wagner electodes, and are discussed in Section 4.

The application of the Hebb-Wagner polarization technique to thin films is less common. Suzuki, *et al.* [108] and Huang, *et al.* [109] used YSZ pellets to measure the ionic partial conductivity of (La,Sr)$CrO_3$ and $La_{0.85}Sr_{0.15}MnO_3$ thin films grown by pulsed laser deposition and DC magnetron sputtering, respectively. Interestingly, the $pO_2$ dependence of the ionic partial conductivity in both studies differed from the expected value based on the diffusion of oxygen by a vacancy mechanism. The slopes of log ionic conductivity with respect to log $pO_2$ in the range of $10^{-3}$ to 1 atm were +1/2 [108] and +1/5 [109]. In both cases, the authors attributed this behavior to the diffusion of oxygen along grain boundaries, rather than through a bulk vacancy mechanism. It should also be noted that in both cases, the authors analyzed the validity of the blocking procedure as presented by Riess [106]; however, in neither study did the authors discuss the contribution of the impedance of the electrochemical reactions at the Pt/MIEC interface to the measured resistance. This potential complication is of particular importance in thin film systems, as the thin nature of the MIEC often entails that surface reactions, not transport in the bulk, are the dominant contribution to the resistance.

## *1.9 Conclusions of the Literature Review*

Despite its status as a young field of endeavor, notable progress has already been achieved in the field of nano-ionics. In some cases, the scaling of dimensions down to the nano- regime yields results that are straightforward to predict, such as shorter diffusion lengths in Li ion battery electrodes resulting in improved power, as the $Li^+$ insertion and removal is accelerated. In other instances, understanding the connection between nanoscale and performance variations is more subtle and complex. As described in Section 1.2, MIECs exhibit electrical conduction that results from the motion of both electronic and ionic species, even though the conduction mechanisms are quite different. Cerium oxide, reviewed in Section 1.3, is a classic example of a MIEC. As described in the analysis of the defect chemistry of ceria, it is often found that the Brouwer approximation in the extrinsic regime yields a reliable model of the behavior of bulk nominally-undoped ceria at or near ambient $pO_2$. Inhomogeneous defect distributions within space charge regions were introduced in Section 1.4. In response to an electrical potential in the grain boundary core relative to the bulk, a framework of equations was outlined to quantitatively describe these profiles according to either the Gouy-Chapman (mobile dopants) or Mott-Schottky (immobile dopants) model.

In Section 1.5, theoretical and experimental research in nano-ionics was reviewed, particularly with respect to ceria. Through the experimental evidence, first by Chiang, *et al.* [37] and space charge modeling by Tschöpe [61] and Kim and Maier [62], a coherent picture of property variations in nanocrystalline ceria emerges. Through the existence of a naturally-occurring space charge potential of positive polarity due to the difference in standard chemical potential of oxygen vacancies in the bulk and grain boundary, a space charge region is formed that is enhanced in electrons and depleted of oxygen vacancies. Macroscopically, this is observed as a change of primary conduction type from ionic to electronic and an increase of the conductivity magnitude upon nanoscaling. In section 1.6, various forms of improvement in properties by heterogeneous doping were described. Finally, the three Harrison diffusion regimes were introduced in section 1.7, with particular emphasis on type C diffusion, in which moving species travel only along grain boundaries at relatively low temperatures.

While the properties and performance of nanocrystalline ceria may be well-understood, no systematic effort to date has been undertaken to ***control*** the properties of nanocrystalline ceria, particularly the space charge regions. However, a synthesis of the concepts presented in this Introduction may yield a toolbox by which the charge transport properties of nanocrystalline ceria are ***systematically modified***.

It has been reproducibly shown by several investigators that the grain boundary core in ceria is

positively-charged, resulting in a negatively-charge space charge region. In such a region, positively-charged oxygen vacancies are depleted exponentially near the grain boundary. If negatively-charged defects are introduced into the grain boundary core, oxygen vacancies will be introduced and the space charge potential will shift to less-positive values. This could be accomplished, for example, by the introduction of Ni onto a Ce site in the space charge layer and the corresponding charge compensation:

$$NiO \xrightarrow{CeO2} Ni'_{Ce} + O_O^x + V_O^{\bullet\bullet} \tag{62}$$

In such a scenario, the boundary depletion effect will be weakened. A schematic decrease in $\Delta\Phi$ from +0.5 to +0.3 V is shown in Figure 33. At the isoelectric point where the space charge potential is zero, the bulk equilibrium defect concentration is found throughout the bulk and boundary regions. If enough negative charge is introduced that oxygen vacancies accumulate in the space charge region, the space charge potential will be inverted to a negative value. Two distinct effects on the grain boundary/space charge conduction of oxygen vacancies are illustrated. First, through the reduction of the space charge potential to a lower, yet still positive value, the blocking of ionic charge transport due to the depletion of carriers and potential barrier at the grain boundary core is weakened. This effect alone may significantly improve ionic conduction in materials.

Second, it may be possible to introduce enough oxygen vacancies that accumulation, not depletion is achieved in the space charge layer. Such a defect reaction as Eq. 62 could also occur in the bulk, and it was shown in Figure 3 that improvements in ionic conduction cannot be achieved simply through increased doping. However, heterogeneous doping differs from homogeneous doping in one important aspect: the spatial separation of a charge carrier from its compensating defect. In this case, it is assumed that the $Ni_{Ce}'$ defect is frozen-in at the grain boundary whereas the oxygen vacancy is free to move. An inverted space charge layer may therefore be thought of as a high-mobility region of oxygen vacanies where defect association effects are reduced. An analogy to electronic materials is the two-dimensional electron gas (2DEG). In devices such as a high electron mobility transistor (HEMT), the separation of electrons from ionized donors in a quantum well results in reduced impurity scattering and increased mobility. As discussed in Section 1.6, the conduction of ionic species along interfaces is often enhanced, though the exact mechanism of this enhancement remains under debate. Another consequence of this effect is increased solid solubility of aliovalent species. For example, Knauth and Tuller reported an increase in the solubility of Cu in nanocrystalline $CeO_2$ relative to the microcrystalline state [110]. It was proposed that this enhancement was accommodated by grain boundary segegration.

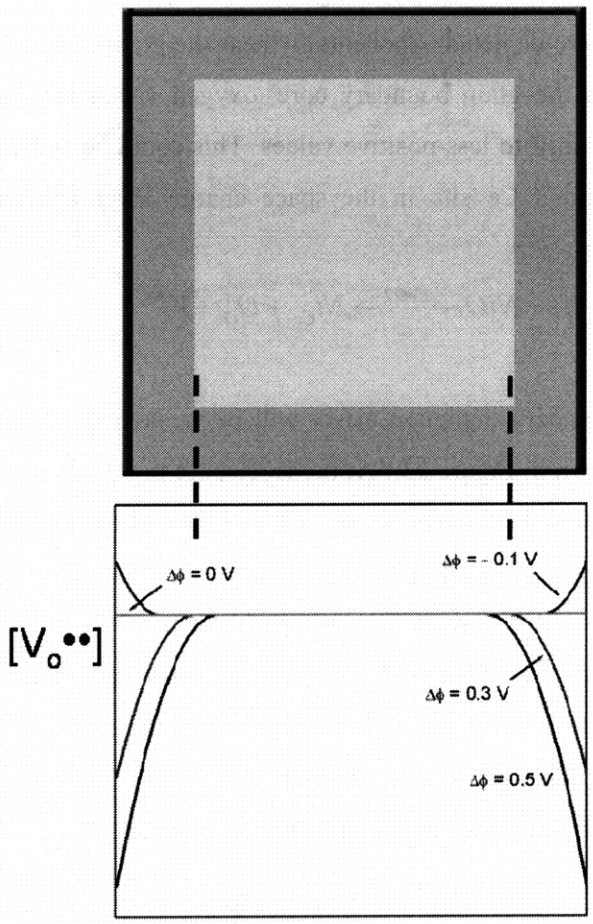


**Figure 33: Schematic diagram (top) of the bulk, space charge layers, and grain boundaries in a polycrystalline material. Shown below are Mott-Schottky oxygen vacancy profiles for ΔΦ values of +0.5, +0.3, 0, and -0.1 V in the space charge layer.**

### *1.10 Objectives of the Thesis*

The primary objective of this thesis is the attempt to modify and control charge transport in space charge regions in nanocrystalline ceria by heterogeneous doping along grain boundaries in ceria thin films. The following research is proposed in support of this objective:

- Prepare pulsed laser deposition (PLD) target(s) by conventional solid state ceramic processing

- Deposit ceria thin films by PLD, with control of film properties achieved by variation of temperature, laser repetition rate, and oxygen working pressure during deposition

- Characterize fundamental film properties such as microstructure, surface morphology, and crystal structure, by X-ray diffraction (XRD), scanning electron microscopy (SEM), atomic force microscopy (AFM), and transmission electron microscopy (TEM)

- Deposit thin film diffusion sources by sputter deposition and electron-beam evaporation

- Determine time and temperature conditions for diffusion within the Harrison regime C and diffusion coefficients through annealing and depth profiling by secondary ion mass spectrometry (SIMS)

- Modify film properties by heterogeneous in-diffusion of cations exclusively along grain boundaries

- Microfabricate reversible non-blocking electrodes and blocking electrodes by photolithography, thin film deposition, and liftoff.

- Measure electrical conductivity by electrochemical impedance spectroscopy and 2-point DC measurements

- Correlate the electrical properties and grain boundary modification through analytical space charge modeling

# CHAPTER 2. EXPERIMENTATION

## *2.1 Deposition of Thin Films by Pulsed Laser Deposition*

Thin film specimens were prepared by pulsed laser deposition (PLD). Lasers, as sources of monochromatic and coherent light of high intensity and energy, are used in a wide range of technical applications such as electronics and medicine. Soon after the invention of the first ruby-based laser of high power, researchers began studying the interaction of laser beams with solids [111, 112]. While the first use of lasers to deposit thin films occurred in 1965 [113], PLD did not fully emerge as a popular deposition technique until the late 1980's [114]. The period in between of relative stagnation has been attributed to competition from molecular beam epitaxy (MBE) and sputtering as rival deposition techniques, as well as a lack of one large central research focus that actually resulted from the versatility of PLD manifesting itself in many small, uncoordinated research efforts [115]. The breakthrough that led to the drastic increase in PLD research was the growth of high $T_C$ superconducting films at Bellcore [116]. Since that time, PLD has been used to deposit many different materials for a variety of scientific and technological applications.

The fundamental description of the electric field, E [in V/cm] of an electromagnetic wave is:

$$E = \sqrt{\frac{2\Phi}{c\varepsilon_o n}} \tag{63}$$

where $\Phi$ is the power density in W/cm$^2$, $\varepsilon_o$ is the dielectric constant in vacuum, $c$ is the velocity of light, and $n$ is the index of refraction. For a material with $n$ = 1.5 and a typical incoming power density of ~ $10^8$ W/cm$^2$, the electric field inside the solid material is on the order of $10^5$ V/cm. Such an electric field is easily large enough to cause dielectric breakdown; any material that absorbs this radiation will create plasma [115]. In the operation of a typical PLD system, an excimer laser is pumped to emit light at a given wavelength. In the laser system used in this work, KrF gas is excited by avalanche electric discharge to create excimer molecules. Soon after formation, this excimer will decay from the excited state to the ground state and emit a photon. The magnitude of the discharge field is typically10-15 kV/cm, requiring system voltages between 20-45 kV [117]. The interaction between the incident laser and the target material is complex. Theoretical models [118, 119] have been devised to describe the ablation process, yet a complete understanding of this phenomenon has yet to be established. What is agreed upon is that the incoming photons first excite the material electronically—the energy from this excited electronic state then relaxes into thermal, chemical, and mechanical modes of energy. This leads to evaporation, plasma formation, and the creation of a

'plume' of material that consists of a distribution of atoms, ions, and clusters. An image of the plume is shown in Figure 34. Similar to other forms of physical vapor deposition (PVD), this vapor condenses on the sample substrate to form a thin film.

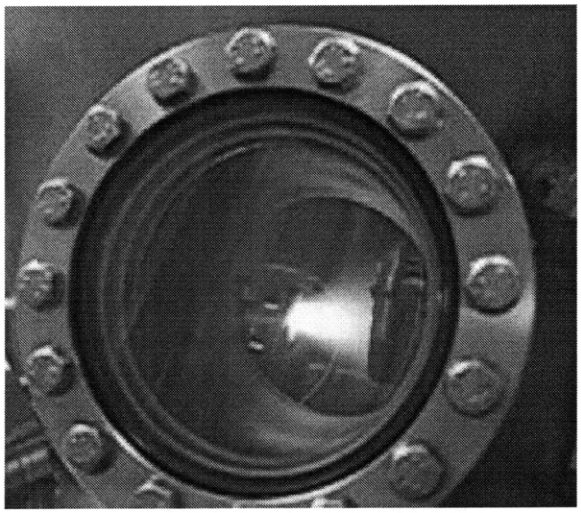

**Figure 34: Image of the PLD system from the viewpoint external to the chamber. The plume emanating from the target, left, is white. The sample holder is to the right, and is glowing orange as a result of heating to 700°C.**

The most desirable aspect of PLD is the ability to transfer the stoichiometry of the target material to the sample substrate with essentially no change in chemical composition. This trait is due to the high heating rate of the target surface, approximately $10^8$ K/s. At such a high rate, all target constituents effectively evaporate at the same rate, in contrast to other deposition techniques such as sputtering or electron beam evaporation.

A cerium oxide target was fabricated from cerium oxide powders (Alfa Aesar, 99.99%). Approximately 20 g of powder was loaded into a cylindrical stainless steel die of 1-3/16'' diameter and uniaxially-pressed at 8000 psi for 90 s. The target was then placed in a plastic bag, evacuated, and pressed in a cold isostatic press at 38,000 psi for 2 min. After pressing, the target was sintered at 1425°C for 10 hr. in air. Single crystal (100) MgO and R-plane sapphire (MTI Crystal, CA) substrates were placed in the PLD chamber and pumped down to high vacuum with a turbomolecular pump. The chamber was pumped down overnight, and the base pressure before deposition was typically 1 to $3x10^{-6}$ Torr. Samples were then heated at a rate of 8°/min to 700°C using a resistive coil heater. The heater was controlled by a thermocouple placed on the surface of the substrate holder. This assembly is shown in Figure 35.

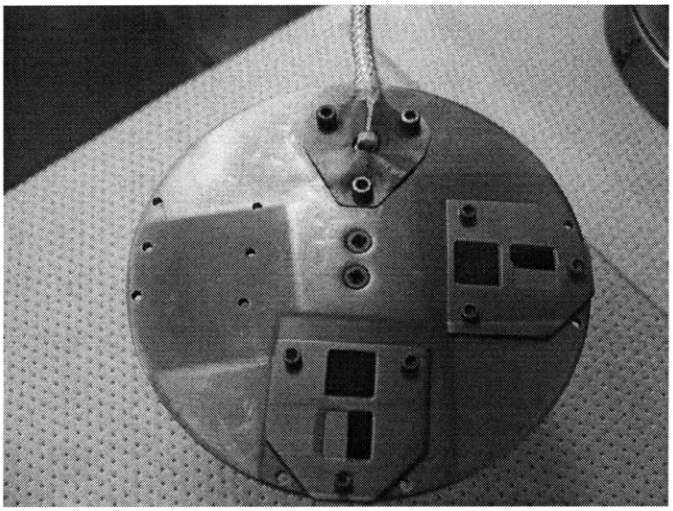

**Figure 35: Digital image of the PLD sample holder, showing two sample positions and the controlling thermocouple.**

The most common deposition parameter configuration was 500 mJ/pulse laser energy, 12-15 Hz laser repetition rate, and an $O_2$ working pressure of 4-6 mTorr. This working pressure was achieved by setting the opening of the gate valve between the turbo pump and the chamber to 5.3%. A Coherent (Santa Clara, CA) COMPex Pro 205 KrF eximer laser emitting at a wavelength of 248 nm was used for ablation. Prior to use, the laser was warmed up for 6 min., and then pre-ablated for 3000 pulses to remove surface contamination of the target. The sample holder was then rotated to position the sample within the location of the plume. Once the desired number of pulses had been reached, the gate valve was closed and additional $O_2$ was flowed until a chamber pressure of 3-5 Torr was reached. Finally, the samples were cooled at a rate of 5°/min to room temperature.

After deposition, the thickness of each film was measured with a Tencor P-10 profilometer (San Jose, CA). Due to the structure of the PLD sample holder, a shadow existed at the perimeter of each substrate where no film was deposited. During the thickness measurement, a stylus tip was brought down and contacted to the surface at a force of 6 mg. The tip was then scanned at a rate of 20 μm/s from the bare substrate onto the film.

## *2.2 Physical characterization*

### *2.2.1 X-ray diffraction*

A comprehensive characterization of film properties such as crystallinity, microstructure, and

morphology was undertaken. The crystallinity of the deposited films was examined by X-ray diffraction (XRD). A Rigaku (Tokyo, Japan) RU300 X-ray diffractometer was used with divergence, scattering, and receiving slit configurations of 1°, 1° and 0.3°, respectively. A rotating, water-cooled copper anode was used to produce X-rays at 50 kV and 300 mA. The X-rays were monochromated to isolate the Cu Kα wavelength of 1.541 Å. Scans of θ-2θ were taken from 15 to 85° at a rate of 3°/min., spanning the theoretical diffraction peaks associated with ceria. The resulting diffraction patterns were compared against existing ICCD crystallographic data using the JADE program [120].

### *2.2.2 Atomic force microscopy*

The grain size, morphology, and surface roughness of the ceria thin films were characterized by a Vecco Metrology (Santa Barbara, CA) D3000 atomic force microscope (AFM) with a Nanoscope IIIa controller. Due to the very fine grain size of the ceria specimens, AFM was the preferred technique over XRD and SEM in order to accurately determine the grain size. The microscope was operated in tapping mode using a standard Si-based cantilever (Veeco Probes, model RTESP). The tip length and radius were 125 μm and approximately 10 nm, respectively. Samples were measured in air with no physical preparation. The target amplitude was set to 2 V and an automatic algorithm was used to tune and detect the resonance frequency of each tip. The z-axis limit of the microscope was reduced from 8 to 1 μm in order to improve the resolution of the surface micrographs. Micrographs were analyzed to determine the root mean square (RMS) surface roughness and grain size using Vecco's Nanoscope software (version 5.12r3). A screen caption of the Nanoscope software routine used to examine the grain size is shown in Figure 36:

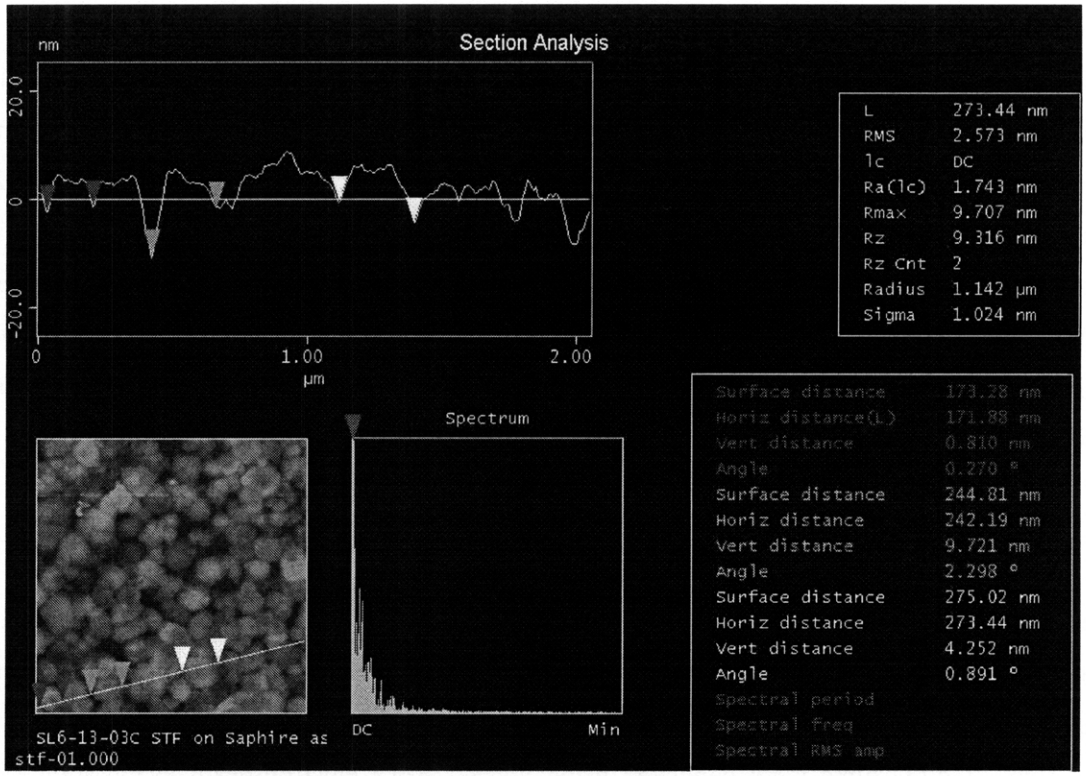


**Figure 36: Screen-capture of the Nanoscope AFM imaging software used to determine the grain size of $CeO_2$ thin films.**

### *2.2.3 Scanning electron microscopy*

Cross-sectional images of the ceria microstructure were obtained with a FEI/Philips XL30 (Hillsboro, OR) environmental scanning electron microscope (E-SEM). The instrument was operated in environmental mode in order to compensate electron charging that resulted from the insulating nature of the sample. This facilitated SEM analysis at a higher acceleration voltage and without the use of a metallic surface coating. The image was collected by a gaseous secondary electron detector. The accelerating voltage of the electron beam was 25 kV and the charge compensating $H_2O$ pressure was 2.5 Torr. Samples were held in place with carbon tape. The cross-section samples were prepared by fracture. First, the backside of a sample was scribed with a diamond tip and then pressure was applied from the backside using tweezers until fracture.

### *2.2.4 Transmission electron microscopy*

Transmission electron microscope (TEM) studies on ceria were undertaken by collaborators at the Laboratory for Electron Microscopy (LEM) at the University of Karlsruhe, Germany. The study was

performed using a 200 keV Philips CM200 FEG/ST transmission electron microscope equipped with a field emission gun and a 2k x 2k CCD camera. Energy dispersive X-ray spectrometry (EDX) was carried out by means of a NORAN Vantage system with a Ge X-ray detector using a probe diameter of about 1 nm. Electron energy loss spectroscopy (EELS) was performed utilizing a 200 keV Zeiss 922 microscope, equipped with an OMEGA energy filter. Cross-section as well as plan-view TEM samples were prepared by standard preparation procedures, including mechanical grinding, dimpling, polishing, and $Ar^+$-ion milling (Gatan Duo mill, 2-4 keV, 12-20°). After preparation, a thin layer of carbon was deposited on the samples, except on the thin region of interest, in order to reduce charging effects in the electron microscope.

### *2.3 Heterogeneous Diffusion Along Grain Boundaries*

The ceria thin films were modified first by deposition of a thin (~ 20 nm) source of aliovalent cations on the ceria surface. NiO films were deposited by reactive sputtering from a Ni target, using an RF power supply of 70 W and a 1:1 gas mixture of $Ar:O_2$ at a pressure of 10 mTorr. The sputtering time was 9 min. $Gd_2O_3$ films were deposited using a NRC 3117 electron-beam evaporation system (Varian, Palo Alto, CA). The film thickness was monitored in-situ using a quartz crystal microbalance and a Maxtek MDC-360 deposition controller. Dense $Gd_2O_3$ pellets of approximately 0.5 mm diameter (Alfa Aesar) were used as the evaporation source. Due to sublimation that occurred upon exposure to the electron beam, the current was held at a relatively low value of 0.06 A.

The diffusion source/ceria samples were annealed at temperatures ranging from 500-800°C for times up to 140 hr. As discussed in Section 1.7, the target diffusion condition was the Harrison regime C. A homologous temperature ($T/T_m$) of 1/3 is considered appropriate for this regime [87]. Given the 2475°C melting point of ceria, the temperature range of 700-800°C is required. This temperature range is also notable because it is, to the author's knowledge, the lowest range in which cation diffusion has been studied in a fluorite material. A schematic of the target sample microstructure and Harrison regime C annealing is depicted in Figure 37:

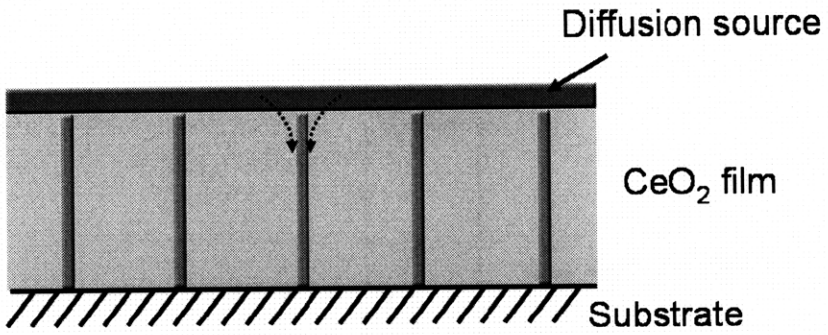


**Figure 37: Cross-sectional schematic of a nanocrystalline, columnar $CeO_2$ with a surface diffusion source. The arrows indicate fast diffusion pathways for cations along the grain boundaries.**

Through the measurement of grain boundary diffusion at SOFC operational temperatures, the study of degradation due to fast diffusion processes in microstructured SOFCs 'stacks' is also enabled [121]. Various tube and box furnaces were heated to the desired annealing temperatures and verified with additional thermocouples. Samples were inserted quickly into the furnace using tongs (box furnace) or a thermocouple rod (tube furnace). Samples were annealed for the desired amount of time and similarly removed from the furnace hot zone. This method was employed to ensure a sample thermal history as close in nature to a square wave as possible.

### *2.4 Secondary Ion Mass Spectrometry*

Diffusion profiles resulting from the annealing conditions described in Section 2.3 were characterized by Time-of-Flight Secondary Ion Mass Spectrometry (ToF-SIMS) at the Institute for Physical Chemistry at RWTH Aachen University, Germany. Typically, 25 keV $Ga^+$ ions raster scanned over (100 μm x 100 μm) were used to generate secondary ions; 1 keV $O_2^+$ ions raster scanned over (300 μm x 300 μm) were used for sputter etching of the surface. A low energy beam of electrons was used for charge compensation. Positive secondary ions arising from the diffusion source as well as from the substrate were monitored; short-circuiting effects due to pinholes were removed by generating 2-D ions maps for each sample and defining regions-of-interest only were ion concentrations were laterally homogeneous. Additional information regarding the SIMS technique and instrument can be found in the literature [122, 123].

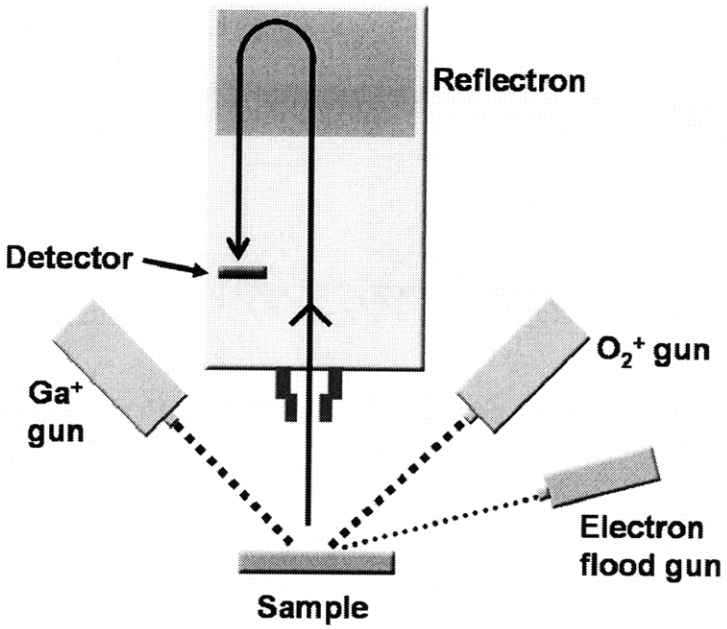


**Figure 38: Schematic of the ToF-SIMS instrument. Shown are the $Ga^+$ gun used for analysis, the $O_2^+$ gun used for depth sputtering, and the electron flood gun used for charge compensation.**

The generation of elemental depth profiles from the raw SIMS data began with calibration of the cumulative spectrum of intensity vs. mass, using predictable and well-known peaks such as H, Li, O, and Al as references. A sample spectrum is shown in Figure 39:

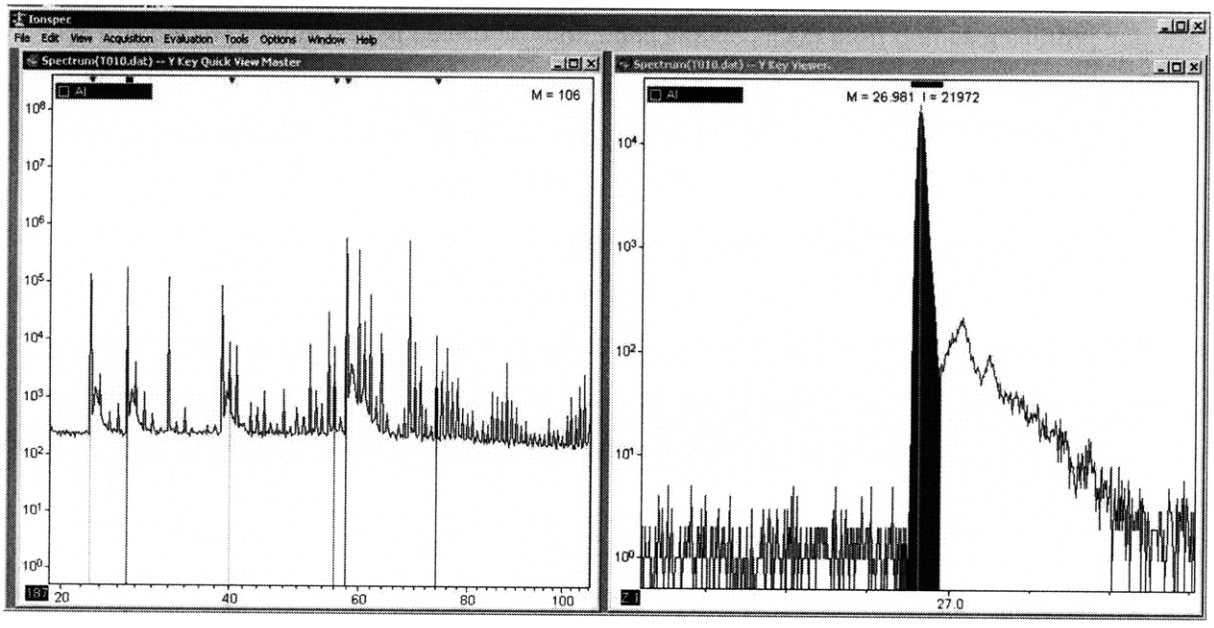


**Figure 39: Snapshot of a SIMS spectrum, showing the entire spectrum range, left, and a close-up of the Al peak, right.**

Spectra such as the one shown in Figure 39 were generated at each discrete depth. Depth profiles were generated with the Ionspec software [124]. Two-dimensional elemental maps were generated for all profiles in order to detect inhomogeneities such as pinholes. For specimens in which inhomogeneities were detected, 'regions-of-interest' (ROIs) were generated that specified which components of the 2-D map would be used for the depth profile generation. Thus, anomalously fast diffusion due to pinholes was excluded from the analysis of the diffusion profiles. A sample 2-D ion map is shown in Figure 40, with Al pinholes evident from the sapphire substrate.

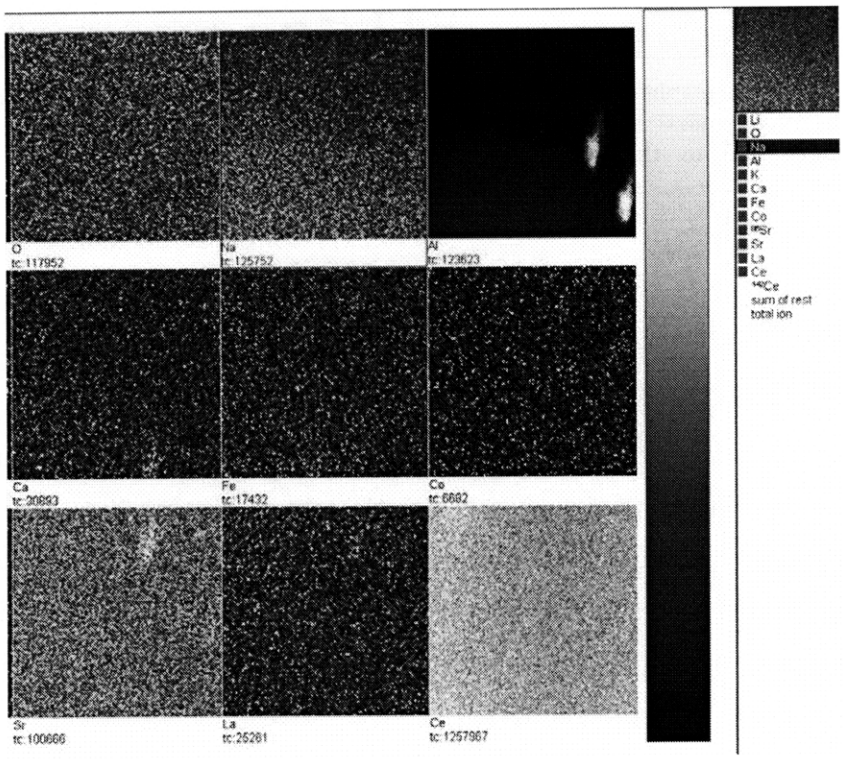


**Figure 40: Two-dimensional ion maps of various cations in a ceria diffusion sample. Two pinholes associated with the sapphire substrate are apparent in the upper right corner of the image.**

Depth profiles were thus created for relevant species such as Mg, Al, Ni, and $^{142}Ce$. The sputtering time was converted into depth first by measurement of each crater by interference microscopy. The high quality of the films, particularly the RMS surface roughness of less than 1.5 nm, ensured uniform sputtering of the craters and increased accuracy of the measured crater depth. Once the crater depth was determined, a linear relation between depth and sputtering time was assumed [122, 123]. An optical micrograph and 3-D reconstruction from the interference microscope are shown in Figure 41 and Figure 42. The Ni and Mg signals were normalized by $^{142}Ce$ in all samples in order to ensure a constant reference point as a function of depth, and also from sample-to-sample.

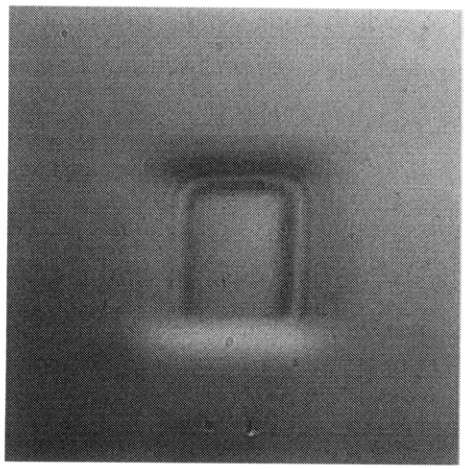

Figure 41: Optical micrograph of a SIMS crater. The observed colors result from interference fringes due to the uniform depth of the crater.

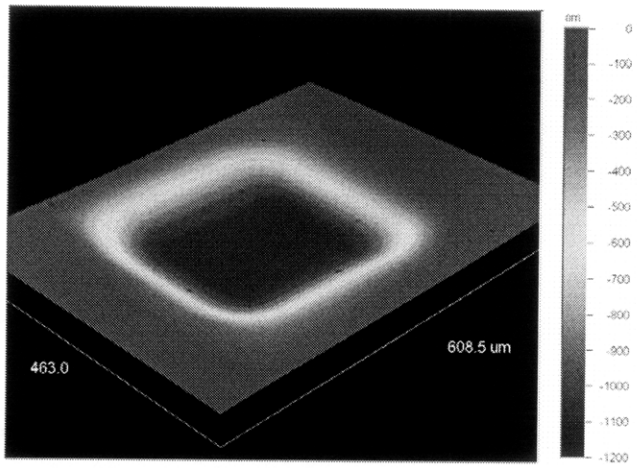


Figure 42: 3-D reconstruction of a SIMS crater using an interference microscope.

### *2.5 Lithographic Preparation of Microelectrodes*

Following the in-diffusion annealing treatments, samples were prepared for electrical characterization. The diffusion source was removed, first by reduction of NiO to Ni at the end of the diffusion anneal by flowing a gas mixture of 95:5 $N_2$:$H_2$ (forming gas) at 800°C. The Ni metal layer was then removed by etching in a solution of 3:1 $HNO_3$:$H_2O$, which removed the diffusion source within 3 minutes, yet removed only ~ 10 nm of the ceria layer. Removal of the Ni was observed visually and confirmed with XRD. The samples were then annealed at 600°C for 1-5 hr. in order to re-oxidize the ceria layer.

A photolithographic 'lift-off' technique was used to create microelectrode patterns. Several 4" x 4" glass masks with chrome features were designed using AutoCAD and fabricated by Advanced Reproductions (North Andover, MA). Two interdigitated electrode (IDE) structures were made on each 1 cm x 1 cm sample, with finger widths and inter-finger spacings of 40 and 50 μm. The samples were cleaned with acetone and isopropanol and heated on a hotplate at 150°C for 10 min. The negative photoresist NR-7 (Futurrex, Franklin, NJ) was spun onto the samples at 2500 RPM for 35 sec. Samples were then pre-baked at 150°C for 1.25 min. on a hot plate, followed by exposure to UV light for 44 sec. Samples were post-baked at 100°C for 1 min., and developed in RD-6 developer (Futurrex) for 20-30 sec. Development of the photoresist was monitored visually and verified with an optical microscope.

Non-blocking, reversible Pt microelectrodes were deposited by sputter deposition. A plasma was created in the sputtering machine with 5 mTorr of Ar gas and DC power of 50 W. The Pt target was sputtered for 7 min., resulting in films of 125 nm thickness. The IDE structure was finally realized by lifting-off the remaining photoresist using Resist Remover 4 (RR4, Futurrex). Samples were placed in a beaker of RR4 and held overnight. Samples were then ultrasonically-agitated to remove any remaining photoresist. A schematic diagram and digital image of the electrode structures are found in Figure 43 and Figure 44, respectively.

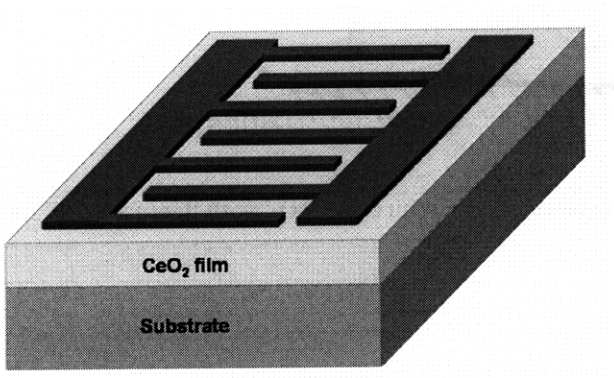


**Figure 43: Schematic of a microfabricated IDE structure on the surface of a $CeO_2$ film.**

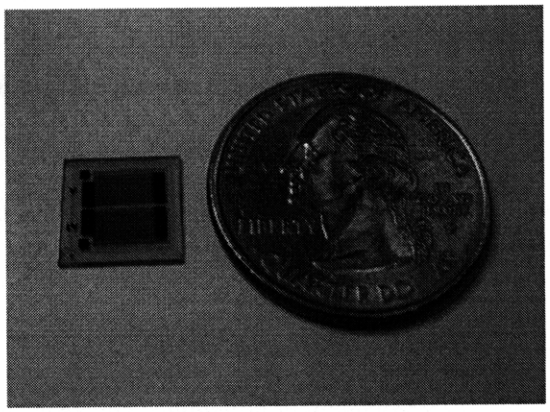

**Figure 44: Image of a $CeO_2$ sample with 40 and 50 μm interdigitated Pt electrodes, with a U.S. quarter dollar shown for scale.**

Electron-blocking electrodes were also grown via sputter deposition. First, dense $Zr_{0.88}Y_{0.12}O_{1.94}$ (YSZ-12) films were reactively sputtered from a Y/Zr metal alloy target (ACI Alloys, San Jose, CA). A plasma of 10 mTorr pressure and 9:1 Ar:$O_2$ gas composition was generated using an RF power supply of 200 W. The target was sputtered for 16 min. and then allowed to cool for 2 hr. Then, the target was sputtered for an additional 10-16 min. and allowed to cool. This cycle was performed either 2 or 3 times for each specimen in order to ensure that the sample temperature did not exceed 180°C, the maximum operating temperature of the photoresist. The estimated thickness of the YSZ-12 layer was 250 nm. Porous Pt was prepared directly on top of the YSZ-12 IDE structures. A plasma of 1:1 Ar:$O_2$ at a pressure of 10 mTorr was used in conjunction with a DC power supply of 30-40 W. The Pt target was sputtered for 5 min. Following liftoff of the photoresist, described above, porosity was introduced to the initially-dense Pt layers by placing the samples into a tube furnace at 610°C for 45 min., followed by cooling at 6°/min. to room temperature. During deposition, the oxygen species in the plasma reacted with Pt to form PtO and $PtO_2$, as detected by X-ray photoelectron spectroscopy [125]. However, such bonds are unstable and subsequent annealing resulted in oxygen evolution and pore formation. A schematic cross-section of the YSZ-12 and

porous Pt layers is shown in Figure 45.

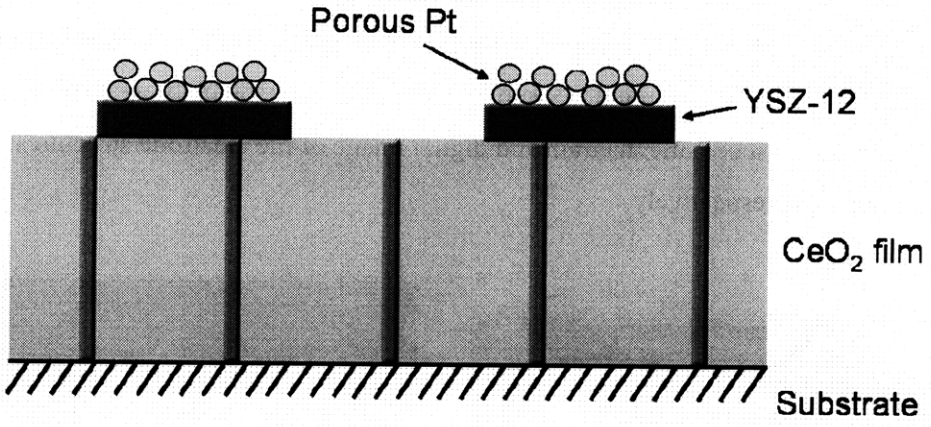


**Figure 45: Cross-sectional schematic of the blocking electrode structure on $CeO_2$, with dense YSZ-12 and porous Pt layers depicted.**

## *2.6 Electrical Characterization*

### *2.6.1 Electrochemical impedance spectroscopy*

Electrochemical impedance spectroscopy (EIS) was employed using a Solartron (Farnborough, UK) 1260 frequency response analyzer. The instrument was controlled with the ZPlot software (Scriber Associates, Southern Pines, NC). A sinusoidal voltage of 50 mV amplitude centered around 0 V was applied from a frequency of 10 MHz to 1 Hz. The frequencies were stepped logarithmically, with 10 data points collected per decade. Each frequency step was accompanied by a 6 cycle delay before measurement and an integration time of 10 cycles.

The impedance spectra were analyzed via least-squares regression analysis with the ZView software (Scriber Associates). Each spectrum was fitted to an equivalent circuit model of a resistor (R) and constant phase element (CPE) in parallel. The impedance of the CPE is expressed as:

$$Z_{CPE} = \frac{1}{Q_O(i\omega)^n} \tag{64}$$

Where $\omega$ is the angular frequency, $Q_O$ is the admittance (1/Z) at $\omega$ = 1 rad/s, and $n$ a measure of the ideality, with values between 0 and 1. The CPE is commonly described as a non-ideal capacitor with a distribution of relaxation times. When $n$ approaches unity, the CPE begins to function as a capacitor and $Q_O$ = C. Initial estimates of each parameter were input to the ZView software and an

optimization routine was run to find the best model fit to the experimental data. Two microprobe stations were utilized to collect the electrical data. The first was an ambient-pressure Karl Suss (Waterbury Center, VT) probe station with a small heating stage manufactured by Linkham Scientific Instruments (Model TS1500, Tadworth, UK). The heater consisted of an alumina cup 7 mm in diameter and a serpentine resistive wire capable of a maximum temperature of 1100°C. However, since the samples measured were larger than the diameter of the cup, a titanium piece of 16 mm diameter and 4 mm thickness was machined to fit inside the cup and provide a larger surface for the samples [126]. Suss PH150 micromanipulators were used to position pieces of Pt thermocouple wire (99.99% purity, Birmingham Metal, UK) to make contact to the microelectrodes. An optical microscope was used to monitor and verify contact of the wire tip to the microelectrode patterns.

Electrical measurements were performed from 400 to 550°C, the proposed operating temperature regime of micro-SOFCs [127]. Due to the gap between the surface of the Ti piece and the resistive heater, as well as the interface between the sample surface and the unheated air above it, the actual temperature of the sample deviated considerably from the heater set-point temperature. This deviation was monitored by the placement of a K-type thermocouple, pressed firmly onto the sample surface by an additional micromanipulator and W probe tip. The reported temperature was measured with this thermocouple. A custom-designed LabVIEW program was used to control the temperature of the heating stage and the ZPlot software. Samples were equilibrated at each temperature for 20-30 min. and then measured.

A newer microprobe station was designed by Dr. Avner Rothschild (present address: Technion, Haifa, Israel) and manufactured by McAllister Technical Systems (Coeur d'Alene, ID). This microprobe system consisted of a 2" heater within an enclosed chamber capable of gaseous environmental control. Four gas channels controlled by MKS 1359C mass flow controllers (MFCs) were combined in a mixing chamber and flowed into the main chamber. Pure $N_2$ and $O_2$, and mixtures of the two were used to vary the partial pressure of oxygen ($pO_2$); this was accomplished by adjusting the flow rates of each MFC independently. The sum of the flow rates was kept constant at 300 sccm. A one-way Swagelok valve was incorporated to prevent backflow from the exhaust gas lines, and so the chamber pressure was approximately 1 atm at all times. The actual $pO_2$ was monitored with a commercial oxygen sensor manufactured by Bosch. The variation of $pO_2$ within the chamber proceeded from low to high $pO_2$. The chamber was first evacuated with a roughing pump (BOC Edwards, Crawley, England) to a total pressure of approximately 0.04 atm, and back-filled with $N_2$ to ~ 0.65 atm. The second was evacuated a second time using a turbomolecular pump (BOC

Edwards) to an estimated total pressure of < $10^{-4}$ atm. After back-filling with $N_2$ to 1 atm, the measured $pO_2$ was approximately $10^{-4}$ atm. The $pO_2$ was then varied according to the parameters listed in Table 2:

| Target $pO_2$ (atm) | Gas 1 | Flow rate (sccm) | Gas 2 | Flow rate (sccm) |
|---|---|---|---|---|
| $10^{-3}$ | 1% $O_2$:balance $N_2$ | 30 | $N_2$ | 270 |
| $10^{-2}$ | 1% $O_2$:balance $N_2$ | 300 | --------- | --------- |
| $10^{-1}$ | $O_2$ | 30 | $N_2$ | 270 |
| $10^{0}$ | $O_2$ | 300 | --------- | --------- |

**Table 2: Gas mixtures and flow rates used to vary $pO_2$ within the enclosed probe station**

The temperature of the samples in the chamber was varied with a 2" heating stage manufactured by HeatWave Labs (Watsonville, VA). The temperature was varied from 400 to 550°C. The controlling thermocouple consisted of an S-type thermocouple sandwiched between two single crystal sapphire substrates. The sandwich structure was held in place in the center by OMEGABOND 300 high temperature insulating ceramic cement (Omega, Stamford, CT) with high thermal conductivity. This structure was used to provide a more realistic measurement of the sample temperature (similar single crystal substrates), as well as a more uniform and reproducible temperature reading. The sample was held in place with a metal clip during measurement to avoid movement.

### *2.6.2 Two-point DC measurements*

Two-point DC measurements were undertaken using a Hewlett-Packard 4142B DC voltage supply (Palo Alto, CA). Current-voltage (I-V) curves were measured on non-blocking electrodes with a LabVIEW program by beginning at V = 0 V, sweeping to a set negative voltage value, sweeping to the same voltage value of positive polarity, and then returning to 0 V. The resistance of the sample, defined at dV/dI, was calculated as the reciprocal of the slope of the I-V curve.

The partial ionic conductivity ($\sigma_{ion}$) of the specimens with blocking electrodes was determined using two-point DC measurements. A separate LabVIEW program was used, in which a constant DC bias was applied and current was measured as a function of time. After an initial high-current transient, the signal stabilized at a constant value after approximately 150 s. Ohm's law was used at this level of constant current to define the partial ionic resistance, and thus the partial ionic conductivity of the

sample. The I-t characteristics for one sample were measured with four different values of applied bias in order to determine whether the I-V properties were linear and thus within the Ohmic regime.

# CHAPTER 3. RESULTS

## *3.1 Cerium Oxide Film Deposition*

As measured by the Tencor P-10 profilometer, the deposition rate resulting from the PLD system with a laser energy of 500 mJ/pulse ranged from 11.2 nm to 26.2 nm per 1000 pulses. The variation in deposition rate is attributed to the protective window covering the port where the laser beam enters the chamber. As material was ablated from the target, a film gradually built-up on the window, reducing the laser intensity reaching the target. This was observed visually as the plume became dimmer with time. Periodically, the window was rotated to a new position free of the deposited film, and this change was accompanied by an appreciable increase in plume brightness and deposition rate. Overall, the average deposition rate was estimated to be 19.4 nm per 1000 pulses.

The XRD spectra for $CeO_2$ thin films grown in this manner on MgO (100) single crystal substrates are shown in Figure 46. The results in (a) indicate that the film is polycrystalline with no strongly-preferred orientation. Reflections from (111), (200), and (311) planes are evident. In contrast, the sample shown in (b) shows a higher degree of preferred orientation with only (200) reflections displayed. All $CeO_2$ films on MgO displayed XRD spectra such as (a) or (b) in Figure 46. There was no evidence of amorphous films, nor diffraction peaks other than the ones previously indicated. The average sample grown on MgO is best-described as polycrystalline, with a slightly, though not exclusively, (100) preferred orientation. The differences in the observed XRD spectra are discussed further in Section 4.1.

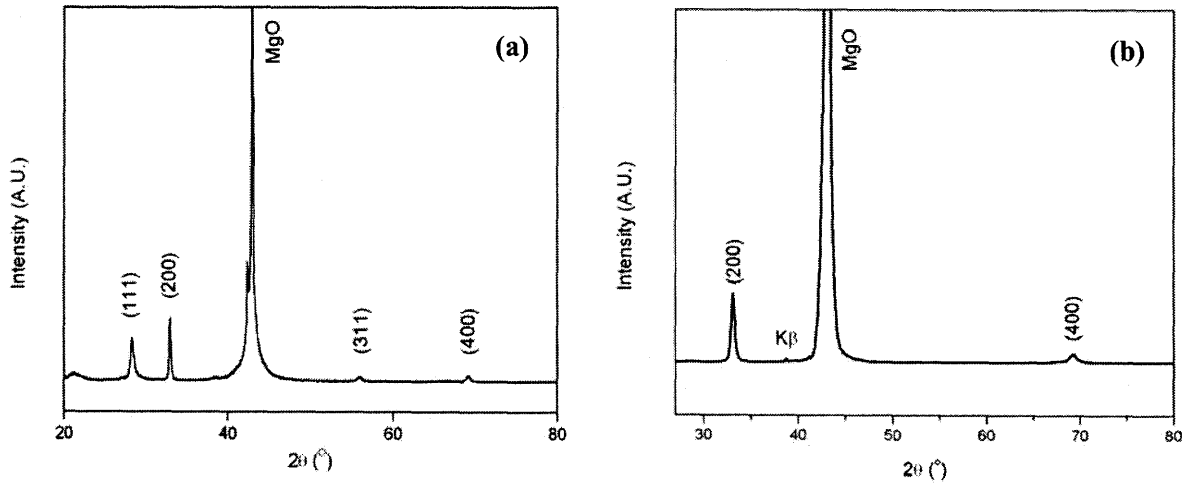


**Figure 46: XRD scans of $CeO_2$ on MgO substrates. The sample in scan (a) is polycrystalline with evidence of (111), (200), and (311) reflections. The reflection near $2\theta = 22^{O}$ is an artifact from the surface of the MgO substrate. In the specimen of scan (b), only (200) reflections are evident, indicating a higher degree of preferred orientation.**

In Figure 47, the XRD spectra of $CeO_2$ films deposited onto single crystal sapphire are shown. In scan (a), diffraction peaks associated with (200) and (311) planes are apparent. In scan (b), only (200) reflections are observed. Similar to the data presented above for $CeO_2$ on MgO, all samples grown on sapphire displayed XRD spectra like the two shown in Figure 47. Thus, the samples grown on sapphire can also be described as polycrystalline, with (100) preferred, though not exclusive, orientation.

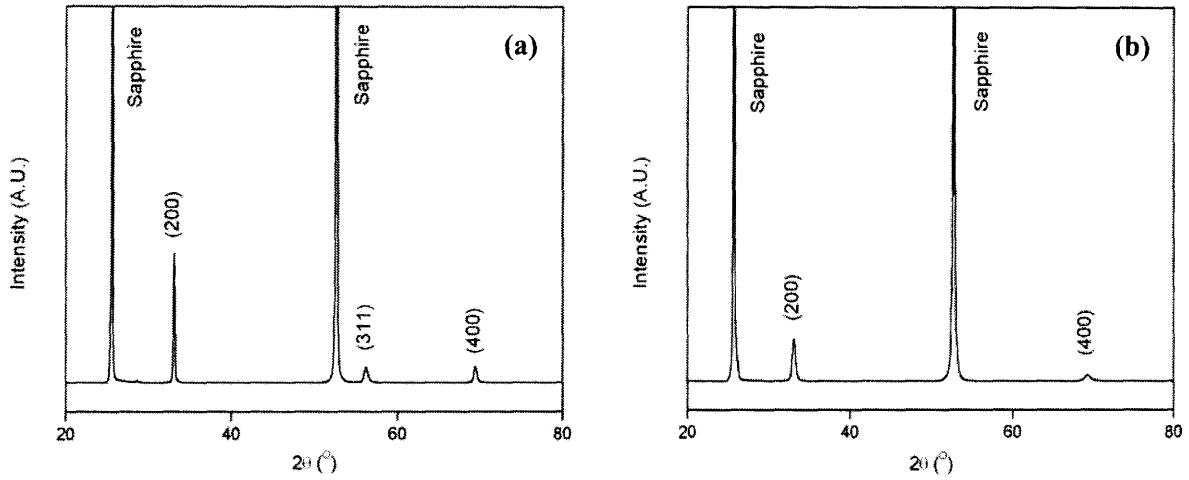


**Figure 47: XRD scans of $CeO_2$ on sapphire substrates. The sample in scan (a), shows (200) and (311) reflections. In the sample from scan (b), only (200) reflections are evident, indicating a higher degree of preferred orientation.**

An AFM micrograph of the surface of an as-deposited $CeO_2$ sample is shown in Figure 48. Using the software described in Section 2.2.2, the grain sizes were determined to fall within the range of 25-45 nm. The root-mean-square (RMS) surface roughness was calculated to be 0.5 nm, indicative of a highly smooth surface.

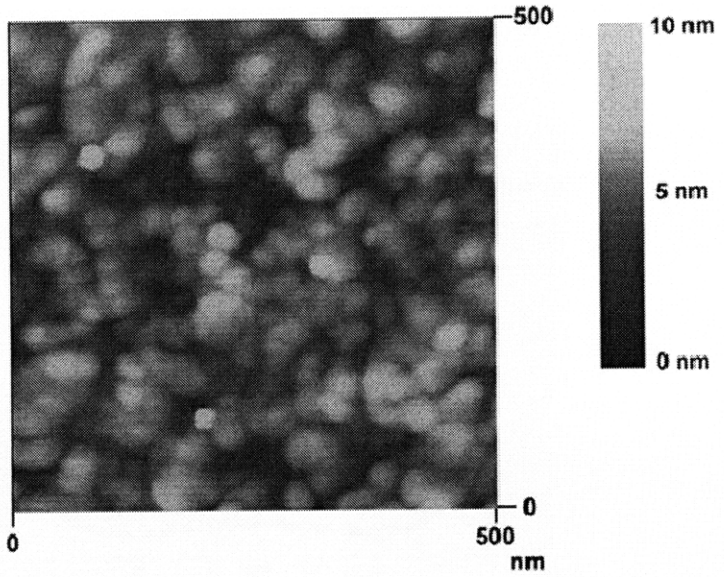


**Figure 48: AFM micrograph of a $CeO_2$ surface. Grain sizes of 25-40 nm are evident.**

AFM micrographs of $CeO_2$ surfaces after annealing are shown in Figure 49. Sample (a) was annealed at 600°C for 5 hr. The average grain size increased to approximately 62 nm, and the RMS surface roughness increased to 2.5 nm. Sample (b) was annealed at 850°C for 12 hr. In this case, the average grain size increased to approximately 75 nm and the RMS surface roughness was calculated as 0.6 nm.

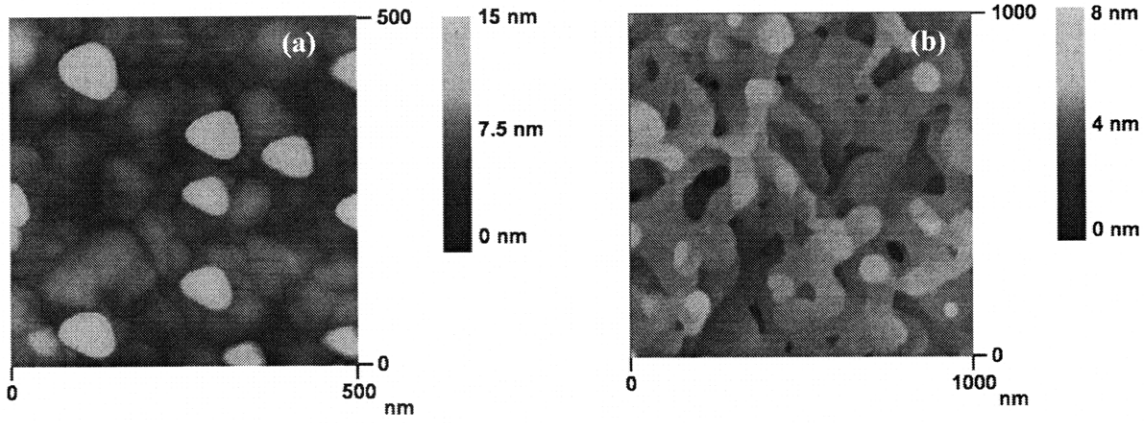


**Figure 49: AFM micrograph of $CeO_2$ surfaces after annealing at (a) 600°C for 5 hr. and (b) 850°C for 12 hr (right).**

Two SEM cross-sectional micrographs of $CeO_2$ layers are shown in Figure 50. Both the reduced-zoom (a) and zoomed-in (b) micrographs indicate a flat film with no visible pores. The microstructure appears to be columnar, with high-aspect ratio grains extending from the substrate to

the surface. However, it should be recalled that the samples were prepared by scribing on the backside of the substrate and fracturing, as described in section 2.2.3. Such a preparation method could conceivably lead to a cross-sectional morphology that is not indicative of the true microstructure, despite the apparent columnar nature in Figure 50.

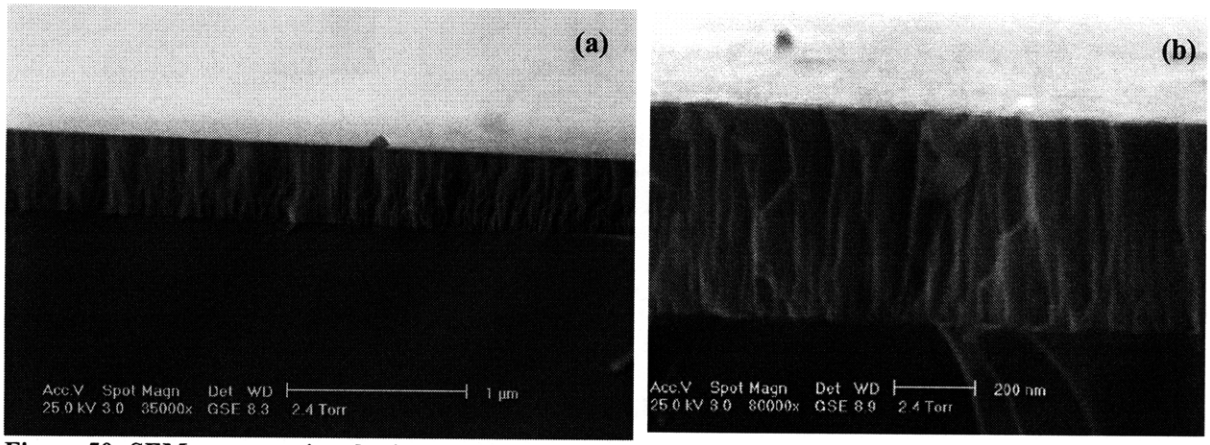


**Figure 50: SEM cross-sectional micrographs of $CeO_2$ thin films, displaying an apparent columnar microstructure.**

In order to determine the microstructure more conclusively, TEM measurements were also performed at the University of Karlsruhe, Germany [128]. Bright-field (a) and dark-field (b) cross-sectional TEM micrographs are shown in Figure 51. In these micrographs, the columnar microstructure, apparent from the above SEM images, is confirmed. High-aspect ratio grains clearly extend from the MgO substrate to the surface. In addition, the grain size distribution resulting from the AFM analysis, 25-45 nm, is confirmed.

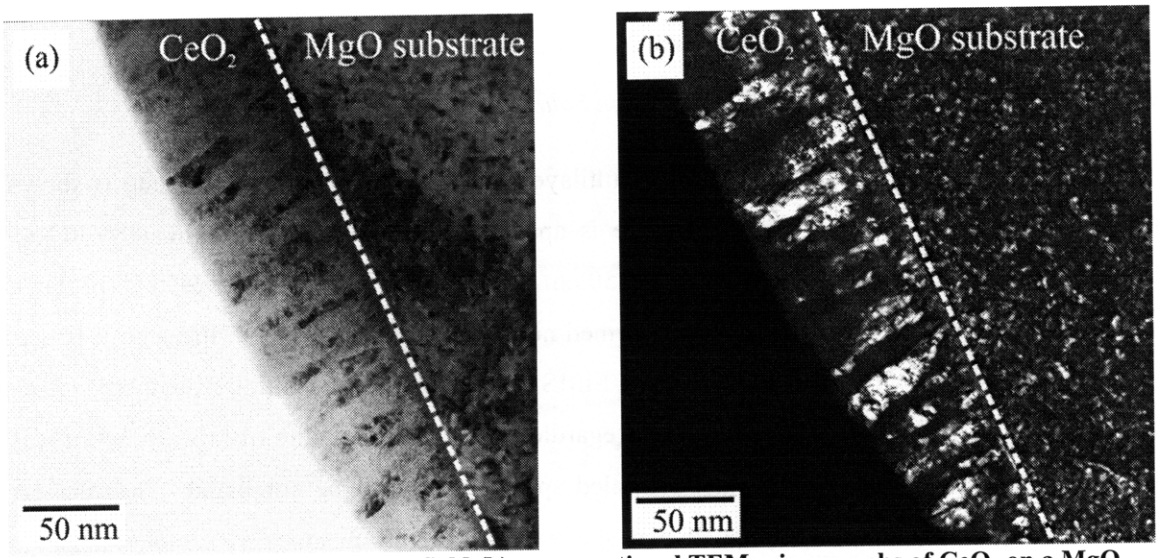


**Figure 51: Bright field (a) and dark field (b) cross-sectional TEM micrographs of $CeO_2$ on a MgO substrate. A nanocrystalline, columnar microstructure is evident.**

A high-resolution TEM (HRTEM) micrograph is shown in Figure 52. The sample was annealed at 650°C for 10 hr. The arrows indicate the grain boundary region separating two adjacent $CeO_2$ grains. Several features from this micrograph are notable. First, there is no evidence of a second phase such as silica in the grain boundary region. Second, the grain boundary itself is limited in spatial extent: there is no amorphous region of 1-2 nm thickness, as is sometimes observed in polycrystalline ceramic materials.

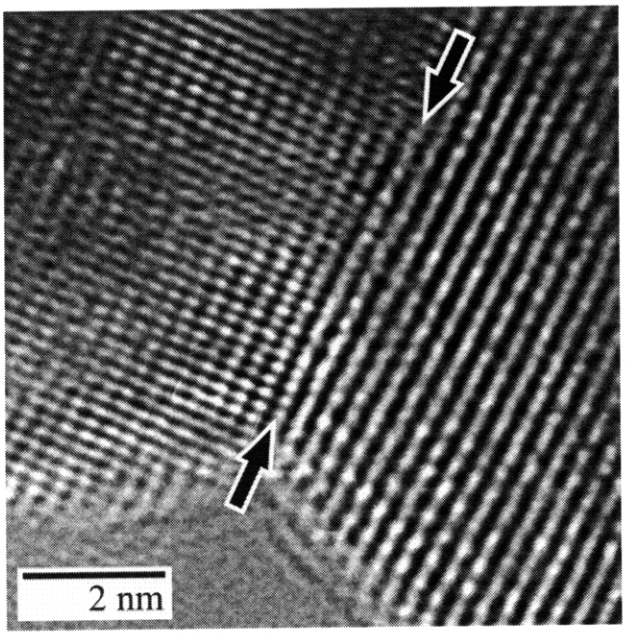


**Figure 52: High-resolution TEM micrograph of a grain boundary in $CeO_2$. The sample was annealed at 650°C for 10 hr. The width of the boundary region is less than 1 nm, and neither secondary phases nor amorphous regions are apparent.**

### *3.2 Cation Diffusion Along Grain Boundaries*

#### *3.2.1 Nickel Diffusion From the Surface Diffusion Source*

The SIMS spectrum of a NiO—$CeO_2$—MgO multilayer sample in the as-deposited state is shown below in Figure 53. The NiO—$CeO_2$ interface is apparent at a depth of approximately 50 nm. Surprisingly, the $^{58}Ni$ signal appears to extend ~ 250 nm into the $CeO_2$ layer. However, this specimen was not annealed. The NiO sputtering was performed near room temperature and diffusion was thus kinetically-limited. This signal is believed to be a SIMS artifact, possibly resulting from a broad peak adjacent to the $^{58}Ni$ peak in the SIMS spectra. Regardless of the exact nature of this artifact, it was used to form the baseline by which other annealed specimens would be compared. In order for diffusion to be apparent, it was stipulated that spectra resulting from annealed samples must be clearly distinct from the spectrum shown in Figure 53.

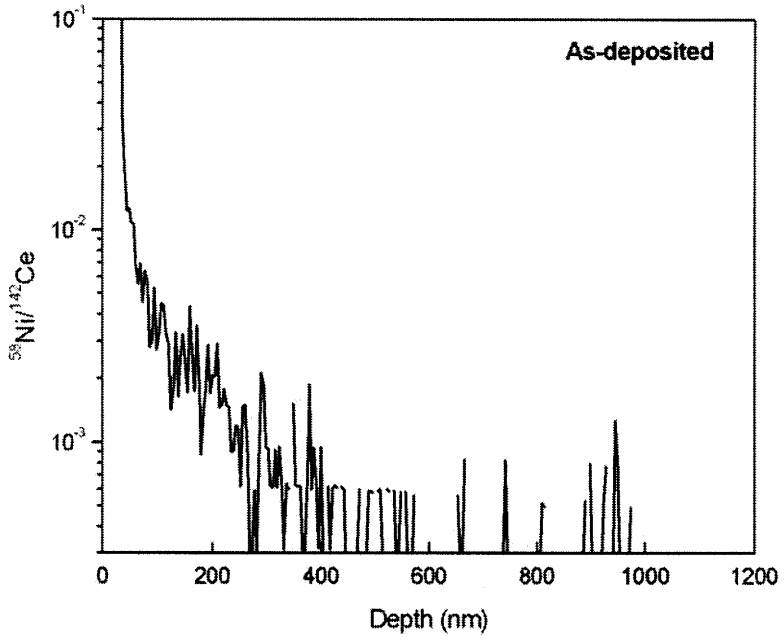


**Figure 53: SIMS spectrum of Ni within a $CeO_2$ film. The Ni signal penetrates approximately 250 nm into the film, though this is believed to be a signal artifact and not Ni diffusion.**

In Figure 54, SIMS spectra of Ni in $CeO_2$ after annealing at 500°C (a) and 600°C (b) are shown. In both cases, the $^{58}Ni/^{142}Ce$ ratio does not appear to deviate significantly from the as-deposited sample. Even though the background level for both samples, particularly the 500°C sample, appears to be higher than the as-deposited sample, such variations occurred at other times during the SIMS analysis. Such a small variation cannot rigorously be considered distinct, and so the conclusion reached with respect to Figure 54 is that no diffusion is apparent. However, since the detection limit

of SIMS is typically on the order of ppm [122], it is still possible that a smaller Ni concentration had diffused undetected.

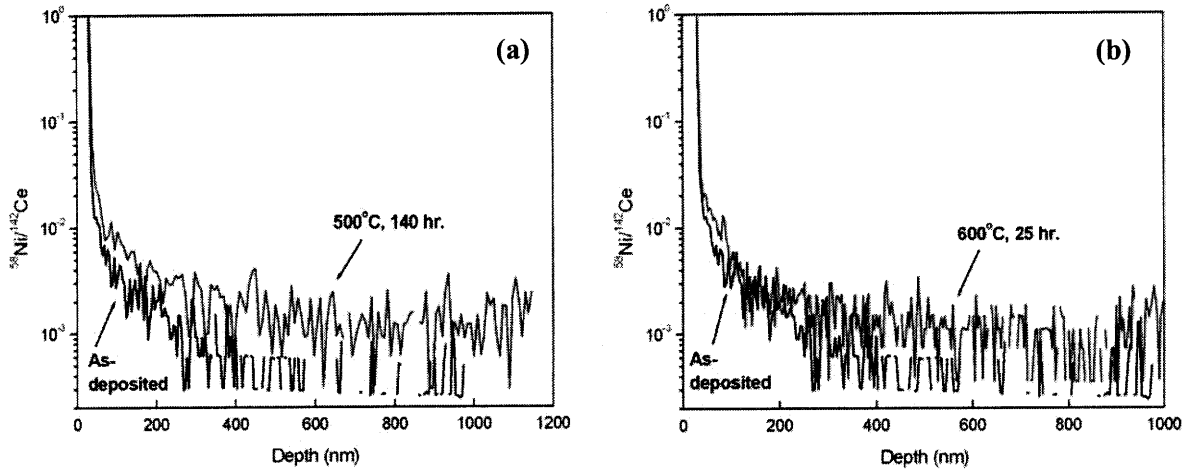


**Figure 54: SIMS spectra of Ni in $CeO_2$, annealed at (a) 500°C and (b) 600°C. Diffusion was not detected in either sample after annealing for 140 and 25 hr., respectively.**

In contrast, the SIMS spectra in Figure 55 demonstrate clearly that Ni diffusion in $CeO_2$ has taken place after annealing at 700°C. The two spectra represent the depth profiles after annealing for 5 and 7 hr. The profiles are consistent, as the 7 hr. data extends to a further depth than the 5 hr. data, and appears to reach the underlying substrate. As will be discussed in Section 4.2, the 7 hr. data is likely not suitable for quantitative diffusion analysis, as the substrate is regarded as a zero-flux plane that is blocking to further diffusion. This assumption has been made because the substrate is a single crystal with no grain boundaries along which diffusion could take place in this temperature range. Because the substrate is a zero-flux plane, the 7 hr. spectrum may represent partial 'backwards' diffusion, as a concentration gradient near the substrate will result in a driving force for diffusion in the opposite direction. For simplicity, only the 5 hr. spectrum, which does not reach the substrate, will be considered in quantitative modeling of the diffusion coefficient.

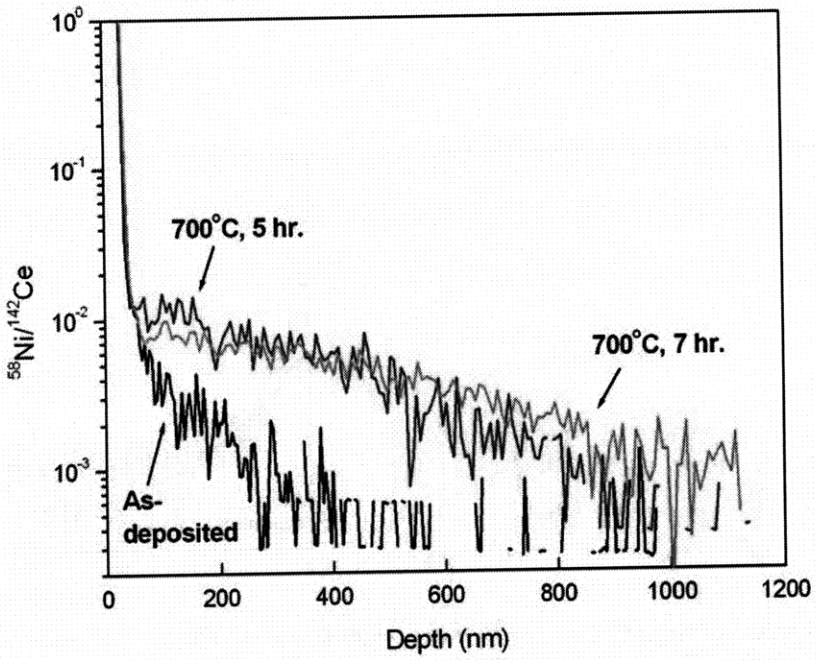


**Figure 55: SIMS spectra of Ni diffusion in $CeO_2$ after annealing at 700°C. Shown are as-deposited data, as well as profiles resulting from anneals of 5 and 7 hr. duration. The depth profile after 7 hr. annealing appears to penetrate through the entire film.**

SIMS spectra resulting from 800°C annealing are found in Figure 56. In this case, the Ni signal penetrates through the entire film and clearly reaches the substrate. The flat profile precludes an accurate determination of the diffusion coefficient. It is of interest to note the similarities in the $^{58}Ni/^{142}Ce$ ratio between the 5 and 10 hr. spectra. Both signals are essentially equivalent, indicating that continued annealed at this temperature has had no impact on the depth profiles. This indicates possible saturation of the grain boundary regions since no increase in the Ni signal is evident upon further annealing.

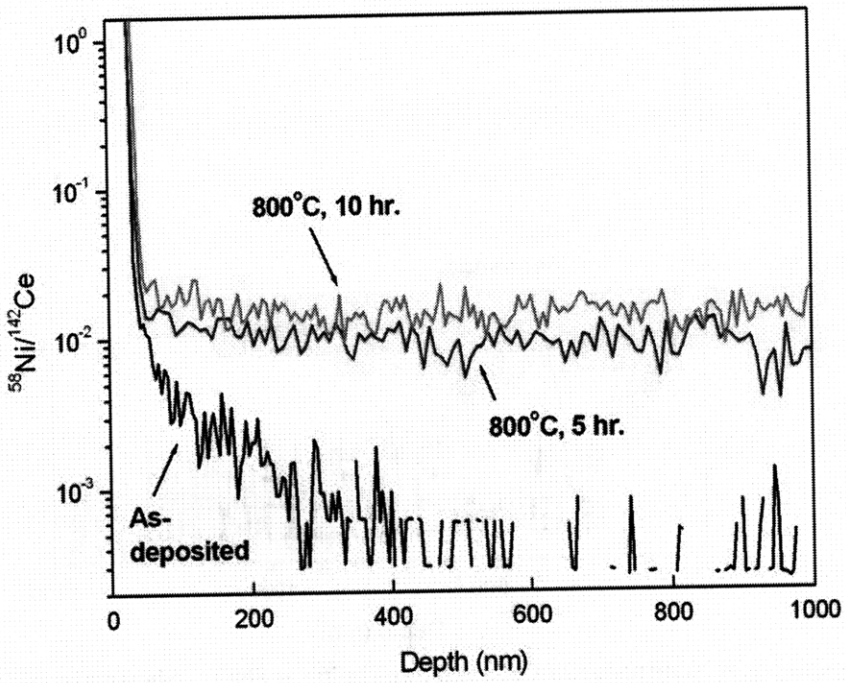


**Figure 56: SIMS spectra of Ni diffusion in $CeO_2$ after annealing at 800°C. Shown are as-deposited data, as well as profiles resulting from anneals of 5 and 10 hr. duration. Both profiles penetrate through the $CeO_2$ film, though increasing time has no apparent effect on the total concentration.**

In order to accurately determine the diffusion coefficient of Ni in $CeO_2$ at 800°C, an additional sample was grown to a greater $CeO_2$ thickness of 2000 nm, and annealed for a shorter time of 45 min. The resulting SIMS spectrum is shown in Figure 57. In this instance, a clear diffusion profile, similar to the ones found in Figure 55, is apparent. The depth profile extends for approximately 900 nm into the $CeO_2$ layer.

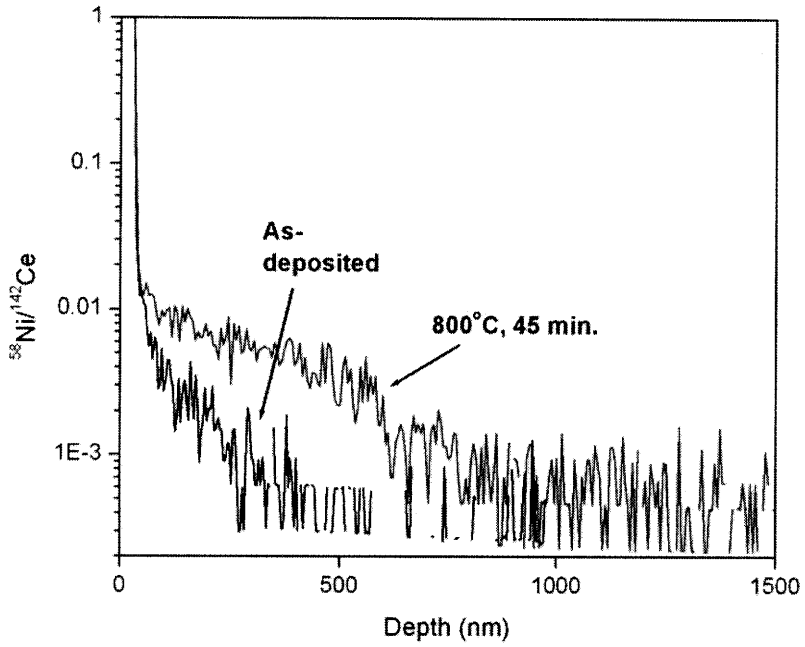


**Figure 57: SIMS spectra of Ni diffusion in $CeO_2$ after annealing at 800°C. Shown are as-deposited data and a profile resulting from an anneal of 45 min.**

### *3.2.2 Magnesium Diffusion From the MgO Substrate*

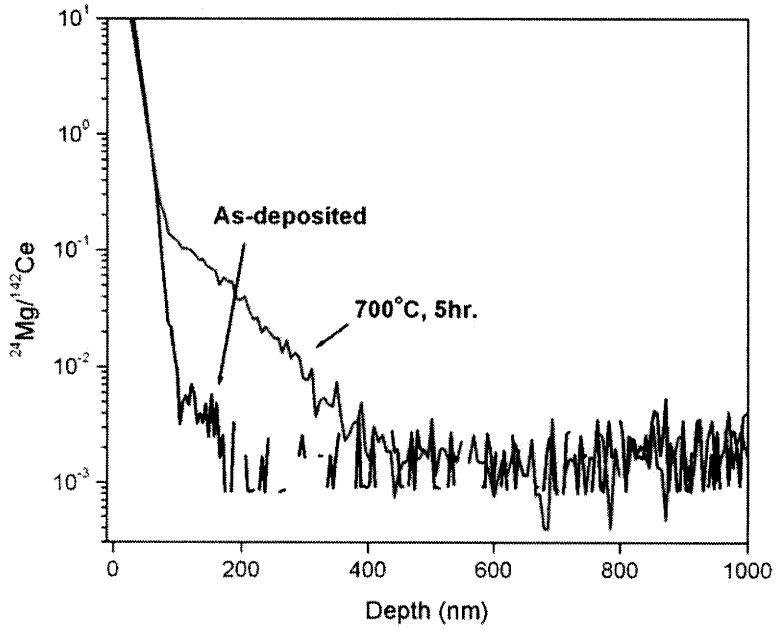


**Figure 58: SIMS spectra of Mg diffusion in $CeO_2$ as-deposited and following an anneal at 700°C for 5 hr. The x-axis has been reversed from the orginal spectrum, so that the MgO—$CeO_2$ interface lies towards the left side of the image. Mg diffusion is apparent after annealing at 700°C.**

The diffusion of Mg in $CeO_2$ at 700°C, emanating from the MgO substrate, is shown above in Figure 58. The as-deposited signal and the spectrum resulting from 700°C annealing for 5 hr. are shown. Because the $CeO_2$—MgO interface lies to the right of raw spectrum, the x-axis has been reversed so that diffusion 'upwards' from the substrate is visualized from left-to-right in Figure 58. A clear depth profile, similar to the Ni profiles in Section 3.2.1, is evident. Likewise, clear diffusion profiles are apparent in Figure 59 after annealing at 750°C for 90 min., and in Figure 60 after annealing at 800°C for 45 min.

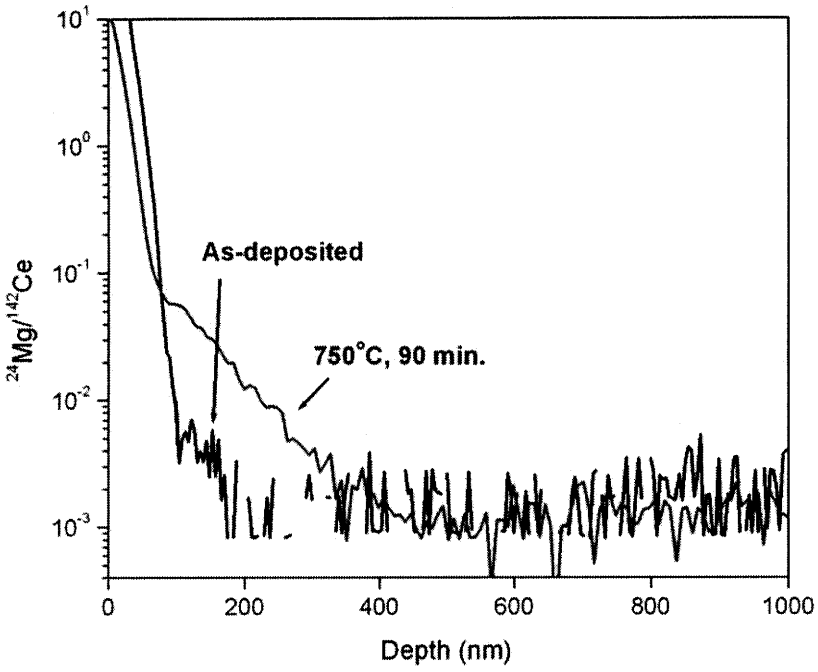


**Figure 59: SIMS spectra of Mg diffusion in $CeO_2$ as-deposited and following an anneal at 750°C for 90 min. The x-axis has been reversed from the orginal spectrum, so that the MgO—$CeO_2$ interface lies towards the left side of the image. Mg diffusion is apparent after annealing at 750°C.**

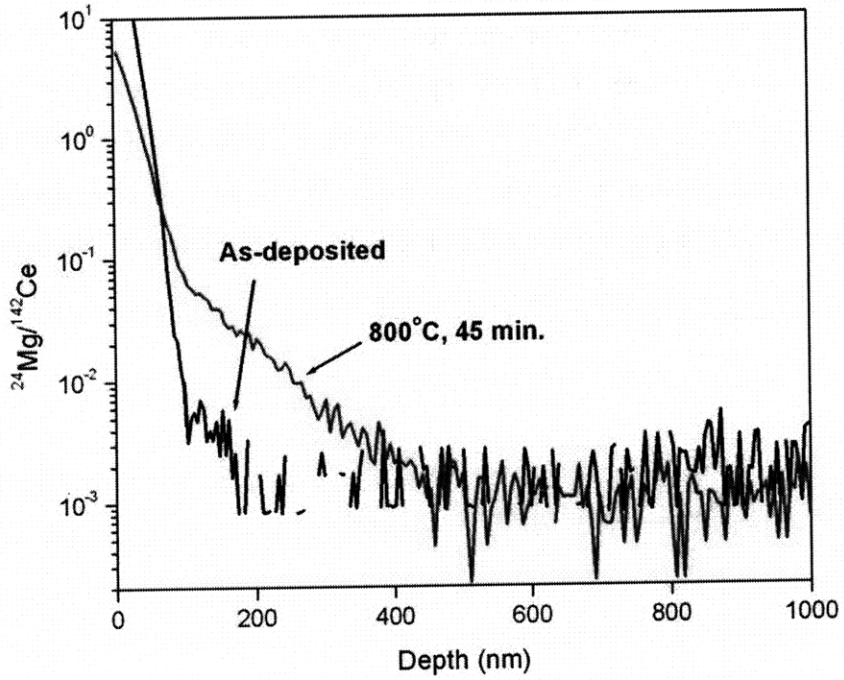


**Figure 60: SIMS spectra of Mg diffusion in $CeO_2$ as-deposited and following an anneal at 800°C for 45 min. The x-axis has been reversed from the orginal spectrum, so that the MgO—$CeO_2$ interface lies towards the left side of the image. Mg diffusion is apparent after annealing at 800°C.**

## *3.3 Electrical Characterization with Non-Blocking Platinum Electrodes*

### *3.3.1 As-Deposited Ceria Films*

A sample EIS spectrum, measured at 438°C, is shown in Figure 61. The electrode structure used was the IDE configuration, as shown in Figure 43 and Figure 44. The frequency range of the measurement (proceeding from left to right in the figure) was 10 MHz to 1 Hz. This semicircle represents one process within the sample, and is often represented by a single RC circuit element. The calculated resistance and capacitance values were $8.5 \times 10^5$ Ω and $1.1 \times 10^{-11}$ F, respectively. While EIS performed on microcrystalline $CeO_2$ samples often results in more than one semicircle due to grain boundary and/or electrode contributions, previous reports on nanocrystalline $CeO_2$ also report a single semicircle [37, 57, 62]. While this single arc may appear to represent bulk processes only, it is not possible to exclude grain boundary contributions. Indeed, Hwang, *et al.* applied a brick layer model (BLM) analysis to micro- and nanocrystalline $CeO_2$ and concluded that the grain and grain boundary arcs cannot be distinguished for very small grain sizes [129]. The resistance of the sample was determined by the low frequency intercept of the spectrum with the Z′ axis.

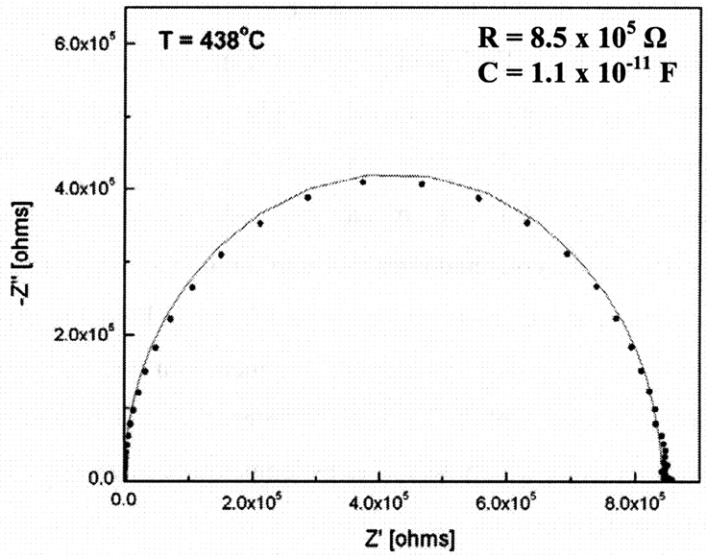


**Figure 61: Sample EIS spectrum of $CeO_2$ at 438°C. One semicircle is evident, consistent with literature reports of nanocrystalline $CeO_2$ [37, 57, 62].**

The current-voltage (I-V) characteristics are shown in Figure 62 below for temperatures ranging from 411 to 538°C. Within the voltage range of these measurements, -150 mV to + 150 mV, all I-V curves are linear, which is indicative of operation within the Ohmic regime. The resistance was calculated to be equal to dV/dI, which is the reciprocal of the slope in Figure 62. The resistance decreased exponentially with increasing temperature for all $CeO_2$ sample, indicative of thermally-activated behavior.

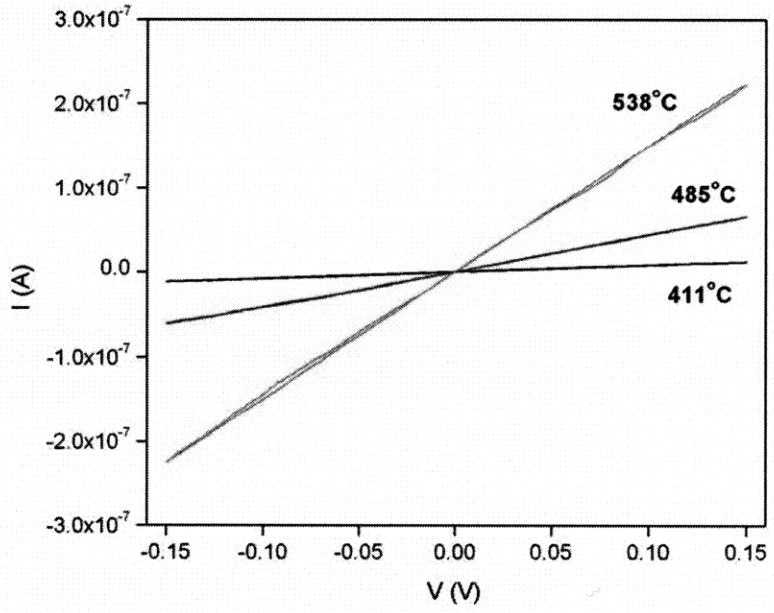


**Figure 62: Sample current-voltage (I-V) curves of a $CeO_2$ sample at various temperatures in air. The resistance, calculated as dV/dI, decreases exponentially with temperature. The linear shapes indicate that the voltages applied (up to 150 mV in this case) lie within the Ohmic regime.**

An Arrhenius plot of electrical conductivity vs. inverse temperature is found in Figure 63 for the temperature range of 300 to 550°C. Each sample was measured several times. In many cases, the conductivity of the first measurement was noticeably higher than in subsequent testing. This was attributed to nonstoichiometry in the form of partial reduction during the growth process. After the first testing cycle which reached 550°C, the conductivity stabilized to a consistent value, indicating proper oxidation. Only data points collected after this equilibration are shown in Figure 63. Shown is the data collected in this study, as well as several examples from the literature. It should be noted that the data labeled 'as-deposited' consists of data points obtained with both EIS and DC measurements for a multitude of samples. This was plotted as such in order to visually provide an indication of the relative error of the measurements, which decreases as temperature increases. The EIS and DC data are in good agreement, suggesting that charge transport was not hindered by the electrodes. In addition, the data was collected both upon heating and cooling of the samples, ensuring that proper equilibration and reproducibility were established. The conductivity is greater in magnitude than the values reported by Chiang, *et al.* [37] and Hwang and Mason [57], and is considerably higher than the values reported by Kim and Maier [62]. The magnitude of the conductivity is similar to the results obtained by Rupp and Gauckler [63]. Since the mobility of both the electrons and vacancies is thermally-activated [26], the activation energy of the electrical conductivity was found through a plot of $\ln(\sigma T)$ vs. $1/T$ (see Eq. 20). These activation energies are reported in Figure 63. The activation energy determined in this study, $1.04 \pm 0.11$ eV, is similar to that of Ref. 37 (1.16 eV) but higher than the value reported in Ref. 63 (0.90 eV) and lower than the values reported in Refs. 57 and 62 (1.36 and 1.35 eV, respectively).

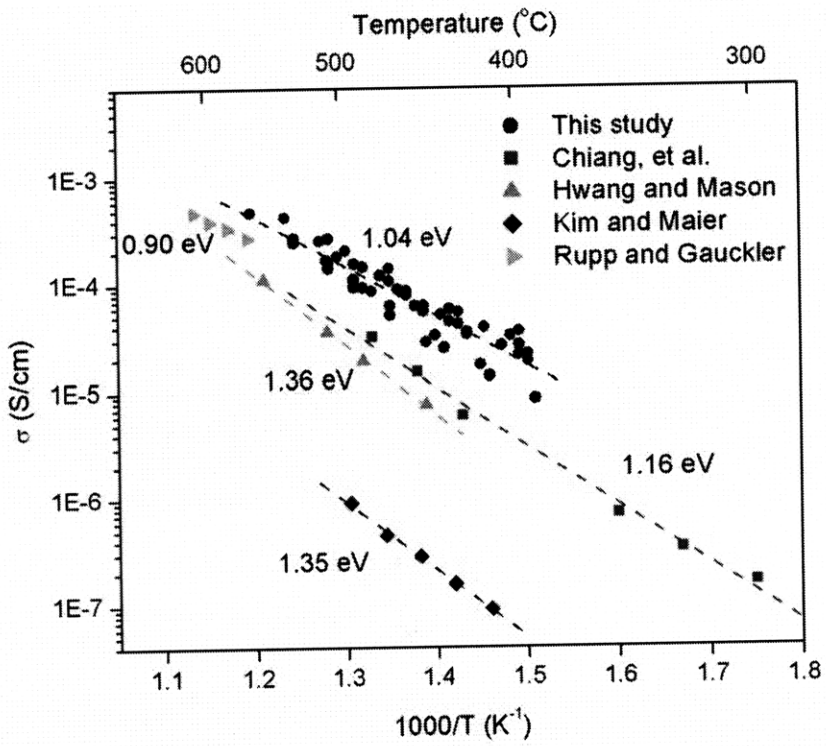


**Figure 63: Arrhenius plot of the electrical conductivity of nanocrystalline $CeO_2$. Shown are data from this work (●), Chiang, *et al.* (■) [37], Hwang and Mason (▲) [57], Kim and Maier (♦) [62], and Rupp and Gauckler (▶) [63]. The activation energies were determined through a plot of ln(σT) vs. 1/T.**

The electrical conductivity is plotted as a function of $pO_2$ at 450°C in Figure 64 below. The $pO_2$ dependence is -0.21 over the range of $10^{-3}$ to 1 atm. This $pO_2$ dependence is similar to previous reports on nanocrystalline ceria [37, 57, 59, 62], as visualized in Figure 12.

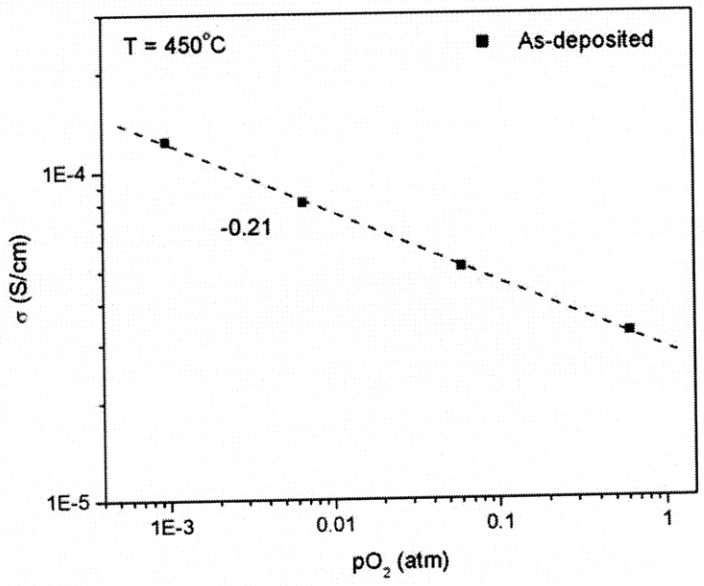


**Figure 64: Log-log plot of electrical conductivity vs. $pO_2$ for as-deposited $CeO_2$ at 450°C. The $pO_2$ dependence is -0.21.**

An Arrhenius plot of the electrical conductivity for the as-deposited samples, as well as samples annealed with no diffusion source, is shown in Figure 65. After annealing at 600°C for 5 hr., the conductivity appears to decrease slightly from the as-deposited samples. The activation energy was 1.30 eV. After annealing at 800°C for 20 hr., the conductivity decreases by a factor of 4-5 from the as-deposited data, though the activation energy, 0.99 eV, is comparable. The observed activation energies are analyzed in detail in Section 4.5.

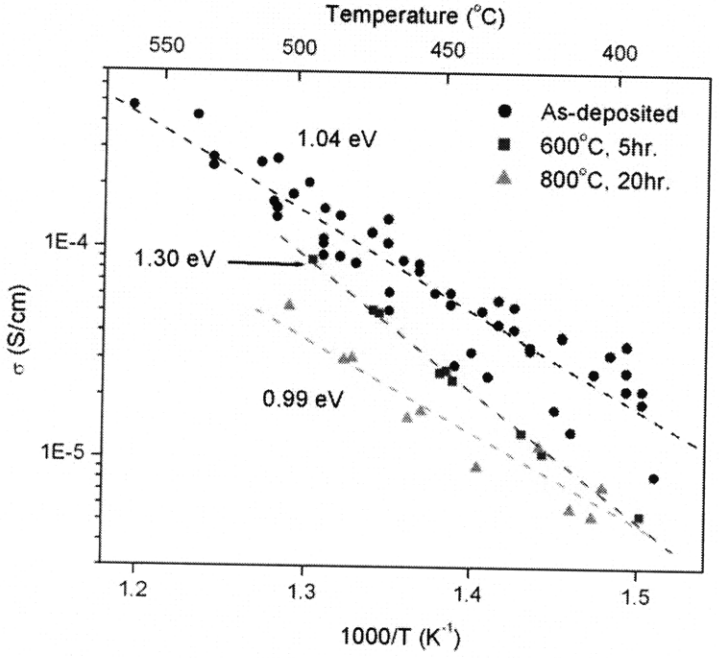


**Figure 65: Arrhenius plot of the electrical conductivity of $CeO_2$. Shown are the as-deposited samples (●), as well as samples annealed with no dopant at 600°C for 5 hr. (■) and 800°C for 20 hr. (▲). The activation energies were determined through a plot of ln(σT) vs. 1/T.**

### *3.3.2 NiO-Doped Ceria Films*

In addition to the as-deposited and annealed data from Figure 65, the conductivity data of samples modified by NiO and $Gd_2O_3$ in-diffusion are shown in Figure 66. The conductivity decreases by a factor of 4-5 from the sample annealed at 800°C for 20 hr. with no dopant, and by a factor of 16-20 from the as-deposited samples. The activation energy of the $Gd_2O_3$ and NiO in-diffused samples was 0.99 and 1.04 eV, respectively, similar to the as-deposited data.

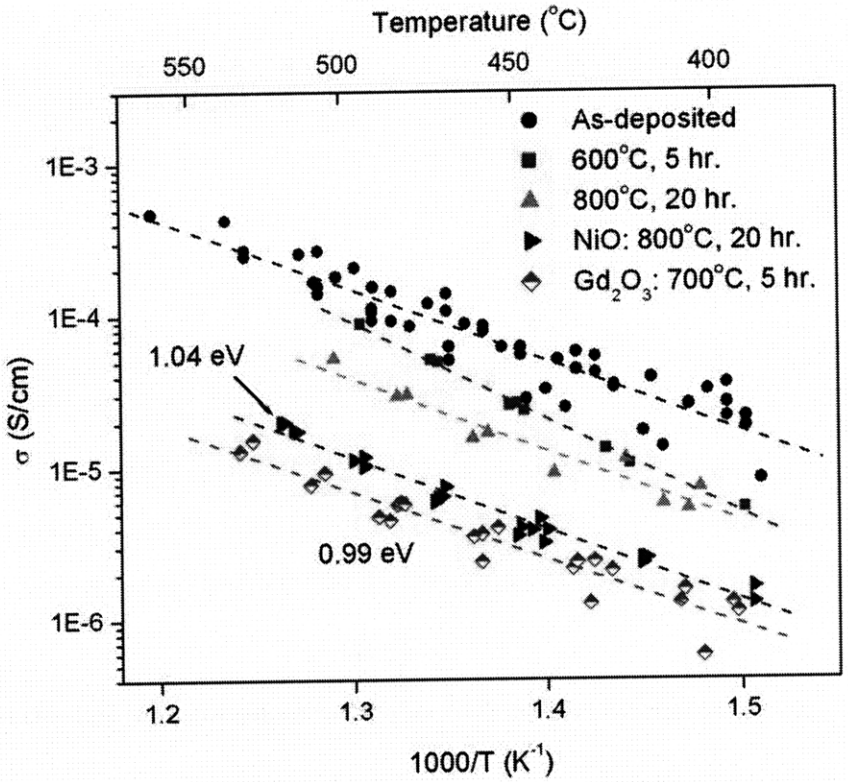


**Figure 66: Arrhenius plot of the electrical conductivity of $CeO_2$. Specimens with no dopant include the as-deposited samples (•) and samples annealed at 600°C for 5 hr. (■) and 800°C for 20 hr. (▲). Also shown are samples following in-diffusion: NiO at 800°C for 20 hr. (►) and $Gd_2O_3$ at 700°C for 5 hr. (◈). The activation energies were determined through a plot of ln(σT) vs. 1/T.**

The electrical conductivity is plotted as a function of $pO_2$ in Figure 67. Shown are the as-deposited data from Figure 64 and a sample annealed at 800°C for 20 hr. with a NiO source. The conductivity decreases by approximately a factor of 5-6 following in-diffusion. The slope of the in-diffused sample, -0.23, does not deviate significantly from the as-deposited sample.

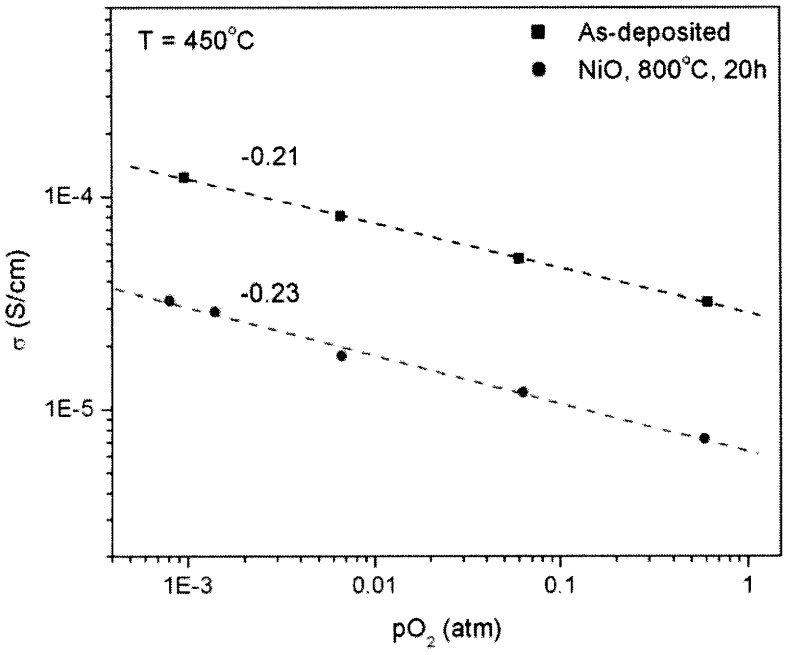


**Figure 67: Log-log plot of the electrical conductivity vs. $pO_2$ for as-deposited (■) and NiO in-diffused (●) $CeO_2$ films at 450°C.**

### *3.4 Electrical Characterization with YSZ-12—Platinum Blocking Electrodes*

The schematic of the blocking electrode arrangement is shown in Figure 45. For simplicity, this arrangement can be represented as an equivalent circuit of resistors $R_i^{YSZ}$, $R_i^{CeO2}$, $R_{el}^{YSZ}$, and $R_{el}^{CeO2}$:

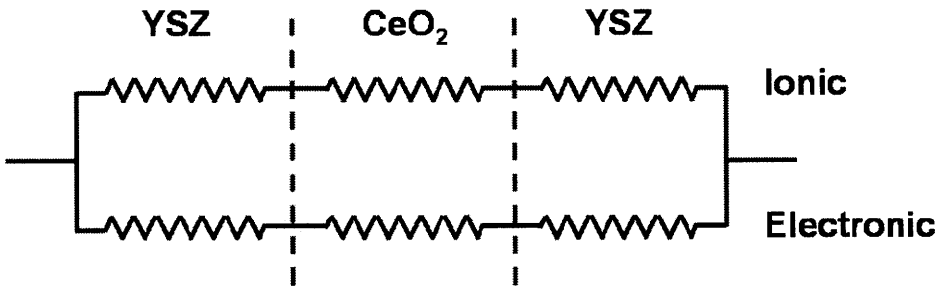


**Figure 68: Equivalent circuit of the electron-blocking geometry. Parallel ionic and electronic 'circuits' traverse the YSZ, $CeO_2$ and YSZ layers in series.**

As discussed by Riess [130], any electron-blocking electrode configuration must satisfy the ratio:

$$\frac{R_i^{CeO2}}{R_{el}^{YSZ}} << 1 \tag{65}$$

Where the relationship between resistance and conductivity is

$$R = \frac{L}{\sigma A} \tag{66}$$

Since the length of the electrode is a common factor in the resistance calculation of the $CeO_2$ and YSZ layers, Eq. 66 can be substituted into Eq. 65 to yield:

$$\frac{R_{ion}^{CeO2}}{R_{el}^{YSZ}} = \frac{\sigma_{el}^{YSZ} L^{CeO2} w^{YSZ}}{2\sigma_{ion}^{CeO2} t^{CeO2} t^{YSZ}} << 1 \tag{67}$$

where $L^{CeO2}$ is the inter-electrode spacing, $w^{YSZ}$ the width of the electrode, and $t$ the thickness of the $CeO_2$ and YSZ films. This relationship may at first appear unusual, but it should be recalled that the current travels through the thickness of the YSZ films and in the plane of the $CeO_2$ film. The primary electronic charge carriers in $CeO_2$ are electrons, as the hole conductivity is negligible [24]. Therefore, one must examine the conductivity of electrons in the YSZ layer. An expression for the transport of electrons in YSZ was reported by Heyne and Beekmans [131]:

$$\sigma_n^{YSZ} = 3.7x10^6 \, pO_2^{-1/4} \exp\left(-\frac{3.7eV}{kT}\right) \left(S/cm\right) \tag{68}$$

Substituting values of 0.21 and 773 for $pO_2$ and T(K), respectively, one finds the electronic partial conductivity of YSZ to be $4.12x10^{-18}$ S/cm at 500°C. Based on literature reports [62] and the results of this work, a reasonable estimate of the ionic partial conductivity of nominally-undoped $CeO_2$ is $6x10^{-6}$ S/cm at 500°C. Substituting these values and the geometrical factors depicted in Figure 45 into Eq. 67, the ratio of $R_i^{CeO2}/R_{el}^{YSZ}$ is found to be on the order of $10^{-8}$, thus readily satisfying the requirement for electron-blocking presented in Eq. 65.

The microstructure of the blocking electrodes is shown in the form of SEM micrographs in Figure 69. In micrograph (a), three of the interdigitated lines can be seen. The line width is approximately 40 μm. In images (b) through (d), the porosity of the Pt layer can be observed with increasing resolution. The Pt appears as light gray and pores percolate throughout the electrode structure. As intended, the porosity of the Pt layer allows for a much larger number of TPB sites, so as to minimize the contribution of the electrochemical reactions at the Pt/YSZ-12 interface to the total impedance.

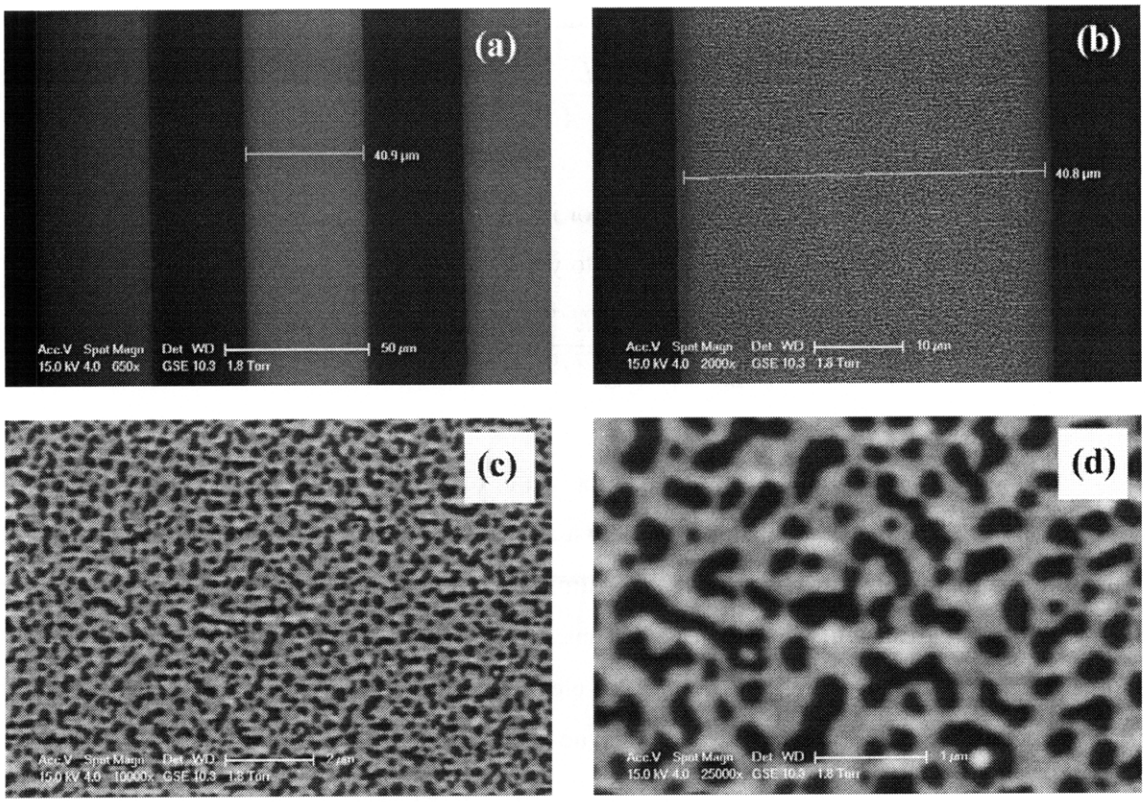


**Figure 69: SEM micrographs of YSZ-12/porous Pt interdigitated electrode lines. The nominal line width is 40 µm. In (c) and (d), the Pt appears as light gray and the underlying YSZ-12 appears as black.**

The basic electrical properties of the blocking structure under applied DC bias are shown in Figure 70. In Figure 70a, a plot of current vs. time for an applied bias of 0.1 V at 500°C is shown. There is an initial higher current transient that decreases in magnitude with time. The current reaches a nearly constant value after approximately 150 s. It is this steady-state current that is used to calculate the DC conductivity, which is attributed to the conduction of oxygen vacancies in the ceria film (ionic current). An I-V plot at 500°C is shown in Figure 70b. For the applied voltage range of 200 mV and lower, the I-V response is linear, indicating transport within the Ohmic regime.

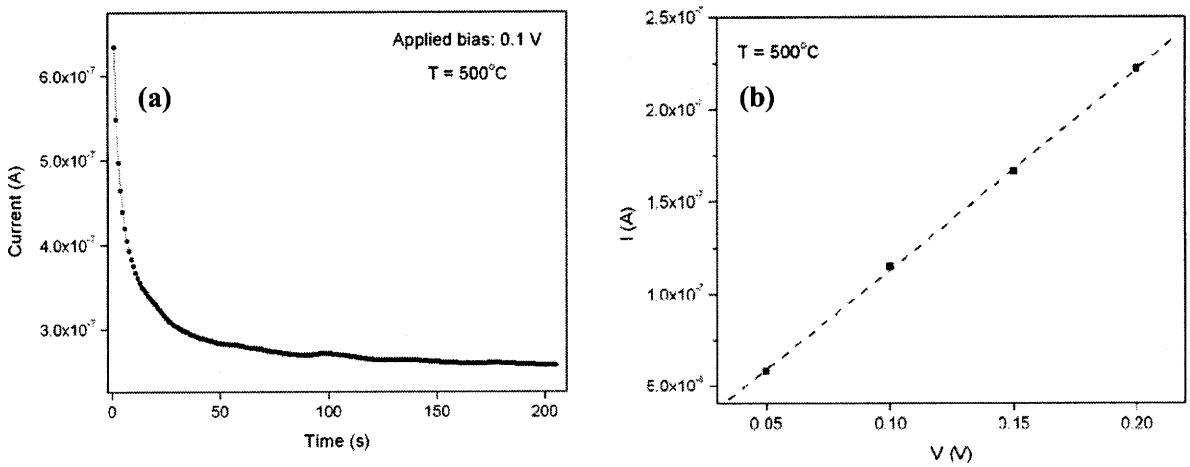


**Figure 70: Sample electrical data from the blocking electrodes. The current vs. time plot (a) demonstrates an initial transient that converges on a steady-state current for an applied bias of 0.1 V at 500°C. The current-voltage (I-V) plot (b) demonstrates a linear dependence, indicative of operation within the Ohmic regime.**

### *3.4.1 As-Deposited Ceria Films*

The total conductivity as well as the ionic and electronic partial conductivities of as-deposited $CeO_2$ thin films are shown in Figure 71. The film thicknesses were (a) 87, (b) 107, (c) 640, and (d) 115 nm. The plots represent the results of the blocking electrode samples as a function of $pO_2$. The total conductivity was calculated from the high frequency EIS spectrum, the ionic conductivity was found by DC blocking of electrons by the YSZ electrodes (see Figure 70), and the electronic conductivity was found from the difference of the two. First, the average $pO_2$ dependence of the total conductivity is -0.23, in close agreement with Figure 64. The ionic conductivity is essentially $pO_2$-independent. The average $pO_2$ dependence of the electronic conductivity is -0.31. It should be noted that, while the absolute value of the conductivities varies from sample-to-sample, the $pO_2$ dependencies are unambiguous and reproducible. The ionic transference number, $t_{ion}$ at T = 475°C and $pO_2$ = 0.21 atm was approximately 0.34.

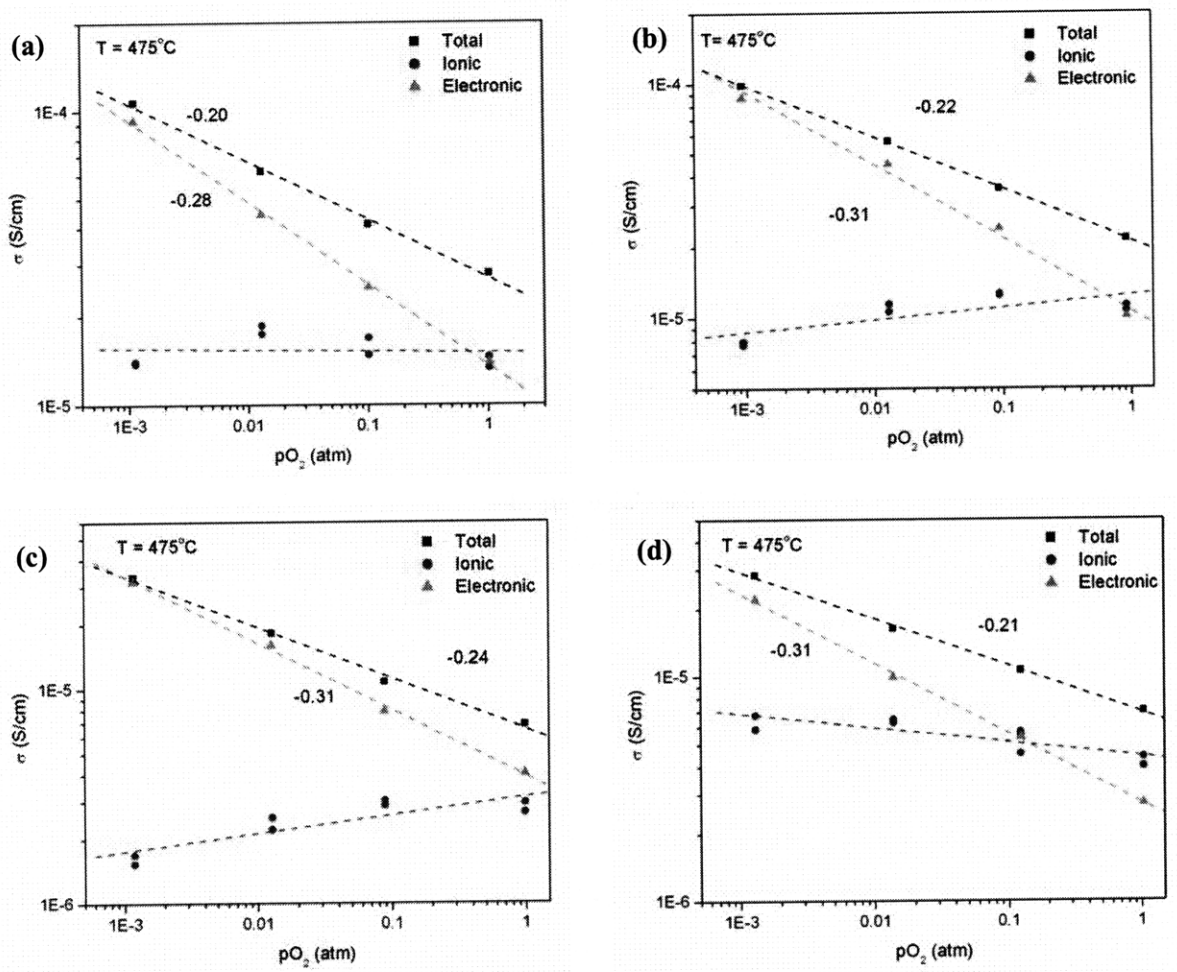


**Figure 71: Electrical conductivity vs. $pO_2$ on as-deposited thin films via blocking electrodes, measured at 475°C. The film thicknesses were (a) 87, (b) 107, (c) 640, and (d) 115 nm respectively. Shown are the total (■), ionic (●), and electronic (▲) conductivities. The average slope of the total, ionic, and electronic $pO_2$ dependencies are -0.23, 0, and -0.31, respectively.**

The same samples were then measured as a function of temperature in air. Arrhenius plots of the total and partial conductivities are found in Figure 72. The activation energy of the total conductivity is 1.33 eV. The activation energy of the ionic and electronic partial conductivities is 1.50 and 1.24 eV, respectively. The activation energy of the total conductivity is higher than the value measured in Figure 63, yet comparable to the literature values reported in the same figure.

.

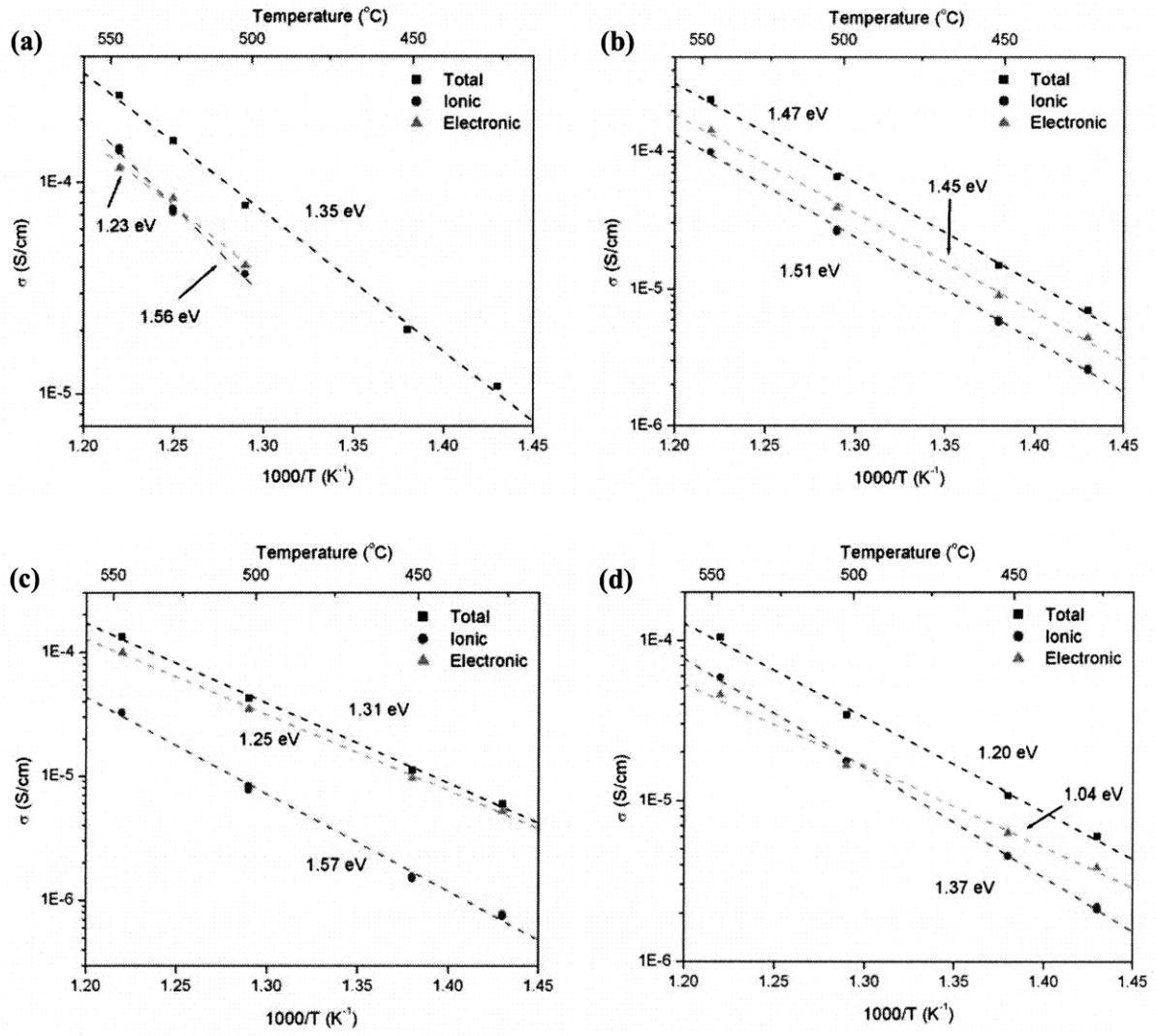


**Figure 72: Arrhenius plot of the electrical conductivity from blocking electrodes on as-deposited thin films, measured in air. The film thicknesses were (a) 87, (b) 107, (c) 640, and (d) 115 nm respectively. Shown are the total (■), ionic (●), and electronic (▲) conductivities. The average activation energies of the total, ionic, and electronic conductivities are 1.33, 1.50, and 1.24 eV, respectively. The activation energies were determined through a plot of ln(σT) vs. 1/T.**

### *3.4.2 Ceria Films Annealed with no Diffusion Source*

Two samples were annealed at 800°C for 3 and 5 hr. with no diffusion source. The plots of the total, ionic, and electronic conductivities as a function of $pO_2$ are shown in Figure 73 at T = 475°C. The film thicknesses were (a) 500 and (b) 257 nm. The average $pO_2$ dependence of the total conductivity was -0.21, in reasonable agreement with Figure 71. Unlike the previous data, however, the ionic conductivity is $pO_2$-dependent, with a slope of -0.13. There is larger scatter in the slope of the electronic conductivity—the average value is -0.37. The corresponding Arrhenius plots are shown in Figure 74. The average $E_A$ value for the total conductivity, 1.46 eV is somewhat, though not

significantly, higher than the value in Figure 72. The slope of the ionic conductivity, 1.50 eV, is equivalent. Again, there is much larger variance in the data for the activation energy of the electronic conductivity. The average value, 1.47 eV, is larger than the as-deposited value. The absolute values of the three conductivities are all at least one order of magnitude lower than in the as-deposited state. The electronic contribution is particularly depressed, and the film is dominated in this case by the ionic conductivity.

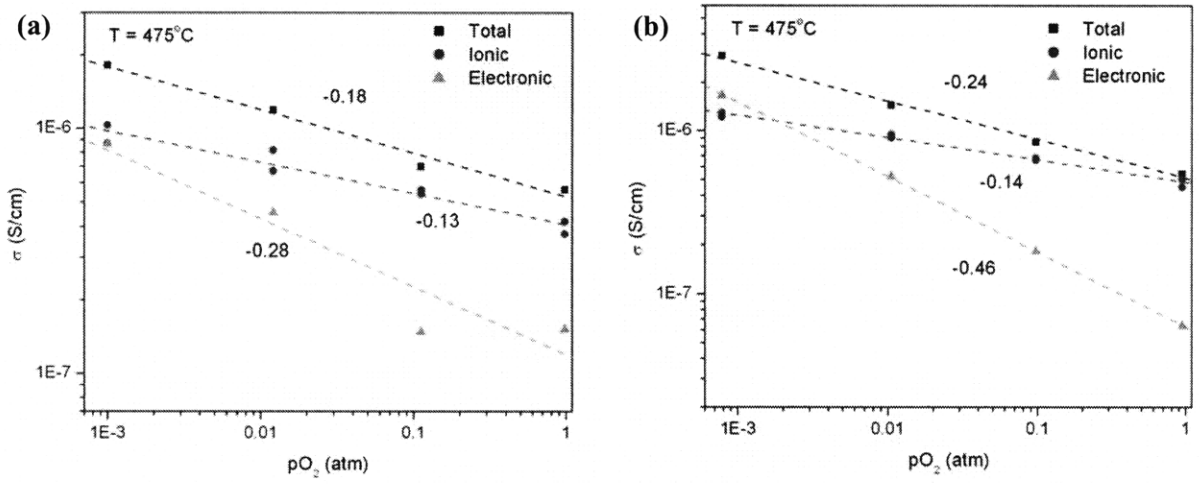


**Figure 73: Electrical conductivity vs. $pO_2$ on thin films annealed at 800°C with no diffusion source for (a) 3 hr. and (b) 5 hr., measured at 475°C. The film thicknesses were (a) 500 and (b) 257 nm respectively. Shown are the total (■), ionic (●), and electronic (▲) conductivities. The average slope of the total, ionic, and electronic $pO_2$ dependencies are -0.21, -0.13, and -0.37, respectively.**

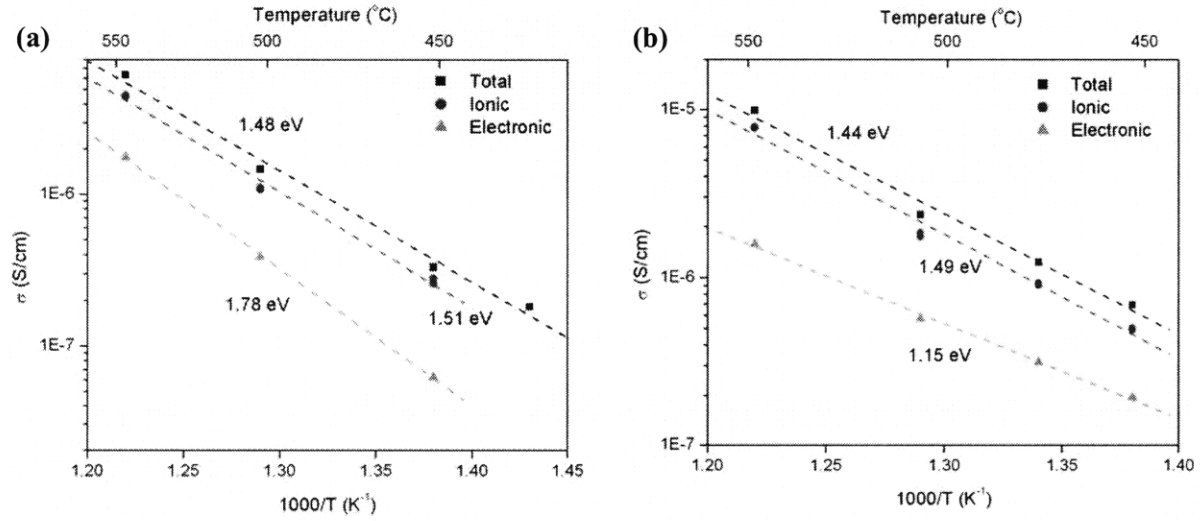


**Figure 74: Arrhenius plot of the electrical conductivity from blocking electrodes on samples annealed at 800°C for (a) 3 hr. and (b) 5 hr. with no diffusion source, measured in air. The film thicknesses were (a) 500 and (b) 257 nm respectively. Shown are the total (■), ionic (●), and electronic (▲) conductivities. The average activation energies of the total, ionic, and electronic conductivities are 1.46, 1.50, and 1.47 eV, respectively. The activation energies were determined through a plot of ln(σT) vs. 1/T.**

### 3.4.3 *NiO and $Gd_2O_3$ In-Diffused Ceria Films*

Plots of the total, ionic, and electronic conductivities as a function of $pO_2$ are shown in Figure 75 after NiO in-diffusion. The film thicknesses were (a) 90, (b) 116, (c) 547, and (d) 113 nm. The average slope of the total conductivity was -0.13, in contrast to -0.22 in Figure 71. The ionic conductivity shows a significant change from the data in Figure 71: rather than displaying no $pO_2$ dependence, the slope after NiO in-diffusion is approximately -0.16. The average slope of the electronic conductivity is -0.13.

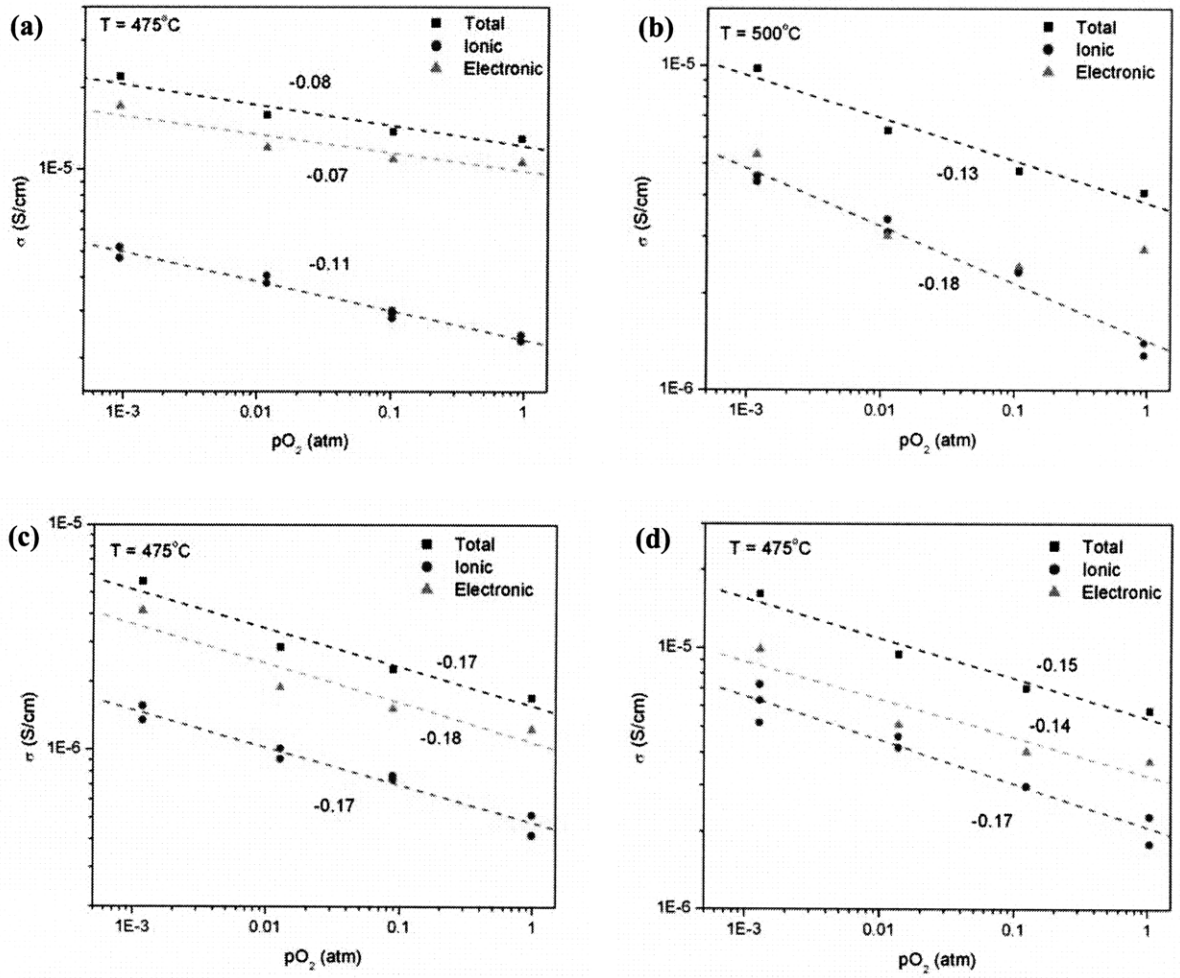


**Figure 75: Electrical conductivity vs. $pO_2$ on NiO in-diffused thin films via blocking electrodes, measured at (a, c-d) 475 and (b) 500°C. The film thicknesses were (a) 90, (b) 116, (c) 547, and (d) 113 nm respectively. Shown are the total (■), ionic (●), and electronic (▲) conductivities. The average slope of the total, ionic, and electronic $pO_2$ dependencies are -0.13, -0.16, and -0.13, respectively.**

Arrhenius plots of the total, ionic, and electronic conductivities of the samples modified by NiO in-diffusion are shown in Figure 76. The average activation energy of the total conductivity is 1.12 eV,

a decrease from the as-deposited value of 1.33 eV. The activation energies of the ionic and electronic partial conductivities also decrease from the as-deposited values. The value of $E_A$ for the ionic conductivity is reduced from 1.50 to 1.23 eV after NiO in-diffusion, and the $E_A$ value for the electronic conductivity decreased from 1.24 to 1.09 eV after NiO in-diffusion. A more thorough discussion of these trends and experimental error is presented in Section 4.4.3.

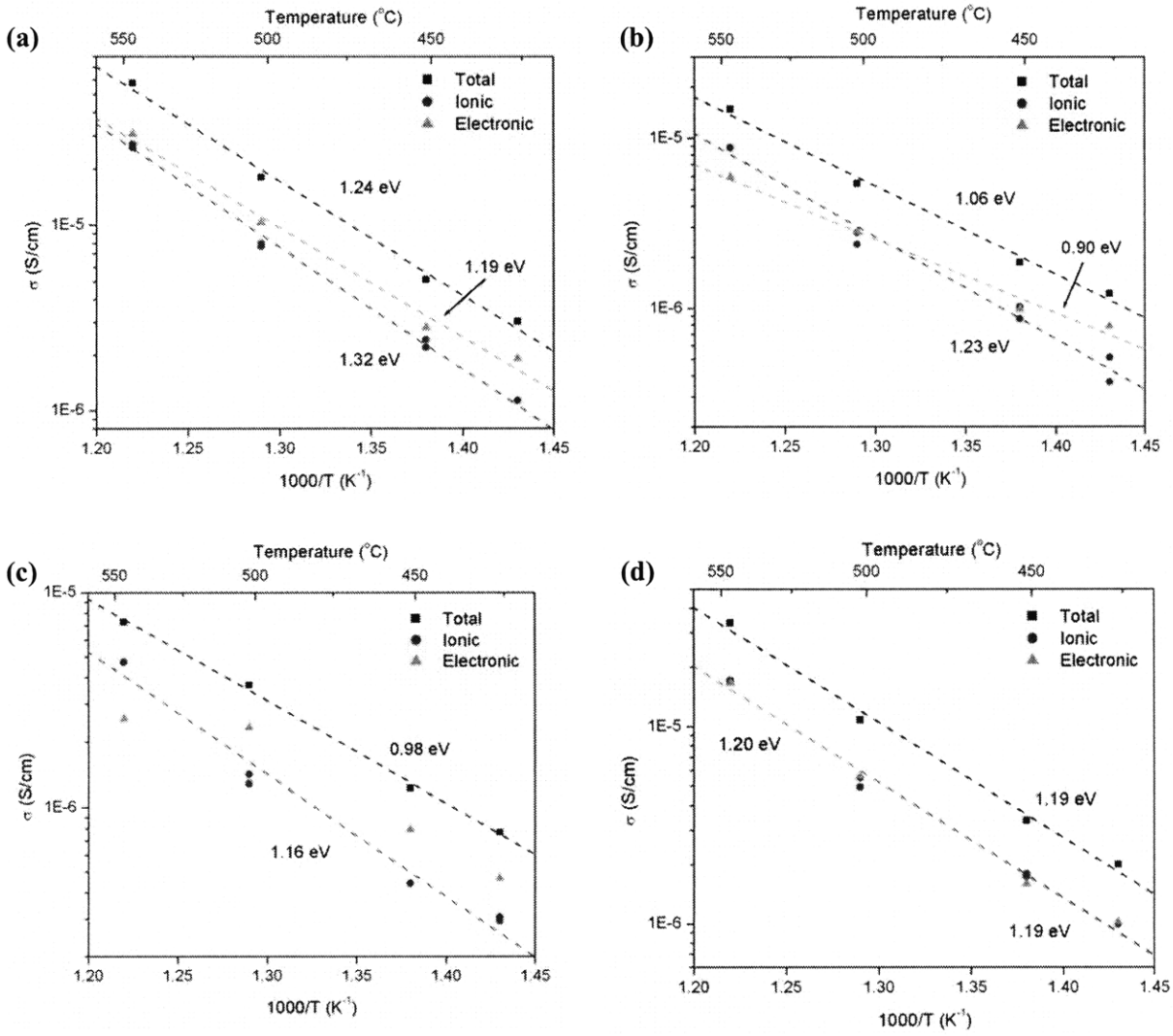


**Figure 76: Arrhenius plot of the electrical conductivity from blocking electrodes on NiO in-diffused thin films, measured in air. The film thicknesses were (a) 90, (b) 116, (c) 547, and (d) 113 nm respectively. Shown are the total (■), ionic (●), and electronic (▲) conductivities. The average activation energies of the total, ionic, and electronic conductivities are 1.12, 1.23, and 1.09 eV, respectively. The activation energies were determined through a plot of ln(σT) vs. 1/T.**

The electrical properties of a sample modified by Gd in-diffusion at 700°C for 5 hr. are shown in Figure 77. In (a), the conductivity is plotted vs. $pO_2$. Overall, the data is somewhat comparable to

the Ni-diffused samples shown in Figure 75. The slope of the total and electronic conductivity is -0.11, and the slope of the ionic conductivity is -0.12. The activation energy for the total conductivity, 1.24 eV is slightly higher than the value in Figure 76. The activation energy for the ionic conductivity, 1.48 eV, is noticeably higher than the Ni-diffused sample, but in good agreement with the as-deposited data. The average activation energy for the electronic conductivity is the same after Ni and Gd in-diffusion, 1.09 eV.

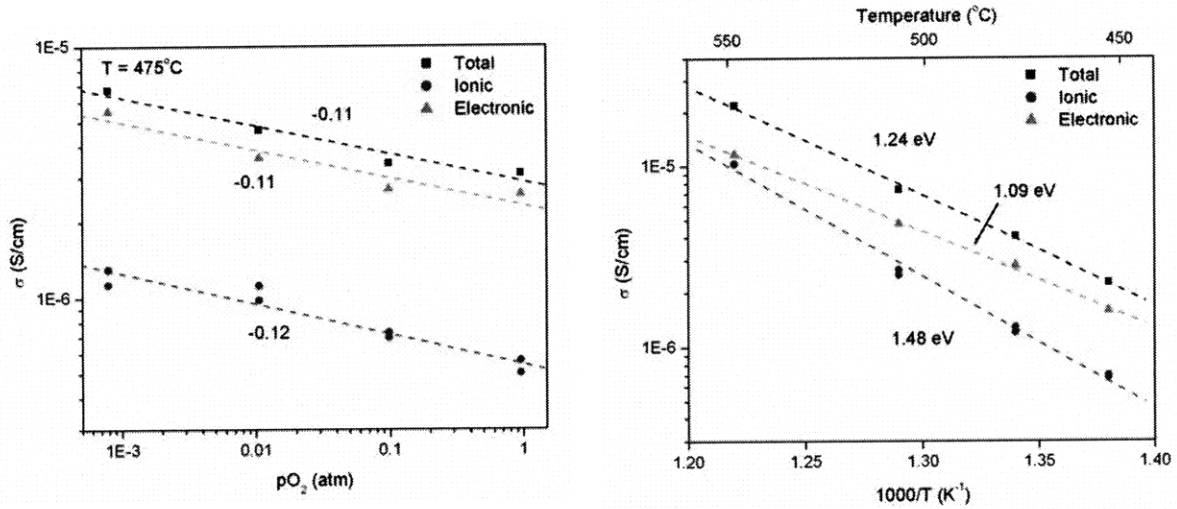


**Figure 77: The electrical conductivity from blocking electrodes after Gd in-diffusion at 700°C for 5 hr. Shown are the total (■), ionic (●), and electronic (▲) conductivities as a function of (a) $pO_2$ and (b) temperature. The activation energies were determined through a plot of ln(σT) vs. 1/T.**

# CHAPTER 4. DISCUSSION

## *4.1 Microstructure of Cerium Oxide Thin Films*

The growth of $CeO_2$ thin films on single crystal MgO and sapphire substrates does not appear to differ considerably. In both Figure 46 and Figure 47, it is evident that the degree of crystalline orientation varied for both substrates. Figure 46a and Figure 47a depict polycrystalline films with a slightly-preferred (100) orientation with other reflections visible. In contrast, Figure 46b and Figure 47b depict films with a highly-preferred (100) orientation. The distribution of film microstructures most likely results from minor variations during PLD deposition. While the target deposition temperature for all samples was 700°C, there were some minor fluctuations in temperature during deposition due to minor inconsistencies in the placement of the controlling thermocouple. In addition, variations in the laser energy due to the build-up of impurity films on the laser window, discussed in Section 3.1, likely impacted the ultimate microstructure. Nevertheless, all samples were found to be single-phase $CeO_2$. The films with enhanced (100) orientation likely resulted from slightly higher temperature, greater laser energy, and lower working pressure during deposition, as all of these factors lead to increased energy of the ad-ions on the $CeO_2$ surface. With this increased energy, it is expected that the ad-ions would have greater ability to diffuse to preferential sites on the growing film surface.

The AFM micrograph in Figure 48 shows the grain size in the as-deposited state to be on the order of 25-45 nm, with an average of 35 nm. The surface roughness is less than 1 nm, which is an important point that will be discussed with respect to the SIMS analysis below. The micrographs in Figure 49a-b demonstrate that grain growth occurs after annealing at 600 and 850°C. After annealing at 600°C for 5 hr., the average grain size increases to 62 nm. After annealing at 850°C for 12 hr., the average grain size increases to 75 nm. Grain growth is commonly observed in polycrystalline materials that have been subjected to annealing; thermodynamically, this process is driven by the decrease in surface energy as small grains are consumed by larger grains. However Rupp, *et al.* studied grain growth in nanocrystalline $CeO_2$ films and concluded that grain growth is "self-limited" for grain sizes less than 140 nm and annealing temperatures below 1100°C [132]. The authors examined isothermal grain growth as a function of time for films grown by spray pyrolysis and PLD, as shown below in Figure 78. There is evidence of grain growth during the first 5-10 hr. of annealing, followed by a plateau. The authors attributed the existence of this metastable state to the lack of bulk diffusion, due to the relatively low annealing temperatures. In this work, a doubling of the grain size is observed, yet according to Ref. 132, continued annealing in this temperature range should result in no

subsequent grain growth

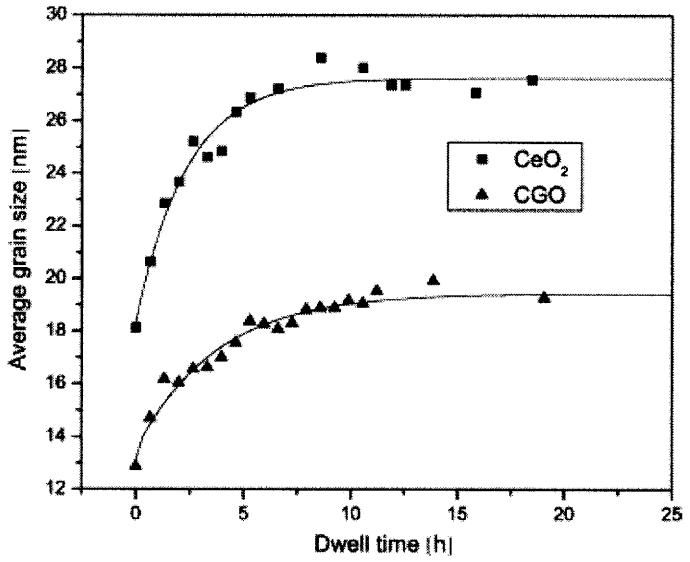


**Figure 78: Grain growth of doped and undoped ceria at 700°C for nanocrystalline thin films grown by spray pyrolysis [132].**

The SEM micrograph in Figure 50 and the TEM micrographs in Figure 51 depict clearly the columnar nature of the $CeO_2$ microstructure. Columns of grains extend from the substrate interface to the surface. As discussed by Thompson in a review of thin film properties, the microstructure of a thin film is strongly dependent on the homologous temperature of deposition, $T/T_m$ [133]. The melting point of $CeO_2$ was given in Table 1 as approximately 2475°C. Since the deposition temperature was 700°C, this equals a homologous temperature of 0.28. Zone maps, which represent various microstructures as a function of homologous temperature, can vary considerably for different material classes [133]. In this case, it is evident that the value of approximately 0.3 for $CeO_2$ is sufficiently high for the film to crystallize, but not for an equiaxed or epitaxial structure to develop.

The HRTEM micrograph shown in Figure 52 demonstrates that the grain boundary core is limited in spatial extent. There is no evidence of an amorphous region in the core region. Likewise, there is no evidence of a glassy second phase in the grain boundary region. For all samples characterized by TEM before and after in-diffusion, the grain boundary region appears to be a single phase and confined to less than 1 nm in thickness.

### *4.2 Cation Diffusion Along Grain Boundaries*

The baseline SIMS spectrum of an as-deposited NiO—$CeO_2$—MgO sample is shown in Figure 53. The $^{58}Ni$ signal normalized by $^{142}Ce$ extends approximately 250 nm into the $CeO_2$ layer. Since the NiO diffusion source was sputtered near room temperature, it is believed that this signal is a SIMS artifact and not the result of in-diffusion. The spectrum in Figure 54a represents the depth profile following an anneal at 500°C for 140 hr. There is no clear distinction between this profile and the as-deposited data and thus in-diffusion is not evident at this temperature. Likewise, a profile is shown in Figure 54b after annealing at 600°C for 25 hr. No diffusion is detected. Given an estimated diffusion coefficient at 500°C of $3.1x10^{-16}$ $cm^2/s$, extrapolated from the 700 and 800°C data points discussed below, the predicted diffusion length after 140 hr. is approximately 250 nm. The estimated diffusion coefficient at 600°C, $5.0x10^{-15}$ $cm^2/s$, results in a predicted diffusion length after 25 hr. of 425 nm. As seen for the as-deposited results in Figure 54b, these distances, particularly the 500°C diffusion length, are likely not large enough to be readily distinguished from the Ni background signal.

In contrast, in-diffusion is readily apparent at annealing temperatures of 700°C and above. For example, clear diffusion profiles are observed after annealing at 700°C for 5 and 7 hr., as shown in Figure 55. A similarly-shaped depth profile is also observed for Mg in Figure 58. As mentioned in Section 1.7, the Harrison regime observed most often is regime B, which is shown schematically in Figure 30. There are two distinctive contributions to the depth profile: bulk and grain boundary diffusion. However, the depth profiles measured in this study bear no resemblance to the Harrison regime B, as only one diffusion mechanism is apparent. In consideration of the literature data on cation diffusion in fluorites [98, 102], bulk diffusion is highly unlikely to occur to any appreciable degree in this relatively low temperature range. In Ref. 98, Sirman and co-workers reported bulk diffusivity values for Co and Fe in microcrystalline CGO on the order of $10^{-14}$ to $10^{-15}$ $cm^2/s$ at 1250°C. As calculated and discussed below, similar orders of magnitude are observed in this study at 700°C. Since the diffusion of cation along grain boundaries is many orders of magnitude faster than in the bulk in metal oxides [53, 135], and since there is such a large cross-section of grain boundaries normal to the surface, it is reasonable to assume that the diffusion profiles result solely from a grain boundary mechanism, thus falling within in the Harrison regime C [128].

Returning to Figure 55, the signal extends well into the $CeO_2$ layer after annealing for 5 hr., but not so far as to reach the substrate interface. The 5 hr. profile is suitable for a quantitative determination of the appropriate diffusion coefficient. Since the depth profile did not extend through the entire $CeO_2$ film, this measurement will be represented by 'semi-infinite' boundary conditions. While the $CeO_2$

film is of course not semi-infinite, this boundary condition is more appropriate then the common alternative, thin film boundary conditions. Under such conditions, the diffusing species is assumed to have reached the substrate, which acts either as a diffusion sink or a zero flux plane [53]. The depth profiles are represented by complex numerical solutions to the diffusion equation in which the complexity added by the substrate interface is taken into consideration. Since this interface is of no relevance for the 5 hr. profile or any of the depth profiles considered quantitatively in this thesis, the traditional and simpler semi-infinite boundary conditions will instead be used.

At this point, the nature of the diffusion source must also be addressed. The two most common boundary conditions are the constant source (also known as the 'infinite' source), and the finite (or 'thin film' source). As implied by its moniker, the constant source solution considers the diffusion source to be an infinite supply of diffusing species so that the surface concentration, $c_O$, is invariant with time. Mathematically, this solution is expressed using the complementary error function, erfc(x). In the finite source solution, the diffusion source is consumed over time and $c_O$ decreases as the diffusion profile flattens out and eventually becomes constant. This solution is expressed mathematically by a Gaussian. Both types of depth profiles are shown in Figure 79.

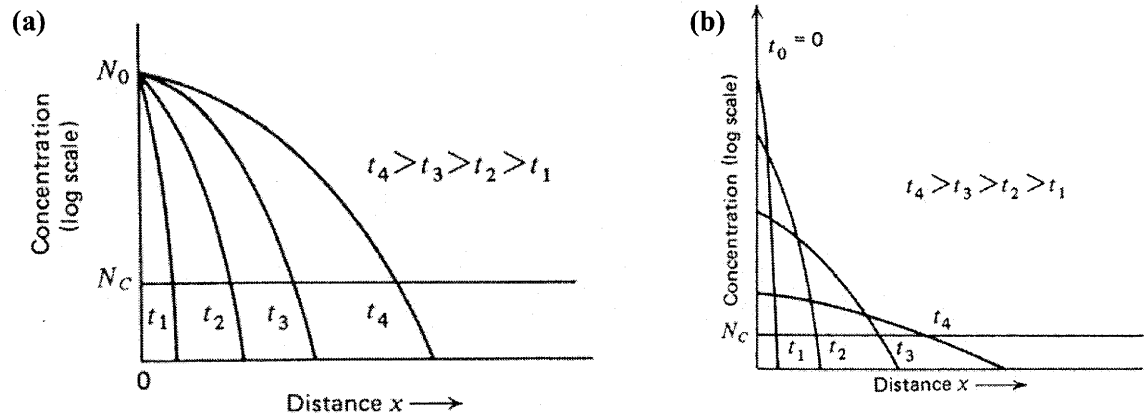


**Figure 79: Schematic diagrams of the evolution of diffusion depth profiles with time for (a) the constant source solution and (b) the finite source solution [134].**

In this study, the constant source solution was chosen as boundary conditions to Fick's Second Law. While this may at first appear counterintuitive given the very thin nature of the diffusion source (20 nm) compared to the $CeO_2$ layer (~ 1,100 nm), this selection is supported by two experimental observations. First, it can be seen in Figure 80 that for Ni diffusion at 700 and 800°C, the Ni levels near the surface remain relatively constant as a function of annealing conditions, and do not decrease as would a finite source. Second, under all annealing conditions, the ToF-SIMS depth profiles for the

source layer show a constant thickness, indicating that the source is still present even after annealing at 800°C for 10 hr. and is not consumed. This indicates that only a small amount of cations has diffused-in from the source, and is supported by TEM cross-section analyses with EDX and EELS, which did not yield any detectable amount of Ni in the bulk or grain boundaries. The SIMS data repeatedly demonstrate that cation diffusion has indeed taken place, but all other evidence suggests that the impurity concentrations are small. Together, these observations support the conclusion of grain boundary diffusion as the prevailing mechanism in this study.

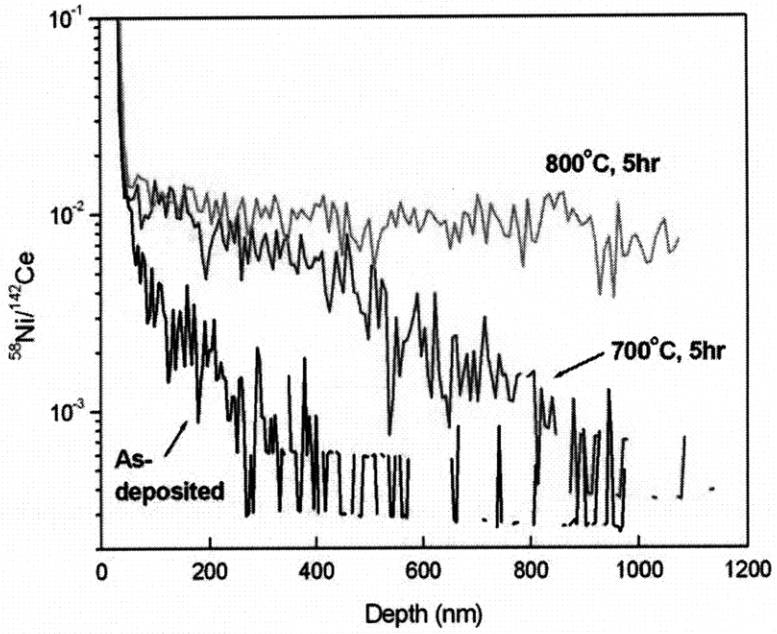


**Figure 80: SIMS spectra of $^{58}Ni/^{142}Ce$ in the as-deposited state, as well as following anneals of 700 and 800°C for 5 hr. At a depth of approximately 100 nm, the 700 and 800°C profiles show similar intensities, indicative of diffusion according to the constant source solution.**

The specific solution to the diffusion equation for constant source boundary conditions is:

$$\frac{c(x,t)}{c_O} = erfc\left(\frac{x}{2\sqrt{Dt}}\right) + c_{BG} \tag{69}$$

where $x$ is the depth, $D$ is the diffusion coefficient, $t$ is time, and $c_{BG}$ is the background concentration, indicative of the detection limit of each species in the SIMS spectrum. The relative intensity and depth of the 5 hr. data from Figure 55 was normalized and re-plotted in Figure 81. A best fit solution to Eq. 69 was determined using the non-linear curve-fitting routine of the Microcal Origin software (ver. 6.0, Northampton, MA). The agreement between the data and the diffusion model is satisfactory. The resulting grain boundary diffusion coefficient for Ni in $CeO_2$ at 700°C was

determined to be $4.6 \times 10^{-14}$ $cm^2/s$. The same procedure was performed for the Ni data at 800°C, shown in Figure 57. The normalized data and model fit are shown in Figure 82. The fit to the model is again satisfactory, and the $D_{GB}$ value was determined to be $2.8 \times 10^{-13}$ $cm^2/s$.

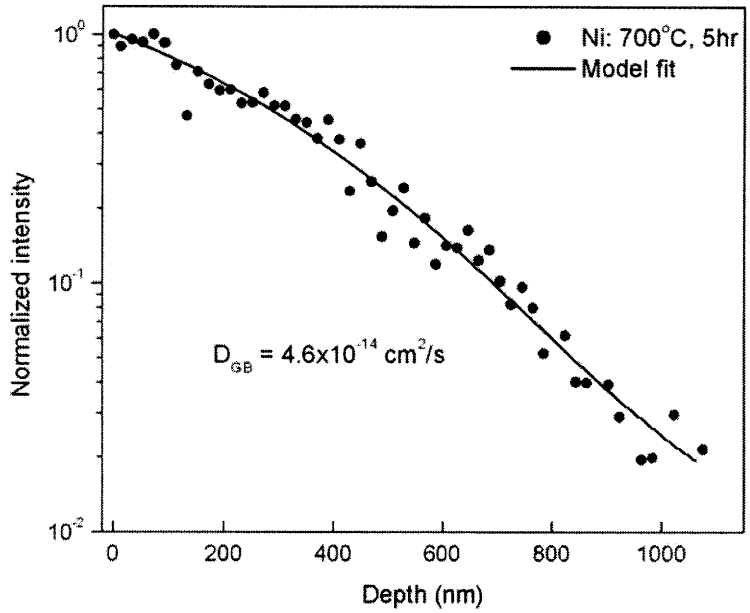


**Figure 81: Diffusion profile for Ni in $CeO_2$ after annealing at 700°C for 5 hr. (data points). The solid line corresponds to the fit to the constant source solution.**

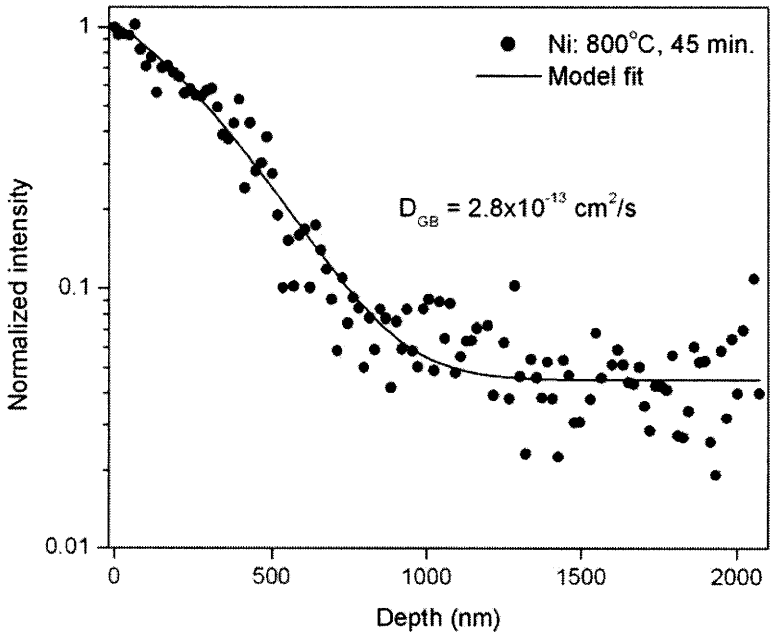


**Figure 82: Diffusion profile for Ni in $CeO_2$ after annealing at 800°C for 45 min. (data points). The solid line corresponds to the fit to the constant source solution.**

Likewise, the Mg data after annealing at 700°C for 5 hr. from Figure 58 was normalized and re-plotted in Figure 83. $D_{BG}$ was calculated to be $2.8x10^{-15}$ $cm^2/s$. The spectrum following annealing at 750°C for 90 min, originally shown in Figure 59, is replotted in Figure 84. $D_{BG}$ was calculated to be $5.9x10^{-15}$ $cm^2/s$.

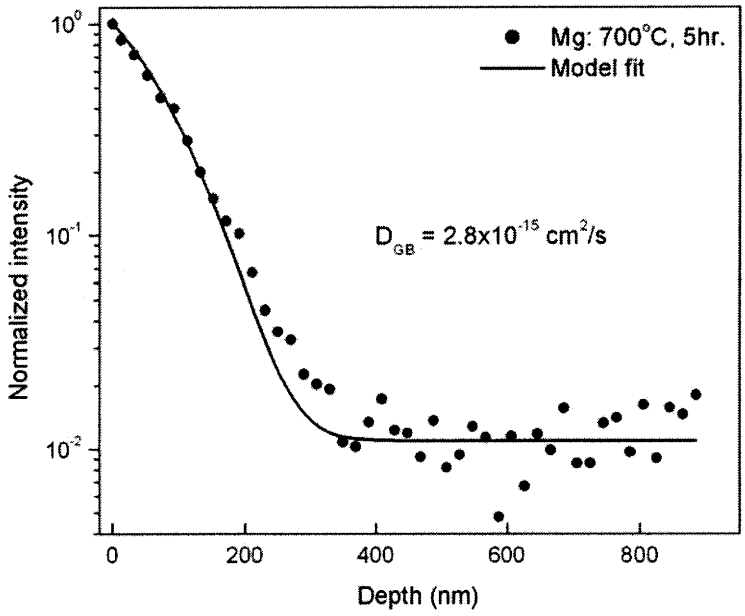


**Figure 83: Diffusion profile for Mg in $CeO_2$ after annealing at 700°C for 5 hr. (data points). The solid line corresponds to the fit to the constant source solution.**

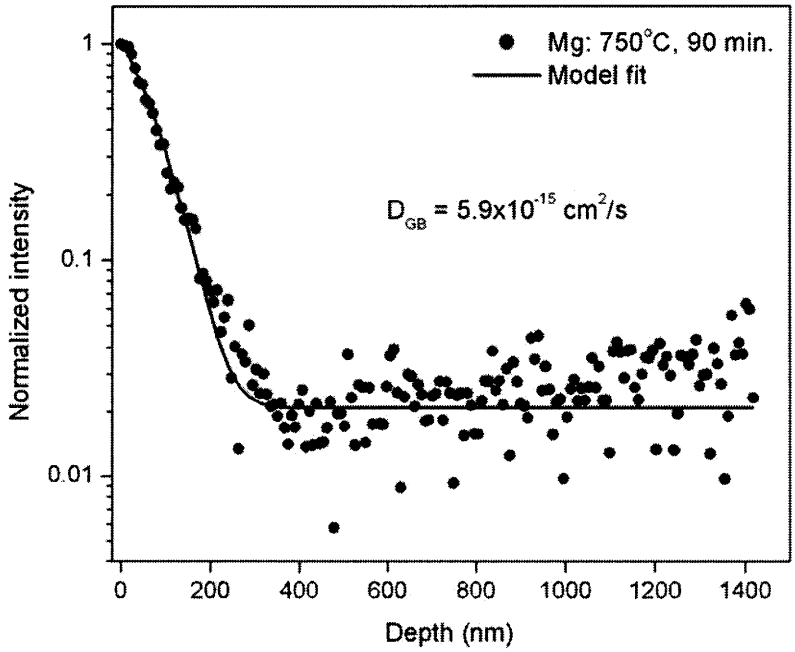


**Figure 84: Diffusion profile for Mg in $CeO_2$ after annealing at 750°C for 90 min. (data points). The solid line corresponds to the fit to the constant source solution.**

Similarly, the data following annealing at 800°C for 45 min., shown in Figure 60, is replotted in Figure 85. $D_{BG}$ was calculated to be $1.2x10^{-14}$ $cm^2/s$. It is well-known that the diffusion coefficient is a thermally-activated quantity, and can thus be represented by an Arrhenius relation:

$$D = D^o \exp\left(-\frac{E_A}{kT}\right) \tag{70}$$

where $D^o$ is a temperature-independent constant. A plot of ln($D$) vs. 1/T will yield a slope of $-E_A/k$. In the case of Ni, only two data points have, to date, been obtained. Obviously, a reliable $E_A$ cannot be obtained with just two data points; despite this, an *estimated* $E_A$ value of 1.62 eV was obtained with the two Ni data points. In the case of Mg, the diffusivity is plotted as a function of inverse temperature in Figure 86; the $E_A$ is 1.31 ± 0.02 eV. The corresponding expression for the Mg grain boundary diffusivity is:

$$D_{GB}^{Mg} = 1.7x10^{-8}\ \frac{cm^2}{s} \exp\left(-\frac{1.31 \pm 0.02eV}{kT}\right)$$

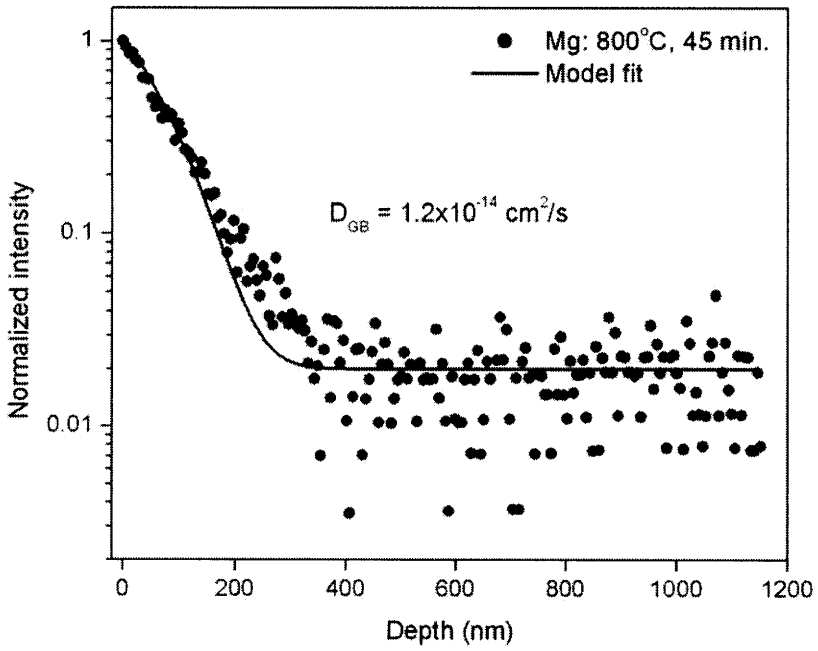


**Figure 85: Diffusion profile for Mg in $CeO_2$ after annealing at 800°C for 45 min. (data points). The solid line corresponds to the fit to the constant source solution.**

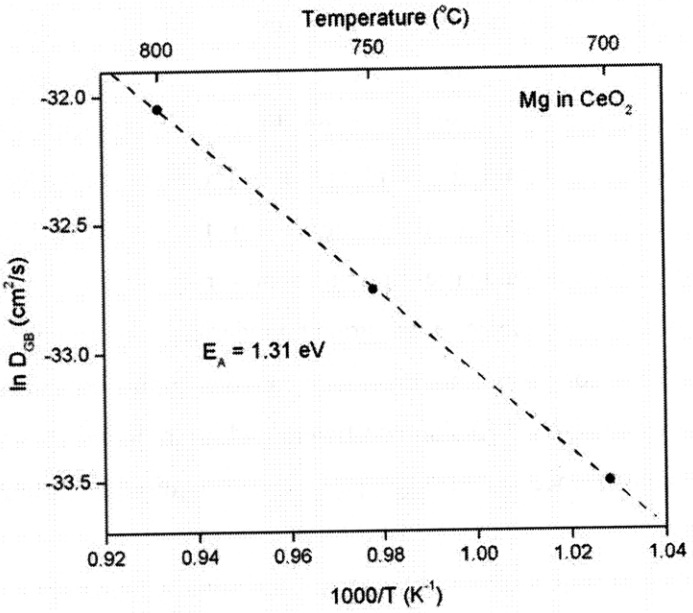


**Figure 86: Arrhenius plot of the natural log of the diffusivity versus inverse temperature for Mg in $CeO_2$. An activation energy of 1.31 ± 0.02 eV is derived.**

Compared to typical values of the $E_A$ for cation bulk diffusion in fluorite compounds, which are often 4 eV or greater [102], the values of 1.62 and 1.31 eV for Ni and Mg may at first appear rather low. As shown in Table 3 however, these values are in reasonable agreement with previous reports of grain boundary diffusion of cations in ionic solids such as YSZ, MgO, and NiO. Likewise, the magnitude of the pre-exponential factor is in good agreement with the diffusion of alkali earth cations in YSZ.

| Cation | Matrix | $D^0$ ($cm^2/s$) | $E_A$ (eV) | Reference |
|---|---|---|---|---|
| Ca | CSZ-15 | $3.4x10^3$ | 4.28 | 136 |
| Mg | YSZ-10 | $2.6x10^{-8}$ | 1.24 | 137 |
| Ca | YSZ-10 | $7.2x10^{-6}$ | 1.96 | 137 |
| Cr | MgO | n/a | 1.87 | 138 |
| Cr | NiO | $6.0x10^{-3}$ | 2.01 | 139 |
| Ni | NiO | $3.5x10^{-1}$ | 1.79 | 139 |
| Co | NiO | 4.3 | 1.87 | 139 |

**Table 3: Activation energies and preexponentials of the grain boundary diffusion coefficient for various cations in specified ionic solids**

The results from the study of cation in-diffusion are relevant from both a scientific and technological point-of-view. From the scientific standpoint, these measurements represent, to the author's knowledge, the lowest temperatures at which cation diffusion coefficients have been measured in $CeO_2$. This has been achieved through the combination of precisely controlled thin films with a low surface roughness, even after annealing, and a highly sensitive depth profiling technique in ToF-SIMS. The high density of grain boundaries normal to the surface allows for signal detection despite the low concentration of diffusant species at the grain boundaries. Experimental conditions within the Harrison regime C allow for direct measurement of the grain boundary diffusivity without prerequisite knowledge of the bulk diffusion coefficient and grain boundary width. The accuracy of the experiments are enhanced since only a single parameter is required for fitting the data.

The technological value of this technique may not be initially apparent, since the $D_{GB}$ values measured are many orders of magnitude slower than the diffusion of oxygen in $CeO_2$. However, it was indicated in Section 1.7 that the rates of important degradation processes such as creep [99] and kinetic demixing [100] are determined by the slowest species—in this case, cations. Thus, the lifetime and performance of SOFCs is likely affected by cation diffusion, particularly along grain boundaries. The magnitudes of $D_{GB}$ measured in this study, $10^{-13}$ to $10^{-15}$ $cm^2/s$, indicate that cations will diffuse hundreds of nanometers to a few microns within a few hours at 700-800°C. While such length scales may not be of primary concern in conventional bulk SOFCs, the increasing focus on microstructured SOFCs for portable power generation [140-142] may well be affected due to the reduced thickness of the electrolyte. A recent study on the intermediate SOFC stack LSCF—CGO—YSZ—Ni/YSZ by Mai and coworkers illustrates this possibility [143]. In that work, the stack shown below in Figure 87 was formed and tested at 700°C for 1000 hr. The authors reported a degradation of the cell voltage between 2 and 6% per 1000 hr. The authors attributed this degradation to the increase in polarization resistance associated with a $SrZrO_3$ reaction product layer that formed between the CGO interlayer and the YSZ electrolyte. This indicates diffusion of Sr across the CGO interlayer and subsequent reaction with the YSZ electrolyte. While diffusion is enhanced in this case because of the porosity and surfaces, a similar phenomenon has been reported in composite $La_{1-x}Sr_xMnO_3$—CGO electrodes, where the electrochemical performance degraded over time due to interdiffusion and formation of reaction products [144]. Overall, it is common for LCSF-related cathodes and YSZ electrolytes to react to form deleterious reactions products [145], and so the diffusion of cations across CGO interlayers remains a crucial topic of study.

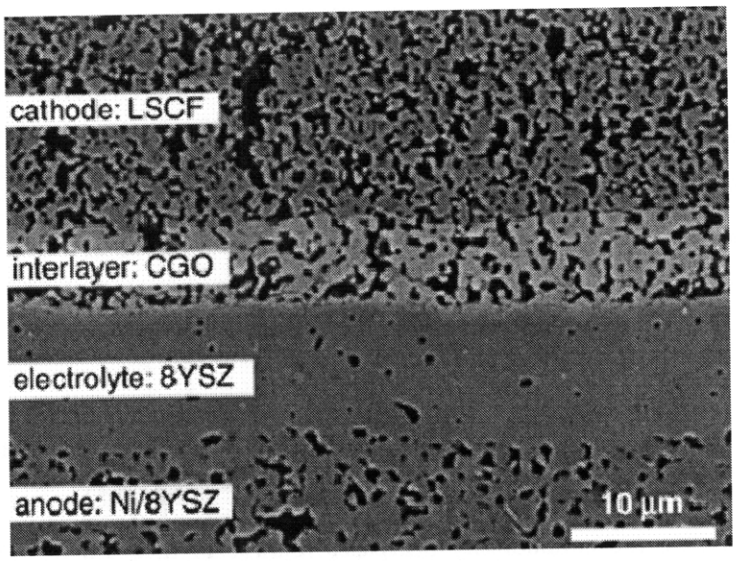


**Figure 87: SEM cross-sectional micrograph of an intermediate temperature SOFC stack, showing the cathode, interlayer, electrolyte, and anode [143].**

### *4.3 Electrical Characterization with Pt Non-Blocking Electrodes*

The electrical conductivity baseline data of the as-deposited samples is compared with literature data [37, 57, 62, 63] in the same temperature range in Figure 63. The magnitude of the electrical conductivity in this study is similar to the work of Rupp and Gauckler on thin films prepared by spray pyrolysis [63], but somewhat higher in magnitude than the other literature reports from bulk nanocrystalline samples. In Figure 63, the two thin film studies result in higher electrical conductivity than three reports on bulk nanocrystalline $CeO_2$—as discussed in Section 4.7 below, this conductivity increase may result from an interfacial layer between the $CeO_2$ film and substrate. A recent study by members of the author's laboratory demonstrated that the properties of oxide thin films, such as the electro-optic coefficient, often vary considerably from that of the bulk [146]. The effect of the nature of the sample (bulk, thick film, thin film, etc.) on properties such as electrical conductivity remains under study.

The activation energies of 0.90, 1.04, 1.16, 1.36, and 1.35 eV also demonstrate the sensitivity of the electrical conductivity to various factors. Indeed, the authors of Ref. 37 fabricated nanocrystalline $CeO_2$ by two separate methods, and obtained $E_A$ values of 1.16 and 0.99 eV (the latter is not shown in Figure 63). As discussed in Section 4.5 below, these differences in $E_A$ are observed throughout the literature and are known to be grain-size dependent [59, 63]. Thus, the electrical conductivity measured as a function of temperature in this study is concluded to be in reasonable agreement with literature reports of nanocrystalline $CeO_2$. In addition, the $pO_2$ dependence of the electrical

conductivity of -0.21, shown in Figure 64, is found to be in good agreement Refs. 37, 57, and 62. The negative slope indicates conduction that is dominated by the transport of electrons. The $pO_2$ dependence of conductivity of near -1/4 on a log-log plot suggests that the extrinsic regime, where oxygen vacancies are compensated by acceptor impurities within the sample, is controlling in this $pO_2$ range. The deviation from the -1/4 slope is consistent with a contribution from the ionic conductivity, which is assumed to be $pO_2$ independent in this range, according to Eq. 17. This topic will be discussed further in Section 4.4 below.

In Figure 65, the effect of annealing at 600 and 800°C with no diffusion source is shown. The activation energy is 1.30 eV after annealing at 600°C for 5 hr. and 0.99 eV after annealing at 800°C for 20 hr. In both cases, the conductivity decreases relative to the as-deposited data, though the change following the 600°C anneal is small. There are several factors that may contribute to this conductivity decrease: (1) a relaxation of residual stress formed during deposition, (2) grain growth, and (3) in-diffusion of Mg from the substrate. All three mechanisms are feasible, and the AFM micrographs in Figure 49 and the $D_{GB}$ of Mg calculated in Figure 83 provide evidence that (2) and (3) do indeed occur. These effects will be discussed in greater depth in Section 4.4.3 below. The electrical conductivity is also dependent the nonstoichiometry of the sample. In principle, the $CeO_2$ thin film could be partially-reduced as a result of deposition inside a vacuum chamber, especially in the grain boundary region. Such a sample would initially display higher conductivity due to an enhanced electron concentration after reduction, and then a conductivity decrease after annealing in an oxidizing environment. This is indeed the trend observed in Figure 65. However, the data labeled 'as-deposited' was measured several times during both the heating and cooling cycles. In doing so, the samples were heated to 520-550°C during testing, allowing for more complete oxidation. In fact, most samples did show enhanced conductivity during the very first measurement, and then a decrease to a lower but consistent value after subsequent testing. The higher values of the initial test were attributed to nonstoichiometry, and this data was discarded from the reported 'as-deposited' data. Thus, the trends in Figure 45 are not attributed to changes in stoichiometry of the thin film specimens.

The electrical conductivity following in-diffusion of Ni at 800°C for 20 hr. Gd at 700°C for 5 hr. is shown in Figure 66. The conductivity decreases by a factor of 4-5 from the samples annealed with no diffusion source, and by a factor of 16-20 from the as-deposited samples. The values for the activation energy, 0.99 and 1.04 eV for the $Gd_2O_3$ and NiO source, respectively, are comparable to the as-deposited values. In this case, it is apparent that annealing in the presence of a diffusion source results in a distinct decrease in the electrical conductivity beyond that is observed with no diffusion

source (see Figure 66). One conceivable mechanism by which these observations could be ascribed is acceptor doping of the $CeO_2$ bulk with Ni and Gd. In the case of substitution of a trivalent cation, for example, on a Ce site, the defect reaction would proceed as:

$$A_2O_3 \xrightarrow{CeO_2} 2A'_{Ce} + V_O^{\bullet\bullet} + 3O_O^x \tag{71}$$

The concentration of oxygen vacancies, $[V_O^{\bullet\bullet}]$, increases as the acceptor doping increases. If the total dopant concentration remains less than the point of conductivity maximum, illustrated in Figure 3, then $\sigma_{ion}$ increases with acceptor doping. According to the mass action relation defined in Eq. 10, an increase in $[V_O^{\bullet\bullet}]$ will result in a decrease in the electronic concentration, $n$. As stated above, since the mobility of oxygen vacancies is more than two orders of magnitude lower than for electrons, a small degree of acceptor doping in the bulk would result in a decrease in $\sigma_{total}$, as is indeed observed. However, there are two arguments as to why this mechanism does not occur. First, it was discussed in length in Section 4.2 that cation diffusion occurs solely along the grain boundaries. Only one diffusion mechanism is apparent in all SIMS spectra and a comparison with literature data [98, 102] of bulk and grain boundary diffusion of cations leaves little doubt that the magnitude of mass transport measured in this study is far too high to be attributed to the bulk in this temperature range. Second, there is general consensus that NiO is not soluble in $CeO_2$ to any appreciable degree [147, 148]. An earlier report by Pound [149] had suggested NiO solubility of 10 mol% at 900°C, though Ranlov and co-workers [147] later highlighted several conceptual and experimental errors in that work. The ionic radii of $Ni^{2+}$ and $Ce^{4+}$ are 83 and 97 pm, respectively [150]. As the authors of Ref. 147 point out, the general ratio rule for ionic structures [151] predicts that smaller cations such as Ni prefer sixfold coordination, and are therefore not stable in the eightfold coordination of a fluorite compound.

Based on this data, it was initially proposed that the decrease of the electrical conductivity in the presence of a diffusion source is brought about by changes at the grain boundary, specifically a change in the space charge potential. As illustrated in Eq. 29, a change of the space charge potential is exponentially proportional to the enhancement and depletion of charge carriers within the space charge regions. Since electrons and oxygen vacancies are of opposite charge, any change in the space charge potential will enhance one type of conduction and lead to depletion of the other. In order to examine this hypothesis in greater depth, the ionic and electronic contributions to the total conductivity must first be deconvoluted in order to obtain a detailed understanding of the changes that occur at the grain boundary.

## *4.4 Electrical Characterization with YSZ-12—porous Pt Blocking Electrodes*

### *4.4.1 Validation of the Electron-Blocking Structure*

In this study, YSZ-12 was employed to block the flow of electrons. The porous Pt layer was used to provide a stable electrical contact; the porosity was introduced in order to minimize the contribution of the electrode impedance to the total DC resistance. The criterion for a valid electron-blocking arrangement was introduced in Eq. 65 [130], and the choices of materials and geometry of the blocking measurement were validated in Section 3.4. However, it is prudent to further consider the nature of electronic conduction in YSZ. Near ambient $pO_2$, YSZ is known to be predominantly p-type [131]. Thus, while it has been shown above that the transport of electrons is negligible in this blocking arrangement, the possibility of electronic conduction via holes must be addressed. Due to a chemical potential gradient, holes may be injected from the YSZ into the $CeO_2$ layer and, in principle, be transported across the $CeO_2$ and collected at the other electrode. However, the injected hole is a minority carrier in $CeO_2$ and if its diffusion length is small relative to the width of the $CeO_2$ path, it will likely recombine before collection. Using literature data, reasonable estimates of $8x10^{-5}$ $cm^2/s$ [152] and $10^{-7}$ s [12] are obtained at 500°C for the hole diffusivity, $D_p$, and carrier lifetime, $\tau_p$, respectively. The resulting diffusion length of 0.03 μm is smaller than the 40 μm required to traverse the $CeO_2$. Furthermore, since the diffusion length of 0.03 μm was based on the carrier lifetime of a hole in epitaxial Si [12], the actual diffusion length in the $CeO_2$ layer will be substantially shorter due to the multitude of recombination sites such as point defects and grain boundaries. Thus, while holes may indeed be injected into the $CeO_2$ layer, recombination will occur so swiftly that the holes will not contribute to the measured current.

Even for a blocking structure that satisfies Eq. 65, there remains a possibility for short-circuiting electron contributions to the measured current. As discussed by Riess [106], the mobile oxygen ions in the YSZ film could potentially participate in an electrochemical reaction at the YSZ—$CeO_2$—gas triple phase boundary (TPB), releasing oxygen to the gas phase and transferring an electron to the MIEC layer. These various electrochemical processes and an equivalent circuit diagram are depicted in Figure 88.

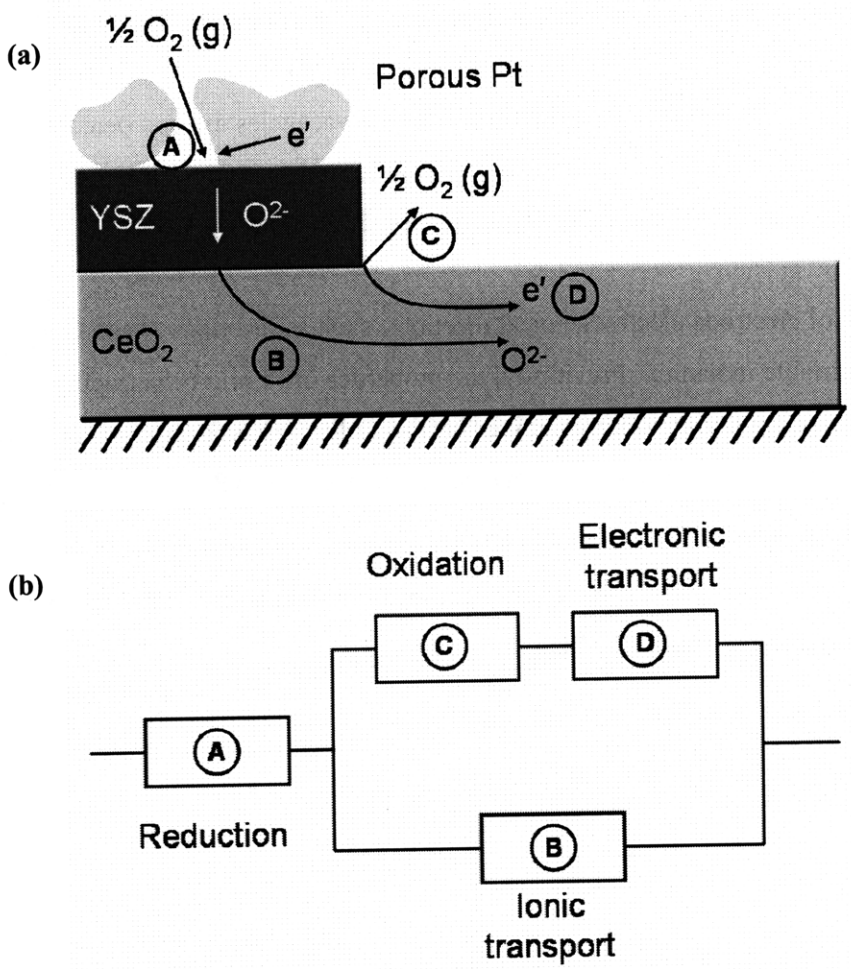


**Figure 88: Schematic diagram (a) and equivalent circuit (b) of the electrochemical processes occurring in the blocking electrode, $CeO_2$ film, and gas phase.**

If a negative bias is placed upon the Pt layer in Figure 88a, the transport process begins with the reduction of gaseous oxygen species at TPB sites. Second, oxygen is transported through the YSZ film as the species $O^{2-}$. At this point, the oxygen ion may be injected into the $CeO_2$ layer and conducted to the other electrode. However, the oxygen ion may travel to the TPB and undergo an electrochemical reaction with the gas phase, resulting in injection of electrons into the $CeO_2$. For a given temperature and $pO_2$, either reaction B or C/D will be favored depending on: (1) the ionic conductivity of the $CeO_2$ film, (2) the activation barrier for the oxygen reaction, (3) the electronic conductivity of the $CeO_2$ film, and (4) the amount of YSZ/$CeO_2$ interface relative to the amount of TPB sites. It may be difficult to predict *a priori* the favored reaction, but existing data does allow for the prediction of the $pO_2$ dependence that would be observed in each case.

In Section 1.3, the defect chemistry of $CeO_2$ was presented. Through the results of this study and other reports in the literature [57, 62], it is clear that the prevailing Brouwer approximation in this $pO_2$ and temperature range is the extrinsic case, in which oxygen vacancies are compensated by acceptor dopants. As such, the ionic conductivity of ceria is $pO_2$-independent, and the electronic conductivity varies with $pO_2$ to the power of -1/4, as demonstrated in Eq. 18.

The $pO_2$ dependence of electrode electrochemical reactions, such as reactions A and C in Figure 88 is more complex and variable in nature. Previously, the properties of Pt microelectrodes on YSZ-9 thin films grown by reactive sputtering were examined in the Tuller research group [126]. In the $pO_2$ range of 0.01 to 1 atm, the electrode conductance normalized by TPB length varied according to $pO_2^{-1/2}$, as shown in Figure 89. At lower partial pressures, the dependence became flatter and eventually assumed a positive $pO_2$ dependence. These observations are consistent with previous reports in the literature (see for example, Mizusaki, *et al.* [153]).

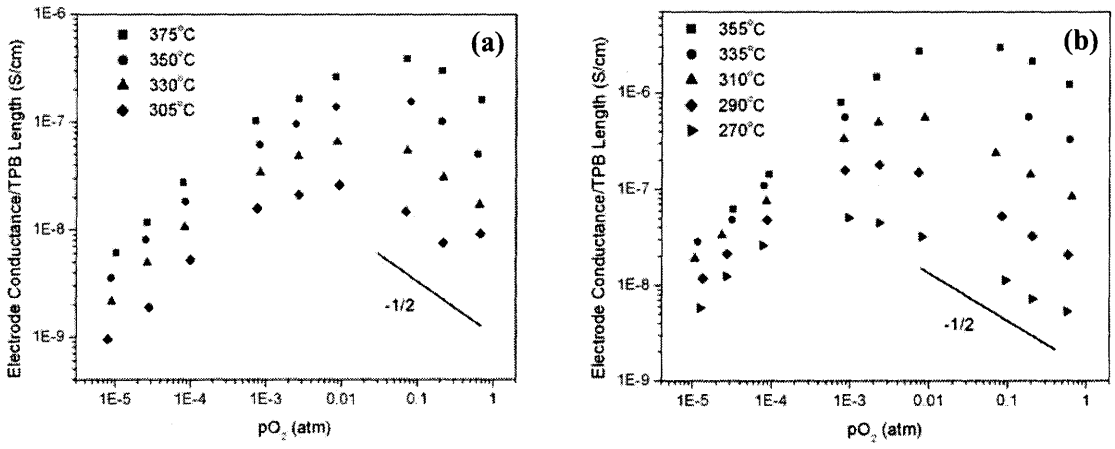


**Figure 89: Plots of the Pt electrode conductance normalized by TPB length vs. $pO_2$ for Pt on YSZ-9 thin films deposited on (a) $SiO_2$ substrate at 300°C and Pt on a YSZ (111) single crystal substrate [126].**

Based on these results, the limiting electrochemical process in the blocking electrode measurement may now be predicted based on the expected $pO_2$ dependence of each process:

| Process | Description | Expected $pO_2$ dependence |
|---|---|---|
| A | Reduction at the Pt/YSZ-12 TPB | -1/2 (subject to variance) |
| B | Ionic transport in $CeO_2$ | 0 |
| C | Oxidation/Reduction at the YSZ-12/$CeO_2$ TPB | -1/2 (subject to variance) |
| D | Electronic transport in $CeO_2$ | -1/4 |

**Table 4: The 4 electrochemical processes depicted in Figure 88 and the corresponding $pO_2$ dependence.**

Based upon the body of evidence in the literature regarding the electrochemical reduction of $O_2$ at Pt/YSZ interfaces, reaction A, the reduction reaction in series with processes B-D, can be ruled out as the rate-limiting step. The electrochemical performance, measured by the TPB-specific resistance, varies considerably across the literature, yet a conservative value of $5x10^6$ Ω-cm can be specified at 500°C [126]. The total electrode area for the 50 μm IDE geometry is 0.074 $cm^2$. However, what is necessary is the TPB length contained within that area. Verkerk, *et al.* estimated the TPB length per unit area of sputtered Pt electrodes to be 120 m per $cm^2$ [154]. Analysis of the interfacial area in Figure 69c-d using the ImageJ software [155] yields a value of approximately 550 m of TPB length per $cm^2$. An intermediate value of 200 m/$cm^2$ will be used for the purposes of this estimate. The TPB length associated with the porous Pt microelectrodes is thus 14.8 m, and the resistance associated with the reduction reaction is approximately 3380 Ω. Based on the TPB-specific resistance and TPB length estimates chosen, this value is conservative in nature. Nonetheless, this value is almost two orders of magnitude smaller than the DC resistances measured in this study, indicating that reaction A in Figure 88 is not the rate-limiting step. This estimation is corroborated by EIS data, which indicate no significant electrode reactions at low frequencies. The question remains as to which circuit pathway is the one of least resistance: ionic transport in the $CeO_2$ film (process B) or the serial combination of electrode reactions and electronic transport (processes C,D)? To address this question, the properties of as-deposited blocking samples are examined.

### *4.4.2 As-deposited Ceria Blocking Samples*

The results of the blocking electrode measurements for as-deposited and in-diffused samples are

shown as a function of temperature and $pO_2$ in Figs. 71-76. In Figure 90a below, a sample as-deposited blocking measurement is compared against (b) the blocking results of Kim and Maier [62], which was originally shown in Figure 19. In both plots, the $pO_2$ dependence of $\sigma_{ion}$ is essentially zero. Based upon the expected $pO_2$ dependencies presented in Table 4, this data indicates that process B in Figure 88, the ionic transport in $CeO_2$, is indeed the quantity that is being observed. The average $pO_2$ dependence of $\sigma_{el}$ in this study was -0.30, compared with -0.26 in Figure 90b. This value is similar to the -1/4 slope that is expected in the extrinsic regime. Two pieces of evidence point toward the as-deposited data falling within this regime: (1) the -0.22 slope of $\sigma_{total}$ and (2) the lack of $pO_2$ dependence of $\sigma_{ion}$. While the ionic transference number, $t_{ion}$, is lower in this study and the magnitude of the conductivity higher than Ref. 62, the two plots are in close agreement overall, further validating the effectiveness of the electron-blocking measurement.

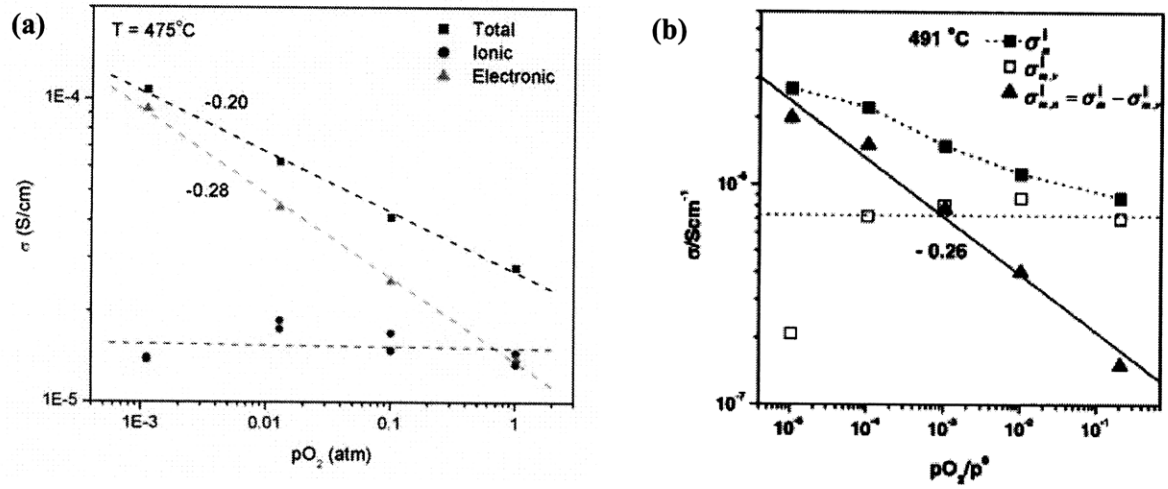


**Figure 90: Electrical conductivity vs. $pO_2$ for various contributions to the conductivity of $CeO_2$. Shown are (a) data from this study, and (b) the work of Kim and Maier [60], including the total (■), ionic (□), and electronic (▲) conductivities.**

### *4.4.3 Samples Annealed with and without a Diffusion Source*

In Sections 3.4.2 and 3.4.3, the electrical data measured from blocking samples annealed at 700 or 800°C in the presence of NiO and $Gd_2O_3$, as well as with no diffusion source were presented. Qualitatively, annealing with or without a diffusion source leads to two common observations; (1) a decrease of the total, ionic, and electronic conductivities, and (2) a notable change from $pO_2$-independent $\sigma_{ion}$ to a dependence of approximately -0.13. To aid in the visualization of these trends, the total and partial conductivities for samples for each type of processing are re-plotted below. In

Figure 91, the total conductivity is shown. The error bars represent the standard deviation of the averaged data. After annealing at 800°C with no diffusion source, the total conductivity decreased by more than one order of magnitude, yet the $pO_2$ dependence did not change appreciably. After Ni or Gd in-diffusion, the total conductivity decreased between approximately a factor of 3 at high $pO_2$ and 10 at low $pO_2$. The $pO_2$ dependence decreased to -0.11.

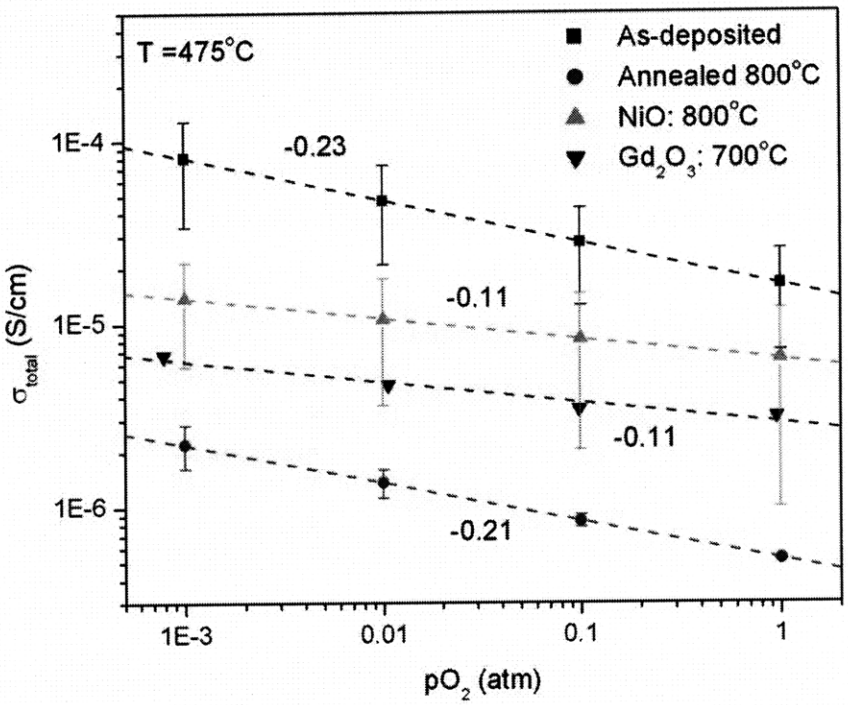


**Figure 91: Total conductivity vs. $pO_2$ for various specimens. Shown are data from as-deposited samples (■), as well as samples annealed with no diffusion source (●), a NiO (▲) and $Gd_2O_3$ source (▼).**

The ionic partial conductivity for the various processing conditions is shown in Figure 92. After annealing either with or without a diffusion source, the ionic conductivity decreases and assumes a pO2 dependence of approximately -0.13. This observation is not consistent with Figure 67, in which the $pO_2$ dependence did not change after in-diffusion. There is no clear explanation for this inconsistency. The data reported in Figure 67 was obtained from a single sample, whereas the data in Figure 92 is a summary of measurements from multiple samples. Based on the greater number of measured samples and reasonable error amount, it is clear that the $pO_2$ dependence of $\sigma_{ion}$ changed after in-diffusion. The ionic conductivity of the samples annealed with no diffusion source is quite similar to the sample annealed with a $Gd_2O_3$ diffusion source.

The ionic conductivity of a $CeO_2$ thin film homogeneously-doped with 0.3 cation% Gd (CGO-0.3%) is also shown in Figure 92 for reference. The total conductivity was measured with EIS and the

resulting contribution was assigned to be predominantly ionic in nature. This is justified by the expected $pO_2$-independence of the conductivity and a literature report of the same composition [62]. While the overall amount of Gd doping is small in comparison to commercially-used CGO systems, it is appreciably larger than the background acceptor impurity concentration that determines the oxygen vacancy concentration in nominally-undoped ceria. As a result, the transport properties of as-deposited $CeO_2$ and CGO-0.3% are fundamentally different. The greater Gd acceptor concentration results in two alterations: (1) increased ionic conductivity in the bulk and (2) a reduced space charge layer thickness. Both factors are expected to result in enhanced ionic conductivity relative to nominally-undoped $CeO_2$, as is indeed observed in Figure 92. This observation provides further credence that the deconvolution of the ionic contribution to the total conductivity via the blocking electrodes occurred as was originally-intended.

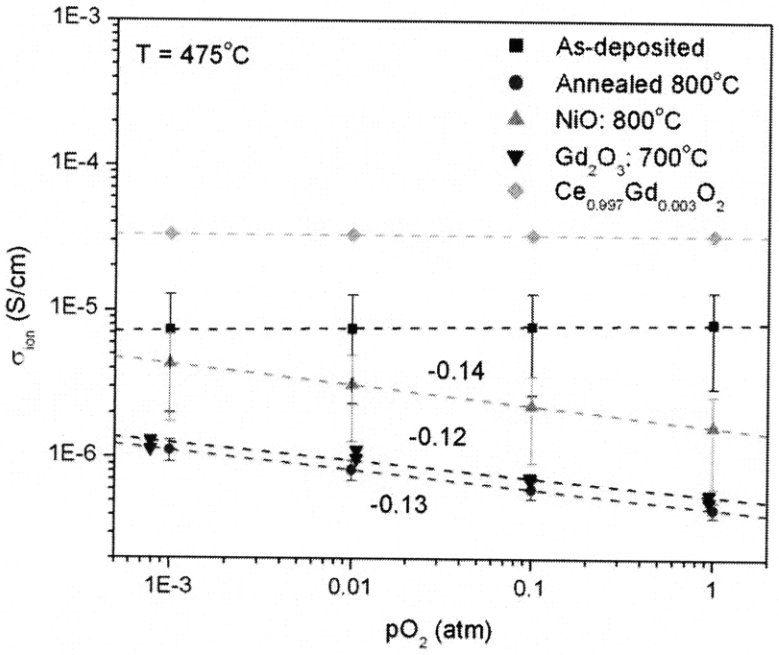


**Figure 92: Ionic conductivity vs. $pO_2$ for various specimens. Shown are data from as-deposited samples (■), as well as samples annealed with no diffusion source (●), a NiO (▲) and $Gd_2O_3$ source (▼). Shown for reference is the ionic conductivity of CeO2 homogeneously doped with 0.3 cat% Gd (♦).**

The electronic partial conductivity for the various processing conditions is shown in Figure 93. The trends in $\sigma_{el}$ are similar in nature to the total conductivity. After annealing with no dopant, $\sigma_{el}$ decreases by two orders of magnitude with no large change in $pO_2$ dependence. After in-diffusion of Ni or Gd, $\sigma_{el}$ decreases between a factor of 2-10 and the slope changes to ~ -0.11.

The deconvolution of the ionic and electronic partial conductivities reveals several interesting and

unexpected observations regarding the conductivity changes first observed with the Pt non-blocking electrodes. First, both $\sigma_{ion}$ and $\sigma_{el}$ decrease after annealing with or without a diffusion source. This observation alone is inconsistent with a model where the conductivity changes result from heterogeneous doping and the space charge potential alone. If that were the case, then one partial conductivity would increase and the other would decrease. The second notable feature is the $pO_2$-dependence of $\sigma_{ion}$; after annealing with or without a diffusion source, $\sigma_{ion}$ becomes $pO_2$-dependent. The slope is approximately -0.13 for all samples and the absolute value of the conductivity does not differ appreciably. On the contrary, there is a notable difference in $\sigma_{el}$ after annealing with no diffusion source and annealing with NiO or $Gd_2O_3$. While the $pO_2$ dependence does not change significantly after annealing with no diffusion source, the magnitude of the conductivity decrease, two orders of magnitude, is quite large. After annealing in the presence of a diffusion source, the $pO_2$ dependence changes but the conductivity decrease is less severe. In order to better understand these observations, it is useful to examine $t_{ion}$ and how it changes with processing. This is summarized in Table 5 for T = 475°C and $pO_2$ = 0.21 atm.

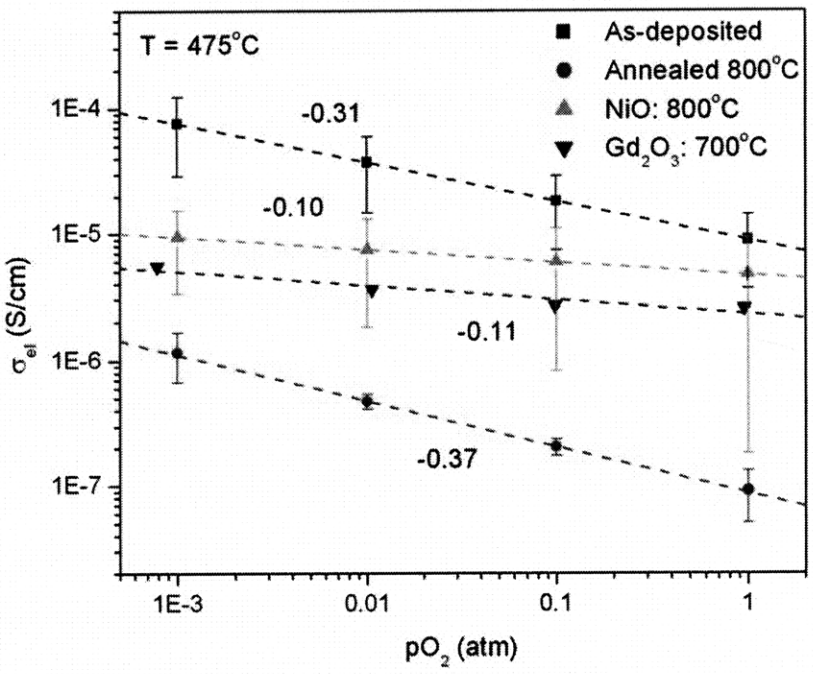


**Figure 93: Electronic conductivity vs. $pO_2$ for various specimens. Shown are data from as-deposited samples (■), as well as samples annealed with no diffusion source (●), a NiO (▲) and $Gd_2O_3$ source (▼).**

| Processing | $t_{ion}$ |
|---|---|
| As-deposited | 0.34 |
| Annealed 800°C | 0.76 |
| NiO: 800°C | 0.27 |
| $Gd_2O_3$: 700°C | 0.25 |

**Table 5: Ionic transference number resulting from various types of processing at T = 475°C and $pO_2$ = 0.21 atm.**

After annealing with no diffusion source, both $\sigma_{ion}$ and $\sigma_{el}$ decrease. However, the decrease in $\sigma_{el}$ is more severe, as shown in Figure 93. As a result, $t_{ion}$ increases from 0.34 in the as-deposited state to 0.76. The ionic conductivity is now the dominant contribution to the total conductivity. In contrast, $t_{ion}$ decreases with Ni and Gd in-diffusion, to 0.27 and 0.25, respectively.

In light of the $pO_2$-dependence of $\sigma_{ion}$, it is prudent to reconsider the validity of the blocking electrodes. It was argued in Section 4.4.1 that the quantity measured with DC polarization of the blocking electrodes was the ionic conductivity of the ceria layer. This was based on (1) the $pO_2$-indedendent conductivity and (2) the lack of a low frequency semicircle associated with an electrode reaction. It is clear that condition (1) does not apply. In Figure 94 below, an EIS spectrum is displayed for a sample that was annealed with $Gd_2O_3$ at 700°C for 5 hr. The measurement was performed at 550°C in air for a frequency range of $10^7$ to 1 Hz. In the range of 3000 to 1 Hz, there is additional impedance not associated with the primary semicircle. The nature of this signal is unclear; however, it is not likely to be associated with an electrode process: electrochemical processes occurring at electrodes in SOFC materials have been studied by many authors (see, for example, Hertz [126]), and the common feature is rather large capacitance, associated with a high $-Z''$ value. In this case, the capacitance associated with the data in the range of 3000 to 1 Hz is not consistent with either the shape or capacitance of a typical electrode electrochemical process, which typically appears as a slightly-depressed semicircle with a corresponding capacitance of $10^{-9}$ F or greater. Therefore, the EIS measurements suggest that the blocking behavior of samples annealed at 700 or 800°C does not vary from the as-deposited state.

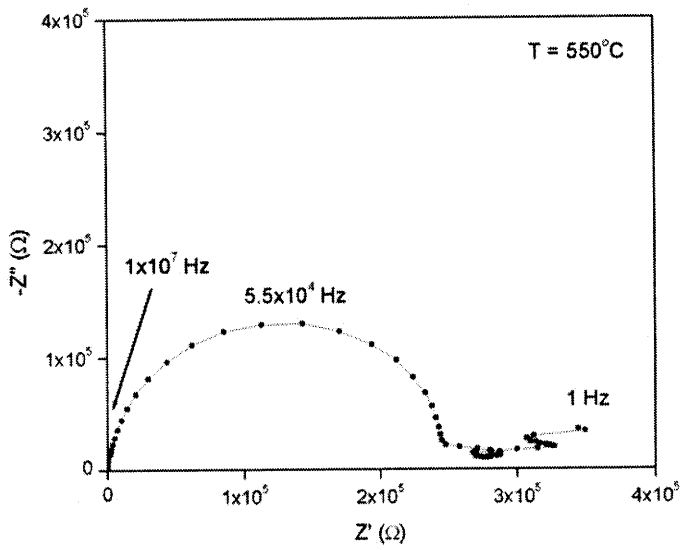


**Figure 94: Impedance spectrum from a sample modified by $Gd_2O_3$ in-diffusion at 700°C. The measurement was performed at T = 550°C in air. There is evidence of additional impedance near 1 Hz, but no readily-apparent electrode semi-circle.**

This conclusion, and the overall validity of the blocking electrodes, is further corroborated by examination of the I-t behavior of the samples. The as-deposited I-t curve, first introduced in Figure 70a, is shown again in Figure 95a. Shown also are the I-t curves from a sample annealed at 800°C with no diffusion source (b), and a sample annealed with $Gd_2O_3$ at 700°C (c). The corresponding value for $t_{ion}$, as calculated from Figure 91 and Figure 92, is shown for each sample. In (a) and (c), there is a noticeable initial current transient that disappears with time; $t_{ion}$ in each case is 0.34 or less. In (b), however, $t_{ion}$ is 0.76, and the dominant contribution to the total conductivity is ionic. Accordingly, there is no initial current transient as in (a) and (c), most of the current is already ionic and is thus not blocked. Thus, the observations resulting from Figure 95 are in agreement with the conclusions reached above with respect to the blocking electrodes.

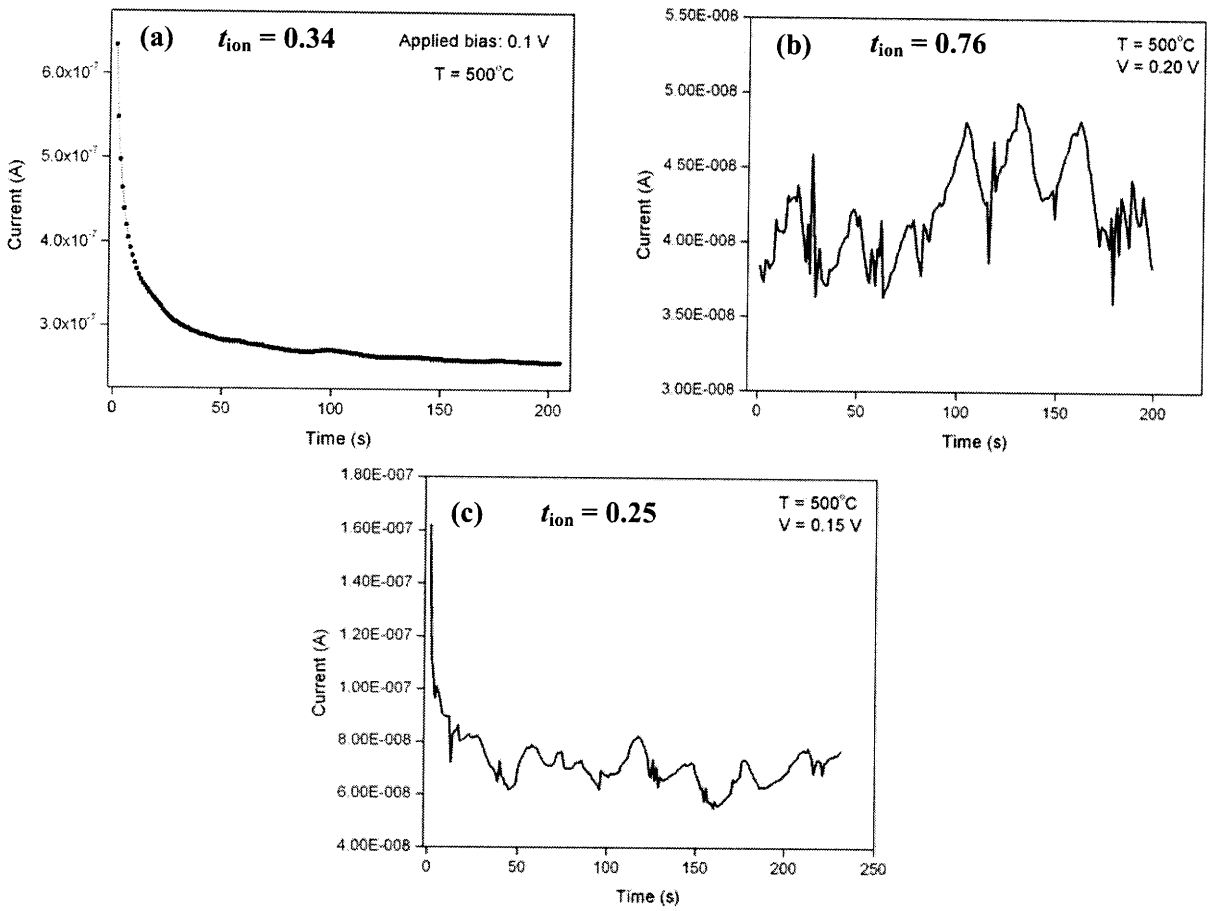


**Figure 95: Current-time plots at 500°C for (a) an as-deposited sample, (b) a sample annealed at 800°C and (c) a sample annealed at 700°C with a $Gd_2O_3$ source. The ionic transference number of each sample is displayed.**

As mentioned above, the experimental observations associated with the blocking electrodes preclude a model where only changes in the space charge potential caused by heterogeneous doping can be considered; an additional effect (or effects) must be introduced in order to fully describe the conductivity changes that occur when the ceria thin films are annealed at 700 or 800°C, with or without a diffusion source. It was stated in Section 3.1 that the grain size increased from approximately 35 to 75 nm after annealing at 800°C. This information will be used to consider below additional effects that may alter the electrical conductivity of the ceria thin films.

### *4.5 Mechanistic Interpretation of the Thermal Activation Energies*

Thermal activation energies serve as an important parameter because mechanistic information regarding the formation and migration of defects can be extracted and compared with theory or related published experimental results. For example, the conductivity of oxygen vacancies, described

in Eq. 7, can be presented as

$$\ln \sigma_{ion} = \ln(2q) + \ln c_v + \ln \mu_v \tag{72}$$

Taking the partial derivative with respect to $1/T$ yields

$$\frac{\partial \ln \sigma_{ion}}{\partial 1/T} = \frac{\partial \ln c_v}{\partial 1/T} + \frac{\partial \ln \mu_v}{\partial 1/T} \tag{73}$$

Since the concentration of vacancies is fixed in the acceptor regime by acceptor impurities, the first term equals zero and the slope of an Arrhenius plot equals $-E_{mig}/k$, where $E_{mig}$ is the migration energy of oxygen vacancies in the bulk. This value has often been reported in the literature, ranging from 0.7 [62] to 0.90 [156] to 1.0 eV [157]. In contrast, both the concentration and mobility of electrons in ceria are thermally-activated. The activation energy in the extrinsic regime was described previously in Section 1.3:

$$E_A = \frac{\Delta H_R}{2} + E_H \tag{74}$$

Substituting in values of 3.94 eV for $\Delta H_R$ [38] and 0.40 eV for $E_H$ [24], a value of 2.37 eV is obtained for bulk electronic transport in ceria.

Using the general space charge model, Kim and Maier derived relations for the activation energy in which the perpendicular and parallel contributions of the grain boundary region is taken into consideration for oxygen vacancies and electrons, respectively [62]. The activation energy of the perpendicular grain boundary contribution for oxygen vacancies can be written as [62]:

$$E_v^{\perp} = k \frac{\partial \ln \rho_v^{\perp}}{\partial 1/T} \tag{75}$$

Where $v$ and $\perp$ denote oxygen vacancies and perpendicular motion, respectively. Since the resistivity is simply the reciprocal conductivity, this expression can be substituted in Eq. 2 to yield:

$$E_v^{\perp} = -k\left(\frac{\partial \ln \mu_v}{\partial 1/T} + \frac{\partial \ln c_{v0}}{\partial 1/T}\right) \tag{76}$$

where $c_{v0}$ is the oxygen vacancy concentration adjacent to the grain boundary. Eq. 29, which is the general description of carrier profiles in a space charge layer, can be re-arranged as:

$$c_{v0} = c_{v\infty} \exp\left(-\frac{2e}{kT}\Delta\phi(0)\right) \tag{77}$$

and substituted into Eq. 76 to yield:

$$E_v^{\perp} = E_{v\infty} + 2e\left(\Delta\phi(0) + \frac{1}{T}\frac{\partial\Delta\phi(0)}{\partial 1/T}\right) \tag{78}$$

Thus, the activation energy associated with the grain boundary region can be described as the summation of the activation energy in the bulk plus a blocking contribution from the potential barrier at the grain boundary. Kim and Maier reported that the temperature dependence of the barrier is "quite small" and that the (1/T) $\partial\Delta\Phi(0)/\partial(1/T)$ term was approximately 0.1 V [62]. Because of the potential barrier, the activation energy increased from 0.7 eV in the bulk to 1.5 eV perpendicular to the boundary.

In a parallel argument to the one presented above for oxygen vacancies, the relationship of the electronic activation energy was given as [62]:

$$E_n^{\parallel} = -E_{n\infty} + e\left(\Delta\phi(0) + \frac{1}{T}\frac{\partial\Delta(0)}{\partial 1/T}\right) \tag{79}$$

Using a value of 0.3 V for $\Delta\Phi(0)$, an expected activation energy of 1.97 eV was obtained by the authors, in good agreement with the experimental results.

Based on this framework, the activation energies obtained in this study can now be analyzed. The average thermal activation energy and corresponding standard deviation, σ (note: not electrical conductivity), for each conductivity are shown in Table 6.

| | **Total** | | **Ionic** | | **Electronic** | |
|---|---|---|---|---|---|---|
| | $E_A$ | $\sigma$ | $E_A$ | $\sigma$ | $E_A$ | $\sigma$ |
| As-deposited | 1.33 | 0.11 | 1.50 | 0.09 | 1.24 | 0.17 |
| NiO, $Gd_2O_3$-doped | 1.12 | 0.12 | 1.28 | 0.13 | 1.09 | 0.17 |
| Annealed 800°C | 1.46 | 0.03 | 1.50 | 0.01 | 1.47 | 0.45 |

**Table 6: Average activation energy and standard deviation for the total, ionic, and electronic conductivities for each type of processing.**

In terms of the total conductivity, the $E_A$ of the as-deposited films measured with the blocking electrodes was 1.33 eV. This is larger than the value from the non-blocking electrodes, 1.04 eV, presented in Figure 63. It is similar, however, to the 1.30 eV $E_A$ after annealing at 600°C for 5 hr. shown in Figure 65. In addition to annealing the electron-blocking samples at 600°C in order to introduce porosity to the Pt layer, the samples were annealed to 600°C before photolithography in order to ensure complete oxidation. Thus, the as-deposited blocking films likely possess a grain size similar to the non-blocking sample annealed at 600°C for 5 hr. In Figure 49a, it was shown that the grain size of this sample was 62 nm, slightly larger than the as-deposited value of 35 nm. It was reported in Refs. 59 and 63 that the activation energy of $CeO_2$ thin films is grain size-dependent, with values of 0.90 to 1.5 eV reported for grain sizes ranging from 35 to 100's of nm. The conductivity was also found to decrease with increasing grain size, which is consistent with the data in Figure 65. Thus, it is possible that the increase in $E_A$ from 1.04 eV for the as-deposited films to ~1.32 eV for films annealed briefly at 600°C results from a small amount (less than 2x) of grain growth. The cause of the decrease in activation energy with decreasing grain size has not been addressed in the literature. However, it can be seen in Eq. 79 that the $E_A$ associated with electrons in the boundary region is lower than the corresponding bulk value. Therefore, in nanocrystalline systems such as ceria that are dominated by electrons, the decreasing grain size results in a specimen that is influenced more and more by space charge regions, which demonstrate reduced $E_A$ for the accumulated electrons.

The $E_A$ of the ionic conductivity in the as-deposited state is 1.50 eV. This is noticeably larger than the accepted values of the oxygen bulk migration energies, which range from 0.7eV [62] to 1.0 eV [157]. However, this $E_A$ is in good agreement with reported values for nanocrystalline $Ce_{0.997}Gd_{0.003}O_2$ [62] and $CeO_2$ [57], which were 1.50 and 1.60 eV, respectively. In both instances, the authors ascribed the larger $E_A$ to grain boundary blocking contributions. These observations are consistent with reports of oxygen migration perpendicular to grain boundary regions that identified larger $E_A$ values of 0.9 to 1.7 eV [158, 159].

The cause of this increase in $E_A$ from 0.7 to 1.5 eV remains under debate. One possibility, presented by Hwang and Mason, is defect association, in which an oxygen vacancy is bound to an acceptor [57]. Such defect association is more common at reduced temperatures, and is reported to increase $E_A$ by 0.17-0.35 eV [156, 160]. Another explanation for the increase in $E_A$ is the space charge model, shown above in Eq. 78. Substituting 0.1 V for (1/T) $\partial\Delta\Phi(0)/\partial(1/T)$ [62], a space charge potential of 0.44 V (presented in Section 4.6), and the measured 1.50 eV activation energy, the calculated value of $E_{v\infty}$ is 0.42 eV. This value is smaller than reported values for the bulk (0.7-1.0 eV). At this time, the

source of this discrepancy is unclear, though errors may have been introduced in the space charge potential or the temperature dependence of the barrier height. For example, if the second term in parenthesis in the above equation is zero rather than 0.1 eV, then $E_{v\infty}$ becomes 0.62 eV, in good agreement with the reported migration energy of oxygen vacancies in ceria.

In Section 4.6 below, it is proposed that the space charge potential after annealing is decreased to 0.35 V. Performing the same calculation as above using a value of 0.42 eV for $E_{v\infty}$, the expected activation energy is 1.32 eV, which is in reasonable agreement with the observed value of 1.28 eV in Table 6.

A similar analysis can be performed for the activation energy associated with electronic conduction. Hwang and Mason reported a value of 1.39 eV and analyzed its meaning according to bulk defect chemistry. Using separate thermopower measurements to determine $\Delta H_R$, the authors used Eq. 19 to determine $E_H$, which was found to be in reasonable agreement with literature reports [24]. In contrast, Kim and Maier reported a value of 1.9 eV and found it to be in good agreement with literature values using Eq. 79.

The effect of the potential barrier can be applied to electrons in this study via Eq. 79 as well. Using a value of 2.37 eV for $E_{n\infty}$ [38], and the same values as above for $\Delta\Phi(0)$ (0.44 V) and the temperature dependence of $\Delta\Phi$ (0.1 V), the expected $E_A$ for the electronic conductivity is 1.83 eV. This value is higher than the measured value of 1.24 eV. If the space charge potential decreases to 0.35 V after annealing, then the expected activation energy would be increased to 1.92 eV. Experimentally, $E_A$ increases to 1.46 eV after annealing with no diffusion source, but $E_A$ decreases to 1.09 eV after annealing with NiO or $Gd_2O_3$. Overall, the fit of the experimental $E_A$ data for the electronic conductivity is not in good agreement with the space charge predictions. The measured activation energies are approximately 0.5 eV lower than the predicted values. This could, in principle, be attributed to a larger potential barrier than is presented here. However, the experimental values are in better agreement with the value of 1.39 eV, reported in Ref. 57.

The activation energies of the samples annealed at 800°C with no diffusion source are of note. While the activation energy of the total conductivity decreases from 1.33 to 1.12 eV after annealing in the presence of NiO or $Gd_2O_3$, it increased to 1.46 eV after annealing with no diffusion source. This is attributed to a fundamental change in the ionic transference number unique to these samples. As shown in Table 5 $t_{ion}$ increases to 0.76, indicating predominant ionic conduction. Correspondingly,

the activation energies of the total and ionic conductivities, 1.46 and 1.50 eV, respectively, are similar because the total conduction is dominated by the ionic component.

### *4.6 Data Analysis using the Space Charge Model*

In Section 1.4, the Goup-Chapman and Mott-Schottky space charge models were introduced. A comparison of carrier profiles in the space charge region was presented in Figure 11. In the Gouy-Chapman model, the majority acceptor impurity is assumed to be sufficiently mobile to redistribute in response to the space charge potential. The enhancement and depletion of carriers is very large near the interface, but the spatial extent of the affected region is limited to approximately twice the Debye length. In the Mott-Schottky model, the acceptor impurity is assumed to be frozen-in due to slow kinetics and cannot redistribute. In this case, the enhancement/depletion of carriers is not as extreme as the Gouy-Chapman model, though still more than two orders of magnitude relative to the bulk equilibrium values. The depletion width is several times greater than the Debye length, as the acceptor impurity can not contribute to the screening of the excess charge in the grain boundary core.

In order to examine the applicability of the space charge models to the experimental data, relationships between the carrier profile equations and the observed electrical conductivity were established. Maier presented a framework with which space charge contributions to the observed conductivity could be modeled [46]. The effect of a grain boundary and the corresponding space charge regions can be understood in terms of the resistance perpendicular to the boundary, $Z^{\perp}$, and the conductance parallel to the space charge layers, $Y^{\parallel}$. This is shown schematically in Figure 96. The widths of the grain boundary core, space charge layer, and grain interior are denoted as $2w$, $2\lambda$, and $d$, respectively.

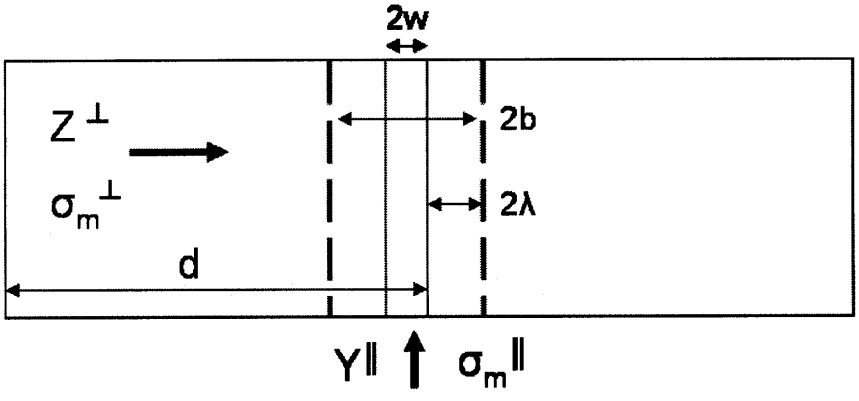


**Figure 96: Schematic diagram of the resistance perpendicular to a boundary and the conductance parallel to it. Adapted from Maier [46].**

For each partial conductivity, denoted above as $\sigma_m$, an effective conductivity of the space charge layer can be defined perpendicular and parallel to the boundary. The derivation in this thesis of the perpendicular and parallel conductivities associated with electrons and oxygen vacancies is presented in Appendix A for both the Gouy-Chapman and Mott-Schottky models. The relevant expressions for each partial conductivity are summarized for the Gouy-Chapman case:

$$\sigma_{el}^{\perp,G-C} = \frac{\sigma_\infty}{\frac{2\Theta}{\Theta+\exp(2)}+1-\frac{2\Theta}{\Theta+1}} \tag{80}$$

$$\sigma_{el}^{\parallel,G-C} = \sigma_\infty\left(1-\frac{2\Theta}{\exp(2)-\Theta}+\frac{2\Theta}{1-\Theta}\right) \tag{81}$$

$$\sigma_{ion}^{\perp,G-C} = \sigma_\infty\left(\frac{\Theta\left[2\Theta^2+3\Theta\exp\left(\frac{8}{3}\right)+3\exp\left(\frac{16}{3}\right)\right]}{\left(\Theta+\exp\left(\frac{8}{3}\right)\right)^3}+1-\frac{\Theta\left[2\Theta^2+3\Theta+3\right]}{(\Theta+1)^3}\right)^{-1} \tag{82}$$

$$\sigma_{ion}^{\parallel,G-C} = \sigma_\infty * \left(1-\frac{\Theta\left[2\Theta^2-3\exp\left(\frac{8}{3}\right)\Theta+3\exp\left(\frac{16}{3}\right)\right]}{\left[\exp\left(\frac{8}{3}\right)-\Theta\right]^3}+\frac{\Theta\left[2\Theta^2-3\Theta+3\right]}{\left[1-\Theta\right]^3}\right) \tag{83}$$

Where $\sigma_\infty$ is equal to the partial conductivity in the bulk and $\Theta$ is the profile parameter, defined in Eq. 41. The corresponding relations for the Mott-Schottky conditions are:

$$\sigma_{el}^{\perp,M-S} = \frac{\sigma_\infty \lambda^*}{\sqrt{\pi}(\lambda)erf\left(\frac{\lambda^*}{2\lambda}\right)} \tag{84}$$

$$\sigma_{el}^{\parallel,M-S} = \frac{\sigma_\infty \sqrt{\pi}(\lambda)erfi\left(\frac{\lambda^*}{2\lambda}\right)}{\lambda^*} \tag{85}$$

$$\sigma_{ion}^{\perp,M-S} = \frac{\sigma_\infty \lambda^*}{1.25331(\lambda)^* erfi\left(0.707107\frac{\lambda^*}{\lambda}\right)} \tag{86}$$

$$\sigma_{ion}^{\parallel,M-S} = \frac{\sigma_\infty {}^*1.25331(\lambda)^* erf\left(.707107\frac{\lambda^*}{\lambda}\right)}{\lambda^*} \tag{87}$$

The overall partial conductivity is obtained as a weighted average of the bulk and boundary contributions, expressed by the boundary fraction $\varphi_{GB}$ [46]:

$$\sigma_m = \frac{\sigma_\infty \sigma_{gb}^{\perp} + (2/3)\varphi_{gb}\sigma_{gb}^{\parallel}\sigma_{gb}^{\perp}}{\sigma_{gb}^{\perp} + (1/3)\varphi_{gb}\sigma_\infty} \tag{88}$$

In order to calculate $\sigma_\infty$, the mobilities and bulk concentration of each carrier must be known. In his work on space charge modeling, Tschöpe [61] utilized existing mobility data for electrons from Tuller [152] and his own experimental results [60] for oxygen vacancies:

$$\mu_e(T) = \frac{3.9x10^2 \frac{cm^2 K}{Vs}}{T}\exp\left(-\frac{0.4\,eV}{kT}\right) \tag{89}$$

$$\mu_{V_O^{\bullet\bullet}}(T) = \frac{1.5x10^2 \frac{cm^2 K}{Vs}}{T}\exp\left(-\frac{0.71\,eV}{kT}\right) \tag{90}$$

Since the experimental conditions in this study fall within the extrinsic regime, the oxygen vacancy concentration is determined simply by the Brouwer approximation: $[A_{Ce}'] = 2[V_O^{\bullet\bullet}]$. The majority impurity acceptor was identified via DC plasma emission spectroscopy to be Al at a concentration of 1700 ppm [161]. Given knowledge of $\Delta H_R$, which was reported by Tuller and Nowick [26], and the oxygen vacancy concentration, the electron concentration in the bulk can be calculated using Eq. 18. Now the integrated space charge profiles can be used to calculate the expected electrical conductivity. The required input parameters are the grain size, $\Delta\Phi$, T, and $pO_2$.

First, the data resulting from the as-deposited samples was analyzed using the Mott-Schottky model. As discussed in the literature, the relatively low temperatures associated with the re-oxidation (600°C) and measurement (highest temperature: 550°C) in this study make it unlikely that the $Al_{Ce}'$ defects are sufficiently mobile to redistribute [62, 78]. The goodness-of-fit in all cases was gauged by the $t_{ion}$

generated from the model. In all cases, the absolute values of the conductivity predicted from the space charge model are typically 3 orders of magnitude lower than the measured value, as shown in Table 7. The source of this discrepancy is unclear, but the mobility data quoted from Refs. 60 and 152, measured from bulk specimens, may not be accurate in the thin film form. In order to verify whether or not errors had been made in the integrated space charge calculations, the computed profiles were compared to previous results by Tschöpe [61]. The profiles from Ref. 61 and this work were in good agreement. It is inferred that the computed values of Tschöpe were likewise lower than experimental values, and that the author based his goodness-of-fit on the ability to "reproduce the essential experimental results," rather than a match of the absolute value of the conductivity [61].

For the conditions of T = 475°C, $pO_2$ = 0.21 atm, and a grain size of 35 nm, the best fit to the experimental data occurs for $\Delta\Phi$ = 0.44 V. This is the value that yields $t_{ion}$ = 0.34, the experimental transference number. The calculated values and experimental results are shown in Table 7. On average, the model predicts values 4200x lower than what is measured; the factor by which they are different is similar for each partial conductivity. Thus, the calculated conductivities from the space charge models will be used in this study only for the purpose of comparison, not for absolute prediction of the observed conductivity. As such, all values obtained from the calculated profiles will be normalized by the factors shown in Table 7.

| Conductivity | Experimental data: as-deposited (S/cm) | Mott-Schottky model: 35 nm, $\Delta\Phi$= 0.44 V (S/cm) | Difference |
|---|---|---|---|
| Total | $2.30\text{x}10^{-5}$ | $5.36\text{x}10^{-9}$ | 4291x |
| Ionic | $7.96\text{x}10^{-6}$ | $1.81\text{x}10^{-9}$ | 4398x |
| Electronic | $1.45\text{x}10^{-5}$ | $3.56\text{x}10^{-9}$ | 4073x |

**Table 7: Comparison of the measured conductivity values in the as-deposited state compared to the best-fit values from the Mott-Schottky model for $t_{ion}$ = 0.34. Shown also is the factor by which the experimental values are larger.**

A diagram of the corresponding carrier profiles is shown in Figure 97. In the bulk, it can be seen that the concentration of electrons is more than 7 orders of magnitude lower than oxygen vacancies. In the vicinity of the grain boundary, however, the electrons are the dominant charge carrier. This is in fundamental agreement with the previous studies of nanocrystalline ceria, in which the contribution

from electronic species is greatly enhanced relative to the bulk [37, 57, 58, 61, 62]. In addition, the estimated space charge potential of 0.44 V is in reasonable agreement with previous reports in ceria, in which values of 0.3 [62] and 0.55 [61] were identified. However, it must be recalled that the space charge potential is not a materials parameter, and could thus vary between specimens of the same material.

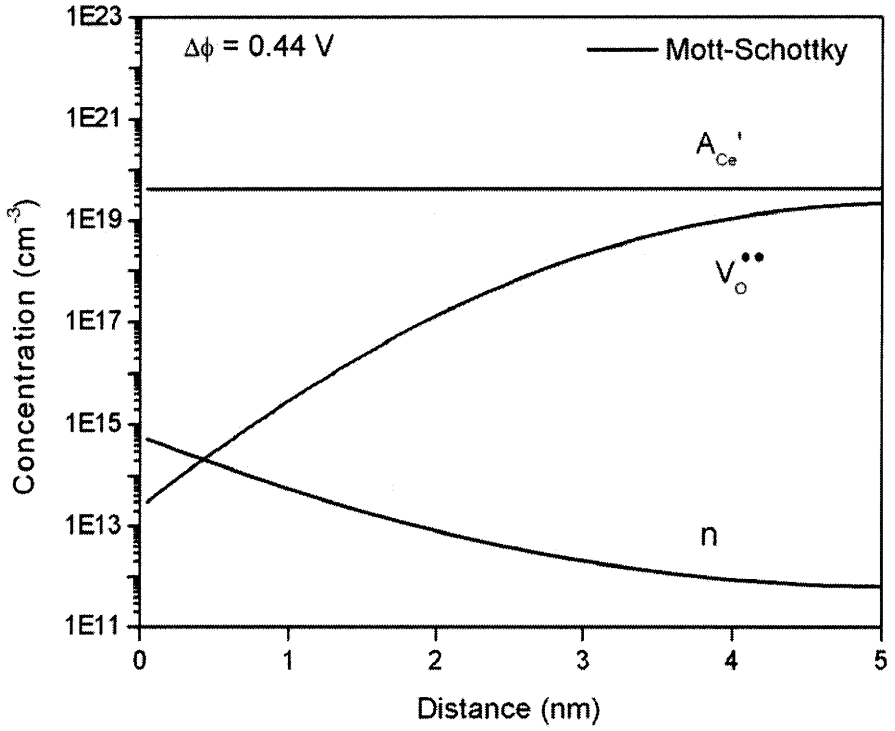


**Figure 97: Space charge profiles in $CeO_2$ at T = 475°C and $pO_2$ = 0.21 atm. The profiles were generated via the Mott-Schottky model for a space charge potential of 0.44 V.**

In order to consider possible mechanisms by which both the ionic and electronic partial conductivity could decrease, the previous assumptions regarding the space charge properties are revisited. Specifically, the acceptor impurity profiles were assumed to be spatially-invariant due to slow kinetics at low temperatures. However, at elevated temperatures, there are two driving forces for redistribution of the $Al_{Ce'}$ defect: (1) the electrostatic interaction with the positively-charged grain boundary and (2) segregation to the grain boundary due to lattice mismatch effects [162]. Thus, the differences between the as-deposited specimens and those annealed at temperatures of 700 or 800°C could conceivably be understood as differences in the Mott-Schottky (as-deposited) and Gouy-Chapman (annealed) models. Since it is known that the grain size after annealing increased to approximately 75 nm, Gouy-Chapman profiles were integrated using the same conditions as above, including the 0.44 V space charge potential. The results of the Gouy-Chapman model are compared

with the Mott-Schottky values in Table 8. A plot of both models in found in Figure 98.

| Conductivity | Mott-Schottky model: 35 nm, $\Delta\Phi$= 0.44 V (S/cm) | Gouy-Chapman model: 75 nm, $\Delta\Phi$= 0.44 V (S/cm) | G-C lower by |
|---|---|---|---|
| Total | $2.24 \times 10^{-5}$ | $1.57 \times 10^{-6}$ | 14x |
| Ionic | $7.94 \times 10^{-6}$ | $4.87 \times 10^{-9}$ | 1630x |
| Electronic | $1.45 \times 10^{-5}$ | $1.56 \times 10^{-6}$ | 9x |

**Table 8: Comparison of predicted conductivities, normalized by the data presented in Table 7, for the Mott-Schottky and Gouy-Chapman models for $\Delta\Phi$ = 0.44 V and grain sizes of 35 and 75 nm, respectively.**

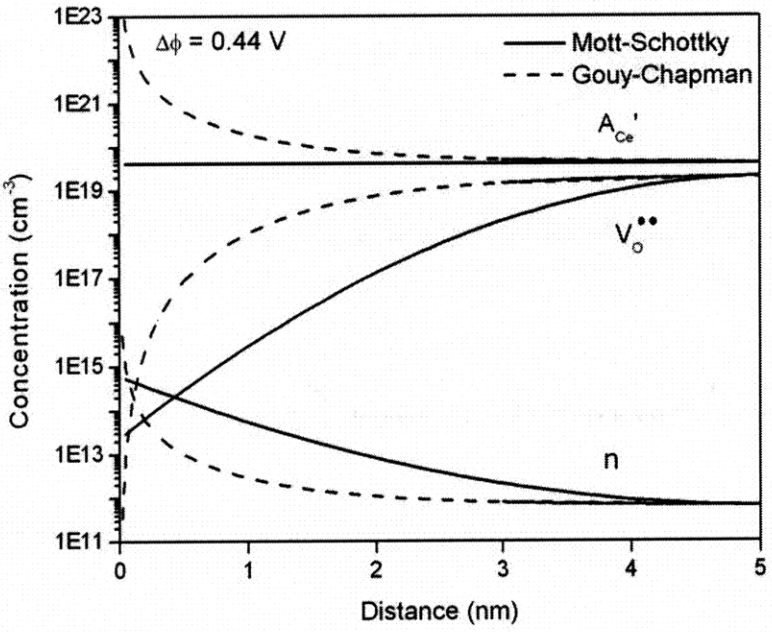


**Figure 98: Mott-Schottky and Gouy-Chapman space charge profiles at T = 475°C and $pO_2$ = 0.21 atm, for a space charge potential of 0.44 V.**

It can be seen in Table 8 that the total and electronic conductivity are predicted to decrease by approximately one order of magnitude as a shift from Mott-Schottky conditions at 35 nm to Gouy-Chapman conditions at 75 nm for the same space charge potential. In contrast, the ionic conductivity is predicted to decrease by 3 orders of magnitude.

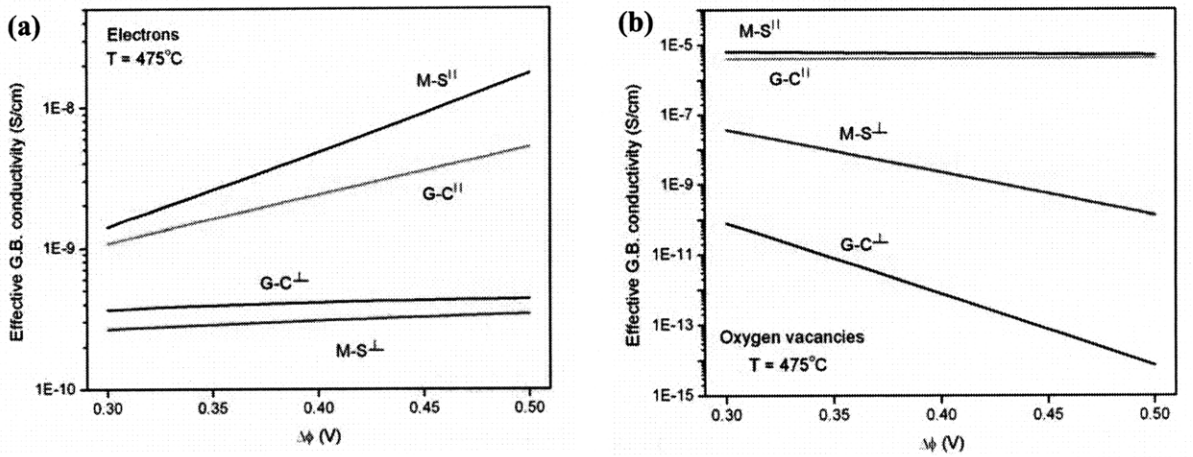


**Figure 99: Calculated effective grain boundary conductivities for transport parallel and perpendicular to the grain boundary for the Mott-Schottky and Gouy-Chapman models. Results for (a) electrons and (b) oxygen vacancies are shown. The calculations were performed for T = 475°C, $pO_2$ = 0.21 atm, and $[A_{Ce}']$ = 1700 ppm for space charge potentials of 0.3 to 0.5 V.**

Qualitatively, these trends can be understood by examination of the profiles shown in Figure 98. The integrals of the electron profiles, which are straightforward to visualize as the parallel contribution to the conductivity, decrease from the Mott-Schottky case to Gouy-Chapman. This is reinforced in Figure 99a, which shows the effective electron conductivities parallel and perpendicular to the grain boundary for both the Mott-Schottky and Gouy-Chapman models. Because the electrons are accumulated in the space charge region, the differences between the parallel and perpendicular contributions are a little more than tenfold in the $\Delta\Phi$ region of interest. The same cannot be said for the oxygen vacancies because they are depleted in the space charge region. The oxygen vacancies integral appears to increase in the Gouy-Chapman case; the crucial effect, however, is the deeper depletion occurring near $x = 0$. As stated above, Gouy-Chapman conditions result in more extreme enhancement/depletion over a small length. In Figure 99b, it can be seen that the parallel conductivities resulting from both models are comparable in the case of oxygen vacancies. However, the more extreme depletion resulting from Gouy-Chapman adjacent to the grain boundary results in an effective perpendicular conductivity that is 3 orders of magnitude lower than the Mott-Schottky model. The serial resistance associated with the deeper depletion of oxygen vacancies, though limited in spatial extent, is sufficient to markedly decrease the overall ionic conductivity.

While the transition from the Mott-Schottky to Gouy-Chapman model is in agreement with the experimental observation that both the ionic and electronic partial conductivities decrease after annealing, the magnitude of each shift is not consistent. This can be seen by a comparison of the magnitude of the total and partial conductivities for each processing condition, shown in Figure 100.

It can be seen that after annealing at 800°C with NiO or no dopant, all 3 conductivities decrease, as discussed above. The results from the Gouy-Chapman model for a grain size of 75 nm and $\Delta\Phi = 0.44$ V demonstrate the extreme depression of the ionic conductivity, and the fact that it does not agree well with the measured results.

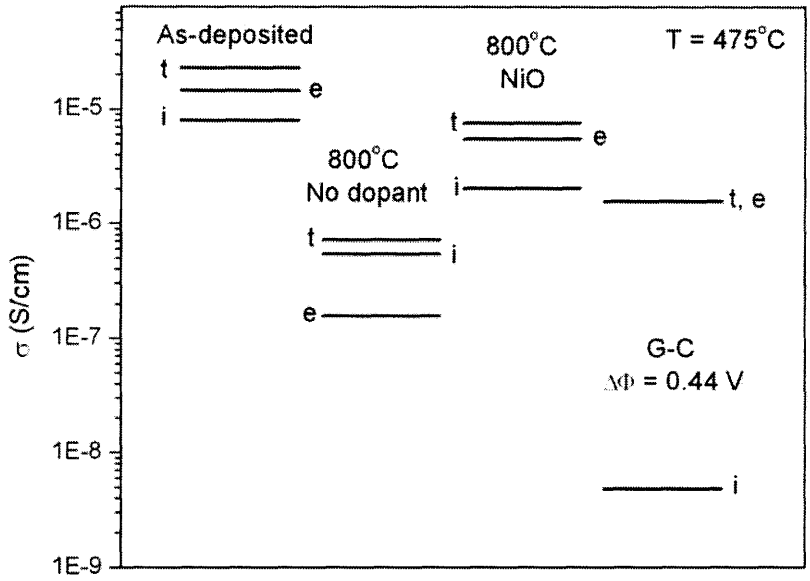


**Figure 100: Plot of the total (t), ionic (i), and electronic (e) conductivities at T = 475°C and $pO_2$ = 0.21 atm for the various processing conditions. Also shown are the calculated values from the Gouy-Chapman model for a grain size of 75 nm and $\Delta\Phi = 0.44$ V.**

An improved fit to the experimental data is obtained if the space charge potential is varied. In this case, the goodness-of-fit was gauged by $t_{ion}$ = 0.26, an average value for the NiO and $Gd_2O_3$ in-diffused specimens. The best fit was obtained with a space charge potential of 0.35 V, as shown in Figure 101. As stipulated by the fitting, the agreement of the partial conductivities of the NiO-diffused samples and the calculated results relative to the total conductivity is reasonable. The magnitude of the calculated conductivities is lower than the experimental values by approximately a factor of 6. The magnitude of the calculated values is in better agreement with the annealing data with no diffusion source, though the sample was found to be predominantly ionic, not electronic.

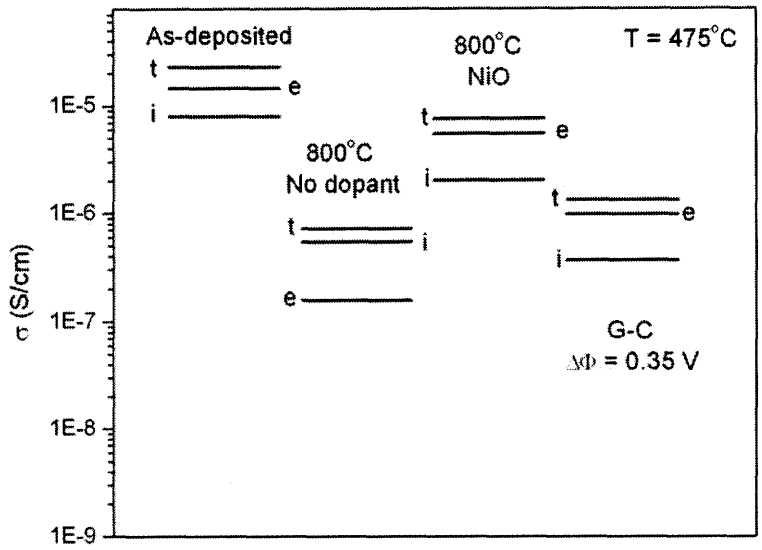


**Figure 101: Plot of the total (t), ionic (i), and electronic (e) conductivities at T = 475°C and $pO_2$ = 0.21 atm for the various processing conditions. Also shown are the calculated values from the Gouy-Chapman model for a grain size of 75 nm and ΔΦ = 0.35 V.**

The closest analytical description of the experimental data occurs for the Mott-Schottky model with a grain size of 35 nm and ΔΦ = 0.44 V in the as-deposited state, and the Gouy-Chapman model with a grain size of 75 nm and ΔΦ = 0.35 V after annealing in the presence of a diffusion source. After annealing, it is evident that both the ionic and electronic partial conductivites decrease, which is inconsistent with a shift in the space charge potential alone. If the acceptor impurities are assumed to be sufficiently mobile to redistribute at temperatures of 700°C and above, the Gouy-Chapman model correctly predicts a decrease of both partial conductivities, though not in the correct proportion. The agreement with the experimental data is markedly improved if the space charge potential is decreased from 0.44 to 0.35 V as a result of heterogeneous doping.

To check the feasibility and consistency of this model, the proposed change in the space charge potential is examined in terms of dopant cation in the grain boundary. The space charge potential is related to the grain boundary charge per unit area as [163]:

$$\Delta\phi = \frac{Q_{core}^2}{8\varepsilon_O \varepsilon_r c_\infty e} \tag{91}$$

For a space charge potential of 0.44 V and $[A_{Ce}']= 4.29x10^{19}$ $cm^{-3}$, $Q_{core}$ is:

$$Q_{core} = \left[0.44V * 8 * 25 * 8.85x10^{-14} C/(V-cm) * 1.6x10^{-19} C * 4.29x10^{19} cm^{-3}\right]^{1/2} \tag{92}$$

$$Q_{core} = 7.31x10^{-20}\frac{C}{nm^2} \tag{93}$$

The proposed space charge potential after annealing is 0.35 V. Combining the top equations yields

$$\frac{0.44\,V}{0.35\,V} = \frac{Q^2_{core,before}}{Q^2_{core,after}} \tag{94}$$

and correspondingly,

$$Q_{core,after} = 6.52x10^{-20}\frac{C}{nm^2} \tag{95}$$

The difference between the initial and final core charge values is approximately $8x10^{-21}$ C/nm$^2$. Assuming an acceptor with a valance of +3, the charge associated with each substitutional defect is $ze$ = $1.6x10^{-19}$ C. If these acceptors are the source of the decrease in charge, then the corresponding number of acceptors per unit area is 0.05 nm$^{-2}$ or $5x10^{12}$ cm$^{-2}$. The number of Ce sites (in the bulk) is $8.6x10^{14}$ ions/cm$^2$. The doping density is thus 0.6%. If the acceptor has a valance of +2, the doping density will be less. This concentration lies below the detection limit of TEM, which is typically ~ 1%. Thus, the proposed decrease of the space charge potential from 0.44 to 0.35 V could be achieved with a doping density smaller than the detection limit of TEM. This conclusion is consistent with the experimental observation (or lack thereof) that Ni was not detected in the grain boundary region by TEM after in-diffusion.

In this model, the structure of the grain boundary region is assumed to be similar to the bulk. The acceptor ions such as Ni, Gd, and Mg are presumed to sit on Ce sites as a defect such as $A_{Ce}'$ or $A_{Ce}''$. While this is of course a simplification, it is not without precedent in the literature. Avila-Paredes and Kim reported the addition of a small concentration (~ 0.5 cation%) of transition metal cations by a solid state synthesis route on the properties of bulk microcrystalline $Ce_{0.99}Gd_{0.01}O_{2-x}$ [164]. It was observed that, while the transition metal cation had no effect on charge transport in the bulk, the addition of cations such as Co and Fe led to a tenfold decrease of the grain boundary resistivity. The authors found that the impurities segregated to the triple point junctions and reported that the space charge potential decreased by as much as 20% in the case of Fe. This was attributed to the introduction of negative charge in the form of ionized acceptors into the grain boundary core. It should be noted that the proposed shift in space charge potential from 0.44 to 0.35 V is virtually the same amount as was reported in Ref. 164.

As stated above, this model is proposed as the best fit to the experimental data recorded in this study. Its predictions are in reasonable agreement with the experimental data, and the two primary mechanisms of change: defect segregation to grain boundaries at elevated temperatures and decrease of the space charge potential due to grain boundary doping with acceptor cations, have precedent in the literature [162,164]. It should be noted though, that there are several experimental observations that remain unexplained. The reason for the shift in the $pO_2$ dependence of $\sigma_{ion}$ from 0 to -0.13 is unclear. This problem is compounded by the overall lack of understanding of the $pO_2$ dependence of the space charge potential. In principle, a $pO_2$-dependent $\Delta\Phi$ could lead to variations in $\sigma_{ion}$, though it is unknown why this would occur only after annealing at 700°C or above. Through measurement of a "small but significant deviation" in the ratio of grain boundary-to-bulk resistance, De Souza and co-workers suggested minor changes in $\Delta\Phi$ in Fe:$SrTiO_3$ with $pO_2$ [165]. In contrast, Kim and Maier reported, based on capacitance measurements in CGO-0.3%, that $\Delta\Phi$ was not dependent on $pO_2$ [62]. Further studies are clearly warranted in this regard. The negative $pO_2$ dependence of $\sigma_{ion}$ could conceivably result from a change in oxidation state of the grain boundary dopants. While Ni sitting in the grain boundary core could indeed change valance from 2+ to 3+ in this partial pressure range [166], both Gd and Mg are expected to remain 3+ and 2+, respectively.

### *4.7 Influence of the Film/Substrate Interfacial Layer*

Another experimental result that is puzzling is the difference between the behavior of the samples annealed at 800°C with no diffusion source and those in-diffused with Ni or Gd from the surface. The change in $\sigma_{ion}$ is quite consistent for both types of processing. However, the change in $\sigma_{el}$ is not. As shown in Figure 93, $\sigma_{el}$ decreases by 2 orders of magnitude from the as-deposited state after annealing with no diffusion source. The conductivity decrease is less if in-diffused with Ni or Gd, and the $pO_2$ dependence decreases to -0.11. Since in-diffusion technically occurs for all samples, due to the motion of cations emanating from the substrate as described above, it is difficult to understand the physical and chemical differences between samples annealed with or without a diffusion source.

Another important consideration in the study of thin film materials is the film/substrate interface. As discussed by Gregori and co-workers, this interface, despite its limited spatial extent of a few nm at most, may be sufficiently conductive to contribute to the measured conductivity in ceria systems [167]. This phenomenon is shown schematically in Figure 102:

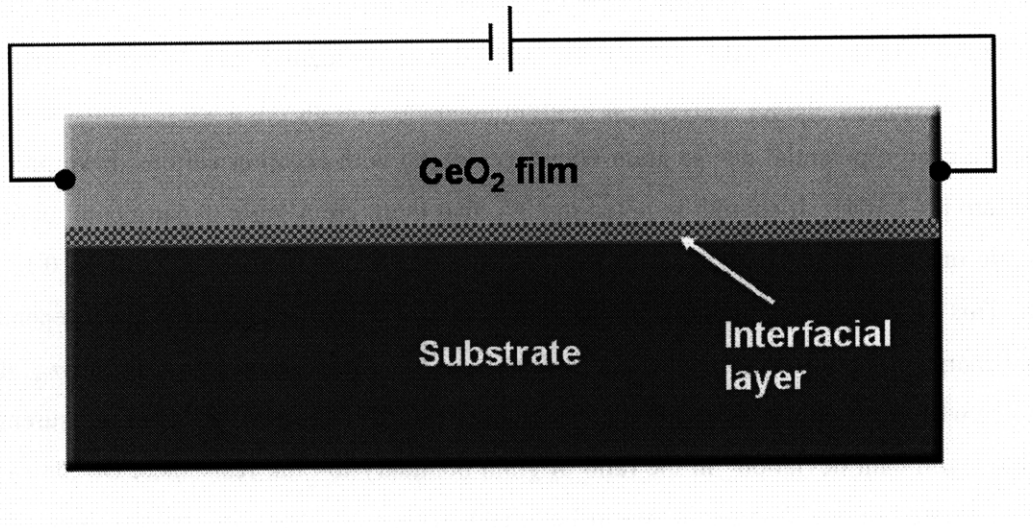


**Figure 102: Schematic diagram of an in-plane electrical measurement. An interfacial layer exists between the $CeO_2$ film and the substrate; this layer serves as a parallel resistor to the $CeO_2$ layer.**

The $CeO_2$ film and the interfacial layer act as resistors in parallel, so that

$$\frac{1}{R_{total}} = \frac{1}{R_{CeO2}} + \frac{1}{R_{interface}} \tag{96}$$

and conversely

$$Y_{total} = Y_{CeO2} + Y_{interface} \tag{97}$$

where $Y$ is conductance. It has previously been proposed that this interfacial layer can be the source of enhanced conductivity, for example in epitaxial thin film YSZ [82, 83] and in doped ceria [167]. This is manifested in a dependence of the conductivity on film thickness, which increases as the thickness decreases. The electrical conductivity of samples in the as-deposited state, as well as annealed at 800°C with no dopant and with NiO is shown in Figure 103 as a function of film thickness:

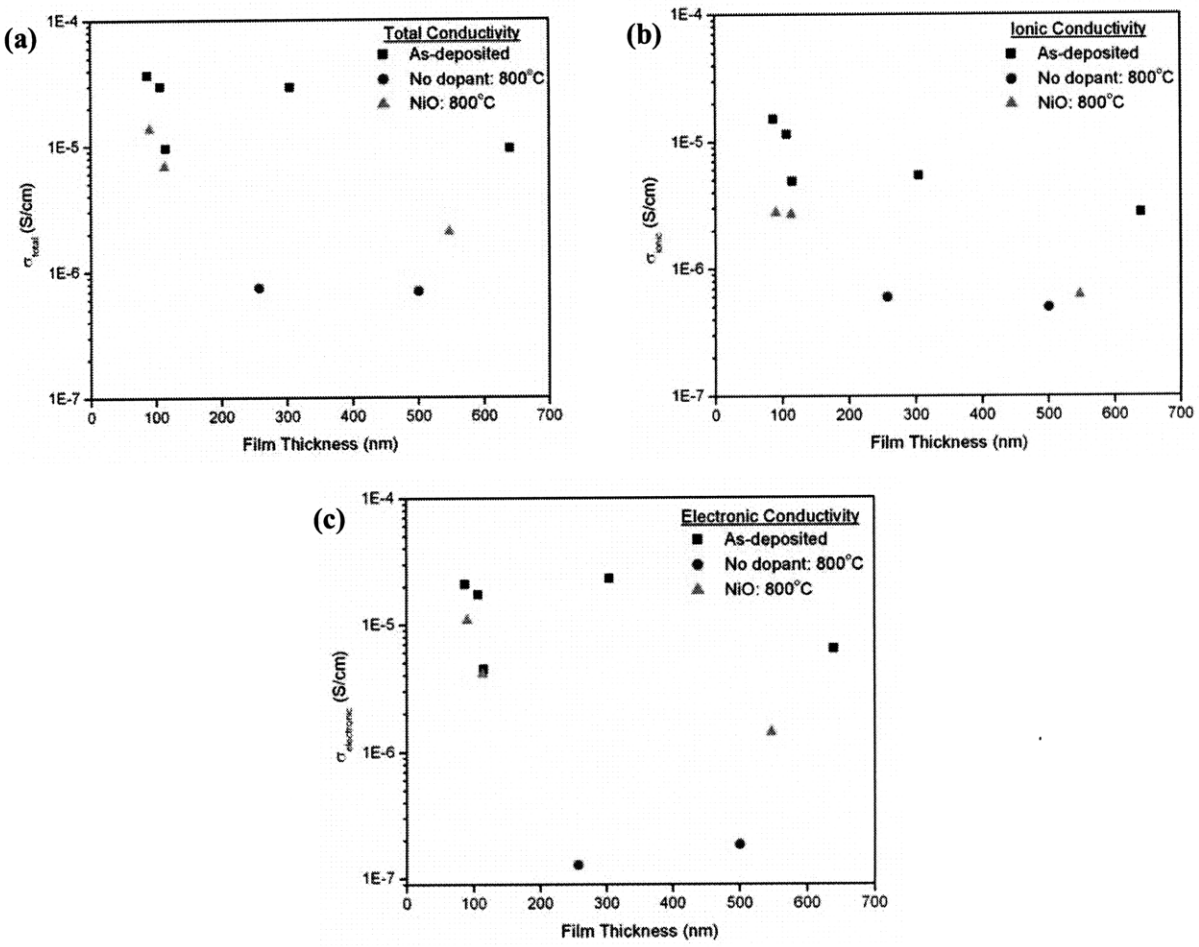


**Figure 103: Total conductivity (a), ionic conductivity (b) and electronic conductivity (c) vs. film thickness for as-deposited samples (■) and samples annealed at 800°C with no diffusion source (●) and with NiO (▲).**

Though there is considerable scatter in the data as evidenced by the error bars in Figure 104 below, particularly for the as-deposited specimens, the electrical conductivity does indeed appear to increase with decreasing film thickness. Since the area normalized conductance of the $CeO_2$ layer is simply the product of the conductivity and film thickness Eq. 97 can be re-written as

$$Y_{total} = \sigma_{CeO2}\, t + \Delta Y \tag{98}$$

where $t$ is the film thickness. This expression is linear and a plot of $Y_{total}$ vs. $t$ yields σ as the slope and $\Delta Y$ as the intercept with the Y-axis. Figure 103 has been correspondingly re-plotted as:

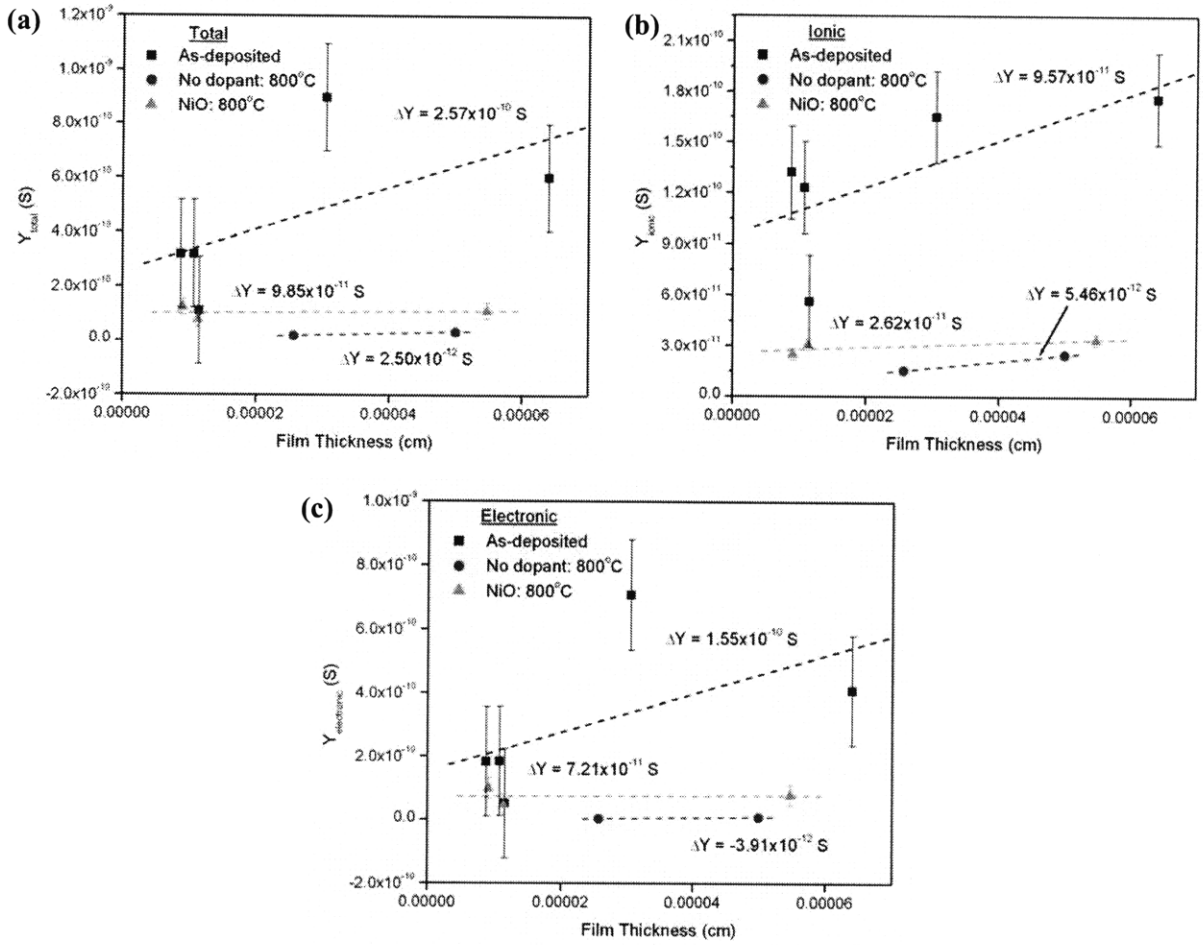


**Figure 104: Total conductance (a), ionic conductance (b) and electronic conductance (c) vs. film thickness for as-deposited samples (■) and samples annealed at 800°C with no diffusion source (●) and with NiO (▲). The error bars represent the standard error.**

If there were no interfacial contribution to the measured conductance, then the Y-intercept would be zero. With the exception of the electronic conduction in Figure 104c, the Y-intercepts are positive non-zero values. For example, $\Delta Y$ in the as-deposited case is on the order of $10^{-10}$ S. If a space charge width of 1 nm (consistent with Gouy-Chapman calculations) is assumed, the corresponding conductivity of this interfacial layer is on the order of $10^{-3}$ S/cm, which is approximately two orders of magnitude more conductive than the rest of the ceria film. Thus, while the thickness of this interfacial layer is much less than the ceria film, the higher conductivity associated with this layer implies that a non-trivial parallel contribution may be present. The key parameters, the conductivity (slope) and $\Delta Y$ (intercept), are summarized in Table 9. The percentage decrease from the as-deposited state for both parameters is shown in Table 10 after annealing at 800°C with no diffusion source and with NiO.

| | | Slope (σ, S/cm) | Y-Int (ΔY, S) |
|---|---|---|---|
| **Total** | As-deposited | $7.71 \times 10^{-6}$ | $2.57 \times 10^{-10}$ |
| | No dopant: 800°C | $6.46 \times 10^{-7}$ | $2.50 \times 10^{-12}$ |
| | NiO: 800°C | $2.26 \times 10^{-7}$ | $9.85 \times 10^{-11}$ |
| **Ionic** | As-deposited | $1.38 \times 10^{-6}$ | $9.57 \times 10^{-11}$ |
| | No dopant: 800°C | $3.87 \times 10^{-7}$ | $5.46 \times 10^{-12}$ |
| | NiO: 800°C | $1.40 \times 10^{-7}$ | $2.62 \times 10^{-11}$ |
| **Electronic** | As-deposited | $6.08 \times 10^{-6}$ | $1.55 \times 10^{-10}$ |
| | No dopant: 800°C | $2.45 \times 10^{-7}$ | $-3.01 \times 10^{-12}$ |
| | NiO: 800°C | $7.83 \times 10^{-8}$ | $7.21 \times 10^{-11}$ |

**Table 9: The slope (σ) and Y-intercept (Δ*Y*) values for the total, ionic, and electronic conduction processes, extracted from Figure 104a-c.**

| | | Slope (σ, S/cm) | Y-Int (Δ*Y*, S) |
|---|---|---|---|
| **Total** | No dopant: 800°C | -92% | -99% |
| | NiO: 800°C | -97% | -62% |
| **Ionic** | No dopant: 800°C | -72% | -94% |
| | NiO: 800°C | -90% | -73% |
| **Electronic** | No dopant: 800°C | -96% | -102% |
| | NiO: 800°C | -99% | -53% |

**Table 10: Percentage change in the slope (σ) and Y-intercept (Δ*Y*) values from the as-deposited state, for the total, ionic, and electronic conduction processes. The percentage change was calculated as [slope or Y-Int (NiO) – slope (as-deposited)] / slope (as-deposited) x 100.**

First, it must be emphasized that these values are susceptible to considerable error, as shown by the error bars in Figure 104, as well as the small number of data points for the samples annealed with no diffusion source (2 points) and NiO (3 points). It is perhaps more appropriate to consider these data as trends and not as absolute values. Nevertheless, several interesting observations arise. First, the slope ($\sigma$) decreases after any sort of annealing at 800°C, in agreement with the data above. Second, it can be seen in Table 9 that the Y-intercept ($\Delta Y$) also decreases after annealing, though the decrease is consistently greater after annealing with no diffusion source. This trend is reinforced in Table 10, in which the percent decrease from the as-deposited state is shown. In the case of all 3 conductivities,

annealing at 800°C with no diffusion source resulted in a greater decease in $\Delta Y$ than in $\sigma$. Conversely, the decrease in $\sigma$ in the NiO in-diffused specimens is noticeably stronger than the decrease in $\Delta Y$. These observations suggest that the mechanism of the measured decrease in conductivity is distinct, depending on whether or not a surface diffusion source is present. In the case of NiO in-diffusion, contribution of the interfacial layer to the conductance decrease is less than the contribution of the ceria film. With no diffusion source, the two contributions are similar, with the interfacial layer being particularly more relevant for the ionic process.

The local mechanisms responsible for such trends are unclear. It was shown in Section 4.2 that the transport of Ni along grain boundaries is faster than Mg (and presumably Al from the sapphire substrates) by more than one order of magnitude. Therefore, for the samples annealed in the presence of NiO, the proposed variations due to defect segregation and grain boundary doping with Ni are likely to be the primary factors in the conductivity decrease. If the grain boundaries possess a limited solubility for aliovalent cations, then it is possible that Mg diffusion is inhibited by the presence of the faster Ni species, which may saturate the grain boundaries. Without a surface diffusion source, the magnitude of $D_{GB}$ (Mg) is still sufficiently high for Mg to diffuse along the grain boundaries and affect the space charge potential. However, the increased motion of Mg may also affect the interfacial layer to a greater extent than the case where it is inhibited by Ni. While this is simply a hypothesis based on limited data, it is supported by an important experimental observation. In Figure 91 and Figure 93, the total and electrical conductivities decrease regardless whether or not a surface diffusion source is present. In both cases, however, the $pO_2$ dependence of the samples annealed with no dopant is more similar to the as-deposited $pO_2$ dependence. After annealing with NiO or $Gd_2O_3$ on the surface, the $pO_2$ dependence of $\sigma_{total}$ and $\sigma_{el}$ changes. This may suggest that the changes associated with surface diffusion sources are caused by fundamental changes in the film properties, whereas the changes associated with no diffusion source are affected to a greater degree by a highly-conductively space charge layer at the film/substrate interface. Experiments are proposed in Section 5.2 that may assist in the verification of this hypothesis.

# CHAPTER 5. CONCLUSIONS

## *5.1 Summary*

This dissertation explored nano-ionic effects in cerium oxide thin films, and in particular, the concept of nano-ionic control by modulation of the space charge potential. This research direction was motivated both by scientific and technological driving forces. Scientifically, nano-ionic materials are of interest because of the unusual physical and transport properties that are not observed in the microcrystalline state. The nanocrystalline cerium oxide system has been studied, though primarily in the bulk form. Space charge models have been applied to understand the effect of grain size on transport, though few studies have been undertaken to control the nano-ionic properties. From a technological point-of-view, there are intense efforts underway in order to develop materials with improved electrical and electrochemical properties for solid oxide fuel cell operation at reduced temperatures. With an increase in the amount of internal interfaces that may be conducive to ionic transport, nano-ionic materials are widely considered to be promising candidates for next-generation SOFC designs, particularly in micro-SOFCs. A prominent example is a recent report of YSZ/$SrTiO_3$ ionic heterostuctures, in which the ionic conductivity was found to be 8 orders-of-magnitude greater than bulk YSZ [168]. However, the mechanism responsible for such enhanced performance remains unclear.

Nanocrystalline $CeO_2$ thin films with a columnar microstructure were grown by pulsed laser deposition. Thin diffusion sources of NiO and $Gd_2O_3$ were deposited on the surface and annealed in the temperature range of 700-800°C in order to drive-in the dopant cations exclusively along grain boundaries. Time-of-flight secondary ion mass spectrometry (ToF-SIMS) was utilized to measure the diffusion profiles. One diffusion mechanism was observed, which was identified as grain boundary diffusion. The constant source solution to the diffusion equation was applied to the depth profiles, and values of $D_{GB}$ on the order of $10^{-15}$ to $10^{-13}$ $cm^2/s$ were obtained. Based on these values, the annealing conditions that were chosen resulted in diffusion of Ni and Gd along the grain boundary region only, with no modification of the $CeO_2$ bulk. Likewise, Mg in-diffusion along the grain boundaries, originating from the MgO substrate, was also detected and characterized.

Microstructured Pt electrodes were prepared by photolithography and sputter deposition. Electrochemical impedance spectroscopy and two-point DC techniques were used to measure the electrical conductivity of the thin films. The as-deposited samples were slightly more conductive than results reported in the literature, though the activation energy was comparable. The $pO_2$

dependence of the conductivity was in good agreement with previous reports on nanocrystalline ceria. After in-diffusion, the electrical conductivity decreased by approximately one order of magnitude. Microstructured dense YSZ-12/porous Pt blocking electrodes were fabricated in order to deconvolute the electronic and ionic contributions to the total conductivity. The blocking electrodes were validated first theoretically by comparison of the partial electronic conductivity of the YSZ-12 blocking layer with the partial ionic conductivity of the $CeO_2$ layer, as well as the geometrical dimensions of the blocking structure.

The blocking electrodes demonstrated that the ionic partial conductivity was $pO_2$-independent in the as-deposited state, and that the $pO_2$ dependence of the electronic partial conductivity was approximately -0.30. Both observations are in good agreement with the theoretical values predicted in the extrinsic regime. The ionic transference number in the as-deposited state was 0.34. After annealing at 700 or 800°C, the ionic conductivity decreased and displayed a $pO_2$ dependence of -0.13, regardless whether or not a surface diffusion source was present. Without a diffusion source, the electronic conductivity decreased by two orders of magnitude; with NiO or $Gd_2O_3$, the decrease occurred by a factor of 3-10, with a decrease in the $pO_2$ dependence. After annealing with no diffusion source, the transference number was 0.76; with NiO and $Gd_2O_3$ sources, the transference number was 0.26.

The experimental data from the as-deposited and annealed processing conditions were considered within the framework of the space charge model. Relationships between the spatial variation of the carrier concentration and the observed electrical conductivity were derived for the Mott-Schottky and Gouy-Chapman models, and values of both the ionic and electronic partial conductivities were predicted. Though the space charge models yield absolute magnitudes of the conductivity that are much less than the experimental values, the models were used to compare trends in the partial conductivities. Since the as-deposited specimens were heated to a maximum of 600°C after deposition, the Mott-Schottky model was chosen to represent this data, since redistribution of the acceptor impurities within the space charge layer was initially deemed unlikely. For a grain size of 35 nm, the best fit to the experimental data occurred for a space charge potential of 0.44 V, in reasonable agreement with literature reports. Since the ionic and electronic partial conductivities decreased after annealing, the alterations could not be attributed solely to a change in the space charge potential. Rather, it is proposed that at the annealing temperatures of 700-800°C, the acceptor impurities redistributed and segregated to the grain boundaries. Such a shift from Mott-Schottky to Gouy-Chapman boundary conditions is associated with a decrease of both partial conductivities,

though a much stronger decrease of the ionic conductivity. The best fit of the Gouy-Chapman model to the annealed data occurs for a space charge potential of 0.35 V, a decrease of 90 mV from the as-deposited state. This decrease is attributed to presence of defects such as $Ni_{Ce}''$ and $Gd_{Ce}'$, introduced in the grain boundary core via heterogeneous doping.

Changes to the observed conductivity were also considered with respect to an interfacial layer at the $CeO_2$—substrate interface with a predicted conductivity as high as $10^{-3}$ S/cm at 475°C. Based on the thickness-dependence of the conductivity, it is believed that this interfacial layer, despite a predicted thickness of only ~ 1 nm, contributes to the observed conduction. After annealing with or without a diffusion source, the conductance of this layer was observed to decrease. However, the contribution of the interfacial layer to the total conductivity decrease was found to be greater in the specimens annealed with no diffusion source, consistent with results of the blocking measurements that demonstrated different $pO_2$ dependencies for the samples annealed with and without a surface diffusion source.

### *5.2 Recommendations for Future Work*

While some questions regarding the properties of nanocrystalline ceria thin films have been answered in this study, many more have been raised. In particular, recommended topics for future study are:

- Measure cation diffusion in the temperature range of 700-800°C, especially for Ni at 750°C and Mg at 800°C, so that the activation energy may be determined. Expand the scope of inquiry to other relevant SOFC cations such as Sr and Co.

- Explore the mechanism of grain boundary diffusion. In this work, it was not possible to determine whether the diffusing cation species traveled in the grain boundary core or along the space charge regions. Through the use of electric fields normal to the boundary, it may be possible to expand or contract the space charge layer. If so, then the measured diffusion profiles would be expected to vary if transport occurred through the space charge layer.

- Improve the design of the blocking electrodes. The current design is susceptible to an alternative current pathway of the YSZ-12/$CeO_2$/gas phase triple phase boundary and subsequent electronic transport in the $CeO_2$ layer. Deactivation of this triple phase boundary by a thin inert layer would simply the blocking analysis.

- Observe the local variation of the space charge potential with electron holography. Electron holography is a powerful TEM-based method in which the interference of two electron beams is used to measure local electric fields in a thin film. In this study, the sample preparation of TEM specimens was not sufficient to ensure an accurate measurement, as the thickness variation across the TEM specimens was too great to allow for a holography measurement.

- Extend the in-diffusion and blocking measurements to other $Ce_{1-x}Gd_xO_{2-x}$ compositions. Through systematic variations of the Gd composition, the bulk ionic and electronic conductivities can be controlled, as well as the space charge width.

- Refine the existing Mott-Schottky and Gouy-Chapman space charge models for ionic solids. The Mott-Schottky and Gouy-Chapman conditions represent two extremes, in which the acceptor impurity concentration is assumed to be either completely immobile or capable of extreme redistribution adjacent to the boundary. A more realistic model would be achieved for an intermediate distribution of the acceptor ions.

- Measure the partial conductivities for samples with systematically-varying thicknesses from 40 to 500 nm. This will yield values for the conductance of the film—substrate interface with improved accuracy, and can be used to corroborate the hypothesis that the impact of the interfacial layer is distinct in samples with and without a diffusion source.

# APPENDIX A. INTEGRATION OF SPACE CHARGE PROFILES

### *A.1 Conduction in Polycrystalline Materials*

A schematic of the transport processes normal to and along the boundary is shown in Figure 96. In considering charge conduction in space charge layers, the resistive contributions perpendicular to the boundary and the conductive contributions parallel must individually be addressed. The following description of these processes was developed by Maier [64]. The total resistance, $Z$, normal to the boundary and the parallel conductance, $Y$, are described by:

$$Z^{\perp} = Z_{\infty}^{\perp} + \Delta Z^{\perp} \tag{A.1}$$

$$Y^{\parallel} = Y_{\infty}^{\parallel} + \Delta Y^{\parallel} \tag{A.2}$$

Where the subscript $\infty$ denotes the bulk and the delta term the space charge region. The total partial conductivity (i.e. ionic or electronic) was derived as:

$$\sigma_m = \frac{\sigma_{\infty}\sigma_{gb}^{\perp} + (2/3)\varphi_{gb}\sigma_{gb}^{\parallel}\sigma_{gb}^{\perp}}{\sigma_{gb}^{\perp} + (1/3)\varphi_{gb}\sigma_{\infty}} \tag{A.3}$$

Where $\sigma_{gb}^{\perp}$ and $\sigma_{gb}^{\parallel}$ represent the perpendicular and parallel conductivities in the space charge region and $\varphi_{gb}$ represents the grain boundary fraction. In practice, $\sigma_{gb}^{\perp}$ and $\sigma_{gb}^{\parallel}$ are effective conductivities of the space charge layer, given as

$$\sigma_{gb}^{\perp} = \frac{d}{\Delta Z^{\perp}} \tag{A.4}$$

$$\sigma_{gb}^{\parallel} = \frac{\Delta Y^{\parallel}}{d} \tag{A.5}$$

where d is the width of the space charge region. In the brick layer model, this is defined as [64]:

$$\varphi_{gb} = 6\frac{d}{grain\ size} \tag{A.6}$$

In this analysis, it is assumed that the carrier mobility is constant throughout the material. The resistance and conductance can then be considered simply by integration of the changes in carrier concentration in the space charge layer:

$$\Delta Z^{\perp} \frac{1}{ze\mu}\int_0^d \frac{dx}{c(x)} \tag{A.7}$$

$$\Delta Y^{\parallel} = ze\mu\int_0^d c(x)dx \tag{A.8}$$

This framework is sufficient to consider the conductivity of electrons and oxygen vacancies perpendicular and parallel to the boundary, for both the Gouy-Chapman and Mott-Schottky models.

### *A.2 Mott-Schottky Solutions*

The carrier profiles under Mott-Schottky conditions are given as [48, 49]:

$$\frac{c_i(x)}{c_{i\infty}} = \exp\left[-\frac{z_i}{z_j}\left(\frac{x-\lambda^*}{2\lambda}\right)^2\right] \tag{A.9}$$

Where $\lambda^*$ is the depletion width:

$$\lambda^* = \lambda\sqrt{\frac{4z_j e}{kT}\Delta\phi(0)} \tag{A.10}$$

Substitution of this relationship into Eqs. A.7 and A.8 yields the following for electrons:

$$\Delta Z^{\perp} = \frac{1}{\sigma_{\infty}}\int_0^{\lambda^*} \frac{1}{\exp\left[\left(\frac{x-\lambda^*}{2\lambda}\right)^2\right]}dx \tag{A.11}$$

$$\Delta Y^{\parallel} = \sigma_{\infty} \int_{0}^{\lambda^*} \exp\left[\left(\frac{x-\lambda^*}{2\lambda}\right)^2\right] dx \tag{A.12}$$

These integrals were solved using the Wolfram Integrator [169], yielding:

$$\sigma_{el}^{\perp,M-S} = \frac{\sigma_{\infty}\lambda^*}{\sqrt{\pi}(\lambda) erf\left(\frac{\lambda^*}{2\lambda}\right)} \tag{A.13}$$

$$\sigma_{el}^{\parallel,M-S} = \frac{\sigma_{\infty}\sqrt{\pi}(\lambda) erfi\left(\frac{\lambda^*}{2\lambda}\right)}{\lambda^*} \tag{A.14}$$

The same analysis can be performed for the oxygen vacancies:

$$\Delta Z^{\perp} = \frac{1}{\sigma_{\infty}} \int_{0}^{\lambda^*} \frac{1}{\exp\left[-\frac{1}{2}\left(\frac{x-\lambda^*}{\lambda}\right)^2\right]} dx \tag{A.15}$$

$$\sigma_{ion}^{\perp,M-S} = \frac{\sigma_{\infty}\lambda^*}{1.25331(\lambda)^* erfi\left(0.707107\frac{\lambda^*}{\lambda}\right)} \tag{A.16}$$

$$\Delta Y^{\parallel} = \sigma_{\infty} \int_{0}^{\lambda^*} \exp\left[-\frac{1}{2}\left(\frac{x-\lambda^*}{\lambda}\right)^2\right] dx \tag{A.17}$$

$$\sigma_{ion}^{\parallel,M-S} = \frac{\sigma_{\infty}{}^*1.25331(\lambda)^* erf\left(.707107\frac{\lambda^*}{\lambda}\right)}{\lambda^*} \tag{A.18}$$

### *A.3 Gouy-Chapman Solutions*

The expression for carrier profiles based on the Gouy-Chapman model is [47]:

$$\frac{c_j(x)}{c_{j\infty}} = \left( \frac{1+\Theta \exp\left(-x/\lambda\right)}{1-\Theta \exp\left(-x/\lambda\right)} \right)^{2z_j} \tag{A.19}$$

$$\Theta = \tanh\left( \frac{z_j e \Delta\phi}{4kT} \right) \tag{A.20}$$

And the width of the space charge region is 2λ for electrons and 8/3 λ for oxygen vacancies [60]. Substitution of this relationship into Eqs. A.7 and A.8 yields the following for electrons:

$$\Delta Z = \frac{1}{\sigma_\infty} \int_0^{2\lambda} \frac{1}{\left( \frac{1+\Theta \exp\left(-x/\lambda\right)}{1-\Theta \exp\left(-x/\lambda\right)} \right)^2} dx \tag{A.21}$$

$$\sigma_{el}^{\perp,G-C} = \frac{\sigma_\infty}{\frac{2\Theta}{\Theta+\exp(2)} + 1 - \frac{2\Theta}{\Theta+1}} \tag{A.22}$$

$$\Delta Y = \sigma_\infty \int_0^{2\lambda} \left( \frac{1+\Theta \exp\left(-x/\lambda\right)}{1-\Theta \exp\left(-x/\lambda\right)} \right)^2 dx \tag{A.23}$$

$$\sigma_{el}^{\parallel,G-C} = \sigma_\infty \left( 1 - \frac{2\Theta}{\exp(2)-\Theta} + \frac{2\Theta}{1-\Theta} \right) \tag{A.24}$$

The corresponding relations for the oxygen vacancies are:

$$\Delta Z = \frac{1}{\sigma_\infty}\int_0^{8\lambda/3} \frac{1}{\left(\frac{1+\Theta\exp\left(-x/\lambda\right)}{1-\Theta\exp\left(-x/\lambda\right)}\right)^4} dx \tag{A.25}$$

$$\sigma_{ion}^{\perp,G-C} = \sigma_\infty \left( \frac{\Theta\left[2\Theta^2 + 3\Theta\exp\left(\frac{8}{3}\right) + 3\exp\left(\frac{16}{3}\right)\right]}{\left(\Theta + \exp\left(\frac{8}{3}\right)\right)^3} + 1 - \frac{\Theta\left[2\Theta^2 + 3\Theta + 3\right]}{(\Theta+1)^3} \right)^{-1} \tag{A.26}$$

$$\Delta Y = \sigma_\infty \int_0^{8\lambda/3} \left(\frac{1+\Theta\exp\left(-x/\lambda\right)}{1-\Theta\exp\left(-x/\lambda\right)}\right)^4 dx \tag{A.27}$$

$$\sigma_{ion}^{\parallel,G-C} = \sigma_\infty * \left( 1 - \frac{\Theta\left[2\Theta^2 - 3\exp\left(\frac{8}{3}\right)\Theta + 3\exp\left(\frac{16}{3}\right)\right]}{\left[\exp\left(\frac{8}{3}\right) - \Theta\right]^3} + \frac{\Theta\left[2\Theta^2 - 3\Theta + 3\right]}{\left[1-\Theta\right]^3} \right) \tag{A.28}$$

These integrated profiles are summarized and applied in Section 4.6.

# REFERENCES


1. W. Shockley, "The path to the conception of the junction transistor," *IEEE Transactions on Electron Devices*, **ED-31**, 1523-1546 (1984).

2. J.S. Kilby, "Invention of the integrated circuit," *IEEE Transactions on Electron Devices*, **ED-23**, 648-654 (1976).

3. G. Moore, "Cramming more components onto integrated circuits," *Electronics Magazine* **38**, [8] (1965).

4. P. Knauth, H.L. Tuller, "Solid-state ionics: roots, status, and future prospects," *Journal of the American Ceramic Society*, **85** [7], 1654-1680 (2002).

5. H.L. Tuller, "Oxygen ion conduction and structural disorder in conductive oxides," *Journal of Physics and Chemistry of Solids* **55** [12], 1393-1404 (1994).

6. "Inventory of U.S. greenhouse gas emissions and sinks: 1990-2005," United States Environmental Protection Agency (2007).

7. P.M. Dehmer, "Facing our energy challenges in a new era of science," Department of Energy, Office of Basic Energy Sciences, *The Fall Materials Research Society Meeting*, Boston, MA (2006).

8. M. Faraday, "On conducting power generally," in *Experimental Researches in Electricity*, Series IV, 119, Royal Institution, London (1833).

9. J.-M. Gaugain, "Note sur une Classe Nouvelle de Couples Gazeux," Comptes Rendus des Seances de l Academie des Sciences **37**, 584-588 (1853).

10. W. Nernst, "Über die elektrolytische Leitung fester Körper bei sehr hohen Temperaturen," *Zeitschrift für Elektrochemie* **6**, 41-43 (1900).

11. W. Nernst, "Material for electric-lamp glowers," U.S. Patent 685,730 (1901).

12. R.F. Pierret, "Semiconductor Device Fundamentals," Reading, Massachusetts: Addison-Wesley Publishing (1996).

13. R.W. Balluffi, S.M. Allen, W.C. Carter, "Kinetics of Materials," New York: Wiley-Interscience (2005).

14. T.H. Etsell, S.N. Flengas, "Electrical properties of solid oxide electrolytes," *Chemical Review* **70**, 339-376 (1970).

15. D.J.M. Bevan, E. Summerville, in *Handbook on the Physics and Chemistry on Rare Earth's*, **4**, edited by K.A. Gschneider, L. Eyring, Amsterdam (1979).

16. H. Yahiro, Y. Eguchi, K. Eguchi, H. Arai, "Oxygen ion conductivity of the ceria-samarium oxide system with fluorite structure," *Journal of Applied Electrochemistry* **18**, 527-531 (1988).

17. M. Mogensen, T. Lindegaard, U.R. Hansen, G. Mogensen, "Physical properties of mixed conductor solid oxide fuel cell anodes of doped $CeO_2$," *Journal of the Electrochemical Society* **141**, 2122-2128 (1994).

18. M. Martin, "The influence of cation and vacancy distributions on the ionic conductivity of acceptor doped oxygen ion conductors," *Zeitschrift für Physikalische Chemie* **219**, 105-122 (2005).

19. B.T. Kilbourn, "Cerium: a Guide to its Role in Chemical Technology," Molycorp, NY (1992).

20. JCPDS – International Committee for Diffraction Data, Card 43-1002.

21. C. Wang, M. Xiao, W. Chen, Chemical Abstract Number 112:46676.

22. J. Lappalainen, H.L. Tuller, V. Lantto, "Electronic conductivity and dielectric properties of nanocrystalline $CeO_2$ thin films," *Journal of Electroceramics* **13**, 129-133 (2004).

23. G. Brauer, K.A. Gingerich, "On the oxides of cerium," *Journal of Inorganic Nuclear Chemistry* **16,** 87-99 (1960).

24. H.L. Tuller, A.S. Nowick, "Small polaron transport in reduced $CeO_2$ single crystals," *Journal of Physics and Chemistry of Solids* **38**, 859-867 (1977).

25. I.K. Naik, T.Y. Tien, "Small-polaron mobility in nonstoichiometric cerium dioxide," *Journal of Physics and Chemistry of Solids* **39**, 311-315 (1978).

26. H.L. Tuller, A.S. Nowick, "Defect structure and electrical properties of nonstoichiometric $CeO_2$ single crystals," *Journal of the Electrochemical Society* **126** [2], 209-217 (1979).

27. I. Riess, H. Janczikowski, J. Nolting, "$O_2$ chemical-potential of nonstoichiometric ceria, $CeO_{2-x}$, determined by a solid electrochemical method," *Journal of Applied Physics* **61**, 4931-4933 (1987).

28. R.J. Panlener, R.N. Blumenthal, J.E. Garnier, "Thermodynamic study of nonstoichiometric cerium oxide," *Journal of Physics and Chemistry of Solids* **36**, 1213-1222 (1975).

29. P.J.M. Bevan, J. Kordis, "Mixed oxides of the type $MO_2$ (flourite)—$M_2O_3$. 1. Oxygen dissociation pressures and phase relationships in the system $CeO_2$—$Ce_2O_3$ at high temperatures," *Journal of Inorganic and Nuclear Chemistry* **26**, 1509-1523 (1964).

30. B.C.H. Steele, J.M. Floyd, "Oxygen self-diffusion and electrical transport properties of nonstoichiometric ceria and ceria solid solutions," *Proceedings of the British Ceramics Society* **19**, 55-76 (1971).

31. Y.-M. Chiang, D. Birnie III, W.D. Kingery, *Physical Ceramics*, Wiley & Sons (1997).

32. V.J. Ruloph, *Zeitschrift für Naturforschung* **14a**, 727-737 (1959).

33. I.V. Vinokurov, Z.N. Zonn, V.A. Ioffe, "Electrical properties of cerium dioxide single crystals," *Soviet Physics-Solid State* **9** [12], 2659-2663 (1968).

34. G.V. Subba Rao, S. Ramdas, P.N. Mahrotra, C.N. Rao, "Electrical transport in rare-earth oxides," *Journal of Solid State Chemistry* **2**, 377-384 (1970).

35. F.S. Brugner, R.N. Blumenthal, "Electrical conductivity of single-crystal $CeO_2$," *Journal of the American Ceramic Society* **54**, 57 (1971).

36. H. Yahiro, K. Eguchi, H. Arai, "Electrical properties and reducibilities of ceria-rare earth oxide systems and their application to solid oxide fuel cell," *Solid State Ionics* **36**, 71-75 (1989).

37. Y.-M. Chiang, E.B. Lavik, I. Kosacki, H.L. Tuller, "Nonstoichiometry and electrical conductivity of nanocrystalline $CeO_2$," *Journal of Electroceramics* **1**, 7-14 (1997).

38. H.L. Tuller, A.S. Nowick, "Doped ceria as a solid oxide electrolyte," *Journal of the Electrochemical Society* **122**, 255-259 (1975).

39. C.J. Kevane, E.L. Holverson, R.D. Watson, "Electrolytic Conduction in Calcium-Doped Solid Cerium Oxide," *Journal of Applied Physics* **34**, 2083-2087 (1963).

40. K. Eguchi, T. Setoguchi, T. Inoue, H. Arai, "Electrical properties of ceria-based oxides and their application to solid oxide fuel cells," *Solid State Ionics* **52**, 165-172 (1992).

41. J. Kilner, "Fast anion transport in solids," *Solid State Ionics* **8**, 201-207 (1983).

42. J. Kilner, R.J. Brook, "A study of oxygen ion conductivity in doped non-stoichiometric oxides," *Solid State Ionics* **6**, 237-252 (1982).

43. D.-J. Kim, "Lattice parameters, ionic conductivities, and solubility limits in fluorite-structured $MO_2$ oxide [M = $Hf^{4+}$, $Zr^{4+}$, $Ce^{4+}$, $Th^{4+}$, $U^{4+}$] solid solutions," *Journal of the American Ceramic Society* **72**, 1415-1421 (1989).

44. B.C.H. Steele, in "High Conductivity Solid Ionic Conductors," edited by T. Takahashi, World Scientific, Singapore (1989).

45. B.C.H. Steele, "Appraisal of $Ce_{1-y}Gd_yO_{2-y/2}$ electrolytes for IT-SOFC operation at 500°C," *Solid State Ionics* **129**, 95-110 (2000).

46. J. Maier, "Ionic conduction in space charge regions," *Progress in Solid State Chemistry* **23**, 171-263 (1995)

47. D.F. Evans, H. Wennerström, *The Colloidal Domain*, Wiley-VCH (New York) (1999).

48. N.F. Mott, "The Theory of Crystal Rectifiers," *Proceedings of the Royal Society of London* **171**, 27-38 (1939).

49. W. Schottky,"Zur Halbleitertheorie der Sperrschicht- und Spitzengleichrichte," *Zeitschrift für Physik* **113**, 367-414 (1939).

50. S.M. Sze, *Semiconductor Devices*, Wiley & Sons (New York) (1985).

51. H. Gleiter, "Nanocrystalline materials," *Progress in Materials Science* **33**, 223-315 (1989).

52. H.L. Tuller, "Solid state electrochemical systems—opportunities for nanofabricated or nanostructured materials," *Journal of Electroceramics* **1**, 211-218 (1997).

53. I. Kaur, Y. Mishin, W. Gust, *Fundamentals of Grain and Interphase Boundary Diffusion*, Wiley & Sons, (West Sussex) (1995).

54. J. Maier, "Thermodynamic aspects and morphology of nano-structured ion conductors (Aspects of nano-ionics Part I)," *Solid State Ionics* **154-155**, 291-301 (2002).

55. J. Maier, "Defect chemistry and ion transport in nanostructured materials (Aspects of nanoionics Part II)," *Solid State Ionics* **157**, 327-334 (2003).

56. J. Maier, "Nano-sized mixed conductors (Aspects of nano-ionics. Part III)," *Solid State Ionics* **148**, 367-374 (2002).

57. J.-H. Hwang, T.O. Mason, "Defect chemistry and transport properties of nanocrystalline cerium oxide," *Zeitschrift für Physikalische Chemie* **207**, 21-38 (1998).

58. T. Suzuki, I. Kosacki, H.U. Anderson, P. Colomban, "Electrical conductivity and lattice defects in nanocrystalline cerium oxide thin films," *Journal of the American Ceramic Society* **84**, 2007-2014 (2001).

59. T. Suzuki, I. Kosacki, H.U. Anderson, "Defect and mixed conductivity in nanocrystalline doped cerium oxide," *Journal of the American Ceramic Society* **85** (6), 1492-1498 (2002).

60. A. Tschöpe, E. Sommer, R. Birringer, "Grain size-dependent electrical conductivity of polycrystalline cerium oxide: I. Experiments," *Solid State Ionics* **139**, 255-265 (2001).

61. A. Tschöpe, "Grain size-dependent electrical conductivity of polycrystalline cerium oxide: II. Space charge model," *Solid State Ionics* **139**, 267-280 (2001).

62. S. Kim, J. Maier, "On the conductivity mechanism of nanocrystalline ceria," *Journal of the Electrochemical Society* **149** (10), J73-83 (2002).

63. J.L.M. Rupp, L.J. Gauckler, "Microstructures and electrical conductivity of nanocrystalline ceria-based thin films," *Solid State Ionics* **177**, 2513-2518 (2006).

64. J. Maier, "On the conductivity of polycrystalline materials," *Berichte der Bunsengesellschaft für Physikalische Chemie* **90**, 26-33 (1986).

65. A. Tschöpe, R. Birringer, "Grain size dependence of electrical conductivity in polycrystalline cerium oxide," *Journal of Electroceramics* **7**, 169-177 (2001).

66. J. Lappalainen, D. Kek, H.L. Tuller, "High carrier density $CeO_2$ dielectrics—implications for MOS devices," *Journal of the European Ceramic Society* **24**, 1459-1462 (2004).

67. J. Maier, "Point defect thermodynamics: Macro- vs. nanocrystals," *Electrochemistry* **68**, 395-402 (2000).

68. T.X.T. Sayle, S.C. Parker, C.R.A. Catlow, "The role of oxygen vacancies on ceria surfaces in the oxidation of carbon monoxide," *Surface Science* **316**, 329-336 (1994).

69. S. Kim, J. Maier, "Partial electronic and ionic conduction in nanocrystalline ceria: role of space charge," *Journal of the European Ceramic Society* **24**, 1919-1923 (2004).

70. A. Ioffe, M.V. Inozemtsev, A.S. Lipilin, M.V. Perfilev, S.V. Karpachov, "Effect of the grain size on the conductivity of high-purity powder-free ceramics," *Physica Status Solidi A* **30**, 87-95 (1975).

71. M.J. Verkerk, B.J. Middelhuis, A.J. Burggraaf, "Effect of grain boundaries on the conductivity of high-purity $ZrO_2$-$Y_2O_3$ ceramics,"*Solid State Ionics* **6**, 159-170 (1982).

72. S.P.S. Badwal, J. Drennan, "Yttria-zirconia: effect of microstucture on conductivity," *Journal of Material Science* **22**, 3231-3239 (1987).

73. R. Gerhardt, A.S. Nowick, "Grain-boundary effect in ceria doped with trivalent cations: II. Microstructure and microanalysis," *Journal of the American Ceramic Society* **69**, 646-651 (1986).

74. R. Gerhardt, A.S. Nowick, M.E. Mochel, I. Dumler "Grain-boundary effect in ceria doped with trivalent cations: I. Electrical Measurements," *Journal of the American Ceramic Society* **69**, 641-646 (1986).

75. M Gödickemeier, B. Michel, A. Orliukas, P. Bohac, K. Sasaki, L. Gauckler, H. Heinrich, P. Schwander, G. Kostorz, H. Hofmann, O. Frei, "Effect of intergranular glass films on the electrical conductivity of 3Y-TZP," *Journal of Materials Research* **9**, 1228-1240 (1994).

76. S.P.S. Badwal, S. Rajendran, "Effect of micro- and nano-structures on the properties of ionic conductors," *Solid State Ionics* **70-71**, 83-95 (1994).

77. M. Aoki, Y.-M. Chiang, I. Kosacki, L.J.-R. Lee, H. Tuller, Y. Liu, "Solute segregation and grain-boundary impedance in high-purity stabilized zirconia," *Journal of the American Ceramic Society* **79**, 1169-1180 (1996).

78. X. Guo, J. Maier, "Grain boundary blocking effect in zirconia: a Schottky barrier analysis," *Journal of the Electrochemical Society* **148**, E121-E126 (2001).

79. I. Kosacki, T. Suzuki, V. Petrovsky, H.U. Anderson, "Electrical conductivity of nanocrystalline ceria and zirconia thin films," *Solid State Ionics* **136-137**, 1225-1233 (2000).

80. C. Peters, A. Weber, E. Ivers-Tiffee, H. Störmer, D. Gerthsen, M. Bockmeyer, R. Krüger, *Fall Materials Research Society (MRS) Meeting*, Boston, MA (2006).

81. N. Sata, K. Eberman, K. Eberl, J. Maier, "Mesoscopic fast ion conduction in nanometre-scale planar heterostructures," Nature 408, 946-949 (2000).

82. I. Kosacki, C.M. Rouleau, P.F. Becher, J. Bentley, D.H. Lowndes, "Surface/interface-related conductivity in nanometer thick YSZ films," *Electrochemical and Solid-State Letters* **7** (12), A459-461 (2004).

83. I. Kosacki, C.M. Rouleau, P.F. Becher, J. Bentley, D.H. Lowndes, "Nanoscale effects on the ionic conductivity in highly textured YSZ thin films," *Solid State Ionics* **176**, 1319-1326 (2005).

84. C.C. Liang, "Conduction characteristics of the lithium iodide-aluminum oxide solid electrolytes," Journal of the Electrochemical Society 120, 1289-1292 (1973).

85. C. Wagner, "The electrical conductivity of semi-conductors involving inclusions of another phase," Journal of Physics and Chemistry of Solids 33, 1051-1059 (1972).

86. X. Guo, I. Mantei, J. Jamnik, J.-S. Lee, J. Maier, "Defect chemical modeling of mesoscopic ion conduction in nanosized $CaF_2/BaF_2$ multilayer heterostructures," *Physical Review B* **76**, 125429 (2007).

87. L.G. Harrison, "Influence of dislocations on diffusion kinetics in solids with particular reference to alkali halides," *Transacations of the Faraday Society* **57**, 1191-1199 (1961).

88. T. Bak, J. Nowotny, K. Prince, M. Rekas, C.C. Sorrell, "Grain boundary diffusion of magnesium in zirconia," *Journal of the American Ceramic Society* **85**, 2244-2250 (2002).

89. J.C. Fisher, "Calculation of diffusion penetration curves for surface and grain boundary diffusion," *Journal of Applied Physics* **22**, 74-77 (1954).

90. R.T. Whipple, "Concentration contours in grain boundary diffusion," *Philosophy Magazine A* **45**, 1225-1234 (1954).

91. T. Suzuoka, "Lattice and grain boundary diffusion in polycrystals," *Transactions of the Japan Institute of Metals* **2**, 25-33 (1961).

92. A.D. LeClaire, "The analysis of grain boundary diffusion measurements," *British Journal of Applied Physics* **14**, 351-356 (1963).

93. J. Crank, *The Mathematics of Diffusion*, Oxford University Press, (London) (1956).

94. Y. Mishin, C. Herzig, "Diffusion in fine-grained materials: theoretical aspects and experimental possibilities," *NanoStructured Materials* **6**, 859-862 (1995).

95. J.M. Floyd, "Interpretation of transport phenomena in non-stoichiometric ceria," *Indian Journal of Technology* **11**, 589-594 (1973).

96. P.S. Manning, J.D. Sirman, J.A. Kilner, "Oxygen self-diffusion and surface exchange studies of oxide electrolytes having the fluorite structure," *Solid State Ionics* **93**, 125-132 (1997).

97. J.A. Kilner, J.D. Sirman, P.S. Manning, "Ionic and Mixed Conducting Ceramics III" in: Electrochemical Society Proceedings **97**, edited by T.A. Ramanarayanan, W.L. Worrell, H.L. Tuller, A.C. Khandar, M. Mogensen, w. Gopel, 560 (1998).

98. J.D. Sirman, D. Waller, J.A. Kilner, "Cation diffusion into a CGO electrolyte," in: Solid Oxide Fuel Cells V, edited by U. Stimming, S.C. Singhal, H. Tagawa, W. Lehnert, The Electrochemical Society, Pennington, NJ (1997).

99. J. Wolfenstine, P. Huang, A. Petric, "Creep behavior of doped lanthanum gallate versus cubic zirconia," *Journal of Solid State Chemistry* **118**, 257-259 (1999).

100. M. Martin, "Electrotransport and demixing in oxides," *Solid State Ionics* **136-137**, 331-337 (2000).

101. O. Schulz, M. Martin, C. Argirusis, G. Borchardt, "Cation tracer diffusion of La-138, Sr-84 and Mg-25 in polycrystalline $La_{0.9}Sr_{0.1}Ga_{0.9}Mg_{0.1}O_{2.9}$," *Physical Chemistry Chemical Physics* **5**, 2308-2313 (2003).

102. M. Kilo, "Cation transport in stabilised zirconias," *Defect and Diffusion Forum* **242-244**, 185-253 (2005).

103. D. Gryaznov, J. Fleig, J. Maier, "Numerical study of grain boundary diffusion in nanocrystalline materials," *Defect and Diffusion Forum* **237-240**, 1043-1048 (2005).

104. M. Hebb, "Electrical conductivity of silver sulfide," *Journal of Chemical Physics* **20**, 185-190 (1952).

105. C. Wagner, "Galvanische Zellen mit fested Electrolyten mit gemischter Stromleitung," *Zeitschrift für Elektrochemie* **60**, 4-7 (1956).

106. I. Riess, "Review of the limitation of the Hebb-Wagner polarization method for measuring partial conductivities in mixed ionic electronic conductors," *Solid State Ionics* **91**, 221-232 (1996).

107. I. Riess, "Four point Hebb-Wagner polarization method for determining the electronic conductivity in mixed ionic electronic conductors," *Solid State Ionics* **51**, 219-229 (1992).

108. M. Suzuki, H. Sasaki, A. Kajimura, "Oxide ionic conductivity of doped lanthanum chromite thin film interconnectors," *Solid State Ionics* **96**, 83-88 (1997).

109. W. Huang, S. Gopalan, U. Pal, "Measurement of partial oxygen ion conductivity of Sr-doped lanthanum manganite," *Journal of Power Sources* **173**, 887-890 (2007).

110. P. Knauth, H.L. Tuller, "Solute segregation, electrical properties and defect thermodynamics of nanocrystalline $TiO_2$ and $CeO_2$," *Solid State Ionics* **136-137**, 1215-1224 (2000).

111. J.F. Ready, "Development of plume of material vaporized by giant-pulse laser," *Applied Physics Letters* **3**, 11-13 (1963).

112. R.M. White, "Generation of elastic waves by transient surface heating," *Journal of Applied Physics* **34**, 3559 (1963).

113. H.M. Smith and A.F. Turner, "Vacuum deposited thin films using a ruby laser," Applied Optics **4**, 147-148 (1965).

114. J.T. Cheung and H. Sankur, "Growth of thin films by laser-induced evaporation," *Critical Reviews in Solid State and Materials Sciences* **15**, 63-109 (1988).

115. J.T. Cheung, in: Pulsed Laser Deposition of Thin Films, edited by D.B. Chrisey and G.K. Hubler, Wiley & Sons, 1-22 (1994).

116. D. Dijkkamp, T. Venkatesan, X.D. Wu, S.A. Shaheen, N. Jisrawi, Y.H. Min-Lee, W.L. McLean, M. Croft, "Preparation of Y-Ba-Cu oxide superconductor thin films using pulsed laser evaporation from high $T_C$ bulk material," *Applied Physics Letters* **51**, 619-621 (1987).

117. S.M. Green, A. Pique, K.S. Harshavardhan, in: Pulsed Laser Deposition of Thin Films, edited by D.B. Chrisey and G.K. Hubler, , Wiley & Sons, 23-54 (1994).

118. J.F. Ready, "Effects due to absorption of laser radiation,"*Journal of Applied Physics* **36**, 462-468 (1965).

119. M. Von Allmen, "Laser drilling velocity in metals," *Journal of Applied Physics* **47**, 5460-5463 (1976).

120. Materials Data, Inc., Livermore, CA.

121. S.J. Litzelman, J.L. Hertz, W.C. Jung, H.L. Tuller, "Opportunities and challenges in materials development for thin film solid oxide fuel cells:," *Fuel Cells*, DOI: 10.1002/fuce.200800034 (2008).

122. R.A. De Souza, J. Zehnpfennig, M. Martin, J. Maier, "Determining oxygen isotope profiles in oxides with Time-of-Flight SIMS ," *Solid State Ionics* **176**, 1465 (2005).

123. R.A. De Souza, M. Martin, "Secondary ion mass spectrometry (SIMS): a powerful tool for studying mass transport over various length scales," *physica status solidi (c)* **4** (6), 1785 (2007).

124. ION-TOF GmBH, Münster, Germany.

125. W.S. Kim, A. Rothschild, J.L. Hertz, H.L. Tuller, "Novel method for fabricating nano-porous platinum thin films," presented at the Fall 2005 Materials Research Society (MRS) Meeting (2005).

126. J.L. Hertz, "Microfabrication methods to improve the kinetics of the yttria stabilized zirconia—platinum—oxygen electrode," Ph.D. Thesis, Massaschusetts Institute of Technology (2006).

127. H. Huang, M. Nakamura, P. Su, R. Fasching, Y. Saito, F. B. Prinz, "High-performance ultrathin solid oxide fuel cells for low-tempearture operation," *Journal of the Electrochemical Society* **154**, B20-B24 , (2007).

128. S.J. Litzelman, R.A. De Souza, B. Butz, H.L. Tuller, M. Martin, D. Gerthsen, "Heterogeneously doped nanocrystalline ceria thin films by grain boundary diffusion: Impact on transport properties," *Journal of Electroceramics* DOI: 10.1007/s10832-008-9445-y (2008).

129. J.-H. Hwang, D.S. McLachlan, T.O. Mason, "Brick layer model analysis of nanoscale-to-microscale cerium dioxide," *Journal of Electroceramics* **3**, 7-16 (1999).

130. I. Riess, "Meaurement of ionic-conductivity in semiconductors and metals," *Solid State Ionics* **44**, 199-205 (1991).

131. L. Heyne, N.M. Beekmans, "Electronic transport in calcia-stabilized zirconia," Proceedings *of the British Ceramic Society* **19**, 229-263 (1971).

132. J.L.M. Rupp, A. Infortuna, L.J. Gauckler, "Microstrain and self-limited grain growth in nanocrystalline ceria ceramics," *Acta Materialia* **54**, 1721-1730 (2006).

133. C.V. Thompson, "Structure evolution during processing of polycrystalline films," Annual *Review of Materials Science* **30**, 159-190 (2000).

134. S.K. Ghandi, *VLSI Fabrication Principles*, Wiley & Sons (New York) (1994).

135. H.L. Tuller, "ZnO grain boundaries: electrical activity and diffusion," *Journal of Electroceramics* **4**, 33-40 (1999).

136. H..-H. Möbius, H. Witzmann, D. Gerlach, "Untersuchungen zur Kationendiffusion im System $Zr_{0.85}Ca_{0.15}O_{1.85}$," *Zeitschrift für Chemie* **4**, 154-155 (1964).

137. T. Bak, J. Nowotny, K. Prince, M. Rekas, C.C. Sorrell, "Grain boundary diffusion of magnesium in zirconia," *Journal of the American Ceramic Society* **85**, 2244-2250 (2002).

138. J.W. Osenbach, V.S. Stubican, "Grain-boundary diffusion of Cr-51 in MgO and Cr-doped MgO," *Journal of the American Ceramic Society* **66**, 191-195 (1983).

139. A. Atkinson, R.I. Taylor, "Impurity diffusion in NiO grain-boundaries," *Journal of Physics and Chemistry of Solids* **47**, 315-323 (1986).

140. C.D. Baertsch, K.F. Jensen, J.L. Hertz, H.L. Tuller, S.T. Vengallatore, S.M. Spearing, M.A. Schmidt, "Fabrication and structural characterization of self-supporting electrolyte membranes for a micro solid-oxide fuel cell," *Journal of Materials Research* **19**, 2604-2615 (2004).

141. Z.P. Shao, S.M. Haile, J. Ahn, P.D. Ronney, Z.L. Zhan, S.A. Barnett, "A thermally self-sustained micro solid-oxide fuel-cell stack with high power density," *Nature* **435**, 795-798 (2005).

142. D. Beckel, A. Bieberle-Hütter, A. Harvey, A. Infortuna, U.P. Muecke, M. Prestat, J.L.M. Rupp, L.J. Gauckler, "Thin films for micro solid oxide fuel cells," *Journal of Power Sources* **173**, 325-345 (2007).

143. A. Mai, M. Becker, W. Assenmacher, F. Tietz, D. Hathiramani, E. Ivers-Tiffée, D. Stöver, W. Mader, "Time-dependent performance of mixed-conducting SOFC cathodes," *Solid State Ionics* **177**, 1965-1968 (2006).

144. V.V. Kharton, A.V. Kovalevsky, A.P. Viskup, F.M. Figueiredo, A.A. Yaremchenko, E.N. Naumovich, F.M.B. Marques, "Oxygen permeability and Faradaic efficiency of $Ce_{0.8}Gd_{0.2}O_{2-\delta}$—$La_{0.7}Sr_{0.3}MnO_{3-\delta}$ composites," *Journal of the European Ceramic Society* **21**, 1763-1767 (2001).

145. L. Kindermann, D. Das, H. Nickel, K. Hilpert, "Chemical compatibility of the LaFeO3 base perovskites ($La_{0.6}Sr_{0.4}Fe_{0.8}M_{0.2}O_{3-\delta}$ (M = Cr, Mn, Co, Ni) with ytrria stabilized zirconia," *Solid State Ionics* **89**, 215-220 (1996).

146. J. Hiltunen, D. Seneviratne, R. Sun, M. Stolfi, H.L. Tuller, J. Lappalainen, V. Lantto, "$BaTiO_3$-$SrTiO_3$ multilayer thin film electro-optic waveguide modulator," *Applied Physics Letters* **89**, 242904 (2006).

147. J. Ranlov, F.W. Poulsen, M. Mogensen, "Comment on 'The characterization of doped $CeO_2$ electrodes in solid oxide fuel cells' by B.G. Pound," *Solid State Ionics* **61**, 277-279 (1993).

148. M. Hrovat, J. Holc, S. Bernik, D. Makovec, "Subsolidus phase equilibria in the NiO—$CeO_2$ and $La_2O_3$—$CeO_2$—$Fe_2O_3$ systems," *Materials Research Bulletin* **33**, 1175-1183 (1998).

149. B.G. Pound, "The characterization of doped $CeO_2$ electrodes in solid oxide fuel cells," *Solid State Ionics* **52**, 183-188 (1992).

150. R.D. Shannon, "Revised effective ionic radii and systematic studies of interatomic distances in halides and chalcogenides," *Acta Crystallographic A* **32**, 751-767 (1976).

151. W.D. Kingery, H.K. Bowen, D.R. Uhlmann, *Introduction to Ceramics*, Wiley (New York) 1976.

152. H.L. Tuller, "Mixed conduction in nonstoichiometric oxides," in *Nonstoichiometric Oxides*, edited by O.T. Sorensen, Academic Press (New York), 271-335 (1981).

153. J. Mizusaki, K. Amano, S. Yamaguchi, K. Fueki, "Electrode-reaction at Pt, O2(G)/stabilized zirconia interfaces. 1. Theortical consideration of reaction model," *Solid State Ionics* **22**, 313-322 (1987).

154. M.J. Verkerk, M.W.J. Hammink, A.J. Burggraaf, "Oxygen transfer on substituted $ZrO_2$, $Bi_2O_3$, and $CeO_2$ electrolytes with platinum electrodes – I. electrode resistance by D-C polarization," *Journal of the Electrochemical Society* **130**, 70-78 (1983).

155. Wayne Rasband, ImageJ software available at http://rsbweb.nih.gove/ij/index.html.

156. D.Y. Wang, D.S. Park, J.Griffith, A.S. Nowick, "Oxygen-ion conductivity and defect interactions in yttria-doped ceria," *Solid State Ionics* **2**, 95-105 (1981).

157. S. Kim, J. Fleig, and J. Maier, in: Ionic and Mixed Conducting Ceramics IV, edited by T.A. Ramamarayanan, W.L. Worrell, M. Mogensen, The Electrochemical Society Proceedings (Pennington, NJ) p. 208 (2001).

158. R.A. Gerhardt, A.S. Nowick, "Grain-boundary effect in ceria doped with trivalent cations. 1. Electrical measurements," *Journal of the American Ceramic Society* **69**, 641-646 (1986).

159. J. Tanaka, J.-F. Baumard, P. Abelard, "Nonlinear electrical-properties of grain-boundaries in an oxygen-ion conductor," *Journal of the American Ceramic Society* **70**, 637-643 (1987).

160. P. Sarkar and P.S. Nicholson, "Electric relaxation studies of defects and defect associates in dilute ceria lanthanum oxide solid-solutions," *Journal of the American Ceramic Society* **72**, 1447-1449 (1989).

161. Analysis performed by Luvak, Inc. (Bolyston, MA).

162. D.A. Blom, "Grain boundary chemistry and morphology of heavily doped cerium dioxide," Sc.D. Thesis, Massachusetts Institute of Technology (1998).

163. E.H. Rhoderick, R.H. Williams, Metal-semiconductor contacts, Claredon Press (Oxford) (1988).

164. H.J. Avila Paredes, S. Kim, "The effect of segregated transition metal ions on the grain boundary resistivity of gadolinium doped ceria: alteration of the space charge potential," *Solid State Ionics* **177**, 3075-3080 (2006).

165. R.A. De Souza, J. Fleig, J. Maier, Z. Zhang, W. Sigle, M. Rühle, "Electrical resistance of low-angle tilt grain boundaries in acceptor-doped $SrTiO_3$ as a function of misorientation angle," *Journal of Applied Physics* **97**, 053502 (2005).

166. S.R. Rotman, H.L. Tuller, "Defect-property correlations in garnet crystals. III. The electrical conductivity and defect structure of luminescent nickel-doped yttrium aluminum garnet," *Journal of Applied Physics* **62**, 1305-1312 (1987).

167. G. Gregori, X.X. Guo, Y.Q. Zhang, J. Maier, "Conduction properties of $CeO_2$-based thin films," Presented at the Electroceramics XI Conference, Manchester, England (2008).

168. J. Garcia-Barriocanal, A. Rivera-Calzada, M. Varela, Z. Sefrioui, E. Iborra, C. Leon, S.J. Pennycook, J. Santamaria," Colossal ionic conductivity at interfaces of epitaxial $ZrO_2$:$Y_2O_3$/$SrTiO_3$ heterostructures," *Science* **321**, 676-680 (2008).

169. Wolfram Integrator: http://integrals.wolfram.com/index.jsp.